Characterisation of Dry Etching Damage in III-V and II-VI Semiconductors

A Thesis submitted to

the Faculty of Engineering of the

University of Glasgow for the degree of

Doctor of Philosophy

by

Abdul Majeed Ali Foad B.Sc. (Phys.), M.Sc. (Chem.)

January 1992

ProQuest LLC.
789 East Eisenhower Parkway
P.O. Box 1346
Ann Arbor, MI 48106 – 1346

Acknowledgements

I wish to remember the late Professor J. Lamb and acknowledge the support he gave me during the last three years, and also for the provision of the excellent research facilities in the department of Electronics and Electrical Engineering.

I would like to sincerely thank my supervisor Professor Chris D. W. Wilkinson for the invaluable advice and encouragement given to me throughout this work. I am indebted to Professor Steve P. Beaumont, Dr Clivia Sotomayor Torres and Dr Steve Thoms for many useful discussions, and Dr Colin Stanley for MBE growing of high quality GaAs.

The collaboration with Professor John Chapman, Dr Stuart Hefferman in the department of Physics and Astronomy and Dr John Fryer in the department of Chemistry regarding the TEM analysis was both fruitful and enjoyable and I would like to thank them for the advice and assistance given to me. I am also grateful to Professor Robin H. Williams, Dr Stephnie Walters and Mr Chris Dunscomb of the department of Physics, University of Wales College of Cardiff for the assistance in X-ray Photoelectron Spectroscopy. Thanks are also due to Dr Morag Watt, Dr Pei Don Wang and Mr Andrew Smart for their collaboration on the Photoluminescence spectroscopy and Raman scattering.

The technical support of the Electronic Engineering department is greatly appreciated, in particular D. M. S. MacIntyre, D. Gourly, S. Ferguson, H. McLelland, G. Hopkins in the UltraSmall Structure Lab., R. Darkin, D. Clifton in the dry etching lab. and L. Hobbs and R. Harkins in the clean room and photolithography masks preparation.

Special thanks go to my fellow research students and friends with whom I shared many enjoyable moments and interesting discussions in particular, K. Thomas, M. Rahman, A. Craig, N. Cameron, I. Thayne, T. Krauss, J. Thompson, Dr M. Holland, Dr A. Kean and my ex-office mates who are scattered across the globe Dr R. K. Henderson, Dr D. Leith, Dr R. Cheung and Mrs G. Hughes with whom I shared many thoughtful philosophical discussions and outdoor activities.

I would like to express my personal gratitude to Chris and Judy Wilkinson and Ray and Irene Hutchins for their help and understanding especially through the final year of my study, and to Francis and Dorothy Smith for their support and financial help during the second and third year of my study.

My deepest appreciation goes to my family and my wife, Wendy, for their love and everlasting support which kept me going during my studying years in the U.K. Special thanks goes again to Ray Hutchins and Wendy for proof reading this thesis.

Finally I would like to acknowledge the financial support of the ministry of higher education in Iraq for the financial support during the first 21 months of this study.

Summary

Dry etching induced surface damage has been characterised, in a novel way, for thin n^+ GaAs epitaxial layers, by measuring the surface conductance using the Transmission Line Model (TLM) technique and Hall measurements. Various dry etching processes have been investigated for example, rf Reactive Ion Etching (rf-RIE) using CH_4/H_2 and $SiCl_4$, Electron Cyclotron Resonance (ECR-RIE) using CCl_2F_2/He and Ion Beam etching using Ar and Ne. The results of which have been compared with wet etching and damage depths have been obtained. Damage saturation effect, predicted by the theory, has been observed for the RIE GaAs. The modification in the depletion layer thickness induced by dry etching has been determined using Raman scattering of coupled LO phonon- plasmon modes on the TLM samples. Criteria for damage free etching are suggested.

Modifications induced by the dry etching to the surface chemistry of GaAs have been investigated using X-ray Photoelectron Spectroscopy (XPS). Information about the top 3nm of surfaces etched using CH_4/H_2 and $SiCl_4$ has been obtained and compared with unetched samples.

Damage to the sidewalls of nanostructures has been examined using Transmission Electron Microscopy using a dark field imaging technique and by High Resolution TEM. Quantum wire-like structures with widths down to 50nm have been etched using CH_4/H_2 and $SiCl_4$ and have been used as TEM specimens. Changes in the stoichiometry of GaAs and disorder in the lattice have been observed. Wires made of etched-regrown material were examined and the quality of the growth interface was evaluated.

A high resolution etch process was developed using ECR-RIE in CCl_2F_2/He. This process produced low damage in nanostructures. The damage has been characterised using TLM, n^+ GaAs quantum wires, Raman scattering using LO coupled Phonon-Plasmon modes and LO phonon Raman scattering using undoped GaAs.

A novel high resolution reactive ion etching process has been developed for a variety of binary and ternary II-VI semiconductor compounds using CH_4/H_2. The process is optimised to produce nanostructures in ZnTe, ZnSe, ZnSSe, ZnS, CdTe, CdMnTe and CdS. Dots 200nm high and 26nm in diameter have been demonstrated in ZnSe. The advantage of this process lies in the fact that exactly the same etching conditions are suitable for all II-VI Semiconductors, so that quantum wells of any variety can be easily etched.

Finally, the modifications induced by the RIE in II-VI semiconductors are investigated by XPS, Photoluminescence and Raman scattering in ZnTe and ZnSe and by XPS and Schottky diode parameter evaluation in CdTe.

Publications arising from the Ph.D. work

1 **"Raman scattering of III-V and II-VI semiconductor microstructures"**, M Watt, A P Smart, M A Foad, C D W Wilkinson, H E G Arnot, and C M Sotomayor Torres, *NATO ARW "Light Scattering in Semiconducto Structures and Superlattices", March (1990), Canada.*

2 **"Evaluation of sidewall damage in nanostructures etched in CH_4/H_2 and $SiCl_4$, by direct TEM Observation"**, M A Foad, S Hefferman, J Chapman, and C D W Wilkinson, *Proceedings of17th Int. Smy. on GaAs and Related Compounds, pp 293, Inst. Phys. Conf. Ser. No 112: Chapter 5, 24-27 September (1990), Jersey.*

3 **"Dry etching of II-VI's and its associated assessment"**, A P Smart, M A Foad, M Watt, C M Sotomayor Torres, and C D W Wilkinson, *a talk presented in the 8th II-VI Interaction Meeting, University of Hull, 27-28 Seprember (1990), Hull, U.K.*

4 **"Reactive ion etching of II-VI semiconductors using a mixture of methane and hydrogen"**, M A Foad, A P Smart, M Watt, C M Sotomayor Torres, and C D W Wilkinson, *Electronics Lett., 27, 73, (1991).*

5 **"High resolution dry etching of zinc telluride : Characterisation of etched surfaces by X-ray photoelectron spectroscopy, Photoluminescence and Raman scattering"**, M A Foad, M Watt, A P Smart, C M Sotomayor Torres, C D W Wilkinson,W Kuhn, H P Wagner, S Bauer, and W Gebhardt, *Semicond. Sci. & Technol. 6, A115, (1991).*

6 **"High resolusion TEM of GaAs nanostructures reactive ion etched in $SiCl_4$ and CH_4/H_2 plasmas: A comparision"**, M A Foad, S J Hefferman, J N Chapman, J R Fryer, and C D W Wilkinson, *poster presented in the 7th Oxford Conference on Microscopy of Semiconducting Materials, 24-28 March (1991), Oxford, U.K.*

7 **"Wide gap II-VI semiconductor nanostructures: Fabrication and optical spectroscopy"**, A P Smart, M A Foad, M Watt, W Kuhn, H P Wagner, H Leiderer, S Bauer C M Sotomayor Torres, C D W Wilkinson, W Gebhardt, and M Razeghi, *paper presented in EPS-CMD meeting, April (1991), Exeter, U.K.*

8 **"Fabrication and optical assessment of wires and dots in ZnTe and ZnSe"**, M A Foad, A P Smart, M Watt, C M Sotomayor Torres, W Kuhn, P Wagner, H Leiderer, S Bauer, C D W Wilkinson, W Gebhardt, and M Razeghi, *paper presented at the Conference on Nanostructures and Mesoscopic Systems, May 20-24, (1991), Santa Fe, to appear in Superlattices and Microstructures.*

9 **"Optical assessment of reactive ion etched ZnTe and ZnSe for nanostructures"**, M A Foad, A P Smart, M Watt, C M Sotomayor Torres, W Kuhn, P Wagner, H Leiderer, S Bauer, C D W Wilkinson, W Gebhardt,and M Razeghi, *presented at the Fifth Int. Conf. on Modulated Semiconductor Structures, July 8-12, (1991), Nara, Japan, to appear in Surface science.*

10 **"Development of High Resolution Reactive Ion Etching of II-VI Semiconductors Using CH_4/H_2"**, M A Foad, C Dunscomb, R H Williams and C D W Wilkinson, *presented at The Topical Meeting for Microfabrication for Photonics and Optoelectronics (Leos), July 29-31, 1991, Newport Beach, USA.*

11 **" Raman scattering of coupled LO phonon-plasmon modes in dry etched n+ GaAs"**, P D Wang, M A Foad, C M Sotomayor Torres, S Thoms, M Watt, R Cheung, C D W Wilkinson, and S P Beaumont, *Accepted for publication in Appl. Phys. Lett. Sept. (1991).*

12 **"CH_4/H_2: An universal dry etch mixture for II-VI semiconductor compounds ?"**, M A Foad and C D W Wilkinson, *submitted to Appl. Phys. Lett. November (1991).*

13 **"A new technique for dry etch damage assessment in GaAs"**, M A Foad, S Thoms, and C D W Wilkinson, *submitted to J. Appl. Phys., November (1991).*

14 **"Dry etch damage in III-V Semiconductors"**, G Doughty, M A Foad, R Cheung, N Cameron, M Rahman, S Thoms, S P Beaumont and C D W Wilkinson, *a talk presented at a one-day meeting on "Plasma Damage in Electronic Devices", Institute of Physics, London, 26 Nov. (1991).*

15 **"Dry etch damage characterised by Raman Scattering"**, P D Wang, M A Foad, C M Sotomayor Torres and C D W Wilkinson, *a talk presented at a one-day meeting on "Plasma Damage in Electronic Devices", Institute of Physics, London, 26 Nov. (1991).*

16 **"Raman Scattering and Luminescence (PL and PLE) Studies of GaAs-AlGaAs Quantum Wires and Dots"**, P D Wang, C M Sotomayor Torres, S Thoms, and M A Foad, *submitted to 'Symposium on Nanostructures II', Aug. (1991).*

17 **"Nanostructure fabrication: Dry etching damage"**, G. F. Doughty, R. Cheung, M. A. Foad, M. Rahman, N. I. Cameron, N. P. Johnson, P. D. Wang, and C. D. W. Wilkinson, *presented in the MRS Fall meeting, 4 Dec , Boston, USA (1991).*

18 **"High resolution reactive ion etching of zinc telluride and znic selenide"**, M A Foad, M Watt, A P Smart, C M Sotomayor Torres, C D W Wilkinson, W Kuhn, H P Wagner, S Bauer, W Gebhardt, and M Razeghi, *to be submitted to J. Appl. Phys., Jan (1992).*

19 **"A model for dry etch damage in GaAs"**, M Rahman, N P Johnson, M A Foad, M Holland, C D W Wilkinson, and A P Long, *in preparation.*

20 **"Electron traps in $SiCl_4$ Reactive ion etched GaAs"**, N P Johnson, M A Foad, and C D W Wilkinson, *in preparation.*

Previous publications arising from the M.Sc. Work

21 **"Chemical and optical properties of proton-exchange lithium niobate optical waveguides"**, Invited talk, R M De La Rue, M A Foad, A Loni, and J M Winfield, *Two day meeting, " Solid State Materials", University of Aberdeen, 10-11 October (1989), Aberdeen, U.K.*

22 **"Characterisation of waveguides for lithium niobate integrated optics"**, Invited paper, R M De La Rue, M A Foad, A Loni, S McMeekin, and J M Winfield, *Technical Digest of Second Optoelectronics Conference, 2-4 October (1988), Tokyo Institute of Technology, Japan.*

23 **"Determination of the extent of reaction in proton-exchange $LiNbO_3$ optical waveguides"**, A Loni, R M De La Rue, M A Foad, and J M Winfield, *Proceeding of the Topical Meeting on Integrated and Guided- Wave Optics, 4-8 February (1989), Houston, Texas, USA.*

24 **"Proton-exchanged lithiun niobate optical waveguides made from phosphoric acid: detailed studies and comparisons with guides made with benzoic acid"**, M A Foad, A Loni, R W Keys, J M Winfield, and R M De La Rue, *SPIE proceedings, "Conference on Integrated Optical Circuits Engineering VII", 5 September (1989), Boston, USA.*

25 **"Optical characterisation of Z-cut proton-exchanged $LiNbO_3$ waveguides fabricated using Orthophosphoric and Pyrophosphoric acid"**, A Loni, R W Keys, R M De La Rue, M A Foad, and J M Winfield, *IEE Proceedings-J "Optoelectronics", 136, 297-300 (1989).*

26 **"Refractive index changes in proton-exchanged $LiNbO_3$ by ion implantation"**, E Glavas, P D Townsend and, M A Foad, *Nuclear Instruments and Methods in Physics Research, **B46**, 156-159 (1990).*

Table of Contents

Chapter 1: Introduction

1.1. General introduction

Since the suggestion of J. R. Schrieffer[1] in 1957, that the narrow confinement potential of an inversion layer may lead to observation of non-classical electron transport behaviour, remarkable advances have been made in growing high quality crystal semiconductors. The advent of ultra-thin epitaxial growth film techniques, for example, Molecular Beam Epitaxy (MBE), began the era of reduced dimensionality physics[2-4] where heterojunction interfaces with large energy band discontinuities, such as GaAs/AlGaAs, were produced routinely. These structures are inherently two dimensional; therefore investigations concentrated on heterostructures, where quantum effects were due to the confinement in the epitaxial direction. The ability to vary composition, band offset, periodicity and other variables created limitless possibilities in producing structures for physical exploration, electron and optical devices.

Within the last decade, advances in microfabrication technology have allowed workers in this field to impose additional lateral dimensions of quantum confinement on 2-dimentional systems with a length scale comparable to the de Broglie wavelength of the electrons.

The turning point in understanding nanometric scale electronic transport and optical properties was the development of a reliable semiconductor fabrication technique on the nanometer scale, for example, the fabrication of semiconductor quantum wires and quantum dots[5-7]. The state-of-the-art fabrication techniques may involve high resolution electron beam lithography for pattern definition and dry etching for pattern transfer. The advantages of dry etching over wet etching are the etch anisotropy, etch depth control, selectivity, uniformity across the wafer and reproducibility from wafer to wafer. However, the action of energetic ions bombarding the surface and sidewalls of the etched structures during dry etching can cause damage to the semiconductor causing degrading of the optical and electrical performance of the material. The damage inflicted on the semiconductor is significant when the etched structures are in the nanometer scale.

This thesis will report on the characterisation of the electrical, optical and structural modifications (or damage) induced by various dry etching processes in GaAs. The strategy adopted in this work to investigate the dry etching damage is to approach the problem from various angles by using many different techniques.

The advances in epitaxial growth techniques have renewed interest in growing quality p- and n- type II-VI semiconductors, in particular the wide band gap compounds, for optical devices. Whilst writing this thesis, the first blue semiconductor laser, based on ZnSe/ZnCdSe single quantum well, has been reported by 3M[8].
This thesis will also give an account of the development of a universal high resolution reactive ion etching (RIE) process for a variety of II-VI semiconductors, and the effect RIE induces on these semiconductors.

1.2. Content of the thesis

Chapter 2 of this thesis gives a brief account of the principles of electron beam lithography as a tool for high resolution pattern definition and various dry etching techniques for transferring the pattern on to the semiconductor substrate. The application, mechanism and proposed chemistry of dry etching, in particular RIE and Electron Cyclotron Resonance-RIE (ECR-RIE), are discussed in the case of GaAs etching in $SiCl_4$, CH_4/H_2 and CCl_2F_2/He. The possible sources of dry etching damage are considered.
In chapter 3, the surface conductance and damage depths of n^+ GaAs dry etched using $SiCl_4$ and CH_4/H_2 RIE, Ar and Ne ion beam etching (IBE) were measured and compared with wet etching. The transmission line method was used in a novel way to measure the conductance, in addition to Hall measurements. Etched n^+ GaAs was also examined by coupled plasmon-LO phonon Raman scattering. Depletion depths estimated by the latter method were compared with the damage depths obtained from the conductance measurements.
Chapter 4 presents a comparative study of the structural damage in sidewalls of quantum wire-like structures etched using $SiCl_4$ and CH_4/H_2. The sidewall damage was examined using these nanostructures as specimens for Transmission Electron Microscope so that low and high resolution TEM images of GaAs lattice were obtained. Wires prepared from etched-regrown GaAs were also examined and the quality of the growth interface was assessed.
Chapter 5 examines the effect of RIE on GaAs surfaces using X-ray Photoelectron Spectroscopy (XPS). Analysis of the detected elements was carried out for the top 1nm and 3nm of surfaces etched under various conditions using $SiCl_4$ and CH_4/H_2.
Chapter 6 reports on the development of a high resolution, low damage ECR-RIE process for GaAs using CCl_2F_2/He. The surface damage was investigated for n^+ GaAs using the

surface conductance method and coupled plasmon-LO phonon Raman scattering, and LO phonon Raman scattering for undoped GaAs. The sidewall damage was examined by evaluating the cut-off width of n^+ GaAs quantum wires.

Chapter 7 involves the development of a universal, high resolution RIE process for II-VI semiconductors using CH_4/H_2. Nanostructures were fabricated in ZnTe, ZnSe, ZnSSe, ZnS, CdTe, CdMnTe and CdS and quantum dots 26nm in diameter 200nm high were demonstrated in ZnSe.

Chapter 8 presents a study of the surface damage induced by the dry etching process on ZnTe, ZnSe and CdTe. Etched surfaces of ZnTe and ZnSe were examined using Photoluminescence, (resonant) Raman scattering, and XPS while etched CdTe surfaces were investigated using XPS and Schottky junction characteristics

Finally, chapter 9 presents an overall view of the findings produced from this work and gives suggestions for future work.

1.3. References

1. J. R. Schrieffer in 'Semiconductor Surface Physics', ed. R. H. Kingston, pp55, University of Pennsylvania press, Philadelphia (1957).
2. J. N. Randall, M. A. Reed, and G. A. Frazier, J. Vac. Sci. Technol., **B7**, 1398 (1989).
3. M. J. Kelly, Semicond. Sci. Technol., **5**, 1209 (1990).
4. M. A. Reed, and W. P. Kirk in 'Nanostructure Physics and Fabrication' ed. M. A. Reed, and W. P. Kirk, pp3, Academic press, CA (1989).
5. H. van Houton, D. J. van Wees, M. G. J. Heijman, and J. P. Andre, Appl. Phys. Lett., **49**, 1781 (1986).
6. G. Timp, A. M. Chang, P. Mankiewich, R. Behrniger, J. E. Cunningham, T. Y. Chang, and R. E. Howard, Phys. Rev. Lett., **59**, 732 (1987).
7. M. A. Reed, J. A. Randall, R. J. Aggarwal, R. J. Matyi, T. M. Moore, and A. E. Wetsel, Phys. Rev. Lett., **60**, 535 (1988).
8. M. A. Haase, J. Qiu, J. M. DePuydt, and H. Cheng, to appear in Appl. Phys. Lett.

Chapter 2: Electron beam lithography and dry etching

2.1. Introduction

In this chapter, the techniques used for patterning and transferring the patterns onto the semiconductor substrate are discussed. For patterning, electron beam lithography as well as the conventional photolithography were used, however only electron beam lithography will be discused in detail. For pattern transfer, dry etching techniques, including ion beam etching (IBE), rf-reactive ion etching (RF-RIE) and electron cyclotron resonance- reactive ion etching (ECR-RIE) were used and therefore, will be discussed.

Electron beam lithography (EBL) is a method of defining patterns on a substrate using a focused beam of electrons in a high vacuum system. The impact of the electrons changes the chemical and physical properties of a thin layer of resist on the substrate. The pattern is transferred by selectively removing the exposed (or unexposed) resist in a chemical development step.

EBL offers much higher resolution in the patterning of features than optical lithography which is currently the standard method used in the semiconductor industry. The resolution limit of EBL is in the order of 10nm on a thin substrate using PMMA, whereas that of optical lithography is in the order of 250nm. For the ultimate electron beam resolution (10nm), 4-6nm of this is caused by the low energy secondary electrons which are created by the primary beam; the remaining 4nm is due to chemical effects in the PMMA- presumably molecular size related. On solids, the resolution is further limited by the electrons which re-emerge from the substrate- often at considerable distances from the point of entry[1,2]. This causes an overall reduction in the contrast of the electron image.

This effect depends on the rate of production of secondary electrons at the point where the primary beam strikes. In a region where this scattering coefficient is large (for example where there is metal patterned earlier) more secondary electron are produced. This phenomena gives rise to the proximity effect - which is the variation of the developed resist pattern from the pattern written by electron beam.

This effect can be compensated for by varying the exposure dose for each shape so that the average exposure for each shape is the same. High accelerating voltages, ≥50kV, also reduce the proximity effect more as the centre of creation of back-scattered electrons is displaced further away from the surface.

EBL allows rapid changes in the pattern design as no mask has to be fabricated. However, EBL exposures are performed serially, one pixel (or block) at a time, whereas in optical lithography the exposure of all pattern features is performed in parallel over a relatively large field. The result is that even with very high data exposure rates (up to 300MHz has been used) and sensitive resists, EBL cannot compete with optical lithography in terms of throughput of exposed resist.
However EBL is the only route for the creation of nanostructures less than 250nm and so has been used for the work described in chapters 4, 6 and 8.

2.2. Electron beam resists

In the context of EBL a resist is used as a medium for transferring a pattern onto a substrate by acting as a stencil for deposition or as a resistant layer for etching. A uniform layer of resist is deposited onto the substrate surface by spin-coating. The action of exposure by the electron beam allows the selective removal of either the exposed resist (in the case of a positive resist) or the unexposed resist (in the case of a negative resist). When a positive resist is exposed to an electron beam, the polymer- electron interaction breaks the polymeric back bone of the resist forming shorter molecular fragments. As a result the molecular weight is reduced in the exposed area and hence can be dissolved in a developer solution leaving a resist stencil on the substrate. When a negative electron resist is exposed, the molecular weight of the exposed area increases due to the cross linking of the molecules thereby decreasing their solubility in the developer. On development, the areas which are not exposed are dissolved, Fig. 2.1.

2.2.1. PMMA

In the work described in this thesis, high resolution pattern definition was achieved using poly(methyl methacrylate) (PMMA) which is a positive resist. It is an organic polymer consisting of long-chain molecules of $[CH_2CCH_3COOCH_3]_n$. Two samples of PMMA of different average molecular weights was used: 185 000 molecular weight (from BDH Chemicals Ltd.) and 350 000 Molecular weight ("Elvacite" from Dupont). These resists are referred to in the text as "BDH" and "Elvacite".

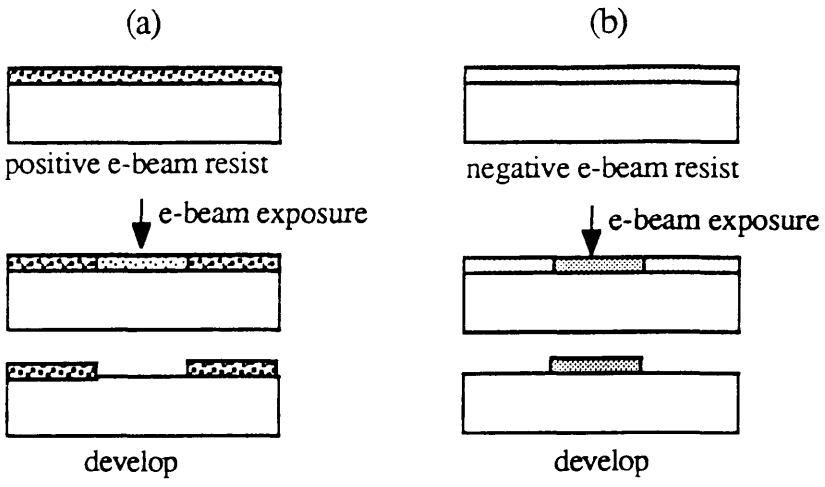

Figure 2.1: Schematic diagrams illustrating the pattern definition processes using (a) positive resist and (b) negative resists.

2.2.2. Deposition

The PMMA was deposited onto the substrate as a thin film. This was achieved by dissolving the resist (supplied as a fine white powder) in a casting solvent then spin-coating the substrate with the solution. The resist forms a uniform film and most of the solvent evaporates during spinning. The remaining solvent is driven out of the resist by baking at a temperature (180°C), well above the glass transition point of the PMMA (118°C).
The thickness of the film is determined by the viscosity of the solution (which depends on the concentration of the PMMA) and the rate of spin. In this work the solvent o-xylene is used for dissolving the PMMA in concentrations of 4% by weight of polymer. For high resolution work, the 4% BDH and 4% Elvacite resists were spun at 6000rpm for 60sec yielding thicknesses of 100nm and 20nm respectively. For low resolution work, chlorobenzene is used to dissolve 15% by weight of polymer (BDH) yielding a thicker layer than possible using o-xylene(a single isomer of xylene). It was found that using mixed isomer xylene yielded unreliable solubility and thickness of PMMA[3]. 15% BDH was spun at 6000rpm for 60sec.

2.2.3. Bilayer Resists

An enhanced undercut profile has been achieved with a PMMA bilayer resist[4], which has been shown to be excellent for high resolution lithography[5,6]. This scheme uses two layers of PMMA) with different sensitivities. High sensitivity (low molecular weight PMMA is

underneath a less sensitive high molecular weight layer. This lower layer responds to the laterally broader, lower dose part of the incident and backscattered beamresulting in an undercut profile, Fig. 2.2.

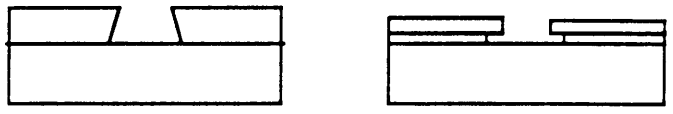

Figure 2.2: Developed profiles of (a) single layer (thick) PMMA and (b) bilayer resist system.

There are several benefits of the bilayer resist.

1) The undercut profile facilitates subsequent pattern transfer by lift-off.

2) Overdevelopment of the resist has little effect on the undercut profile, unlike the profile of a single layer which will be more severely affected. Thus the bilayer gives an increase in development latitude.

3) The top layer which defines the pattern is shielded from the substrate backscattered electrons by the lower layer effectively reducing the proximity effect [7].

4) A bilayer resist allows use of exposures just above the critical dose for the top layer, which would not lead to a developed undercut in the absence of the more sensitive bottom layer. In this way higher resolution can be obtained with a bilayer.

The bilayer resist was developed in a 3:1 solution of Isopropyl alcohol (IPA): Methylisobutylketone (MIBK) for 90sec at 23°C, followed by a 30sec rinse in IPA. On the other hand, the 15% BDH resist was developed in 1:1 solution of IPA:MIBK for 45sec at 23°C, followed by a 30sec rinse in IPA .

2.2.4. Lift-off

Metal was deposited by evaporation onto the samples. The metal adhered to the substrate where the resist had been cleared by development and also to the remaining resist. The metal on top of the resist was unwanted and was dislodged by removing the underlying resist with a soak in warm acetone. This process is called lift-off. The metal in the exposed area should be unaffected by metal on top of the resist. This can be ensured by restricting the thickness of the metal to less than about two thirds of the resist thickness and also by

utilising the undercut profile obtained with a bilayer resist as described above. The metals used, Nichrome and Titanium, both have small grain size which is suitable for high resolution patterning. NiCr was used with $SiCl_4$ etching and Ti when the gas is CH_4/H_2 as each metal has a low sputtering rate with the respective gases. The etch ratio of NiCr:GaAs in $SiCl_4$, also called the selectivity, is >1:50 and Ti:GaAs in CH_4/H_2 >1:20.

2.2.5. Negative resist

A negative resist , used only occasionally in this work, was Philips High Resolution Negative resist (HRN)[8]. 8% HRN was spun coated on the substrate at 6000rpm for 60sec and baked at 120°C for >1hr to give a thickness if 0.1μm. After exposure, the resist was developed by two successive cycles of immersion in MIBK for 15sec at 23°C then a rinse in IPA for 30sec.

2.3. Electron beam writing

The lithography in this work was performed with a Philips PSEM 500 scanning electron microscope, shown schematically in Fig. 2.3. The machine has been modified for electron beam lithography as described by Mackie[7]. The PSEM 500 is a general purpose SEM with up to 50kV accelerating voltage, a beam diameter (spot size) variable from 1μ m down to 8nm, and magnifications selectable from 20x up to 80000x. The magnification rather than field size is quoted below, this being a more natural parameter to the user of the electron beam lithography system. The electrons, generated by an electron gun using a tungsten filament, are accelerated to a high energy and magnetic lenses are used to focus the beam. Beam-blanking plates are used to deflect the beam onto the objective aperture to prevent unwanted exposure of the specimen, and beam deflection coils are computer controlled to direct the focussed beam to any location in the scan field.
Secondary electrons are detected to form the image, although a transmitted electron detector is fitted. The machine has a eucentric stage which gives x and y motion in 1μm steps, as well as height (z), rotation, and tilt adjustment.

2.3.1. Electron Beam Scanning Software (EBSS)

The electron beam scanning system (EBSS) is a computer program which controls the PSEM 500 electron beam writing system. The main function of the software is to direct pattern files to the scan generator of the EBL system. Functions have been added to control the repeated patterning (step and repeat) across an array of exposure sites (stage positions) and to align and focus automatically at each exposure site.

Patterns are transferred to the system as ASCII files containing numbers defining rectangle co-ordinates and special functions. The general format for the data is four integers separated by spaces, terminated by a carriage return.

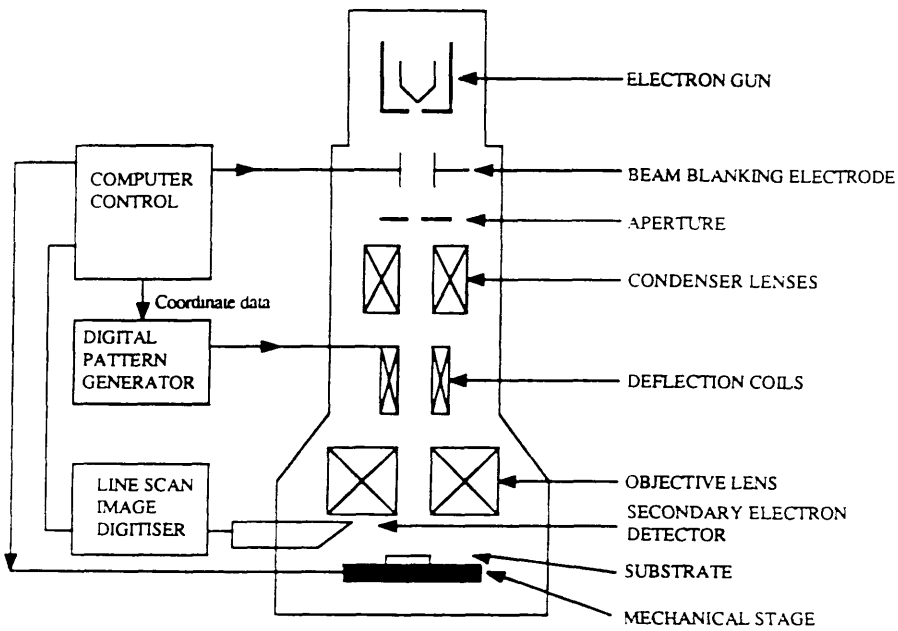

Figure 2.3: The Electron-beam lithography system used in this work.

The format for the simplest pattern element is ;

$$x_1\ y_1\ x_2\ y_2$$

where each number is an integer in the range 1-4095 and the co-ordinate points x_1, y_1 and x_2, y_2 define the opposite corners of a rectangle in the field ($x_1 < x_2$ and $y_1 < y_2$).

2.3.2. Field Size and Spot Size

The PSEM 500 has a range of magnifications and spot sizes. Large features can be written using a low magnification/large field size and small features using a high magnification/small field size. With a small field size the exposure dose per unit area was increased for a given spot size, because the density of pixels is increased with the smaller separation of pixels generated by the fixed resolution scan generator DACs.

The range of spot sizes were accompanied by a range of different beam currents which result in a greater exposure charge dose to the resist. For a given exposure dose needed to develop the pattern, the use of a larger spot size meant a reduced overall pattern exposure time. At lower magnification, the large frame size led to a larger distance between each pixel. If too small a spot size were chosen, the individual pixels were found to develop out, especially at the edge of pattern features. If too large a spot size were chosen the very small dwell time on each pixel could produce a similar effect. To avoid these rough edges around features, and long pattern exposure times, the spot size was generally chosen to be slightly less than the pixel separation. For example, the wires prepared in chapter 4 were exposed at a magnification of 5000X and a spot size of 8nm.

The field size was chosen such that the pattern spanned a large area of the field, allowing the 4096x4096 pixel resolution of the field to be used. Table I below gives the field magnifications and corresponding field sizes used in this work.

Magnification	Field Size (μm x μm)
640	195 x 145
1250	100 x 75
5000	25 x 19

Table I: Magnifications and field sizes used in this work.

2.3.3. Automatic Focusing

A simple yet very effective automatic focusing system has been implemented both in hardware and software[9]. The focusing method involves software calculation of an interpolated focus setting at a point of the sample, using four manual focus settings recorded near each corner of the chip.

The automatic focus routine used a set of three of the recorded position/focus data to interpolate the expected focus setting at the current stage position. This is repeated for the other three sets (combinations) of position/ focus recordings, and the average of the four calculated settings was used to adjust the SEM focus. This routine was instigated directly using the FOcus command or automatically at each exposure site in a Step and Repeat.

2.4. Dry Etching

In general, when transfering patterns into solid substrate, material can be removed in two ways: wet or dry etching. In wet etching, material is removed by immersing the substrates into the required chemical solutions for an appropriate time. While wet etching is highly selective (defined as the ratio of etch rates between two materials e.g. substrate and mask) and fast, it usually leads to an isotropic etch profile, Fig. 2.4b, because the etch front moves at the same rate in the vertical as well as the horizontal direction. However, wet etching can produce anisotropic profiles in crystalline materials in special cases where the etch proceeds along some crystallographic planes faster than others. This is called 'crystallographic etching'[10].

As the dimensions of electronic devices and quantum structures shrink to the nano-metric scale, the need for producing anisotropic profiles with good uniformity is of prime importance in their fabrication, and therefore, the development and use of dry etching techniques are essential, Fig. 2.4a. There is one potential problem associated with the use of dry etching, that is, the presence of energetic ions which bombard the substrate and can cause damage to the material. The following chapters contain investigations of this damage using a variety of characterisation techniques. At present, an account of the variations in the dry etching techniques available, in particular, mechanisms associated with the etching process and damage in reactive ion etching is discussed.

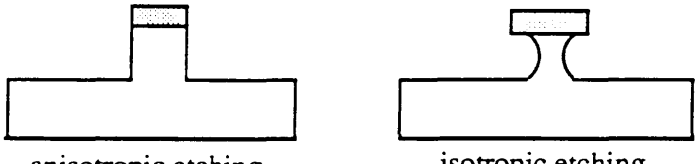

Figure 2.4: Schematic diagram showing the resultant profile of (a) anisotropic dry etching and (b) isotropic wet etching.

Dry etching is classified into various techniques, depending on the etching gas state (e.g. neutral or ionised) and gas type, excitation method (e.g. radio, or microwave frequency) and geometrical configuration of the etching system (e.g. barrel, parallel plates or down stream). For example: ion beam etching (IBE), plasma etching (PE) [barrel and planar], reactive ion etching (RIE), reactive ion beam etching (RIBE), chemically assisted ion beam etching (CAIBE), radical assisted ion beam etching (RBIBE), chemically assisted reactive ion beam etching (CARIBE), magnetron ion etching (MIE), magnetron reactive ion etching (MRIE), and electron cyclotron resonance reactive ion etching (ECR-RIE). In these processes, material is removed by either subjecting the surface to ions and reactive radicals, generated in a plasma, which form volatile compounds with the substrate composits or by bombarding the surface with an energetic beam of ions/reactive ions. In the next sections, PE will be described briefly and a more detailed account will be given for IBE, RIE and ECR-RIE since the present work is mostly concerned with the latter techniques.

2.4.1. Ion beam etching

In ion beam etching (IBE), an inert gas is fed into the ion gun at which it is ionised by a hot filament. It is then drawn out into a beam through a series of grids and accelerated by an acceleration grid to a specific energy. Electrons, emitted by a hot tungsten filament, are then injected into the ion beam so that the overall charge of the beam is neutral and also to minimize the lateral spread of the beam. The ions pass from the gun into the etch chamber in the form of a beam which impinges onto the substrate and material is removed by physical sputtering[11-16]. The substrate is mounted on a rotatable stage which also allows tilting with respect to the direction of the ion beam. Chamber pressures below 10mTorr are usually employed with ion energies in the range of 100-1000eV. For this work, an Oxford ion beam miller, equipped with double broad ion beam guns, was used. The base pressure was ~ 10^{-6}mbar, maintained using a rotary and a large diffusion pump (pumping speed = 1700l.sec^{-1}). Inert gases, namely Ne and Ar, were fed into the ion gun to a partial pressure of $\leq 10^{-4}$mbar, accelerated to 500-800V and an ion beam with current densities in the region of 0.1mAmp was used.

Since the etch mechanism in IBE is solely physical, most materials have a similar etch rate and consequently etch selectivity is poor. Nevertheless, this can be improved by the use of a reactive gas instead of an inert one (RIBE)[17]. The etching process then becomes a combination of physical sputtering and chemical reaction at the surface thus enhancing the etch rate and through a proper choice of reactive gas, selectivity can also be improved.

However, the introduction of reactive gases into the ion source can cause a reduction in lifetime of the exposed filaments and grids. This then leads to a variant of RIBE, which is CABIE, also known as IABE. In this configuration, inert gas is fed into the ion gun as in IBE, but a reactive gas is admitted just in front of the substrate. In this way, the etch rate and etch selectivity can be enhanced compared with IBE. Moreover, since the angles of incidence of the inert beam and the reactive gas can be independently varied, the process can be easily controlled and a wide range of etch profiles can be achieved[18,19]; this technique also overcomesthe problem of short filament lifetime. There also exists another etching technique using a combined radical beam and ion beam etching (RBIBE)[20] which uses a microwave excited radical beam combined with an inert ion beam. This differs from CAIBE in that the reactive etch gas is microwave excited and etch rates have been observed to be higher than using CAIBE.

2.4.2. Plasma etching

In barrel plasma etching, rf power usually at 13.56MHz frequency, is applied to the barrel shaped reactors via external capacitive or inductive coupling. Normally, the samples sit in the glow on an insulating (often quartz) holder surrounded by the cylindrical column of plasma. This configuration is characterised by a high operating pressure ≈ 1Torr and the etching results solely from the chemically reactive species created in the plasma diffusing into the substrate region. Therefore, the process is highly selective, but isotropic in nature. In this work, the barrel etcher was mainly used for stripping resist in an oxygen plasma.
In planar plasma etching, the etch chamber consists of two parallel electrode plates. The bottom electrode is grounded and the top electrode is driven by an rf generator (either 13.56MHz or low frequency, 0-100kHz), connected through a capacitor and an impedance matching circuit. The sample is normally mounted on the grounded electrode. An etchant gas is fed into the etch chamber which is kept under a pumped evacuated environment. Free electrons in the chamber gain energy by following the oscillation of the applied rf power which lead to the ionisation of some of the feed-gas molecules via electron- molecule collisions creating a plasma. The gas is chosen such that it dissociates to produce reactive radicals which will react with the substrate material to be etched and form volatile compounds.
If a radio frequency signal in the megahertz range is applied to the top electrode through an impedance matching network, similar to Fig. 2.5a, with the exception that the top electrode is rf driven, the response of the plasma to the positive and negative cycles are different. When the electrode is positive, many highly mobile electrons are accelerated towards the electrode

causing a significant accumulation of a negative charge. When the electrode (the cathode) is negative, heavy, immobile ion are accelerated towards it; however, significantly fewer of these ions strike the electrode than electrons did on the previous cycle. As a result of the dc bias, a high electric field region is formed around the cathode. This region known as Crookes dark space, also known as the 'plasma sheath' or the 'the dark space', is where the ion acceleration takes place before impinging on the electrode.

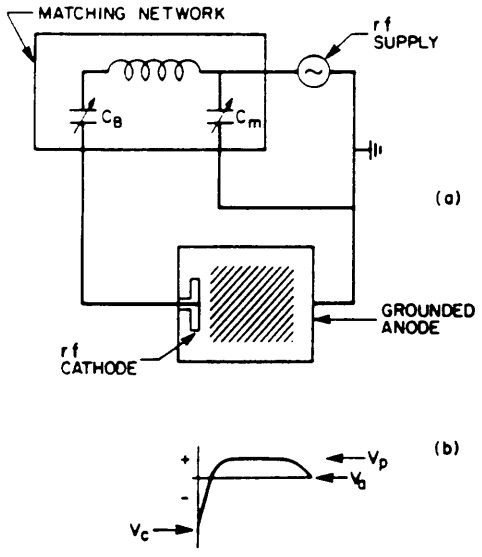

Figure 2.5: (a) A schematic representation of an rf plasma discharge where the power is supplied to the rf cathode through a matching network[21]. (b) A plot of the average potential between the anode (V_a), the cathode (V_c) and the plasma (V_p). The horizontal position axis is meant to coincide with (a).

In plasma etching, because the sample being etched is placed on the grounded electrode, the ions bombarding the etched surface are of relatively low energy (<50eV). In addition, relatively high chamber pressures in the range 0.1 to 10Torr are usually used. This implies that as the ions and reactive radicals are accelerated across the plasma sheath, they suffer many collisions, and their momentum is randomised. Hence in general, the etching process is isotropic due to the non-directionality of the low energy ions bombarding the etch surface, but highly selective because of the chemical nature of the reactive radicals.

2.4.3. Reactive ion etching

Reactive ion etching is very similar to planar plasma etching except that the bottom electrode, where the sample is mounted is now the driven electrode (at an rf frequency, often 13.56MHz). In addition, the bottom electrode is smaller in area than the top electrode leading to an asymmetrical configuration.

It can be seen from Fig. 2.5a that the rf driven electrode is dc isolated from the power supply by a capacitor C_B. This blocking capacitor does not allow the electrode to discharge through the power supply.

Since the plasma potential can be determined by the following expression[21]:

$$V_c = V_a \cdot (A_c/A_a)^4$$

where V_c is the potential difference between the powered electrode (cathode) and the plasma and V_a is the potential difference between the grounded electrode (anode) and the plasma and A_c/A_a is the ratio of the respective electrode areas. As a result, the accelerating field for the ions near the sample is greatly enhanced and the resultant potential distribution is shown in Fig. 2.5b. The negative dc voltage component (described in the previous section) in this configuration is developed across the bottom electrode (where the sample is situated) and is largely increased in comparison to the case of PE. If no collisions occur in the sheath regions, then the average kinetic energy of singly ionised positive ions striking the cathode is $(V_p-V_c)eV$, where V_p is the plasma potential and the units of V_p and V_c are volts. This results in the bombarding ions having a higher energy (~300-1000eV) , proportional to the negative dc bias ($-V_{dc}$). Furthermore, the pressure used in reactive ion etching is lower than that used for plasma etching, being in the range 5-100mTorr. Hence, the mean free path of the ions is increased so that they are not randomised in direction while traversing the plasma sheath. The above features such as the driven electrode being the bottom one (where the sample is placed), electrode asymmetry and low pressure operation all lead to an enhancement in the energy and directionality of the ions bombarding the surface being etched, thus increasing the degree of anisotropy obtained in RIE. (Note that increasing the power density in RIE also increases the dc bias and the ion energies.) Therefore RIE utilises both chemical and physical etch mechanisms. While the energetic ions bombarding the sample may cause physical damage to the material, contribution to damage from etch chemistry is also possible. Therefore, in order to gain a fuller understanding of the induced damage, knowledge of the fundamental processes involved during etching concerning the

roles of reactive radicals and ion bombardment is beneficial and will be discussed in the sections next.

2.4.4. Reactive ion etching using Electron Cyclotron Resonance

In this breed of RIE, the frequency used to excite the plasma is in the microwave region of the electromagnetic spectrum. The concept of operation of RIE-ECR technique relies, as the name ECR suggests, on coupling the microwave energy to the natural resonant frequency of the electron gas in the presence of a static magnetic field[22-24]. The resonant frequency occurs when the electron cyclotron frequency, which is defined as

$$\omega_{ce} = eB / 2\pi m_e \qquad (2.2)$$

where e is the electron charge, B is the strength of a static magnetic field and m_e is the electron mass, equals the excitation frequency ω which is 2.45GHz. In an actual discharge this condition can be satisfied in a volume or surface layer within the discharge where the static magnetic field strength is 875Gauss, adjusted to satisfy the resonance condition i.e. $\omega = \omega_{ce}$ and a component of electric field is perpendicular to the static magnetic field. This surface layer is called the 'ECR surface'.

The microwave energy absorption by both the electron and ion gases can be understood as follows: Since the work done on a charged particle by the electric field between collisions varies inversely as the particle mass, the energy imparted to an electron is much greater than the energy imparted to an ion. Therefore, in the case of ECR etching, direct energy transfer from the field to the ions usually can be neglected and electromagnetic energy transfer to the discharge takes place through Joule (elastic and inelastic collisional heating) and electron cyclotron heating of the electron gas[22]. In turn, the heated electron gas transfers energy to the neutral and ion gases by elastic and inelastic collisions. The electrons are accelerated in the ECR volume and inturn ionise and excite the neutral gas.

ECR discharges make use of a nonuniform static magnetic field. The magnetic field, produced by magnetic coils, is usually mirror-like reflecting the electrons back into the plasma . In the absence of an accelerating electric field, the motion of an electron in such a magnetic field is well known and is shown as the solid trajectory in Fig. 2.6a. When moving into a magnetic mirror, a charge particle will spiral with ever decreasing transverse orbits into the converging field until it is reflected. It then reverses direction and spirals out of the mirror with increasing orbits. The radii of these orbiting trajectories is small for a

typical; electron, e.g. a 4eV electron will have a radius of gyration of 0.05mm in a 875G field.

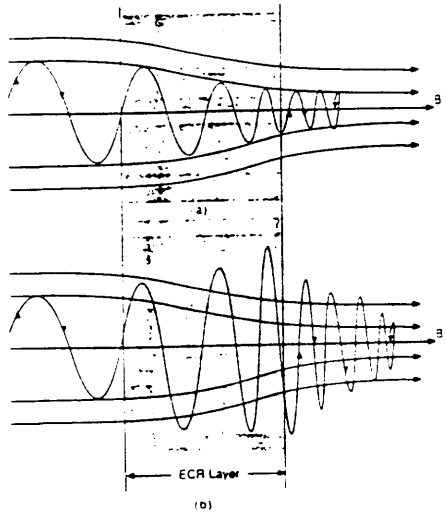

Figure 2.6: Electron motion in a mirror-like static magnetic field (a) without an accelerating electric field, (b) with a perpendicular electric field where the shaded region represents the ECR layer. (The figure is reproduced from reference 22).

If a transverse, time varying microwave electric field is present in the mirror, ECR acceleration of the electron takes place when the electron passes through a region where $\omega = \omega_{ce}$ i.e. the ECR surface, shown as the shaded region in Fig. 2.6b. If the electron is outside this region, little microwave energy is coupled to it, an average electron can experience many oscillations of electric field during the time it spends in the ECR surface. For an ECR-based plasma , high ionisation efficiency can be obtained with about 1% of the feed gas is ionised, giving rise to a plasma density of $10^{11}cm^{-3}$ [25]. This is compared to conventional rf RIE plasmas where only 0.01% of the feed gas is ionised giving rise to plasma density of ~ $10^{9}cm^{-3}$.

It has been observed that the most efficient ECR coupling occurs at very low gas pressures below 10mTorr, at the higher pressures the energy absorption becomes collisional and the magnetic field has little influence on the heating of the electron gas.

After generating a dense plasma by the ECR process, the plasma is extracted by an rf field applied to the substrate electrode and since very low pressures can be used, it is possible to obtain collisionless plasma sheaths. This allows the bombarding ions to keep their high angle of incidence on the substrate thus producing anisotropic etching profile even at very low dc biases. Very low dc bias (hence very low bombarding energy) can be obtained by

applying low rf powers to the driven electrode, and therefore control independently the ionisation efficiency of the plasma.

2.4.5. Plasma surface interactions

There are basically four processes which occur in reactive ion etching (and plasma etching). They are the 'production' of reactive species in the plasma, 'adsorption' of the reactants on the substrate surface, 'reaction' with the surface material and 'desorption' of the reaction products.
The generation of reactive species in the plasma are due to the collisions of electrons with the etch gas molecules whose rate R is given by:

$$R = k\, n_e\, N \qquad (2.2)$$

where n_e is the electron concentration and N the concentration of the reactant. k is the rate coefficient which is a function of the reaction cross section and the electron distribution function.
However, accurate expressions for these parameters are usually not available and therefore, R can only be determined qualitatively, e.g. via Langmuir probe measurements[26,27].
Before any reaction can take place on the substrate surface, the reactive radicals have to be adsorbed at surface sites. After the reaction has taken place, the reaction product has to be desorbed from the surface. Often in an etching process, the rate limiting step (which determines the etch rate of a particular material) is governed by one of these mechanisms and its identification vary depending on the chemical system. In reactive ion etching, since the gases chosen are such that they will adsorb and react with the substrate, the rates of adsorption and reaction will be finite but fast, a more important parameter to note is the desorption rate, which is related to the vapour pressure of the etch products, the higher the vapour pressure, the faster the desoprtion rate. However, the presence of ion bombardment in RIE can also play an important role in the etching process. While ions can etch the substrate by physical sputtering processes, as in IBE, there are also other ways in which the ions can participate in enhancing an etching reaction:

1) on an adsorption/reaction level, by creating surface damage. Ion bombardment serves to create or enhance reactive sites on the substrate surface. The former mechanism implies no reaction will take place without ion bombardment and has been used by Balooch et al[28] to explain why GaAs can only be etched in the presence of argon ions in an IBAE study using

molecular Cl_2. The effect of enhancement of adsorption was observed by Coburn et al[29] by independently controlling the impingement of Ar^+ and XeF_2 on silicon. Moreover, a mechanism involving the creation of surface damage has been proposed for the production of anisotropy[30], as long as the ions are directional, as in the case of RIE.

2) on a desorption level, by chemically enhanced physical sputtering. Ion bombardment can stimulate or increase the rate of desorption and help remove reaction products held on the substrate surface[31]. In particular, the rate of desorption of GaF_3 has been found to be the rate limiting step in the reactive ion etching of GaAs using CCl_2F_2[32], and similarly, $GaCl_x$ in the RIE of GaAs in Cl_2[33], RIBE in Cl_2[34].

2.4.6. RIE in $SiCl_4$

2.4.6.1. Chemistry

Stern et al[35,36] were the first workers to report using $SiCl_4$ for the high resolution reactive ion etching of GaAs and InP; 20nm wide patterns, defined by electron beam lithography, were transferred into GaAs using NiCr as the dry etch mask. At pressures around 20mT and at a lower power than was used in this work, crystallographic etching in the (100) orientation of GaAs has also been observed[37,38]. Furthermore, using optical emission spectroscopy, the type of products excited in a $SiCl_4$ microwave plasma were monitored by Rowe[39], who found that $SiCl_4$ gas is broken down to $SiCl^+$,$SiCl_2$ and Cl^+. Since the Cl^+ reactive radicals excited in the $SiCl_4$ plasma are believed to be responsible for the etching of GaAs, it is highly possible that the type of etch mechanism and products produced in the $SiCl_4$ process are similar to the species produced from studies of the ion-assisted etching GaAs using molecular Cl_2 and argon ions[28,40]. In Balooch's experiment[28], etching of GaAs in molecular chlorine was observed only in the presence of argon ion bombardment. Using a Cl_2 flux of 1×10^{17} molecules/cm^2·sec to impinge on the GaAs surface, they observed $AsCl_3^+$, $AsCl_2^+$, $AsCl^+$, $GaCl_3^+$, $GaCl_2^+$ and $GaCl^+$ molecules, and suggested that they had arisen from $AsCl_3$ and $GaCl_3$. It was also evident, according to their data, that ion bombardment did not cause sputtering of Ga or As but instead, enhances the production and/or desorption rate of $GaCl_3$ leading to their belief that the rate limiting step for the etching of GaAs in their experiment is the rate of desorption of $GaCl_3$. On the other hand, McNivin et al[40] employed a maximum Cl_2 flux of 5×10^{14} molecules/cm^2·sec and found $AsCl_3$, $GaCl_2$ and possibly GaCl as major species leaving the GaAs surface. In addition, from their experimental data, they proposed a very different reaction model which involves the enhancement of the reaction of adsorbed Cl_2 with arsenic on the GaAs surface which

produces $AsCl_3$. The difference in the reaction products observed and possibly the models proposed in the two cases may be explained by a thermodynamic analysis of the steady state chemical etching of GaAs using Cl_2 performed by McNiven[41]: by minimising the Gibbs free energy and assuming that the fluxes of Ga and As leaving the surface were equal, it was predicted that under chlorine deficient conditions, the less than fully chlorinated species, $GaCl_2$ will be formed while under chlorine excess conditions, the fully chlorinated species, $GaCl_3$ and $AsCl_3$ will be formed. However, this analysis only takes into account the chemical component of etching and has been applied by McNiven et al[40] to their ion enhanced chemical etching experiment and they predicted that the reaction products should be ($AsCl_3$ and $GaCl_3$) as in chemical etching. Experimentally, they observed $AsCl_3$ as expected, but not $GaCl_3$, rather $GaCl_2$ and GaCl. Nevertheless, the etch chemistry involved in etching of GaAs using $SiCl_4$ based on the above information suggests the following:

Plasma excitation

$$SiCl_4\ (g) \text{ ----------> } SiCl_2 + SiCl^+ + Cl^+ + GaAs\ (s) \text{ -----> } GaCl_x + AsCl_y + \text{excess}$$

Where (g) and (s) refer to gas and solid respectively, x = 1,2,3 and y = 3.
The vapour pressures of the reaction products ($GaCl_2$, $GaCl_3$ and $AsCl_3$) are plotted against temperature, Fig. 2.7. It is clear that $AsCl_3$ is the most volatile, followed by $GaCl_3$, with the least volatile product being $GaCl_2$. At Glasgow University, RIE using $SiCl_4$ was developed by S. Thoms for the high resolution etching of GaAs[42]. A useful etch mask for this etchant was found to be NiCr lifted-off from PMMA polymer resist, see section 2.2.5, with the ratio of GaAs etch rate to mask etch rate of >50:1. High resolution negative resist HRN was found not to be so resistant to the etch, at best, a ratio of > 10:1 was observed.

2.4.6.2. Machine

The reactive ion etching system (Plasmatch RD80) used for $SiCl_4$ etching is a conventional 13.56MHz parallel plate reactive ion etcher. The anode and cathode are aluminium with hard anodisation. Three NiCr pins are fitted around the perimeter of the cathode to enable dc voltage measurement. The cathode is 17cm in diameter and the anode to cathode area ratio is 2.8:1. The pumping system consists of an Edwards two stage rotary pump and a Roots blower (mechanical booster). In all experiments, the etch chamber was evacuated to a base pressure of around 10^{-3} to 10^{-4}Torr range and the temperature of the cathode, where the GaAs samples were mounted, was kept constant at 40°C. The optimum etch condition found to give clean, vertical sidewalls and maximum reproducibility was at a power density

of 0.44W/cm^2, true volume flow rate of 9sccm, (after applying a calibrated correction factor of 0.28) at a pressure of 11-12mTorr giving a dc bias of 300±10V. The etch rate of GaAs etched under this condition is ~200nm/min.

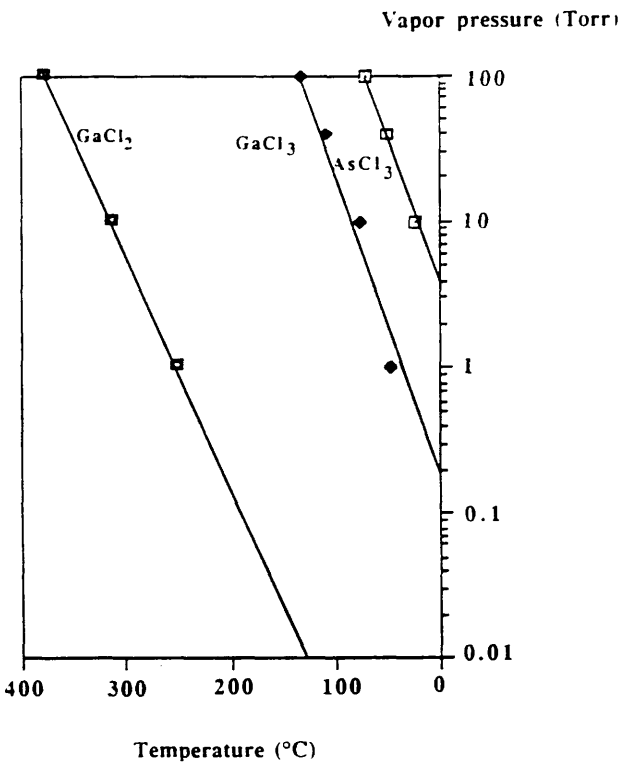

Figure 2.7: Vapour pressures of $GaCl_3$, $GaCl_2$ and $AsCl_3$. The figure is produced from CRC handbook of Chemistry and Physics (1987).

2.4.7. RIE in CH_4/H_2

2.4.7.1. Chemistry

The use of CH_4/H_2 for the etching of semiconductor compound materials was first developed by Niggebrügge et al [43]. They reported reactive ion etching of indium phosphide (InP), indium gallium arsenide (InGaAs) and the quarternary compound indium gallium arsenide phosphide (InGaAsP). By choosing the appropriate parameters, (1 to 3 Pa total pressure, volume flow rate of 15 to 20% CH_4), a good degree of anisotropy and an excellent surface morphology was produced. The high selectivity was maintained by using

photoresist and SiO_2 as dry etch masks. However, they were unable to use this mixture to etch GaAs. With 20% CH_4 in H_2, a power density of 0.4W/cm^2 and pressures of 10 and 20mTorr, very slow etch rates below 10nm/min. and considerable surface roughness were observed.

Using mass spectometry, a detailed analysis of the plasma species present during the reactive ion etching of InP with CH_4/H_2 has been studied by Schmid[44]. The mass spectra of neutral compounds with and without the plasma are depicted in Fig. 2.8a and 2.8b. Ethine, ethene, ethane and molecules with carbon chains of higher order appear as products formed in the plasma. The spectrogram of positive plasma ions were also taken and is shown in Fig. 2.9.

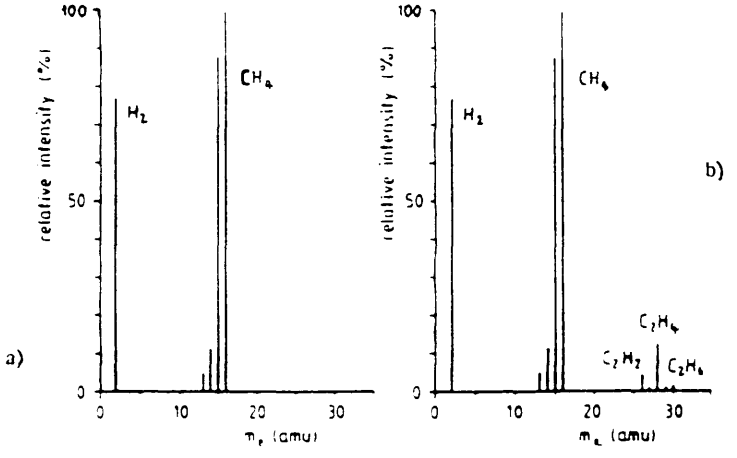

Figure 2.8: Spectrogram of neutral species (a) without plasma (b) with plasma. (The figure is reproduced from reference 44). The process parameters are: 20% CH_4 in H_2; flow rate 25sccm; pressure 2.6Pa; power density 0.4Wcm^{-2}.

It is a common belief that the chemistry of the RIE of InP in a CH_4/H_2 plasma relies on the formation of phosphine and group III alkyls. Indeed phosphine was clearly resolved by mass spectroscpy as a neutral compound as well as in an ionic state, Fig. 2.10. Although the limited resolution of the mass spectrometer did not allow the identification of group III etching products, the author believes that the similar dependence of the InP etch rate and the concentration of neutral products on total pressure Fig. 2.11 suggests that the methyl radicals play an important role in the etching mechanism.

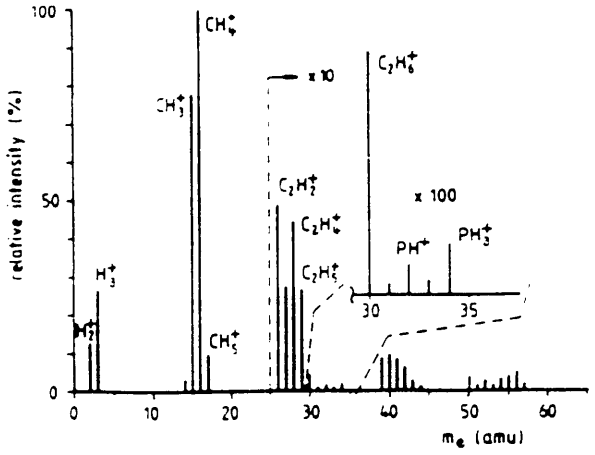

Figure 2.9: Spectrogram of positive plasma ions using the same process parameters as in figure 2.8. (The figure is reproduced from reference 44).

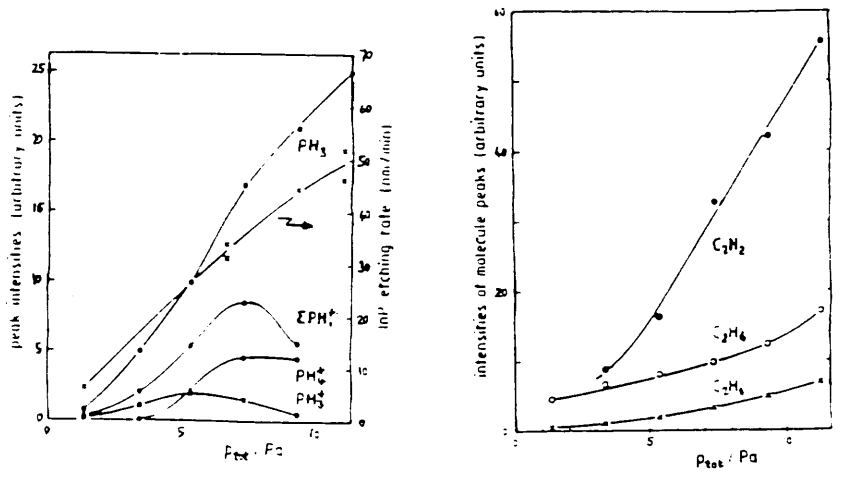

Figure 2.10 (*left*): InP etch rate and intensities of neutral and ionised phosphorous compound vs. total pressure. (The figure is reproduced from reference 44). The process parameters are: 6% CH_4 in H_2; power density 0.4Wcm^{-2}; flow rate 25sccm.

Figure 2.11 (*right*): Dependence of neutral product concentration on the etch pressure using the same process parameters as in Fig. 2.10. (The figure is reproduced from reference 44).

Unfortunately, no such detailed analysis has been done in the etching of GaAs using CH_4/H_2 , nonetheless, it is likely that the etch chemistry involved with GaAs is similar to InP and may be written as follows :

Plasma excitation

$$CH_4 + H_2 \text{ ----------> } C_xH_y + H_a^+ + CH_b^+ + C_xH_z^+ + GaAs\ (S)$$

$$\text{-------> } (CH_3)_3Ga + AsH_3 + \text{excess}$$

where x = 1,2; y = 2,4,6; a = 2,3; b = 3,4,5; z = 2,4,5,6. This is similar to the inverse metal organic chemical vapour deposition (MOCVD) process. In MOCVD, the reactant products, $(CH_3)_3Ga$ and AsH_3 are transported in a H_2 carrier gas to the growth zone where GaAs is formed through the chemical reaction:

$$(CH_3)_3Ga + AsH_3 \text{ -----> } GaAs + 3(CH_4)$$

A plot of vapour pressure vs temperature is shown in Fig. 2.12 illustrating the volatility of products from the suggested reaction.

2.4.7.2. Machine

The reactive ion etching machine used was also a conventional 13.56MHz parallel plate reactive ion etcher, (Electrotech SRS Plasma-fab 340) with an anode/cathode ratio of 3.3:1. Both electrodes are made of aluminium with titanium oxide coated on the cathode which is 17cm in diameter. The pumping system used and the base pressure acquired are the same as in the RD80 RIE machine. The temperature of the cathode, where the GaAs samples were situated, was kept constant at 30°C. The optimum condition for the high resolution etching of GaAs was a 1/5 parts of CH_4/H_2 with true volume flow rates of 5sccm/25sccm and a pressure in the range of 15-18mTorr. The power density was $0.66Wcm^{-2}$ giving a dc bias of 930±30V and an etch rate of ~$20nm.min^{-1}$.

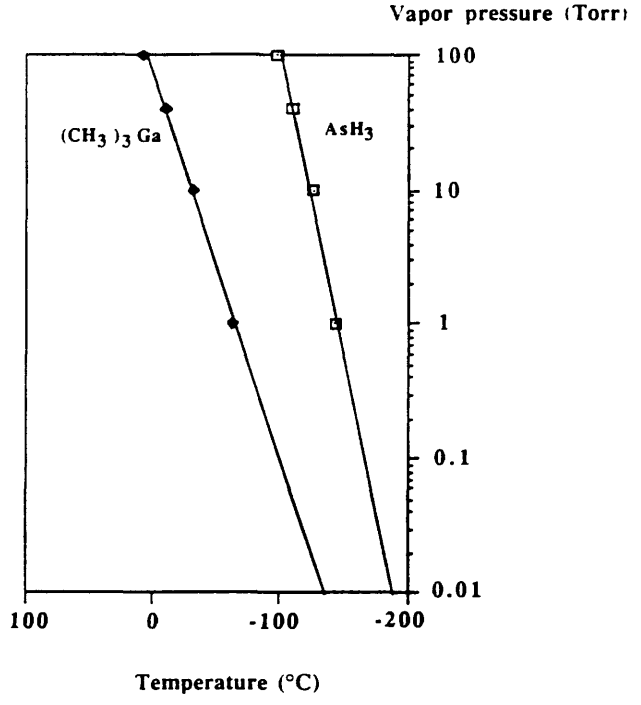

Figure 2.12: Vapoure pressures for $(CH_3)_3Ga$ and AsH_3. The figure is produced from CRC handbook of Chemistry and Physics (1987).

2.4.8. ECR-RIE in CCl_2F_2/He

2.4.8.1. Chemistry

To gain a better understanding of the chemistry involved in the CCl_2F_2/He etching process using ECR-RIE, Cheung[45] has analysed the light emitted by He and CCl_2F_2/He plasma using optical emission spectroscopy. In the He plasma, the major species detected was neutral He_I , whereas in CCl_2F_2/He plasma Cl and CF^*_x radicals were the major species present, where the Cl radicals are mainly responsible for etching of GaAs to form the relatively volatile gallium chlorides ($GaCl_2$, $GaCl_3$) and arsenic chloride ($AsCl_3$)[28,32,40]. Moreover, the fluorine present in a CCl_2F_2/He plasma can also react with GaAs leading to the formation of the volatile arsenic fluorides (AsF_3, AsF_5) and the involatile, high boiling

point solid gallium fluoride (GaF_3). It has been reported that the rate limiting step to this process is the ion induced removal of GaF_3, while the removal rate of $GaCl_x$ also benefits significantly from ion bombardment[32]. The presence of CF^*_x radicals in the ECR plasma was undesirable since it will lead to the formation of the involatile GaF_3 and also to the formation of fluorine containing polymers (e.g. C_2F_6) which may easily deposit on the substrate surface thus roughening the surfaces by forming micromasks or in extreme cases, inhibiting the etch process.

2.4.8.2. Machine

The ECR machine used in this work was fully computer-controlled, designed and manufactured by Plasmatech. It has a loadlock chamber at which samples are loaded and transfered automatically into the etching chamber through a gate valve. The pumping system consists of two turbo molecular pumps and two backing pumps (one for each of the chambers). The etcher consists of the following, Fig. 2.13: 1) A well filtered variable power (0-600W) but constant frequency (2.45GHz) microwave power supply.

2) A circulator which allows the microwave generator to work into a matched load independent of the discharge variations. It also protects the generator from large reflected power that may occur from an unmatched plasma (unstable or flickering) by dumping it in a dummy load.

3) There are two E-H stub tuners for matching of the discharge for high microwave coupling efficiency, they produce standing waves between the plasma and the tuner increasing the coupling to the plasma and reducing the reflected microwave power.

4) A waveguide applicator coupling the microwave power into the plasma, meters for the forwarded and reflected powers. The waveguide changes from rectangular to circular to improve microwave power coupling to the ECR plasma chamber.

5) A microwave transparent window (quartz) to isolate the waveguide from the ECR plasma chamber.

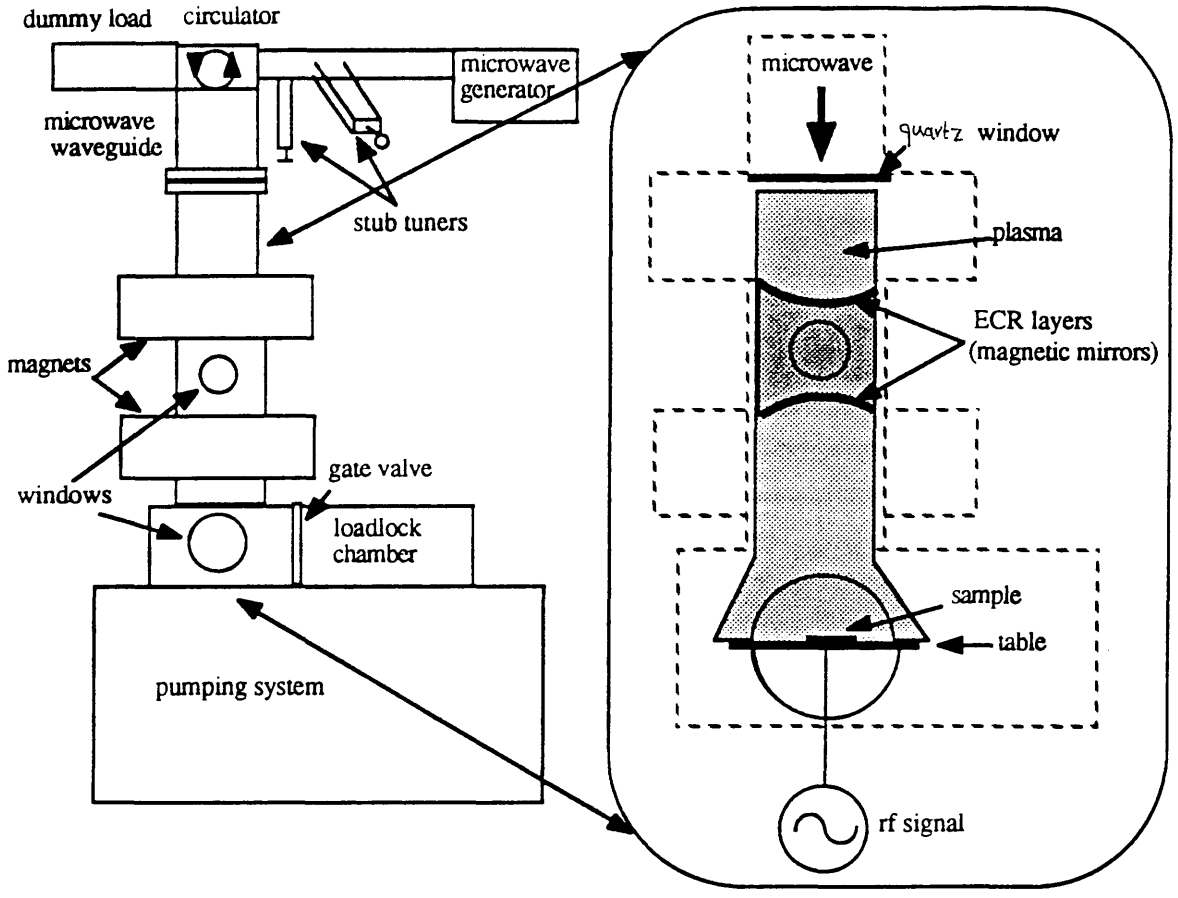

Figure 2.13: Schematic diagram illustrating the ECR etcher used in this work with the inset on the left showing the plasma and sample configuration in more detail. The diagram is not to scale.

6) An ECR chamber surrounded by two magnetic solenoids (magnetic mirrors), the top magnet, usually set to strong magnetic field to keep the intense ECR layer away from the quartz window. The lower magnet is weaker, but with B> 875Gauss, so that eventually the ions generated in the ECR chamber flow out of the diverging magnetic field into the etching chamber and impinge on the substrate surface. There are two connections for the etching gases at the top and bottom of the ECR chamber. The plasma flow down of the ECR chamber and diverge to a characteristic triangular shape ingulfing the electrode where the substrate is placed. The electrode (cathode) is covered with a 17cm-diameter graphite plate and is rf driven to provide directionality and hence a near vertical etch profile. The temperature of the cathode was kept at 11°C.

2.9. Dry etching damage

In dry processing, the action of the energetic ion bombardment can cause damage on the material being etched. In ion beam etching, the crystal can suffer from a high degree of damage since the etch mechanism is purely physical. Studies on the damage induced in GaAs and GaAs/AlGaAs structures by ion beam etching involve the introduction of a reactive gas resulting in the addition of a chemical component during etching, the damage caused in those configurations is expected to be lower, and has been demonstrated by various authors[46,47]. In this work, damage characterisation has been carried out in the areas of ion beam etching, reactive ion etching and electron cyclotron resonance RIE. While in general, it is expected that the presence of a reactive component in etching gas can reduce the induced damage, it can contribute indirectly to the etching induced damage, as will be shown later. Reduction of damage is also possible by passivation of defects[48,49] or by using very low ion energies[50-52]. It is important at this point to note that damage can occur both on the surface and sidewalls of etched structures, the latter being particularly important for nanostructures. This effect is illustrated in Fig. 2.14.

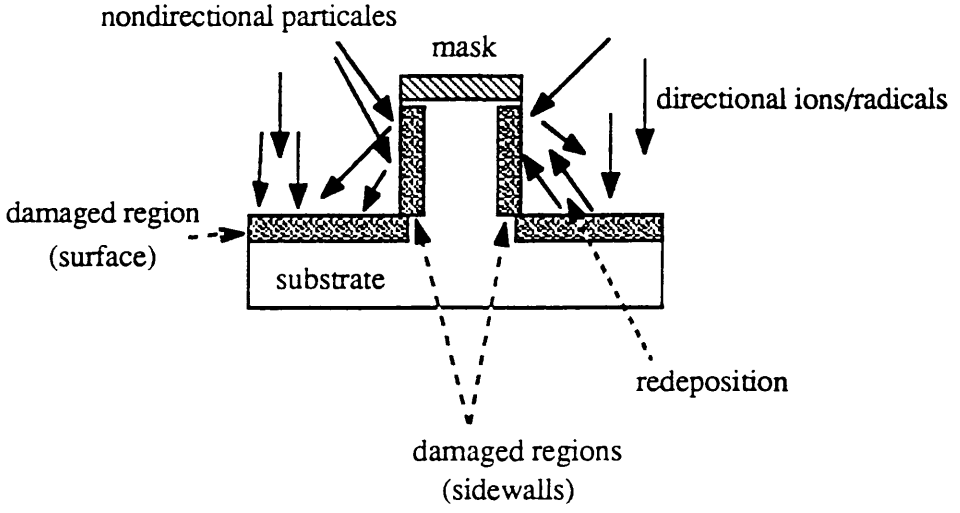

Figure 2.14: Schematic representation of the possible causes of the surface and sidewall damage resulted from dry etching.

In RIE and ECR-RIE, the surface may suffer damage from the physical bombardment of directional ions and reactive radicals and/or chemical damage from the reactive radicals. On the other hand, effects from the directional and non-directional ions and reactive radicals and possibly redeposition[13,53,54] from the bottom surface can contribute to the causes of

damage induced on the sidewalls. The study and minimisation of sidewall damage is at least as important as surface damage in applying dry etching techniques for the fabrication of electronic devices with nanometric dimensions. Although there have been many investigations on RIE surface damage[47,55-59], not including the work of Glasgow University, less effort has been directed towards sidewall damage studies[42,60,61]. These studies will be discussed in detail later. A variety of electrical, optical and analytical characterisation techniques can be used to investigate damage[56-58,62,63]. It is, in fact, essential that complimentary techniques are used in order to obtain both quantitative and qualitative information about the damaged layer due to the different depth resolution and origin of sensitivity associated with the various techniques as will be shown later.

2.10. References

1. M. P. Lepselter, and W. T. Lynch in ' VLSI Electronics', ed. N. G. Einspruch, vol.1, Academic press, New York, pp84 (1981); also C. D. W. Wilkinson, and S. P. Beaumont, Proc. winter school Les Houches, France, ed. M. J. Kelly, and C. Weisbuch, Springer proceeding in Physics 13, pp36 (1986).
2. S. A. Rishton, Ph.D. thesis, University of Glasgow (1984).
3. J. A. Adams, Ph.D. thesis, University of Glasgow (1990).
4. M. Hatzakis, J. Paraszczak, and J. Shaw, Proc. Microcircuit Engineering, Delft University press, Amsterdam, pp386 (1981).
5. S. P. Beaumont, T. Tamamura, and C. D. W. Wilkinson, Proc. Microcircuit Engineering, Delft University press, Amsterdam, pp381 (1981).
6. M. J. Rooks, S. Wind, P. McEuen, and D. E. Prober, J. Vac. Sci. Technol., **B5**, 318 (1987).
7. W. S. Mackie, Ph.D. thesis, University of Glasgow (1984).
8. Data sheet from P. W. Whipps, Philips Redhill Lab., Surrey.' Negative-acting electron beam resist: type HRN and HSN', (1980).
9. G. Blance, Final year undergraduate project report, Department of Electronics and Electrical Engineering, University of Glasgow (1989).
10. K. E. Bean, IEEE Trans. Electron. Dev., **ED-25**, 1185 (1978).
11. X. Y. Wang, and P. H. Holloway, J. Vac. Sci. Technol., **B2**, 613 (1984).
12. J. W. Coburn, J. Vac. Sci. Technol., **13**, 1037 (1976).
13. P. G. Glöersen, J. Vac. Sci. Technol., **12**, 28 (1975).

14. 'Erosion and Growth of Solids Stimulated by Atom and Ion Beams', ed. G. Kiriakidis, G. Carter, and J. L. Whitton, (1986).
15. P. Sigmund, Phys. Rev., **184**, 383 (1969).
16. 'VLSI Electronics Microstructure Science', Vol. 8, ed. N. G. Einspruch, and D. M. Brown, Academic press (1984).
17. K. Asakawa, and S. Sugata, J. Vac. Sci. Technol., **A4**, 677 (1986).
18. M. W. Geis, G. A. Lincoln, N. Efremow, and W. J. Piacentini, J. Vac. Sci. Technol., **19**, 1390 (1981).
19. J. D. Chinn, A. Fernandez, I. Adesida, and E. D. Wolf, J. Vac. Sci. Technol., **A1**, 701 (1983).
20. J. A. Skidmore, L. A. Coldern, E. L. Hu, J. L. Merz, and K. Asakawa, J. Vac. Sci. Technol., **B6**, 1885 (1988).
21. S. M. Sze,' VLSI Technology', second ed.,198 (1988); also H. R. Koenig, and L. A. Maissel, IBM J. Res. Dev, **14**, 168 (1970).
22. J. Asmussen, J. Vac. Sci. Technol., **A7**, 883 (1989).
23. C. Constantine, D. Johnson, S. J. Pearton, U. K. Chakrabarti, A. B. Emerson, W. S. Hobson, and A. P. Kinsella, J. Vac. Sci. Technol., **B8**, 596 (1990).
24. Y. Tobinaga, N. Hayashi, H. Araki, S. Nakayama, and H. Kudoh, J. Vac. Sci. Technol., **B6**, 272 (1988).
25. Y. H. Lee, J. E. Heidenreich III, and G. Fortuno, J. Vac. Sci. Technol., **A7**, 903 (1989).
26. I. Lungmuir, and M. Mott-Smith, Phys. Rev., **28**, 727 (1926).
27. C. Steinbrüchel, J. Electrochem. Soc., **130**, 648 (1983).
28. M. Balooch, and D. R. Olander, J. Vac. Sci. Technol., **B4**, 794 (1986).
29. J. W. Coburn, and H. F., Winters, J. Appl. Phys., **50**, 3189 (1979).
30. D. L. Flamm, and V. M. Donnelly, Plasma Cham. Plasma Proc., **1**, 317 (1981).
31. J. L. Mauer, J. S. Logan, L. B. Zielinski, and G. S. Schwartz, J. Vac. Sci. Technol., **15**, 1734 (1978).
32. R. E. Klinger, and J. E. Green, J. Appl. Phys., **54**, 1595 (1983).
33. E. L. Hu, and R. E. Howard, J. Vac. Sci. Technol., **B2**, 85 (1984).
34. R. A. Barker, T. M. Mayer, and R. H. Burton, Appl. Phys. Lett., **40**, 583 (1982).
35. M. B. Stern, and P. F. Liao, J. Vac. Sci. Technol., **B1**, 1053 (1983).
36. M. B. Stern, H. G. Craighead, P.F. Liao, and P. M. Mankiewich, Appl. Phys. Lett., **45**, 410 (1984).
37. J. Z. Li, I. Adesida, and E. D. Wolf, Appl. Phys. Lett., **45**, 897 (1984).
38. J. Z. Li, I. Adesida, and E. D. Wolf, J. Vac. Sci. Technol., **B3**, 406 (1985).

39. M. D. Rowe, 5th Int. Conf. on Ion and Plasma Assisted Techniques (IPAT), pp87 (1985).
40. S. C. McNevin, and G. E. Barker, J. Appl. Phys., **58**, 4670 (1985).
41. S. C .McNevin, Internal report of AT&T Bell Lab., MurryHill, New Jersey.
42. S. Thoms, S. P. Beaumont, C. D. W. Wilkinson, J. Frost, and C. R. Stanley, Microcircuit Engineering 1986, ed. H. W. Lehmann and Ch. Bleicker, North-Holland, Amesterdam, pp249 (1986).
43. U. Niggebrügge, M. Klug, and G. Grarus, Proc. 12th Int. Symp. on GaAs and related compounds, Int. Phy. Conf. Ser. no. 79, pp367 (1986).
44. H. Schmid, Proc.6th Int. Conf. on Ion and Plasma Assisted Techniques (IPAT), pp98 (1987).
45. R. Che ung, Ph.D. thesis, University of Glasgow (1990).
46. S. W. Pang, M. W. Geis, N. N. Efremow, and G. A. Lincoln, J. Vac. Sci. Technol., **B3**, 398 (1985).
47. S. W. Pang, J. Electrochem Soc., **133**, 784 (1986).
48. J. S. Wang, S. J. Fonash, and S. Ashok, IEEE Electron device Lett., **EDL-4**, 4326 (1983).
49. S. J. Pearton, A. J. Tavendale, and E. M. Lawson, Radiation Effect, **79**, 21 (1983).
50. R. Cheung, Y. H. Lee, C. M. Knoedler, K. Y. Lee. T. P. Smth III, and D. Kern, Appl. Phys. Lett., **54**, 2130 (1989).
51. H. F. Wong, D. L. Green, T. Y. Liu, D. L. Lishan, M. Bellis, E. L. Hu, P. M. Petroff, P. O. Holtz, and J. L. Merz, J. Vac. Sci. Technol., **B6**, 1906 (1988).
52. R. Cheung, Y. H. Lee, K. Y. Lee, T. P. Smth III, D. Kern, S. P. Beaumont, and C. D. W. Wilkinson, J. Vac. Sci. Technol., **B7**, 1462 (1989).
53. H. W. Lehmann, L. Kraubauer, and R. Widmer, J. Vac. Sci. Technol., **14**, 281 (1977).
54. P. G. Glöersen, Sol. State technol., **19**, 68 (1976).
55. S. W. Pang, G. A. Lincoln, R. W. McClelland, P. D. DeGraff, M. W. Geis, and W. J. Pacentini, J. Vac. Sci. Technol., **B1**, 1334 (1983).
56. S. J. Pearton, U. K. Chakrabrati, and W. S. Hobson, J. Appl. Phys., **66**, 2061 (1989).
57. S. Semura, H. Saitoh, and K. Asakawa, J. Appl. Phys., **55**, 3131 (1984).
58. K. L. Seaward, N. J. Moll, D. J. Coulman, and W. F. Stickle, J. Appl. Phys., **61**, 2358 (1987).
59. S. J. Pearton, M. J. Vasile, K. S. Jones, K. T. Short, E. Lane, T. R. Fullowan, A. E. Von Neida, and N. M. Haegel, J. Appl. Phys., **65**, 1281 (1989).
60. R. Cheung, S. Thoms, I. McIntyer, C. D. W .Wilkinson, and S. P. Beaumont, J. Vac. Sci. Technol., **B6**, 1911 (1988).

61. S. W. Pang, W. D. Goodhue, T. M. Lyszczarz, D. J. Ehrlich, R. B. Goodman, and G. D. Johnson, J. Vac. Sci. Technol., **B6**, 1916 (1988).
62. M. Watt, C. M. Sotomayor Torres, R. Cheung, C. D. W. Wilkinson, H. E. G. Arnot, and S. P. Beaumont, J. Modern Optics, **35**, 365 (1988).
63. R. Cheung, A. Birnie, J. N. Chapman, S. Thoms, and C. D. W. Wilkinson, 5th Int. Conf. on Microlithography, Microcircuit Engineering, Cambridge (1989).

Chapter 3: Characterisation of dry etching surfaces damage in n^+ GaAs by the Transmission Line Model technique and Raman Scattering of coupled LO phonon-plasmon modes.

Acknowledgments

I would like to thank Dr S. Thoms for suggesting the novel idea of using the TLM technique for characterising dry etching damage in GaAs. I would also like to thank Dr. P D. Wang for performing the Raman scattering measurements on my TLM samples.

3.1. Introduction

This chapter deals with the implementation of the Transmission Line Model (TLM) technique to measure the electrical damage depth in n^+ GaAs epitaxial layers as a result of ion beam or reactive ion etching in Ne, Ar, $SiCl_4$ and CH_4/H_2. The TLM technique together with Hall measurements, using Van der Pauw geometry, can provide information on the sheet resistance, carrier concentration and Hall mobility of the epitaxial layer.

While Hall measurements give an independent check on the conductivity, the conductance measurements using the TLM technique sheds light on the evolution of the damage associated with etching, giving an accurate determination of the physical extent of the electrical damage. However it does not give any data on the nature of that damage.

The dry etching damage is defined as any change in the electron transport or optical properties after etching in comparison with an untreated or wet etched sample. Wet etching is usually believed not to cause any damage to the epitaxial layer since it does not involve ion bombardment.

For this work, a comparison between dry and wet etching is vital since parameters such as the resistance of the epitaxial layer changes as the thickness of the layer changes, i.e. the reduction in resistance is due to both the damage created during etching and also to the reduction in the thickness of the epitaxial layer.

Etching in CH_4/H_2 has been found to passivate the Si donors in Si-doped GaAs[1]. It was known previously that donors and acceptors in GaAs and other semiconductors were passivated after prolonged exposure to a hydrogen plasma [2,3]. The effect of de-passivation of the Si donors via post rapid annealing of the GaAs samples was verified through a range of temperatures and times.

Raman scattering of the coupled LO phonon plasmon modes can only be performed in highly doped GaAs. Information about the thickness of the depletion layer can be obtained using this technique which agreed reasonably well with the TLM estimates of the damage depth. Suggestions were made to explain why and how the damage extends to regions well beyond the estimated penetration depth of the bombarding ions.

3.2.1. The Transmission Line Model (TLM) method

The transmission line model[4,5,6] has been developed to obtain values of the specific contact resistance of ohmic contacts as well as the sheet resistance of the semiconductor layer outside the contact region. The ohmic contacts are modelled as a distributed circuit analogous for an (R-G) transmission line, hence the name. The sheet resistance of a semiconductor R_{sh} can be obtained from simple resistance measurements made between contacts on a TLM test structure. The structure used in this study consists of ten contacts of identical geometry (300μm wide and 30μm long), patterned on a strip of active material, i.e. n^+ GaAs. The separation distance between adjacent contacts L were 1, 2, 4, 8, 16, 32, 64, 128 and 256μm. The resistance is measured and plotted as a function of the separation distance L. From the gradient (R_t / L) of the graph, Fig. 3.1, the sheet resistance R_{sh} of the semiconductor can be determined as:

$$(R_t / L) .W = R_{sh} \qquad (3.1)$$

where W is the contact width.

3.2.2. The Hall effect

The Hall effect is a phenomenon which may be observed when a semiconductor is subjected to an electric and magnetic fields orthogonal to each other. A voltage (the Hall voltage) appears across the sample in a direction at right angle to both these fields.
The Van der Pauw technique allows Hall measurements to be made on planar samples of arbitrary shape[7]. In determining the resistance, current is applied to two contacts and the potential difference developed between the other two contacts is measured. Thus the resistivity of the sheet can be deduced from two resistance measurements without any knowledge about the distances between the contacts, providing there is a uniform current flow through the thickness of the sheet. The conductivity of the sheet σ will then equal the reciprocal of the measured resistivity.

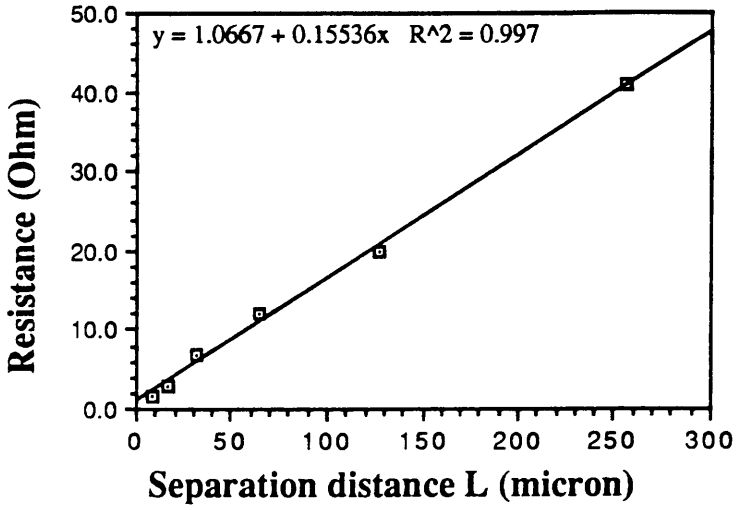

Figure 3.1: An example of the plot of resistance measured between ohmic contacts separated by a distance L. The sheet resistance can be obtained from the gradient of the line using equation 3.1.

The Hall mobility μ_H is related to the conductivity σ through[8]:

$$\mu_H = R_H \sigma \qquad (3.2)$$

where R_H is the Hall coefficient. The sheet carrier concentration n and the sheet resistance R_{sh} can be obtained from:

$$n = 1 / qR_H$$
$$R_{sh} = 1 / \sigma W \qquad (3.3)$$

Where q is the electronic charge and W is the thickness of the epitaxial layer.

3.3. Sample preparation and measurements.

Four epitaxial layers of n^+ GaAs doped with Si were grown for this study by MBE on semi-insulating substrates. These are: wafer A111 (50nm, ~$3x10^{18}$ cm^{-3}), wafers A85 and B81 (both 140nm, 2-3 $x10^{18}$ cm^{-3}) and wafer B40 (500nm, ~$1x10^{18}$ cm^{-3}). Highly doped n type GaAs was chosen for this study because the depletion depth of such epitaxial layers is relatively small (~17-28nm) and so the layers are sensitive to surface effects induced by etching. During the progress of the experiments, it was found that the measured damage

depth varied considerably from etch to etch; those etches which gave more damage were characterised using the grown material with the thicker epitaxial layers (140 and 500nm).

The samples were prepared as follows, Fig. 3.2:

1. The wafers were cleaved to give 5x5mm^2 samples. The samples were degreased and cleaned ultrasonically using trichloroethane then acetone and finally methanol for 5min each, respectively. The samples were then rinsed in isopropyl alcohol (IPA) and blown dry in nitrogen.
2. TLM and Hall patterns were produced lithographically using the mask aligner and AZ1450J or S1400-31 photoresists
3. After development, native oxides were removed by a dip in a 4:1 solution of H_2O:HCl for 30sec after which the samples were rinsed in de-ionized water, blown dry and loaded immediately into the evaporator. Low resistivity ohmic contacts were evaporated at a base pressure of about 2x10^{-6}mbar. The contacts consisted of Au /Ge /Ni /Au[10] layers with corresponding thicknesses of 88 /50 /23 /25nm. A scaled down version with thicknesses of 61 /35 /16 /17nm was also used preserving the quality of the contacts. The contacts were alloyed at temperature range between 340 and 350°C for 1min in 95%: 5% of Ar: H_2 ambient. The contactswere checked for true ohmic behaviour.
4. The TLM and Hall contacts were then masked for isolation. The isolation was achieved by removing the conducting material surrounding the contacts using wet etching at room temperature in (20: 8: 1000) solution of NH_3:H_2O_2:H_2O for 2min (etch rate ~200nm.min^{-1}), rinsed in de-ionized water then blown dry.
5. A series of steps were patterned using AZ5214J reversible photoresist and ~30nm of NiCr (10% Cr in Ni) was deposited to form the steps which will be used to measure the etch depth. A schematic diagram of the sample is shown in Fig. 3.3.

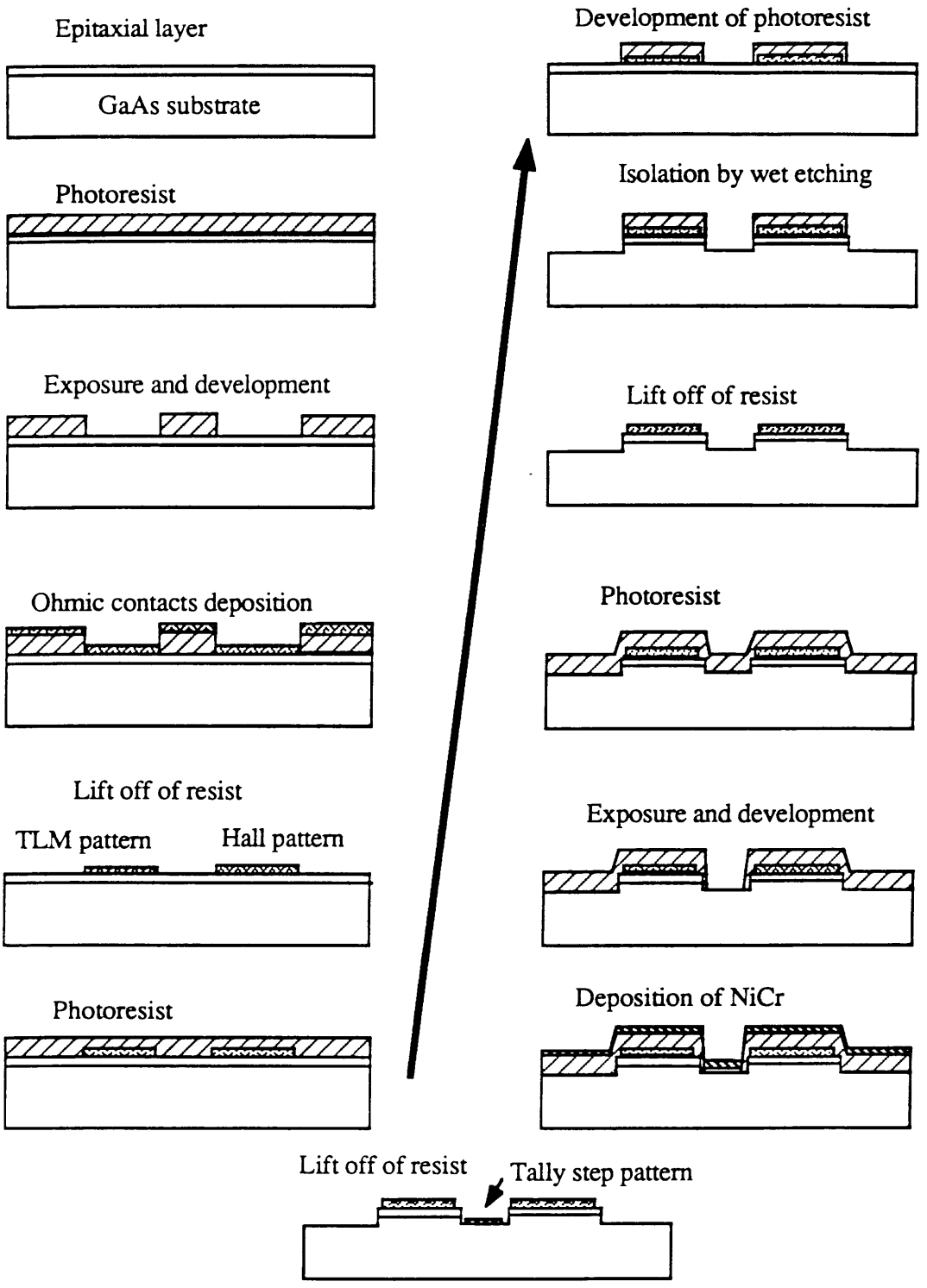

Figure 2: Stages of fabrication of the samples used for TLM and Hall measurements.

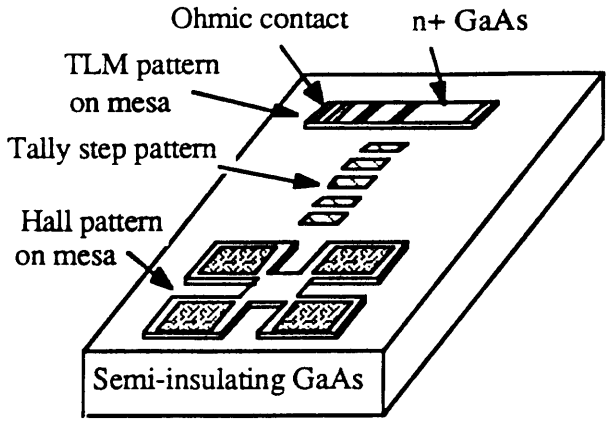

Figure 3.3: A schematic of a sample ready for etching experiment using TLM and Hall measurements.

The samples were then dry etched using various etching processes. In the case of etching using CH_4/H_2, the samples were post annealed using a strip heater in a 95%: 5% of Ar: H_2 ambient. The ramp up and ramp down time was approximately 90sec in total. This step is essential to reactivate the Si donors as will be explained later.

The conductivity measurements were performed using the four point probe technique in conjunction with a HP4145B semiconductor parameter analyser. The Hall effect measurements were performed at room temperature and at 77K using HL 5200 Polaron Division Hall measurement system controlled by a SMS 1000 computer.

The sheet conductance was obtained from the gradient of the straight line relationship between the separation distance L and the measured resistance using equation 3.1.

It was noted that the conductivity and mobility of the unetched material varies by approximately 11% across the wafers, and so the conductivity and mobility of each piece were also measured prior to etching.

The etch depth was measured using tally step after etching the NiCr film using a 1:1 solution of $HCl:H_2O$. The uncertainty in measuring the depth is $\pm$ 2nm.

For each sample the resistance was measured before and after etching (and after annealing in the case of CH_4/H_2) by both the TLM and Hall techniques. From these measurements, the percentage of the remaining conductance (%C) was obtained by taking the reciprocal of the ratio (resistance after etching / resistance before etching x100). The %C was then plotted as a function of the etch depth to produce the final result. A set of conductance measurements was produced by wet etching samples in a (20: 8: 1000) solution of $NH_3:H_2O_2:H_2O$.

3.4. Results of dry etching

3.4.1. Results of RIE in CH_4/H_2 and the effect of donor passivation

For reactive ion etching in CH_4/H_2 plasma, a ratio of one part CH_4 to five parts H_2 and flow rate of 5sccm of CH_4 and 25sccm of H_2 with a gas pressure of 11-12mtorr were used. The applied rf power was 150W, yielding a power density of $0.66W.cm^{-2}$ and a dc bias voltage of 930±30V.

By measuring the sample etch depth, a calibration curve of the etch time as a function of the etch depth was obtained. The etch rate was approximately $21nm.min^{-1}$ which agrees well with the previously reported value $20nm.min^{-1}$ [11]. The calibration curve is depicted in Fig. 3.4.

Inspection of samples etched for times longer than 90sec by SEM has revealed the formation of a very thin film deposited on the surface of the samples. This film is believed to be a carbon-containing polymer[12] which is a common occurrence in hydrocarbons in a gaseous discharge. The film can be removed by ashing in oxygen plasma for 30min using inductively coupled etcher (plasmafab 505).

Samples etched in CH_4/H_2 for times ranging from 30 to 160sec showed very poor or no conduction when measured immediately after etching (without annealing). For example, the sample A (etched for 90sec) showed about a 30 fold reduction in conductivity from 17.8mS before etching to 0.618mS after etching. The carrier mobility of this sample had increased from $1570±100cm^2v^{-1}s^{-1}$ before etching to $2650±150cm^2v^{-1}s^{-1}$ after etching (the mobility of the untreated GaAs used in this work is less than that reported by Sze[8], $\sim 2000cm^2v^{-1}s^{-1}$ for the same doping concentration). Meanwhile, the sheet carrier concentration decreased from $6.6x10^{13}cm^{-2}$ before etching to $4.6x10^{12}cm^{-2}$ after etching. The later decrease in the sheet carrier concentration may indicate that electron traps have been introduced into the semiconductor.

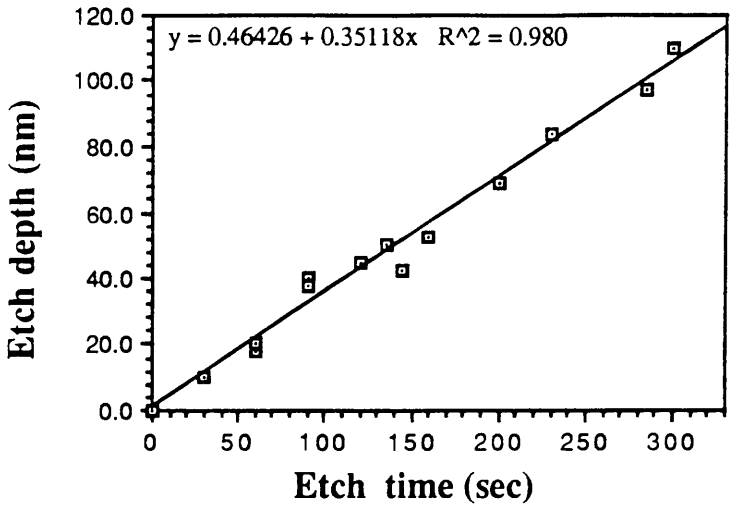

Figure 3.4: The etch depth of GaAs as a function of the etch time for CH_4/H_2 RIE. The etch rate 21nm.min^{-1} at a flow rates of 5/25sccm and pressure range of 11-12mtorr. The power density was 0.66W.cm^{-1} and the dc bias voltage was 930±30V.

When annealed for 1sec at 380°C, the sample A showed an increase in conductance to 11.5mS, decrease in carrier mobility to 1450±100cm^{2}v^{-1}s^{-1} and an increase in carrier concentration to 5.5x10^{13}cm^{-2}. This example displays clearly the effect of passivation of the silicon donors by hydrogen thus reducing the conductivity[1], and the partial reversibility of this effect by annealing. This agrees with the work by Cameron et al[13]. The resistance measured by the TLM technique before and after etching, and before and after annealing, were plotted as a function of the distance separating the TLM contacts and are presented in Fig. 3.5a and 3.5b respectively.

For all the samples etched for times ranging from 190 to 300 seconds, no conductance measurement was possible by either the TLM or the Hall techniques. It has been reported[31] that for samples 80nm thick of highly doped (4.5x10^{18}cm^{-3}) n$^+$ GaAs and etched at lower rf power (80W) to remove 10nm, annealing at temperatures ranging from 300 to 400°C for up to 10min can recover all the carrier concentration and almost the full mobility.

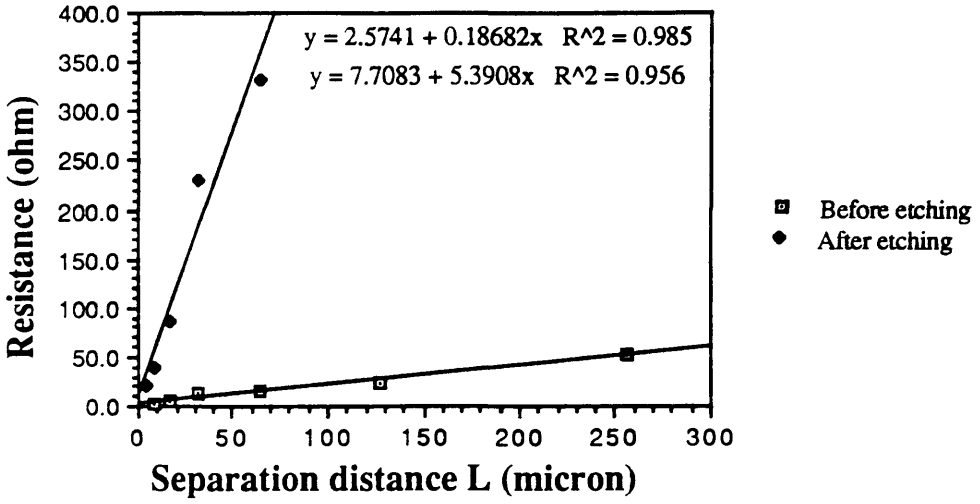

Figure 3.5a: TLM resistance measurement of sample A before and after etching in CH_4/H_2 RIE for 90sec.

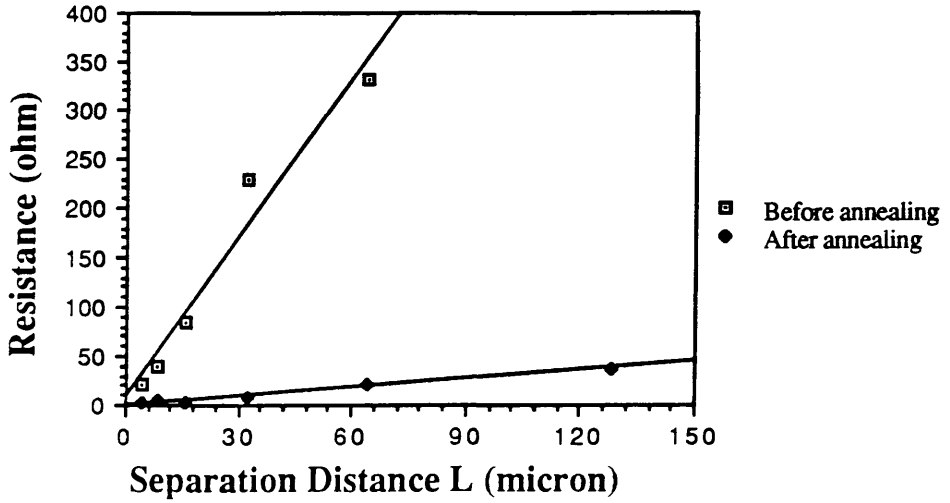

Figure 3.5b: TLM resistance measurement of sample A before and after annealing at 380°C for 1sec in 95%Ar : 5%H_2. The sample was etched earlier in CH_4/H_2 for 90sec.

To investigate whether this suggestion is valid for samples etch to depths deeper than 10nm, two samples B and C were etched to depths of 50 and 80nm respectively. Sample B was annealed firstly at 380°C for 1sec then at 400°C for 2min and further 3min (total annealing time at 400°C is 5min). Sample C, on the other hand, was annealed for 1sec at 380°C, then for 1min and a further 3min at 400°C (total annealing time at 400°C is 4min). TLM and Hall measurements were performed after each annealing step. The results are presented in table I. The table shows clearly no significant changes in the resistance measured after each annealing step. Fig. 3.6a shows the resistance measured by the TLM method as a function

of L for sample C before and after etching, while Fig. 3.6b presents the results of the three successive annealing .

Sample	R (Hall) (Ω)	R (TLM) (Ω)	μ_H	C_{sh}	comments
B	64	60	1570	6.3E13	before etching
	109	102	1160	4.9E13	anneal 1sec at 380°C
	110	99.4	1200	4.7E13	anneal 2min at 400°C
	113	102.2	1570	3.7E13	anneal 5min at 400°C
C	63	60	1570	6.4E13	before etching
	623	647	1440	7.0E12	anneal 1sec at 380°C
	628	638	1541	6.5E12	anneal 1min at 400°C
	565	604	1505	7.3E12	anneal 4min at 400°C

Table I: The effect of annealing on the resistance (measured by Hall and TLM methods), Hall mobility μ_H (uncertainty is ~±100cm^2 V^{-1}s^{-1}) and sheet concentration C_{sh} (cm^{-2}) of GaAs samples reactive ion etched in CH_4/H_2. Samples B and C were etched for 60 and 150sec respectively.

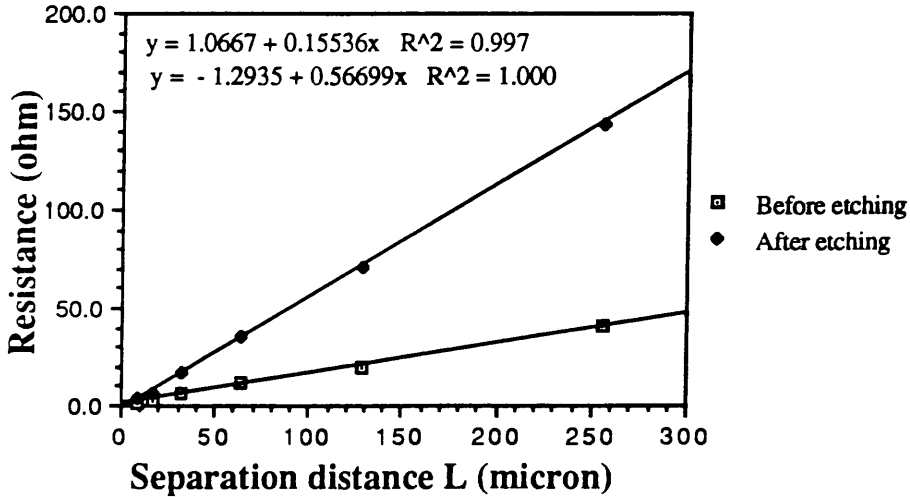

Figure 3.6a: TLM resistance measurement of sample C prior to and after etching in CH_4/H_2 to of 80nm.

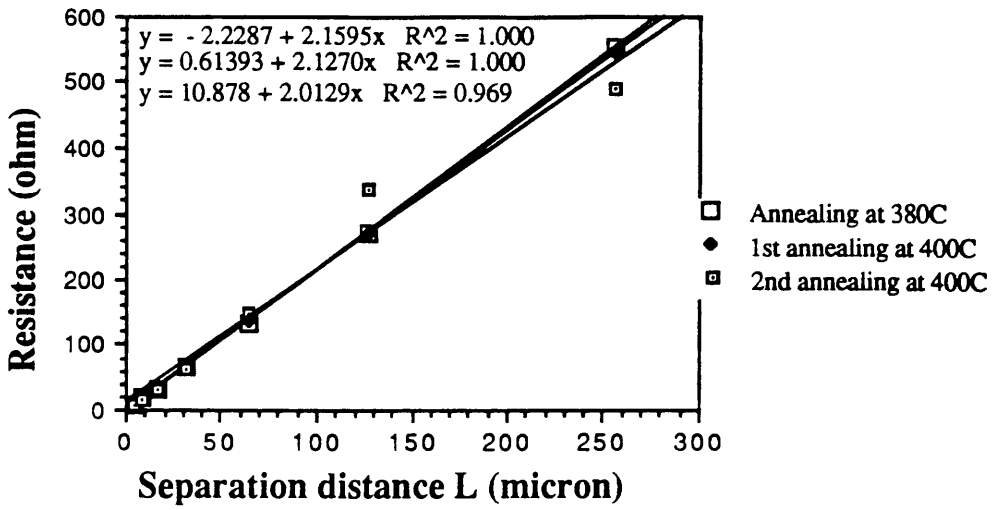

Figure 3.6b: TLM resistance measurement of sample C after annealing for 1sec at 380°C followed by annealing at 400°C for 2min and a further 3min. The sample was etched earlier in CH_4/H_2 to a depth of 80nm.

When the etch depth is plotted against the remaining conductance measured by, the TLM technique was plotted as a function of the etch depth, and compared with similar plot for wet etched samples, the results show a difference in the cut off depth i.e. when %C = 0, Fig. 3.7. The figure shows the conductance of CH_4/H_2 etched samples to decrease, firstly, rapidly then it saturates and run parallel to the wet etching conductance line. The %C measured by both the TLM and Hall techniques were plotted for comparison, as a function of the etch depth and are shown in Fig. 3.8. After etching, the mobility was measured for each sample and a percentage of the remaining mobility (mobility after etching/mobility before etching x100) was obtained. This procedure was adopted to eliminate the fluctuations in the mobility across the wafer. The remaining mobility was plotted as a function of the etch depth as shown in Fig. 3.9.

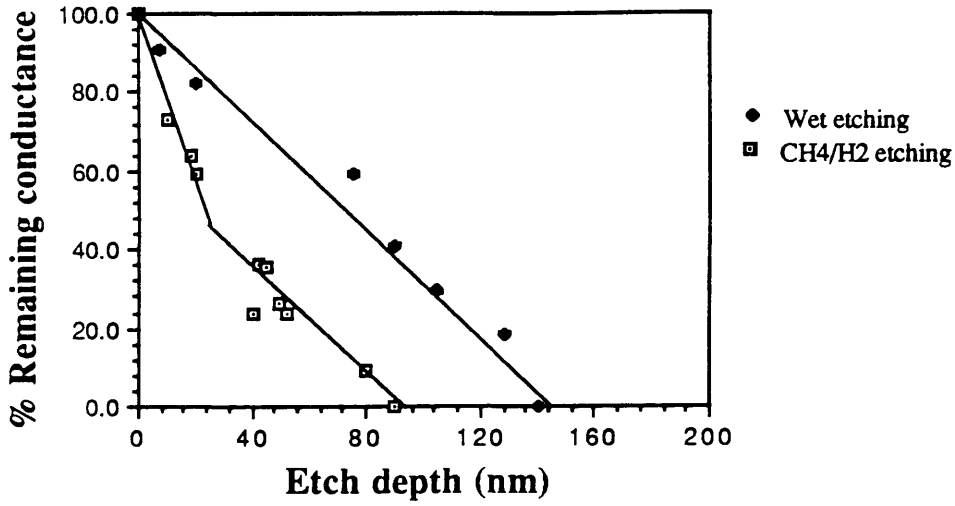

Figure 3.7: % Remaining conductance, measured using the TLM method as a function of the etch depth for samples etched in CH_4/H_2. The control samples were wet etched and are plotted for comparison

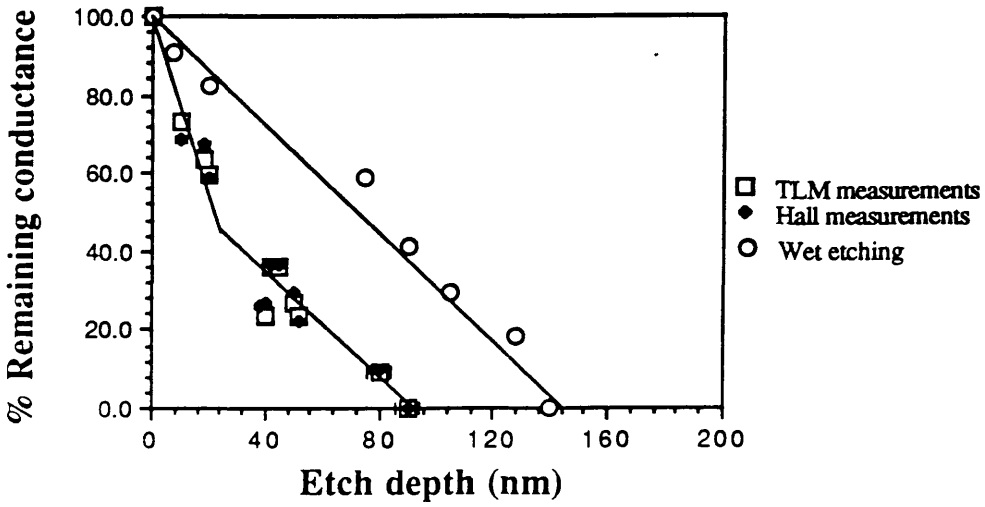

Figure 3.8: % Remaining conductance, measured using both the TLM and Hall methods, as a function of the etch depth for GaAs samples RIE in CH_4/H_2. The etch pressure was 11-12mtorr and the dc bias voltage was 930±30V. The epitaxial layer is 140nm thick, $3x10^{18}cm^{-3}$ Si-doped. The control samples were wet etched and plotted for comparison.

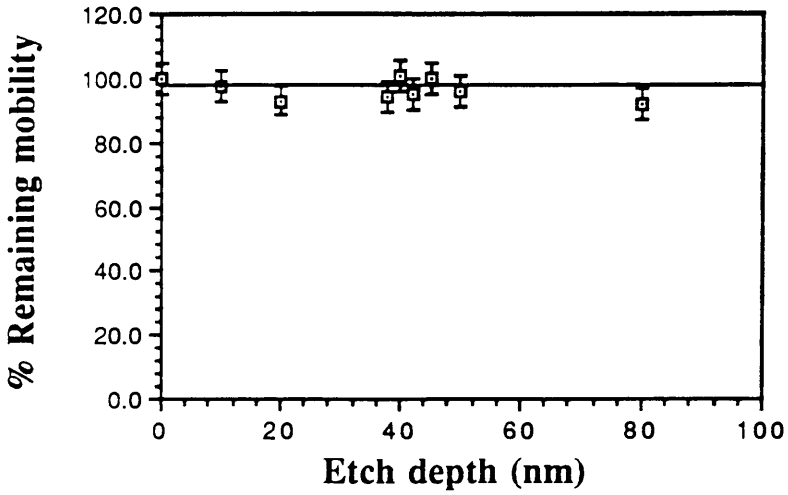

Figure 3.9: % Remaining mobility as a function of the etch depth for samples etched in CH_4/H_2 RIE as in figure 3.8.

3.4.2. Results of RIE in $SiCl_4$

The TLM samples used for the $SiCl_4$ etching were patterned using electron beam lithography with the final pattern dimensions similar to those of the CH_4/H_2 samples. However this set of samples was without the Van de Pauw configuration, so that mobility measurements could not be performed. The etching machine and parameters were similar to those describe in section 2.4.4. The dc bias developed during etching was 240±10V. Epitaxial layer with thicknesses of 50 and 140nm were used. The conductance was measured for each individual sample prior to and after etching and the % remaining conductance was plotted as a function of the etch depth and is shown in Fig. 3.10a and 10b. It should be mentioned that the relatively high etch rate of the $SiCl_4$ etch process ($\approx$ 200nm.min^{-1}) made it difficult to control the etch depth as desired.

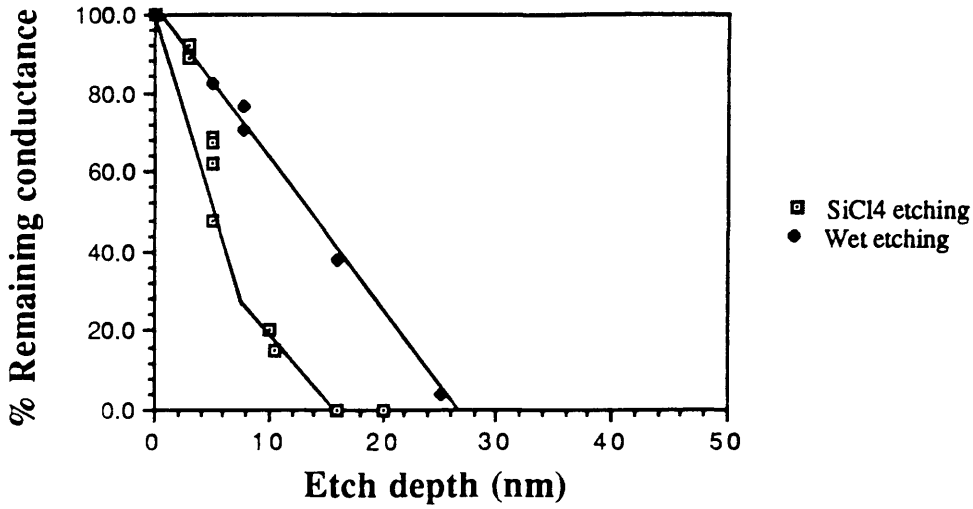

Figure 3.10a: % Remaining conductance, measured using the TLM method, as a function of the etch depth for GaAs samples etched in $SiCl_4$ RIE. The etch pressure was 11mtorr and the dc bias voltage was 240±10V. The epitaxial layer is 50nm thick, $3x10^{18}cm^{-3}$ Si-doped. The control samples were wet etched and plotted for comparison. Data point at depth of 20nm belongs to an overetched sample.

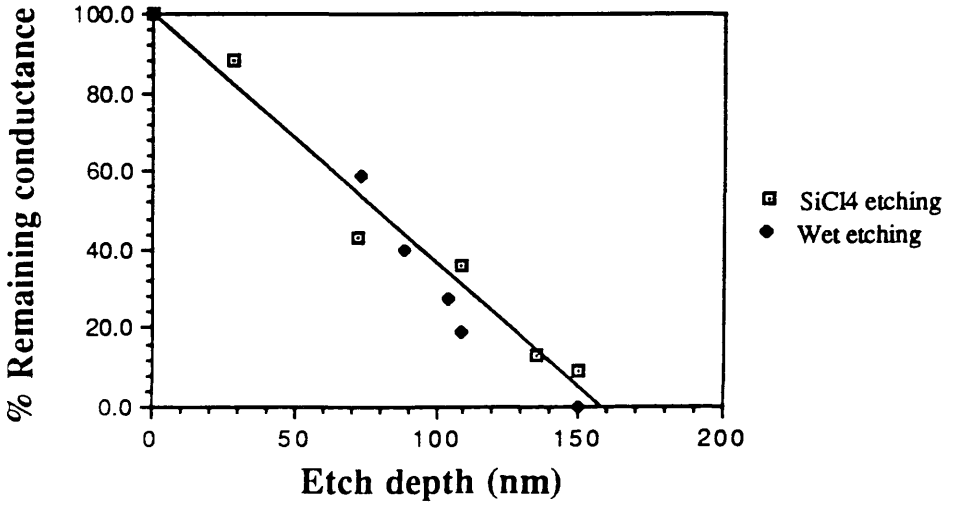

Figure 3.10b: % Remaining conductance, measured using both the TLM method, as a function of the etch depth for GaAs samples etched in $SiCl_4$ RIE. The etch pressure was 11mtorr and the dc bias voltage was 240±10V. The epitaxial layer is 140nm thick, $3x10^{18}cm^{-3}$ Si-doped. The control samples were wet etched and plotted for comparison.

3.4.3. Results of Ne and Ar ion beam etching

Two sets of samples were ion beam etched in Ar and Ne at 500V. For each set, two epitaxial layers with thicknesses of 140 and 500nm were used. In addition two more samples were etched using Ar at 800V for comparison. For the 140nm thick epitaxial layer, the % of the remaining conductance was obtained for each sample and plotted as a function of the etch depth for both Ar and Ne, Fig. 3.11. The data obtained from the samples etched at 800V was also added for comparison. The mobility of samples etched using Ar and Ne IBE was constant through out the etching, Fig. 3.12. The behaviour of the conductance with the etch depth was different from the RIE samples i.e. samples etched in CH_4/H_2 and $SiCl_4$, and it was speculated that similar behaviour may be observed if thicker epitaxial layer was used, e.g. 500nm thick.

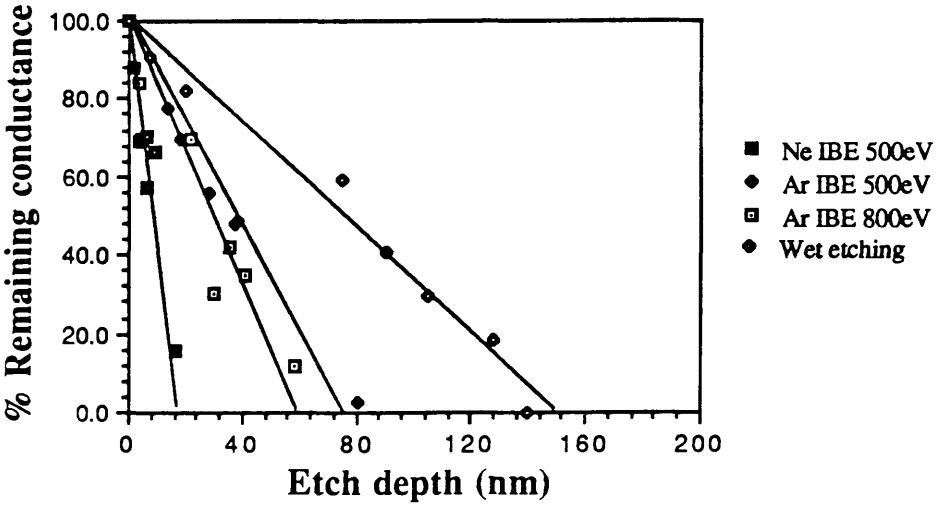

Figure 3.11: % Remaining conductance as a function of the etch depth for GaAs samples etched in Ne (500eV) and Ar (500eV and 800eV) IBE. The epitaxial layer is 140nm thick, $3x10^{18}cm^{-3}$ Si-doped. The control samples were wet etched and plotted for comparison. The conductance was measured using the TLM method.

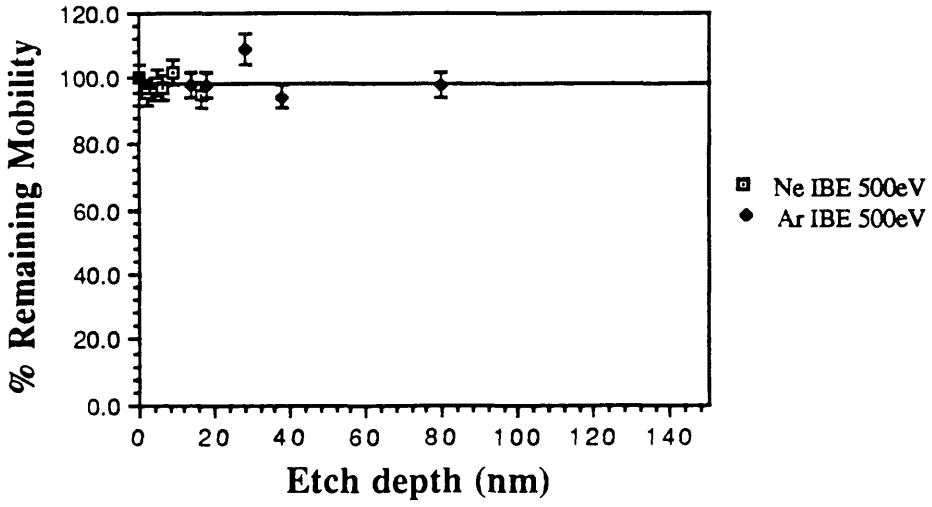

Figure 3.12: % Remaining mobility as a function of the etch depth for samples etched in Ar IBE at 500 and 800eV and also in Ne at 500eV. The epitaxial layer is 140nm thick, $3x10^{18}cm^{-3}$ Si-doped.

The conductance of the samples with epitaxial layer 500nm thick, etched using Ar and Ne at 500eV, were measured and a further set of samples were wet etched to be used as a control. However, the relationship of the conductance as a function of the etch depth for the wet etched samples was not linear as can be seen in Fig. 3.13. The as-grown material was then profiled for the donor concentration by means of Polaron electrochemical profiler. The results, Fig. 3.14, showed a non-uniform doping profile in which the material 280nm beneath the surface is doped to a carrier concentration of $1x10^{18}cm^{-3}$ after which the concentration drops to about $7x10^{15}cm^{-3}$ at 500nm. The surface depletion layer, on the other hand, was 52nm thick, almost double the thickness of the depletion layer at this level of doping. Unfortunately, these facts complicate the interpretation of results and makesit non-trivial.

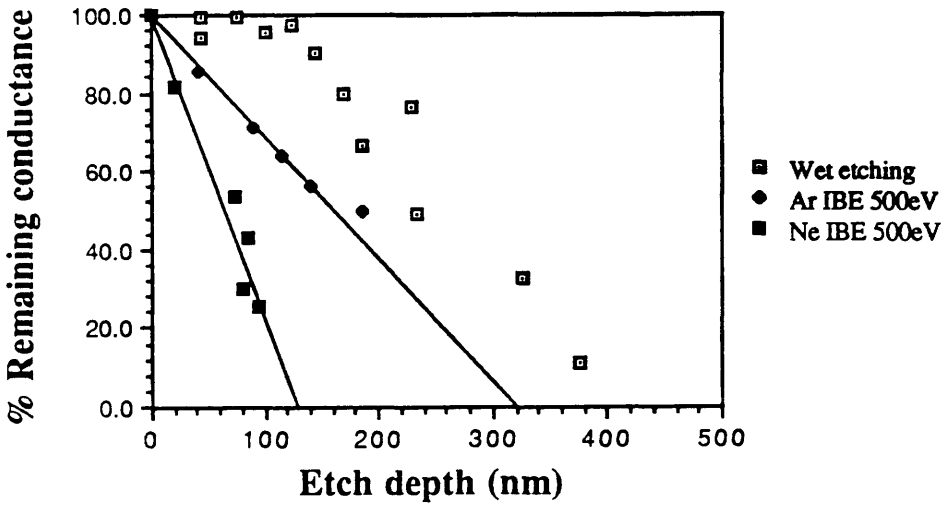

Figure 3.13: % Remaining conductance as a function of the etch depth for GaAs samples etched in Ne (500eV) and Ar (500eV) IBE. The epitaxial layer is 500nm thick, $1x10^{18}cm^{-3}$ Si-doped. The control samples were wet etched and plotted for comparison. The conductance was measured using the TLM method.

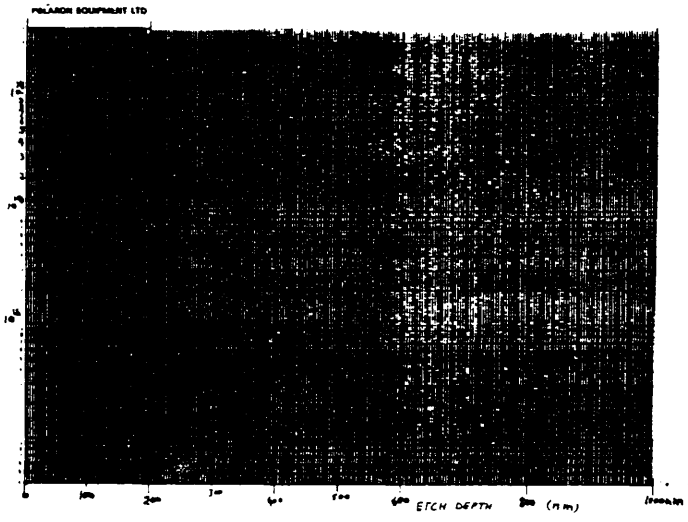

Figure 3.14: Profile of the carrier concentration of the 500nm thick epitaxial layer used in the TLM measurements of ion beam etching using Ar and Ne at 500eV. The profile was obtained using Polaron electrochemical porfiler.

3.5. Discussion and conclusions of TLM/ Hall measurements

3.5.1. The "dry etch damage' model

The dry etching damage can be thought of as an accumulative process. It builds up beneath the surface as the substrate is etched, Fig. 3.15, eventually reaching an equilibrium where

further etching produces no additional damage. Region I in Fig. 3.15 is where the etch damage is building up and region II is where it has reached equilibrium.

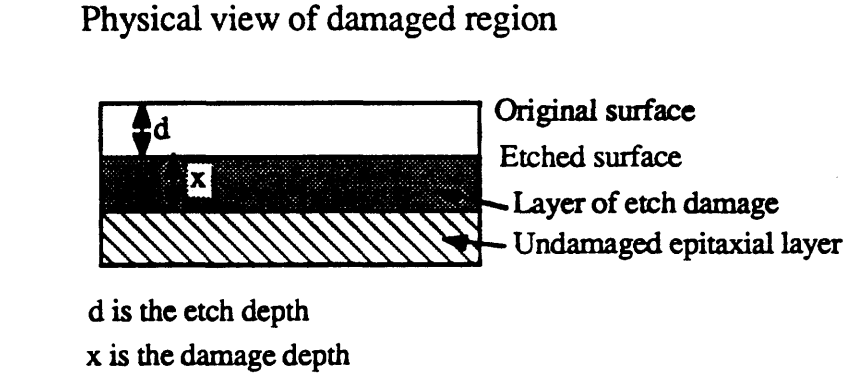

T1 is the thickness of the epilayer minus the surface depletion depth

Figure 3.15: Schematic showing the dry etch damage model.

If a simple " dry etch damage" model is assumed in which the bombarding ions introduce a distribution of defects which gives rise to a distribution of charge; thus creating an additional depletion layer where there is a non-conducting damaged region. Therefore, the reduction or diminishing of conduction, as measured by the TLM and Hall methods, is caused by the introduction of defects[1].

Fig. 3.15 demonstrates that if a non-conducting damaged region near the surface is followed by an undamaged region, then the distance x is a measure of the damage thickness at any given etch depth. By measuring the Hall mobility of the etched region the validity of

[1] The defects introduced during dry etching of n-GaAs are electron traps of which five have been detected in samples etched using CH_4/H_2 and $SiCl_4$. The etched samples were prepared and examined by the author using Deep Level Transient Spectroscopy but the results are not reported in this thesis

this simple model can be assessed further since if there was a graded interface between the damaged and non-damaged regions one would expect to see a decrease in the mobility, due to an increase in the electron scattering, especially for samples where most of the conducting material has been removed.

3.5.2. Discussion of CH_4/H_2 results

It can be seen from Fig. 3.9 for CH_4/H_2 RIE that the mobility remains constant for all etch depths. It was found that the conductance results (%C) measured using the TLM and Van de Pauw structures agreed to within ±2%. At an etch depth of 80nm the conductance had dropped to ≈10% of its initial value, as can be seen from Fig. 3.7, while the mobility remained constant both at 77K and 300K.

From the conductance plot it is evident that the conductance decreases faster for the CH_4/H_2 RIE than for the control wet etch and that after an etch depth of 20nm the divergence between the two plots ceases, implying that the region of damage saturation has been reached, region II in Fig 3.15. The extent of the damage can be seen from the graph to be 60nm. These results were taken after the samples had been annealed at 380°C for 1sec to remove the hydrogen passivation produced by the etching. It should be mentioned that the diffusion coefficient of hydrogen in n^+ GaAs ($3x10^{18}cm^{-3}$ Si) is $D= 4.08x10^{-2}\mu m^2.s^{-1}$ at 400°C[14], therefore hydrogen atoms can diffuse a distance of 0.2μm in 1sec at 400°C which is considerably higher than the thickness of the epitaxial layer. Further annealing produced no change in the results, whereas the results for no anneal can be seen to be almost no conduction whatever. It is concluded from this that the effect of hydrogen passivation has been removed entirely in the presented results.

3.5.3. Passivation of doped GaAs by hydrogen

There have been numerous reports and review articles on hydrogenation of III-V semiconductors in general and GaAs in particular[16-26]. Hydrogen passivates shallow donors[16] and shallow acceptors[17], and in the case of Si doped GaAs, vibrational spectroscopy had established that the hydrogen atom chemically bonds directly to the substitutional Si atom[18,19]. It was also suggested that , depending on the Fermi level position, hydrogen can be negatively charged in Si-GaAs, and neutral or positively charged in the depletion layer[20].

Chen et al[21] have used photochemical vapour deposition system to introduce hydrogen to GaAs and AlGaAs at 250-350°C. They observed an increase in the intensity of the excitonic recombination (shallow impurity bound excitons) with respect to the donor-acceptor pair recombination. Chevallier et al[16] had introduced hydrogen by low frequency

plasma and electrochemically both at 250°C. They showed that the depth of neutralization depends on the dopant concentration and the diffusion coefficient of hydrogen in GaAs decreases with increasing Si concentration. They suggested that the formation of Si-H bond produces a deep level which traps the extra electron from the Si dopant atom which otherwise would have been donated to the GaAs conduction band. Morrow[22] had suggested a mechanism by which native defects such as oxygen and V_{As} bond strongly to deuterium and diffuse deeper into the epitaxial layer at 500°C.

Although most hydrogenation experiments had been carried out at temperature range of 200-375°C and for times ranging between 1-3 hours, and in some cases, deuterium was used instead of hydrogen. These are not the typical temperature and time used in the reactive ion etching experiments performed in this study.

However, there has been a report by Creighton[23] in which a temperature programmed desorption experiments have been performed on both As- and Ga-rich GaAs surfaces. It was found that there is a measurable amount of arsine desorption occurring between 150 and 300K. Therefore, exposure to hydrogen atoms around room temperature should lead to a change in surface stoichiometry through loss of arsine. However, Creighton did not find any evidence that gallium hydrides were occurring. He suggested that the surface GaH_x species decompose efficiently by molecular hydrogen formation.

3.5.4. Discussion of the $SiCl_4$, Ar and Ne etching results

Etching in other systems produces similar results, but with greatly varying amounts of observed damage. Fig. 3.16 shows conductance versus etch depth for five different dry etches - CH_4/H_2 RIE, Ar IBE at 500eV, Ar IBE at 800eV, $SiCl_4$ RIE, Ne IBE at 500eV. Table II summarises the damage results using the two parameters D_s (depth at which damage saturation is reached) and D_d (damage depth at saturation). For some of the etches, such as Ar and Ne IBE, saturation was not reached, and so minimum figures are presented in these columns. In all cases the measured mobility remained constant with etch depth as in the case of methane hydrogen etching indicating the validity of the 'dry etch damage' model. It is worth mentioning that saturation effect has been observed by Yamasaki et al[15] in the barrier heights of Schottky diodes made after removing 10nm by sputter etching of GaAs using Ar plasma (50W).

There are two clear trends which can be seen to emerge from table II. The first is that damage increases with etch energy. This can be seen from the difference between Ar IBE at 500eV and 800eV. The difference here is small however, although more noticeable for the case of CH_4/H_2 etched at different energies[13].

Etching method	D_s (nm)	D_d (nm)
CH_4/H_2 RIE 930±30eV	27±3	60±5
$SiCl_4$ RIE 240±10eV	8±2	11±2
Ar IBE 500eV	>60	>80
Ar IBE 800eV	>80	>80
Ne IBE 500eV	>10	>50

Table II: The depth at which damage saturation is reached D_s and the damage depth at saturation determined by the TLM method for a variety of etch processes.

The second trend is that lighter atoms produce greater damage, as can be seen very clearly from the Ar and Ne results. This is not surprising because the energy deposited at the surface of the substrate by the bombarding ion (and thus the energy available for sputtering the surface atoms) increases with increasing the ion mass and energy. The sputtering yield, therefore, is higher for Ar than for Ne, hence for a constant ion flux i.e. a constant rate of energy deposition on the surface, less disordered material is being removed per unit time if Ne is used. This phenomenon has been reported in the literature[24].

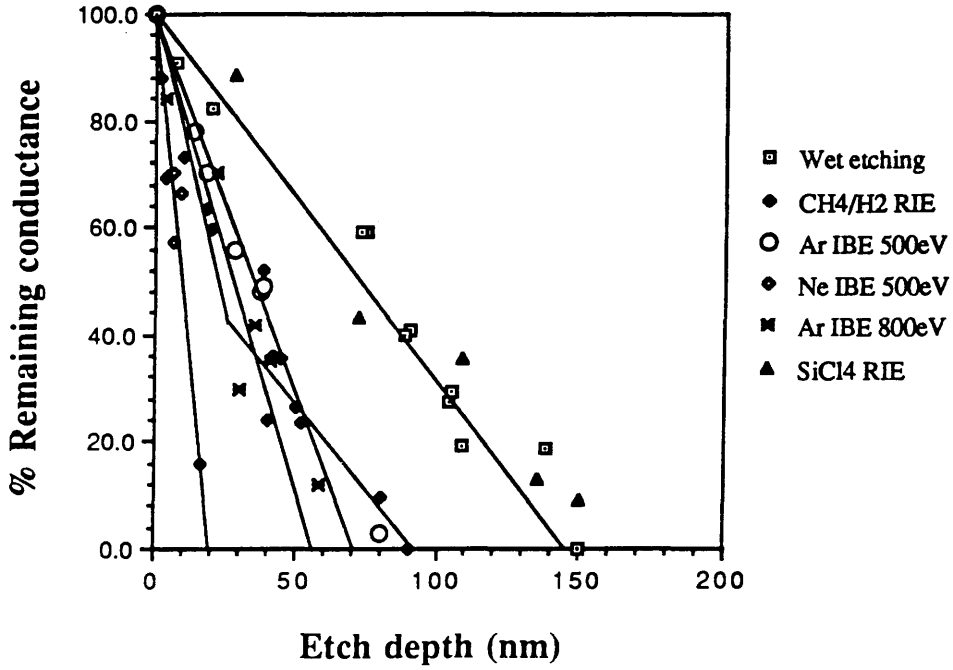

Figure 3.16: % Remaining conductance as a function of the etch depth for GaAs samples etched in CH_4/H_2 and $SiCl_4$ RIE and Ar (500eV and 800eV) and Ne (500eV). The epitaxial layer is 140nm thick, $3x10^{18}cm^{-3}$ Si-doped. The control samples were wet etched and plotted for comparison. The conductance was measured using the TLM method.

3.6. Is channeling possible at very low energies (E < 1keV) ?

In this and the following section, the fundamental question of 'why does the etch damage occur so deep in the material ?' will be discussed and arguments will be presented for and against some of the mechanisms suggested in the literature.

There have been contradictory reports about the penetration range of low energy ion beam in GaAs, for example 1keV Ar ion beam. Hidaka et al[27] have reported a projection range of 2.5nm, Pang et al[28] on the other hand have estimated a range of about 7.6nm. However several workers have reported in the literature that their estimates of the depth of damage induced by dry etching is much larger than the penetration depth of ions in the substrate. Various techniques have been used for the characterisation of etch damage.

Germann et al[29] estimated the damage depth in GaAs/GaAlAs MQW structure using photoluminescence quantum wells at different depths. They estimated damage depths of 35nm and 160nm for Ar ion beam etching at 250eV and 1000eV, respectively.

Hidaka et al[27], on the other hand, had determined a damage depth of 120nm for rf plasma etching of GaAs in Ar at bias voltage of 76V using wet etching and photoluminescence. They compared their results with Pang's report[30] of 50nm damage depth using a 500eV Ar ion beam and Ghandhi's[31] damage depth of 90nm for an Ar ion beam at 100eV. Hidaka suggested that the relatively large damage depth they determined may be due to the different evaluation methods used. Pearton et al[32] have estimated a minimum damage depth of ~50nm after etching GaAs in an Ar ion beam at 500eV at a tilt angle of 45°. The damage depth was determined by Schottky diode characterisation and wet etching. They also reported the presence of dislocation loops 6-7nm in diameter at depths between 13 and 46nm below the surface after annealing the samples to 800°C for 10sec. This depth is higher than their estimate of the mean range of 500eV Ar ion in GaAs (2.4nm with a straggle of 1.2nm). Pang et al[33] have also reported that the breakdown voltage and the barrier height of Schottky diodes reduced drastically upon Ar ion beam etching at 500eV. I-V and C-V measurements had indicated the formation of an insulating layer on the surface. They also concluded that electrical measurements are more sensitive to defects generated in the substrate than most surface analytical techniques such as RBS, RHEED and cross section TEM. Scherer et al[34] had used Ne ion beam to pattern GaAs/GaAlAs two-dimensional electron gas (2DEG) heterojunction. By measuring the resistance *in situ*, they found that upon etching 10nm of the cap layer, the 2DEG, which lies at 50nm beneath the cap layer, ceases conduction.

All the above workers have observed a large damage depth in comparison with their estimates of the ion penetration depth. Germann et al[29] had investigated the dependence of the photoluminescence intensity of the angle of incidence of Ar ions (250eV) on multiple

quantum well material, Fig. 3.17. Their results were interpreted in terms of axial channeling along the <110> and <111> directions. The results in Fig. 3.17 clearly show an orientation-dependent effect.

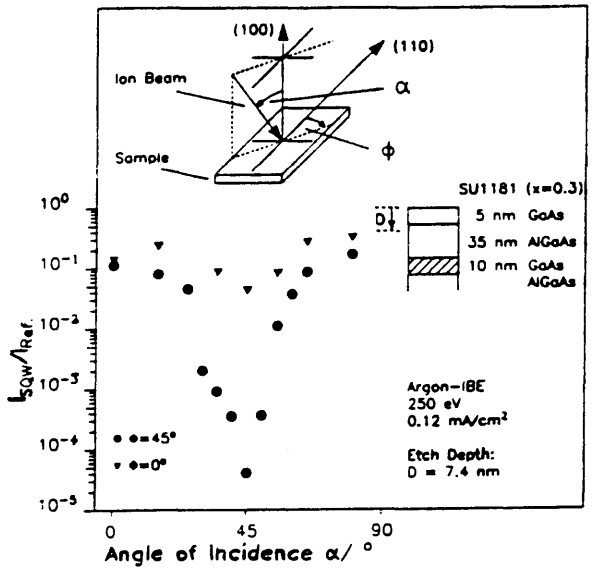

Figure 3.17: The normalized PL intensity as a function of the angle of incidence α of the argon beam on two different sample orientations: (a) sample rotated to Φ = 45° round the normal direction relative to the <110> direction (circle); (b) sample aligned parallel (Φ =0°) to the <110> direction. All samples were etched with an ion energy of 250eV to a depth of 7.4nm. The upper part of the figure shows the geometry of the etching process. (The figure is reproduced from Germann et al[29])

To investigate whether an effect such as channeling can occur at very low energy, the theory of channeling will be considered briefly, and quick estimates of some of the channeling parameters will be performed. The results of an experiment devised to examine any orientation-dependent effect will be described and discussed.

In the classical theory of channeling,when an energetic particle (few tens keV ≤ E ≤ few MeV) enters the crystal lattice within a certain angle Ψ of a low index axis each time it approaches one of the aligned rows of atoms, the gradually increasing repulsion between the screened Coulomb fields of the projectile and the lattice row is sufficient to steer it away again thereby preventing violent nuclear collisions from occurring. One obvious consequence of this steering mechanism is that the rate of energy loss is greatly reduced and so the ion penetrates more deeply than in an amorphous target.
There are two mechanisms responsible for stopping an energetic particles[35]:

a. Nuclear collisions in which the momentum and kinetic energy are transferred to translatory motion of the target atom as a whole (elastic encounter) and predominates at lower energies (E < 4keV). This is the energy loss mechanism of interest for the energy range used in the ion beam and reactive ion etching.

b. Electronic collisions in which the energy is transferred to the individual electrons of the atoms resulting in atomic excitation or ionization processes (inelastic encounter), dominating at high energies (E > 4keV).

For a given projectile and a single crystal target, the energy and the trajectory of the particle determine which stopping process predominates. Eriksson et al[36] had experimentally derived nuclear stopping powers for perfectly channeled Xe ions along the <100> direction of tungsten.

By measuring R (the range of the most perfectly channeled part of the incident beam) as a function of beam energy E, the total stopping cross section S can be derived by differentiating the R versus E curve.

So the stopping power S for perfectly channeled beam can be defined by

$$S = (1/N).\Delta E/\Delta R \qquad (3.4)$$

In Fig. 3.18, the stopping power was plotted as a function of $E^{1/2}$, and for E > 4keV the relationship is linear, characteristic of the electronic stopping power[36]. The values of the nuclear stopping power were obtained by subtracting the extrapolated electronic stopping contribution from the measured stopping power. Values of the total and partial stopping cross sections (in units of 10^{-14}eV.cm^2/atom) for perfectly channeled Xe^{133} ions along the <100> direction in tungsten is presented in table III[36].

E(keV)	S	S_e	S_n
0.5	3.2±0.4	0.24±0.01	3.0±0.4
1	2.3±0.3	0.34±0.02	2.0±0.3
2	1.6±0.2	0.48±0.03	1.1±0.2

Table III: The total stopping power S, extrapolated electronic stopping S_e and the derived nuclear stopping S_n for perfectly channeled Xe^{133} ions along the <100> direction in tungsten[34].

As can be seen in table III, the contribution of the nuclear stopping power become increasingly large as the ion beam energy decreases. It should be mentioned that the literature on the theory and experiments on channeling at very low energies is very scarce especially on GaAs.

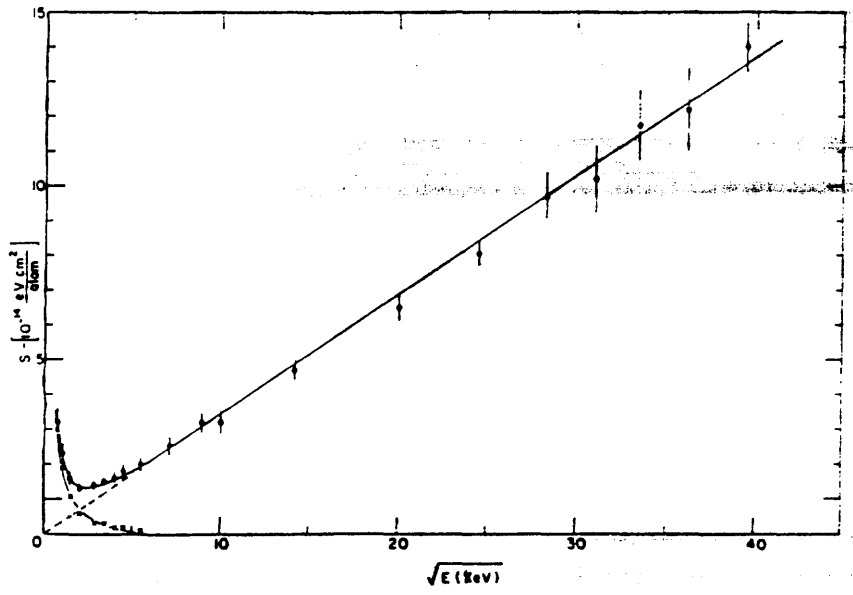

Figure 3.18: Experimentally derived values of the total stopping cross section (open circle) as a function of $E^{1/2}$ for well channeled Xe ions incident on the <100> axis of a W crystal. The dotted line is an extrapolation of the electronic contribution to lower energies. Crosses indicate the nuclear stopping obtained by subtracting the extrapolated electronic stopping power from the measured total values. (The figure is reproduced from Eriksson et al[36])

At energies less than 1keV, the range even of a channeled atom becomes comparable to the lattice spacing: for example, for 250eV Xe^{133} in the <100> direction, removal of 10Å of tungsten (which is only six atomic layers) left less than 0.08% of the injected activity in the crystal indicating that in this energy region one has a "quantized" range distribution, i.e. a significant fraction of the beam becomes stopped within a single atomic layer. Eriksson[36] had attempted to apply the momentum approximation model for E > 0.5keV to predict the energy loss properties. However, this model breaks down at very low energies because the stopping power must go through a maximum and then decrease as the energy of the particle is spent.

The above examples have demonstrated that channeling is likely to occur at high energies, but not at the energy range used for RIE and IBE.

Lindhard[37] had demonstrated that classical mechanics can be applied to the channeling case (involving a series of collisions) even though individual scattering events may not be amenable to classical treatment. It should be mentioned that the need for quantum mechanical consideration does not arise since the energy of the particles is very low. For axial channeling, Lindhard treated two approximations, the continuum string and the perfect string of which only the first will be considered here. In the continuum approximation, the

potential due to a row of atoms is considered to be uniformly smeared out along the row i.e. a continuum potential.

Using Lindhard's theory[35,37], the continuum approximation, some characteristic channeling parameters such as the angle of incidence of the particle upon a row of atoms Ψ_1 and the half angle of the axial channeling dip $\Psi_{1/2}$ will be estimated, see Fig 3.19, for Ne and Ar in GaAs at energies of 500 and 1000eV using the data, quoted for low energy, given by Gemmell[35].

For axial channeling, the angle of incidence of the particle upon a row of atoms Ψ_1 is given by

$$\Psi_1 \approx 0.307(Z_1 Z_2 / dE)^{1/2} \text{ degrees} \qquad (3.5)$$

where Z_1 and Z_2 are the atomic numbers of the incident ion and the target atom, E is the energy of the incident particle and d is the spacing between atoms in the row. The half angle of the axial channeling dip $\Psi_{1/2}$ is given by

$$\Psi_{1/2} = 0.8\, F_{RS}\, (1.2U_1 / a)\Psi_1 \qquad (3.6)$$

Where $F_{RS}(\xi)$ is the Moliere potential can be obtained from Fig. 3.20[35], U_1 is the thermal vibration amplitude which may be estimated from Debye approximation[38] as follows:

$$U_1 = 1.21\, \{[\Phi(x) / x + 1/4] / M_2\, \Theta\}^{1/2} \text{ nm} \qquad (3.7)$$

Where $\Phi(x)$ is the Debye function which can be obtained from Fig. 3.21, M_2 is the atomic weight (amu) of the crystal atoms, Θ is the Debye temperature (K) and x is given by

$$x = \Theta / T \qquad (3.8)$$

where T is the crystal temperature (K). Values of Θ and M_2 were obtained from Gemmell. The value of a in equation 3.6 is the Thomas-Fermi screening radius. If the incident ion is not fully ionized, the Thomas-Fermi screening radius is given by

$$a = 0.04685\, (\sqrt{Z_1} + \sqrt{Z_2})^{-2/3} \text{ nm} \qquad (3.9)$$

For GaAs, Z_2 is (31+33)/2 =32, Z_1 is 10 for Ne and 18 for Ar, therefore a = 0.011nm for Ne and 0.0102nm for Ar. The ion beam energy will be taken as 10^{-3}MeV and 5×10^{-4} MeV, (1keV and 500eV). The lattice spacing d is equal to 0.565nm along the <100> direction,

0.401nm along the <110> direction and 0.326nm along the <111> direction. The results of Ψ_1 in GaAs are presented in table IV

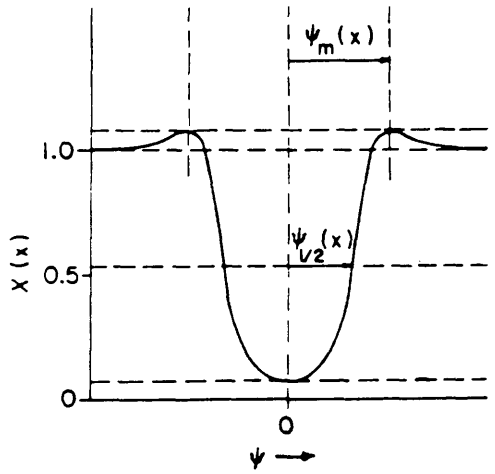

Figure 3.19: The normalized depth dependent yield X(x) of a close encounter process as a function of the angle Ψ (the angle between the incident beam and axial or planar direction in the crystal) measured in a channeling experiment. The angle $\Psi_{1/2}$ is half the value of Ψ at X(x) = 0.5. The curve is commonly known as the channeling dip.

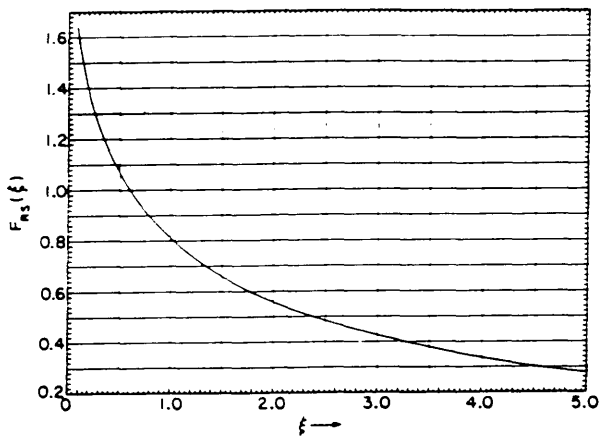

Figure 3.20: Graph of the function $F_{RS}(\xi)$ as defined by Moliere's potential. (The figure is reproduced from Gemmell[35]).

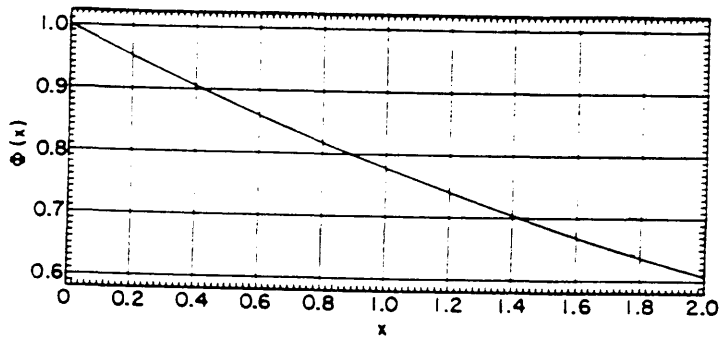

Figure 3.21: Graph of the Debye function $\Phi(x)$ as a function of x. (The figure is reproduced from Gemmell[35]).

Ion energy	Ψ_1<100>	Ψ_1<110>	Ψ_1<111>
Ne 1keV	73.06	86.72	96.18
Ne 0.5keV	103.32	122.64	136
Ar 1keV	98.02	116.53	129.04
Ar 0.5keV	138.62	164.54	182.49

The results in table IV are unreasonably large and can not be interpreted physically. Debye temperature Θ for GaAs is 346K, and the crystal temperature T is 291K, the value of x in equation 3.8 is 1.19. From Fig. 3.21[35], $\Phi(x)= 0.74$, and M_2 is 72.6amu (as for Ge). Using equation 3.7, the thermal vibration amplitude U_1 for GaAs is 0.0071nm. From Fig. 3.20, F_{RS} $(1.2U_1 / a) = F_{RS}$ $(0.7745) = 0.90$ for Ne and F_{RS} $(0.8353) = 0.88$ for Ar. The value of the half angular width of the channeling dip $\Psi_{1/2}$ for axial channeling can be obtained using equation 3.6 for Ne and Ar at 1keV and 500eV and are listed in table V.

Ion energy	$\Psi_{1/2}$<100>	$\Psi_{1/2}$<110>	$\Psi_{1/2}$<111>
Ne 1keV	52.60	62.43	69.24
Ne 0.5keV	74.39	88.30	97.92
Ar 1keV	69.00	82.03	90.84
Ar 0.5keV	97.58	115.83	128.47

It can be seen from the values calculated for Ψ_1.and $\Psi_{1/2}$ for very low energy ions that the channeling theory does not apply correctly at this energy range.

The energy used in the RIE and IBE is of the same order as that of a channeling particle at the final stage before it come to rest, namely the dechanneling stage. In this stage, the transverse energy of the particle become significantly modified through multiple scattering with electrons and nuclei. When the transverse energy of the particle become larger than the critical value for stable channeling, the particle will then dechannel and eventually come to rest after one or a series of collisions with the lattice atoms thereby creating disorder in the form of vacancies and interstitials.

It has also been observed that for well channeled ions of equal energy, the higher the mass the lower the velocity and hence the lower the stopping power. Therefore, contrary to the case of amorphous ranges where the nuclear stopping power usually dominates, channeled particles of high mass penetrate deeper than the lower mass particales[35].

The arguments presented above clearly show that channeling is a high energy phenomenon and is not likely to occur at very low energies, therefore it is suggested that channeling is not responsible for producing the deep damage observed in the case of RIE and IBE studied. Alternatively, an efficient momentum transfer mechanism or a diffusion related effect may be responsible for creating the damage.

An experiment was devised to test whether there is any crystallographic orientation- related effect during ion beam etching in Ar at 500eV.

3.6.1. Experimental

Six TLM/Hall samples were prepared as described earlier in section 3.3. the samples , with epitaxial layer 140nm, thick n-doped to $3x10^{18}cm^{-3}$, were mounted on a special graphite-coated holder suitable for use on the ion beam etcher. The samples were aligned, using straight line grooves in the holder, at various angles with respect to the <011> direction i.e. the edge of the sample. The angles were 0, 5, 10, 30, 40 and 45 degrees with uncertainty of ±2 degrees. The sample holder was then mounted on the etcher stage so that the ion beam direction is at a right angle with the plane of the samples. Care was taken to insure that the lines on the holder are positioned as vertically as possible. The sample holder was then tilted to an angle of 45 degrees with respect to the ion beam direction. The samples were etched for 75sec using Ar ion beam at 500eV. The etch depth was measured for each sample and etch rates was found to vary between 23 to 65nm/min depending on the crystallographic direction[32]. The conductance was measured for each sample and the %C was obtained. Since the samples were etched simultaneously, it was assumed that they received the same dose of ions. Since the damage depth increases linearly with the etch depth as was found earlier in section 3.4.3., the %C was normalized by dividing it by the etch depth measured for each sample to eliminate the effect of conductance variation due to the thickness of the epitaxial layer. The normalized conductance (remaining conductance

per unit etch depth) was plotted as a function of the angle of the <011> direction. The Hall mobility after etching was found to be similar to that prior to etching. The same samples were examined by Raman scattering as described in section 3.7. and the depletion depth were obtained. The same normalization process was followed as above by taking the ratio of the depletion depth to the etch depth and the result was plotted together with the % conductance as a function of the angle off the <011> direction in Fig. 3.22. The result, Fig. 3.22, shows an orientation dependency of the remaining conductance on the rotation angle.

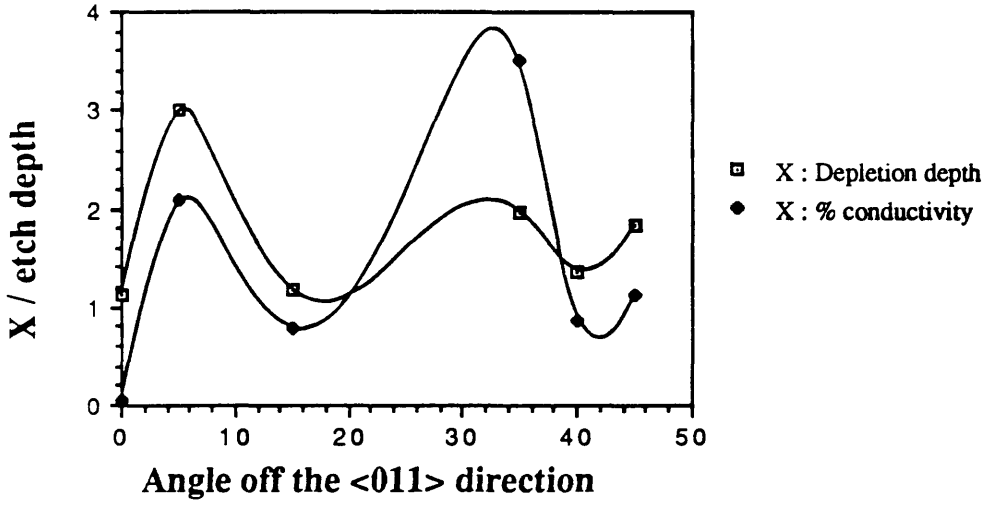

Figure 3.22: The normalized % remaining conductance (%C/d) and normalized depletion depth as a function of the rotation angle Φ off the <110> direction. The samples were ion beam etched in Ar at 500eV. The tilt angle was 45° off the direction of the ion beam.

3.6.2. Discussion of results

The result presented at Fig. 3.22 clearly shows some kind of orientation dependent effect. It can be seen that at an angle of about 35°, the %C / etch depth reaches a local maxima showing that lower damage is produced at this angle. Again the depletion depth / etch depth curve shows a weak maxima indicating that a small depletion depth was formed at this angle. From simple geometry[2], it can be shown that 35° is the angle between the (110) and (111) planes and the low damage produced at this angle may be related to the fact that the (111) is the close-packed plane in a face-centred cubic structure.

As argued above, it is rather unlikely that channeling occursat the energy range used for ion beam and reactive ion etching, i.e.E ≤ 1keV.

2 For a cube with a unit cell 'a', by defining the (110) and (111) planes, it can be shown that the angle between these plane $\theta = \tan^{-1}(1/\sqrt{2}) = 35.26°$.

It is suggested that other diffusion or efficient momentum transfer mechanisms such as radiation enhanced diffusion, interstitial diffusion, focusing sequence collisions and assisted focusing may be responsible for the formation of deep damage. These mechanisms will be discussed briefly.

a. Radiation enhanced diffusion: Can be explained by the generation and diffusion of vacancies created during irradiation with ions. Pfister[39] had proposed the creation of point defects by ion irradiation leads to enhanced substitutional diffusion via vacancy mechanism.

b. Interstitial diffusion: This rapid diffusion process occursafter the atoms have lost their initial energy without producing damage in the surrounding lattice. Such atoms must be at interstitial site and hence diffuse interstitially until they encounter a suitable trapping centre such as a vacancy, a dislocation or perhaps another impurity atom.

c. Focusing sequence collisions: Silsbee[40] had pointed out that for successive collisions between atoms in a close-packed row of atoms, the momentum vector may become more and more parallel to that row after every collision. Neglecting the thermal vibrations, the energy transferred in a head-on collision is 100%. However, the focusing mechanism is only possible in rather close-packed directions like <100> in FCC structures. When the starting angle of collision is not small, the energy transferred per collision become appreciably less than the maximum.

d. Assisted focusing: Consider a <100> direction in a FCC structures, (see Fig. 3.23) when the lattice atom receives an impulse in a direction near <100> it has to travel through a square consisting of four nearest neighbour atoms before hitting the next atom in the <100> row. The angle between the momentum direction and the <100> direction will decrease when passing through the ring due to the repulsion by those ring atoms. As a result, focussing may occur and collision sequences may travel in the <100> direction. These are always replacement sequences.
It is believed that one or more of these mechanisms may be responsible for the observation of the deep damage in GaAs.

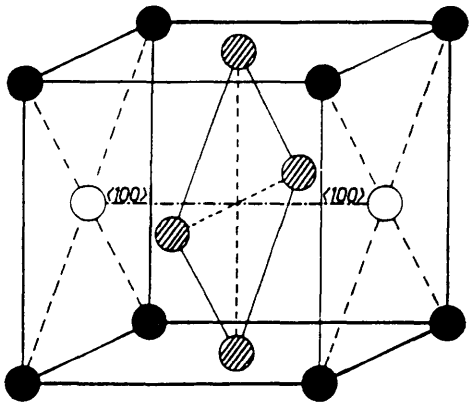

Figure 3.23: A sketch of unit cube on an FCC crystal to show the ring of the neighbouring atoms (hatched) around a <100> direction.

3.7. Raman scattering of coupled LO phonon-plasmon modes

3.7.1. Introduction

Raman scattering of the coupled LO phonon-plasmon scattering was investigated on heavily doped n^+ GaAs ($3x10^{18}cm^{-3}$) after reactive ion etching in CH_4/H_2 and Ar and Ne ion beam etching (IBE) .

Although Raman scattering uses a probe having a wavelength $\lambda > 300nm$, it has the capability of being sensitive to various localized electronic and vibrational interactions in solid[41], for example, the interaction of optical phonons (polar lattice vibrations) with the plasma oscillationsof free carriers. This interaction produces coupled plasmon-LO phonon modes (cp-LO) which replace the LO phonons and the free carrier oscillations with two modes L_1 and L_2 (high and low frequency modes respectively), Fig. 3.24[41]. In heavily doped materials the lower branch L_2 will approach the TO phonon frequency ($269cm^{-1}$) with longitudinal characteristics while high branch L_1 approaches plasma frequency and therefore the carrier concentration can be deduced readily[42].

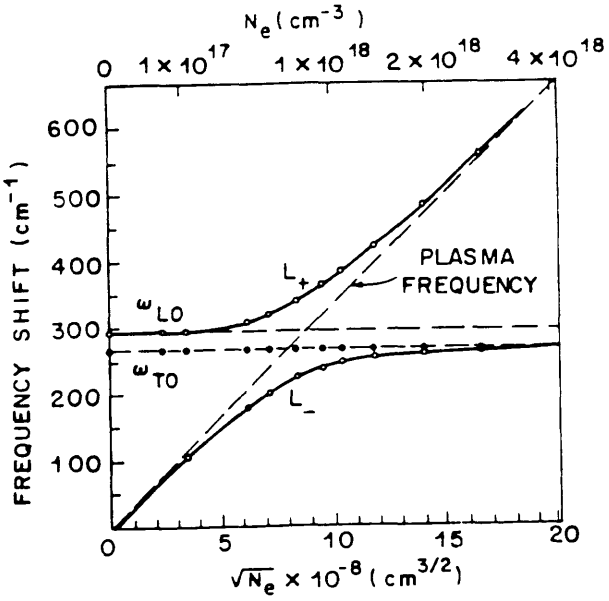

Figure 3.24: Frequency shifts measured in light scattering spectra of coupled plasmon LO-phonon modes of n-GaAs. (The figure was reproduced from Cardona and Guntherodt[41]).

3.7.2. Theory

The frequencies of the cp-LO modes are given by[41]

$$L_{1,2}^2 = 1/2 \left(\omega_{LO}^2 + \omega_p^2 \right) \pm 1/2 \left\{ \left(\omega_{LO}^2 + \omega_p^2 \right)^2 - 4\omega_p^2\omega_{TO}^2 \right\}^{1/2} \qquad (3.10)$$

where ω_{TO} and ω_{LO} are the bare TO and LO phonon frequencies, while ω_p is the plasma frequency of the electrons. By solving the system dielectric function $\varepsilon(\omega) = 0$ for longitudinal modes[42]

$$\varepsilon(\omega) = \varepsilon(\infty)\left[(\omega^2 - \omega_{LO}^2) / (\omega^2 - \omega_{TO}^2) - \omega_p^2(q)/\omega^2 \right] \qquad (3.11)$$

where $\omega_p(q)$ is the wave-vector-dependent plasma frequency which is

$$\omega_p^2(q) = N_e e^2/\varepsilon_o \varepsilon_r m^* + 3/5\, K^2 V_F^2 \qquad (3.12)$$

here, N_e is the free carrier density, ε_o, ε_r is the permitivity in vacuum and of the semiconductor respectively, m^* is the effective mass and K is Bolt zmann constant. The V_F is the Fermi velocity, assuming a parabolic band,

$$V_F = (h/m^*) (3\pi^2 N_e)^{1/3} \qquad (3.13)$$

q is the wave-vector of plasmon-phonon mode which, for back scattering configuration, is equal to q = 2νn, where ν is the wave-vector of the excitation light, and n is the refractive index at the excitation frequency.

The plasma frequency is a function of the electron effective mass, the carrier density and the wave vector of the incident radiation. For GaAs, the plasma frequency varies from 100 to 700 cm^{-1} for doping densities between 10^{17} and $10^{19} cm^{-3}$. Because of this, the cp-LO modes can be well separated from the bare LO frequency. This allows the probe of depletion layers in heavily doped semiconductors, whose Fermi level is pinned to the surface. In this circumstance, the region nearer to the surface of the sample is carrier free. Therefore only bare LO phonon modes exist within the depletion layer width. Beyond the depletion layer, the carrier density increases rapidly and coupled plasmon- LO modes replace the bare LO mode.

Because the LO and the cp-LO modes have different frequencies, it is then possible to observe them simultaneously in the Raman spectrum. The presence of the bare LO modes gives information about the crystal quality of the near surface region. The relative intensity of the cp-LO mode to the bare LO phonon mode is a direct measure of the depletion layer width and any process induced changes. Assuming an abrupt change of carrier densities from the depletion region to the bulk region, the surface depletion layer thickness d can be calculated from the integrated intensity I(LO) as compared with $I_o(LO)$ of an undoped or semi-insulating GaAs material ($n < 1x10^{14} cm^{-3}$)[43] of known thickness using

$$I(LO) = I_o(LO) [1 - e^{-\alpha d}] \qquad (3.14)$$

where α is the absorption coefficient of GaAs.

Therefore the LO phonon intensity decreases with the increase of material doping level. Assuming $I(LO) - I_o(LO)$ is proportional to the intensity of the coupled LO phonon-plasmon intensity $I(L_1)$, one can get

$$I(LO) / I_o(L_1) = ß [e^{\alpha d} - 1] \qquad (3.15)$$

where ß is a scattering constant obtained from

$$I_o(LO) - I(LO) = ß I(L_1) \qquad (3.16)$$

The relative change of the intensity between L_1 and the bare LO modes can give information about the change in the surface depletion layer thickness which, in turn, is related to the

surface damage caused by the etching.

Surface structural change such as surface roughness can also be revealed by the polarisation of incident and scattered light on the grounds of crystal symmetry[44].

3.7.2. Experimental setup

The same TLM samples examined in section 3.4.1 and 3.4.3 were used for this study and the active layer in the centre of the Van der Pauw geometry was probed ($400x400\mu m^2$).

Two lines from Ar ion laser (Spectra-physics model 2045), namely, 364nm and 488nm were used to probe the different depth of the surface region. The absorption coefficients[45] of these lines in GaAs are $7.27x10^5$ and $1.27x10^5$, which correspond to laser penetration depths ($1/\alpha$) of 13.8 and 78.7nm respectively. The experiments were carried out at room temperature. The scattered light was dispersed by a Jobin-Yvon double grating spectrometer and detected by a cooled GaAs photomultiplier (253K) or a CCD multichannel system operating at 140K. The spectrometer is also equipped with both the UV and visible gratings to optimise the detected signal. The spectra of Raman scattering on unetched control samples are shown in Fig. 3.25.

The coupled phonon-plasmon mode was not observed under the UV line of 364nm hence, as shown in Fig. 3.26, the penetration depth of this line is smaller than the depletion depth of the control material. No detectable difference in peak intensities has been found between 488nm and 514.5nm laser lines, as expected.

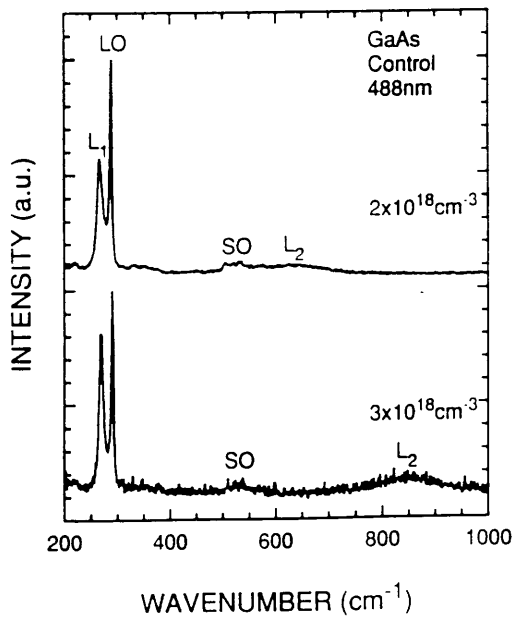

Figure 3.25: Raman spectra of heavily doped GaAs. The coupled plasmon-LO phonon mode and bare LO phonon line can be observed simultaneously due to the presence of

surface depletion layer. In high doping regions, the oscillation strength of L_1 is larger than L_2. The second order scattering is also observed.

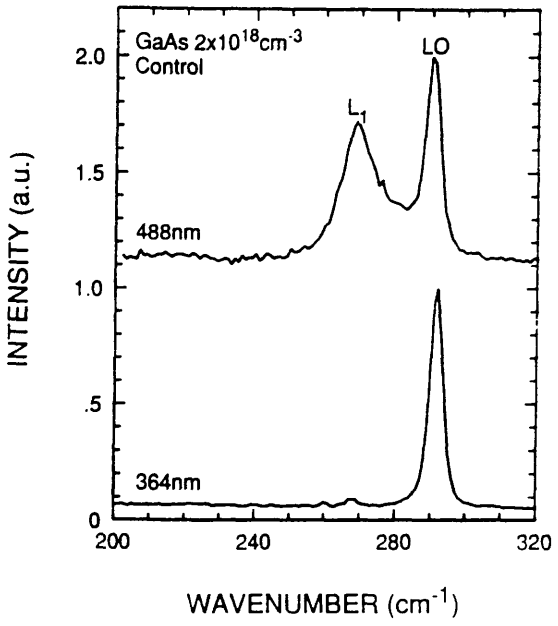

Figure 3.26: Raman spectra taken using the 364nm and 488nm laser lines. The coupling of LO phonon with plasmon was not observed in the surface depletion region.

Two limitations must be considered on the analysis of Raman scattering of RIE and IBE GaAs. One is that the Raman scattering cannot probe damage depths larger than its own penetration depth. Therefore, the maximum damage depth assessed in our experiment is limited to 80nm by employing 488nm laser lines. The other limitation is the etching depth must be controlled to such a level that the Raman scattering does not probe the substrate region. Again, one can only analyse the sample with maximum etching depth of 60nm in the epitaxial GaAs layers (140nm thick) by using the 488nm laser line. This is because the epitaxial layer as grown on semi-insulating GaAs substrate in which bare LO phonons exist.

The experiments were performed under two commonly used polarisation configurations with back scattering geometry, designated by the notation $Z(X,Y)\bar{Z}$ and $Z(X',Y')\bar{Z}$, where X, Y, Z donate $[0\bar{1}1]$, [011] and [100] while X' and Y' denote [010] and [001]. Transverse optical (TO) phonon scattering is forbidden in this back scattering geometry. This Raman scattering selection rule for LO phonon also holds very well for the coupled LO phonon-plasmon mode[46] as shown in Fig. 3.27. The selection rules for Raman scattering are very well observed in the control material for both polarisation configurations (Fig.3.27 shows one of the configurations).

3.7.3. Results and discussion of Raman scattering.

The thickness d of the surface depletion layer can be calculated from equation 3.14 by careful comparison between the integrated intensity of the scattered bare LO phonons in the n^+ GaAs samples and that of an undoped GaAs.

The calculated depletion layer thickness in control sample (2x $10^{18}cm^{-3}$ is about 17.5 ±1.0nm. This value is in a good agreement with the theoretical degenerate model by Shen et al[47] and also verifies the observation discussed in Fig. 3.26.

The transition region beside the depletion region is typically 4.5nm[43]. This region should have little effect on the Raman spectra for penetration depth and depletion layer thickness larger than 25nm[41]. The band bending in the control sample can also be calculated to be 0.48eV from Poisson equation[48].

From equation 3.15, the scattering constant ß was evaluated to be 2.73 after the depletion layer thickness was calculated independently by comparing with an undoped sample.

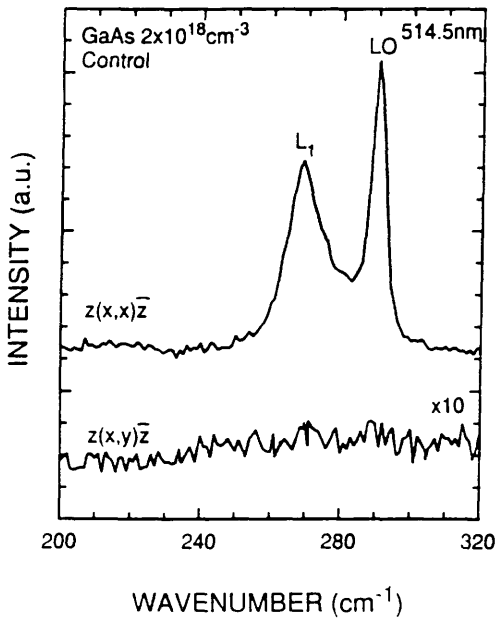

Figure 3.27: Raman spectra in the allowed $Z(X,X)\bar{Z}$, and forbidden $Z(X,Y)\bar{Z}$ scattering geometry under the back scattering configuration in the control sample. X,Y, and Z denote $[0\bar{1}1]$, [011] and [100] respectively.

The Raman spectra of GaAs reactive ion etched in CH_4/H_2 for 2 minutes is shown in Fig. 3.28. The L_1 and LO phonon can be seen in the $Z(X,Y)\bar{Z}$ and $Z(X',X')\bar{Z}$ configurations while scattering by both screened and bare LO phonons should be prohibited.The Raman spectra of samples ion beam etched in Ar at energies of 500 and 800 V are shown in Figure 3.29. It can be seen that the L_1 peak intensity has decreased for the sample etched in Ar IBE at 800 V.

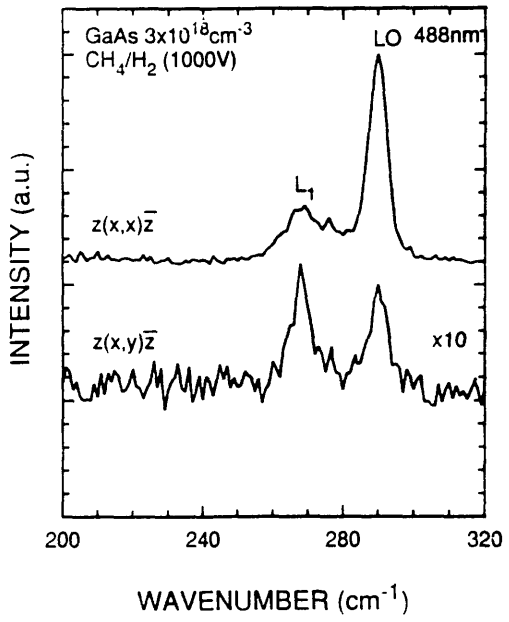

Figure 3.28: Raman spectra in the allowed and forbidden scattering geometry under the back scattering configuration after the reactive ion etching of GaAs in CH_4/H_2 for 2 minutes. The breakdown of selection rules, although not severe, can be observed clearly. It is also clear that L_1 mode is more sensitive to the damage than LO mode. The geometry is the same as figure 3.27.

While dry etching generally produces damage, wet etching tends to reduce the surface defects already present in the material by reducing the surface roughness and removing the surface contamination. Fig. 3.30 shows that the L_1 intensity increases after etching away 40nm. This corresponds to a reduction of surface depletion depth from 17.5±1.0nm to 16.0±1.0nm on this sample.

The depletion depth determined from the Raman spectra was plotted as a function of etch depth for samples etched in CH_4/H_2, ion beam etching in Ne (500V), Ar (500 and 800V) and wet etching, Fig. 3.31.

For CH_4/H_2 etching, the figure shows that at the start of the etching, the damage increases and then saturates with a constant depletion depth. The saturated depletion depth is 50.0±2.0nm for dc bias voltage of 930±30V.

Ne ion beam etching (500V acceleration voltage) produces the largest damage in this set of samples.

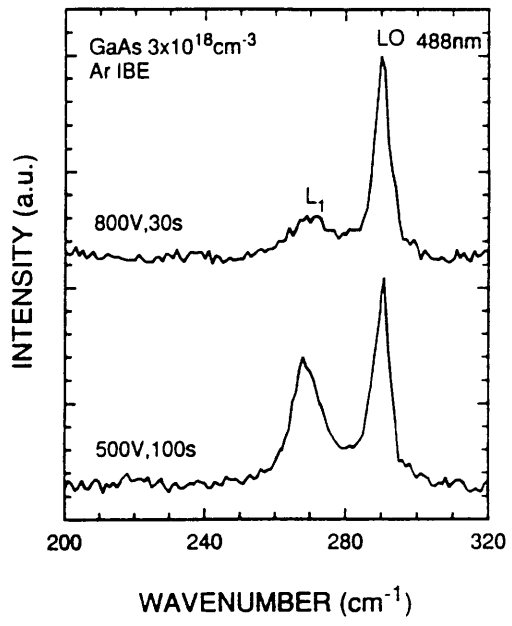

Figure 3.29: Raman spectra of GaAs after Argon ion beam etching. It shows clearly that etching at relatively high accelerating voltage (800V) induces larger damage than etching at lower accelerating voltage (500V) by comparing the relative intensities of L_1 and LO phonons.

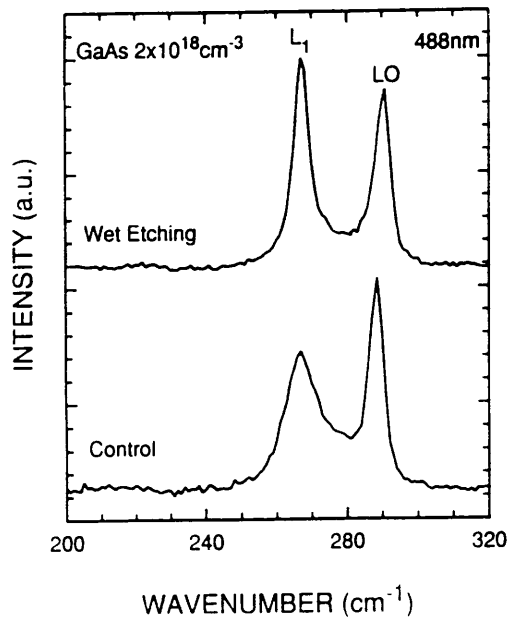

Figure 3.30: Raman spectra of GaAs after wet etching. Wet etching tends to reduce the surface defects already present in the sample. This is corresponding to the decrease of depletion layer thickness after wet etching.

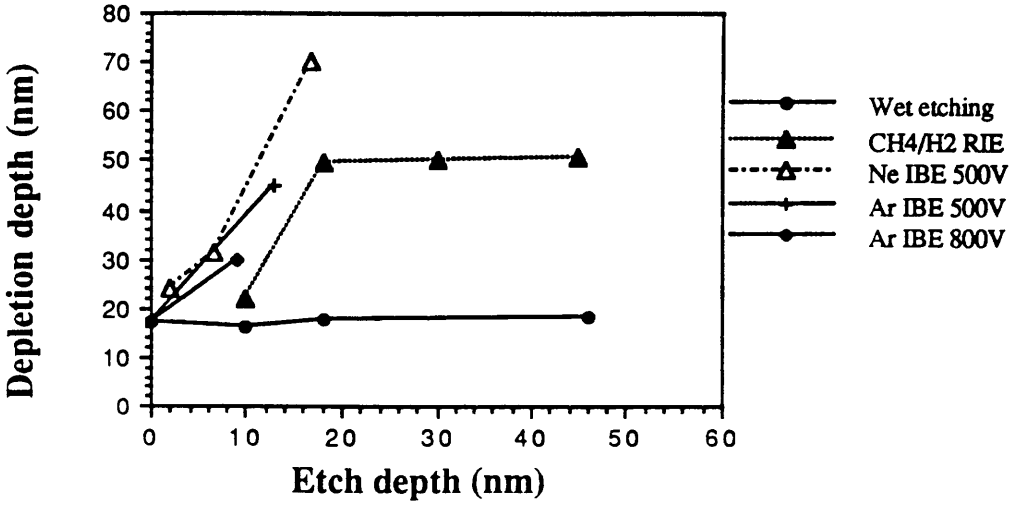

Figure 31: Depletion depth of GaAs as a function of etch depth in various dry etching techniques. In CH_4/H_2 RIE, the damage saturation was observed after an etch depth of 20nm.

Glembocki and Dobisz[49] have measured the ratio of intensities of the cp-LO and the bare LO modes of GaAs dry etched by Ar or Cl_2 sputtering, RIE in BCl_3 and chemically assisted ion beam etching (CAIBE) using Ar/Cl_2 with ion energies between 0.2-3keV. However, they have not measured the depletion layer thicknesses. They concluded that while CAIBE and RIE both reduce the above ratio similarly, their effect is smaller than the Ar sputtering. The best results they found were for the Cl_2 sputtering where the least reduction in the ratio was observed. Mlayah et al[50] have observed LO coupled-damp ed plasmon modes in highly p-doped GaAs and their estimate of the doping level was in agreement with the Hall measurements.

3.8. Conclusions

1. Low dc bias voltage in the case of RIE, and low accelerating voltage in the case of IBE is a key parameter to reduce the damage induced by the energetic ion bombardment.
2. The use of ions (reactive or inert) with high masses helps to reduce the etching induced damage.
3. The employment of etching processes with high etch rates is an important factor in reducing the accumulated damage in the epitaxial layer, since the saturation condition will be reached at an area nearer to the surface via allowing less damage to accumulate (this is the case in $SiCl_4$ etching). In comparison, the dc bias voltage used in the case of CH_4/H_2

etching was approximately four times higher and the etch rate was about an order of magnitude lower which resulted in larger damage depth.

4. The TLM method has proved to be a powerful technique for evaluating the damage depth accurately, and both the TLM and Raman scattering of the coupled plasmon- LO phonon method have produced reasonably close results.

5. The surface damage in GaAs can be described using an 'abrupt damage model' by which the thickness of the non-conducting subsurface layer saturates as the etching proceeds, and the interface between the conducting and non-conducting layers is abrupt.

6. Arguments were presented against the possibility of channeling at very low energy as a cause for the deep damage observed by this study and other workers. Alternative diffusion and efficient momentum transfer mechanisms, such as radiation enhanced diffusion, interstitial diffusion, focu sing sequence collision and assisted focusing may be responsible for the deep propagation of damage.

Table IV shows results obtained using different techniques on either the same or similar material systems. It can be seen that they agree fairly well on the main points, but that there are some discrepancies. Most notable is the saturated damage depth using CH_4/H_2 RIE at 930±30V as measured using Raman and TLM methods described here. The same samples were used for both measurements.

Etching method	D_s (nm)	D_d (nm)	Technique	comments
CH_4/H_2 RIE 930±30eV	27±3	60±5	TLM	
$SiCl_4$ RIE 240±10eV	8±2	11±2	TLM	
Ar IBE 500eV	>60	>80	TLM	
Ar IBE 800eV	>80	>80	TLM	
Ne IBE 500eV	>10	>50	TLM	
CH_4/H_2 RIE 930±30eV	20	32	Raman	
Ar IBE 500eV	>10	>20	Raman	
Ne IBE 500eV	>10	>60	Raman	
CH_4/H_2 RIE 800eV	-	>10.6	CV	10nm etch depth
CH_4/H_2 RIE 300eV	-	>6.6	CV	10nm etch depth
CH_4/H_2 RIE 80eV	-	>2.6	CV	10nm etch depth

Table IV: Results of CV measurements are taken from reference 13.

The Raman scattering of the coupled LO phonon-plasmon mode in n^+ GaAs proves to be a sensitive tool for the investigation of dry etching damages by analysing the relative change of its intensity with the bare LO phonons in the surface depletion region. It is evident from

the argon ion beam etching data that low accelerating voltage produces less damage than high accelerating voltage, and in CH_4/H_2 RIE, the damage saturates after an etch depth of 20nm.

3.8. References

1. R. Cheung, S. Thoms, I. McIntyre, C. D. W. Wilkinson, and S. P. Beaumont, J. Vac. Sci. Technol., **B6**, 1911 (1988).
2. J. Chevallier, W. C. Dautremont-Smith, C. W. Tu, and S. J. Pearton, Appl. Phys. Lett., **47**, 108 (1985).
3. G. S. Jackson, J. Beberman, M. S. Feng, K. C. Hsieh, N. Holonyak, Jr, and J. Verdeyen, J. Appl. Phys., **64**, 5175 (1988).
4. W. Kellner, Siemens Forsch.-u. Entwickl-Ber., **4**, 137 (1975).
5. H. B. Harrison, proc. IREE, **41**, 95 (1980).
6. G. K. Reeves, and H. B. Harrison, IEEE Electron Devices Letters, **EDL-3**, 111 (1982).
7. I. J. Van Der Pauw, Phillips Tech. Rev., **20**, 220 (1958).
8. S. M. Sze in' Physics of Semiconductor Devices', 2nd edition, J. Wiley & son , pp31 (1980).
9. A. Chandra, C. E. Wood, D. A. Woodard, and L. F. Eastman, Solid State Electronics, **22**, 645 (1979).
10. W. Patrick, W. S. mackie, S. P. Beaumont, and C. D. W. Wilkinson, Appl. Phys. Lett., **48**, 986 (1986).
11. A. J. Carter, B. Thomas, D. V. Morgan, J. K. Bhardwaj, A. M. McQuarrie, and M. F. Stephens, IEEE proc. **136**, 2 (1989).
12. D. L. Flamm, and V. M. Donnelly, 'The Design of Plasma Etchants', Plasma Chem. and Plasma Process., **1**, 317 (1981).
13. N. I. Cameron, S. P. Beaumont, C. D. W. Wilkinson, N. P. Johnson, A. H. Kean, and C. R. Stanley, J. Vac. Sci. Technol., **B8**, 1966 (1990).
14. J. M. Zavada, H. A. Jenkinson, R. G. Sarkis, and R. G. Wilson, J. Appl. Phys., **58**, 3731 (1985).
15. K. Yamasaki, K. Asai, K. Shimada, and T. Makimura, J Electrochem Soc., **129**, 2761 (1982).
16. J. Chevallier, W. C. Dautremont-Smith, C. W. Tu, and S. J. Pearton, Appl. Phys. Lett., **47**, 108 (1985).
17. N. M. Johnson, R. D. Burnham, R. A. Street, and R. L. Thornton, Phys. Rev. B, **33**, 1102 (1986).

18. A. Jalil, J. Chevallier, J. C. Pesant, R. Mostefaoui, B. Pajot, P. Murawala, and R. Azoulay, Appl. Phys. Lett., **50**, 439 (1987).
19. H. J. Stein, Appl. Phys. Lett., **57**, 792 (1990).
20. G. Roos, N. M. Johnson C. Herring, and J. S. Harris, Appl. Phys. Lett, **59**, 461 (1991).
21. Y. F. Chen, C. S. Tsai, and Y. Chang, Appl. Phys. Lett., **57**, 70 (1990).
22. R. A. Morrow, Appl. Phys. Lett., **57**, 276 (1990).
23. J. R. Creighton, J. Vac. Sci. Technol., **A8**, 3984 (1990).
24. U. K. Chakrabartii, S. J. Pearton, W. S. Hobson, J. Lopata, and V. Swaminathan, Appl. Phys. Lett., **57**, 887 (1990).
25. N. Pan, B. Lee, S. S. Bose, M. H. Kim, J. S. Hughes, G. E. Stillman, Ken-ichi Arai, and Y. Nashimoto, Appl. Phys. Lett., **50**, 1832 (1987).
26. S. J. Pearton, J. W. Corbett, and T. S. Shi, Appl. Phys. A, **43**, 153 (1987).
27. H. Hidaka, K. Akita, M. Taneya, and Y. Sugimoto, Electronics Letters, **26**, 1112 (1990).
28. 5. S. W. Pang, M. W. Geis, N. N. Efremow, and G. A. Lincoln, J. Vac. Sci. Technol., **B3**, 398 (1985).
29. R. Germann, A. Forchel, M. Bresch, and H. P. Meier, J. Vac. Sci. Technol., **B7**, 1475 (1989).
30. S. W. Pang, J. Electrochem. Soc., **133**, 784 (1986).
31. S. K. Ghandhi, P. Kwan, K. N. Bhat, and J. M. Borrego, IEEE Electron Device Lett., **EDL-3**, 48 (1982).
32. S. J. Pearton, U. K. Chakrabarti, A. P. Perley, and K. S. Jones, J. Appl. Phys., **68**, 2760 (1990).
33. S. W. Pang, M. W. Gies, N. N. Efremow, and G. A. Lincoln, J. Vac. Sci. Technol, **B3**, 398 (1985).
34. A. Scherer, M. L. Roukes, and B. P. Van der Gaag, Proc. Int. Sump. Nanostructure Physics and Fabrication, ed. M. A. Reed, and W. P. Kirk, Academic press, pp341 (1989), Texas, USA..
35. D. S. Gemmell, Rev. Mod. Phys., **46**, 129 (1974).
36. L. Eriksson, J. A. Daves, and P. Jaspersgaard, Phys. Rev., **161**, 219 (1967).
37. J. Lindhard, and K. Dan Vidensk. Selsk, Mat-Fys. Medd., **34**, 14 (1965).
38. M. Blackman, in ' Encyclopedia of Physics, ed. S. Flugge, Springer, Berlin **7**, part I, pp377 (1955).
39. J. C. Pfister in "Radiation Damage in Semiconductors", Paris-Rayamount, Dound , pp28 (1965).
40. R. H. Silsbee, J. Appl. Phys., **28**, 1246 (1957).
41. G. Absteiter, M. Cardona, and A. Pinczuk, in ' Light Scattering in Solids IV', ed. M. Cardona and G. Guntherodt, pp5, Springer, New York (1984).
42. A. Mooradian, and G. B. Wright, Phys. Rev. Lett., **22**, 999 (1966).

43. A. Pinczuk, A. A. Ballman, R. E. Nahory, M. A. Pollack, and J. M. Worlock, J. Vac. Sci. Technol., **16**, 1168 (1979).
44. A. Kirillov, C. B. Cooper, III, and R. A. Powell, J. Vac. Sci. Technol., **B4**, 1316 (1986).
45. D. E. Aspnes, and A. A. Studna, Phys.Rev. **B27**, 1985 (1983).
46. D. Kirillov, C. Webb, and J. N. Eckstein, J.Cryst.Growth, **81**, 91 (1987).
47. H. Shen, F. H. Pollak, and R. N. Sacks, Appl. Phys. Lett., **47**, 891 (1985).
48. J. W. Conley, and G. D. Mahan, Phys. Rev., **161**, 681 (1967).
49. O. J. Glembocki ,and E. A. Dobisz, J. Vac. Sci. Technol., **A9**, 1403 (1991).
50. A. Mlayah, R. Carles, G. Landa, E. Bedel, and A. Munoz-Yague, J. Appl. Phys., **69**, 4064 (1991).

Chapter 4: Characterisation of sidewall damage in GaAs nanostructures by TEM (dark field imaging technique) and High Resolution TEM

Acknowledgement

I would like to thank S. Hefferman (Department of Physics and Astronomy, Glasgow) for examining my TEM specimens and Dr. J. Fryer (Department of Chemistry, Glasgow) for interpreting the HRTEM images. I would also like to thank Dr. C. Stanley for regrowing a GaAs epitaxial layer on an etched surface by molecular beam epitaxy.

4.1. Introduction

There is an increasing interest in structures on the nanometric scale i.e. quantum wires and quantum dots for device applications in electronics[1] and to explore the associated physical phenomena[2] when the dimensions of the device are in the order of the electron wavelength. Such devices can be best defined by electron beam lithography and reactive ion etching (RIE). However, reactive ion etching involves the physical bombardment of the substrate with ions of energy between 100eV and 1000eV. This ion bombardment causes deterioration of the electrical and optical characteristics of the semiconductor (dry etch damage).

Several techniques have been used to evaluate the dry etch damage indirectly in III-V semiconductors, for example, evaluation of Schottky diode characteristics[3,4] (ideality factor, barrier height and the reverse leakage current), variation in Photoluminescence intensity around the band edge due to damage[5], the asymmetric broadening of the LO phonons and the existence of the geometry forbidden TO phonons in Raman scattering[6]. X-ray photoelectron spectroscopy, Auger electron spectroscopy and Infrared spectroscopy shed[7] some light on the surface chemistry. In addition the conductivity measurements of surfaces and sidewalls[8] provide a mean to estimate the dry etching damage depth.

However, all these techniques while helping to evaluate the extent of the damage do not give direct information on the microscopic nature of the damage. The present method helps in this regard.

This TEM examination method was first used by Cheung[9] to evaluate the dry etching damage in quantum wire-like structures, ≥150nm wide etched in $SiCl_4$ RIE. The non-

reproducibility and relatively thick wires made it difficult to interpret the diffraction images formed since the diffracted electrons are frequently involved in multiple-scattering events.
In the present work, the technique has been refined and wires 50-80nm wide, reactive ion etched using CH_4/H_2 and $SiCl_4$ have been prepared in a reproducible fashion. Thin wires make image interpretation simpler.
Wires have been modified to suit high resolution TEM (lattice imaging) which have been used to examine the lattice disorder produced by the etching processes.
Wires have been prepared using an epilayer regrown by MBE on an etched surface to examine the effect of an As rich atmosphere upon annealing the etched surface.

4.2. Theory of the dark field imaging technique - structure factor contrast

As described above, Cheung had dry etched wires ≥150nm wide using $SiCl_4$ RIE. This wire thickness is larger than the extiction distance ξ_g[1], a parameter which measure the 'mean free path' of the Bragg diffraction, which was calculated to be $\xi_{200} = 67.8$nm for the (200) reflections of GaAs using 120keV electrons. Therefore, multiple electron scattering events occured which made it difficult to interpret the resulting image using the kinematical theory of diffraction.
It was therefore necessary to use the dynamical theory of diffraction, which assumes that the crystal is perfect and the only one set of Bragg reflection planes is near or at the reflecting position (the two beam approximation). In the present work, the technique has been refined and wires 50-80nm wide, reactive ion etched using CH_4/H_2 and $SiCl_4$ have been prepared reproducebly. For wires in this thickness range the kinematical theory, which assumes that the diffracted wave intensities are negligible compared to the incident beam intensity and the incident electrons suffer only one if any reflection, can be used for image interpretation.

Using techniques with high spatial resolution available in the transmission electron microscope, it is possible to interpret the contrast variation within certain types of images as having arisen from damaged regions within the wire itself. The dry etch damage is defined here as any change in the stoichiometry, lattice disorder or defects introduced as a result of the etching process. Direct investigation of the damage in the wires is then possible. The

(1) The extinction distance is defined to be twice the distance in the crystal which must contribute to the diffracted beamto build up a unit amplitude.

following section describes a contrast mechanism which can reveal the damaged regions in the wires.

A parallel beam of electrons incident on the specimen is diffracted through various different Bragg angles (θ_B), as shown schematically in Fig. 4.1. Using the description first given by Bragg, see e.g. Kittel[10], the "Bragg" angle (θ_B) is defined as

$$2d_{hkl} \sin(\theta_B) = n\lambda \qquad (4.1)$$

where d_{hkl} is the plane spacing between successive (hkl) planes; h, k and l are the Miller indices and λ is the wavelength of the incident beam of electrons.

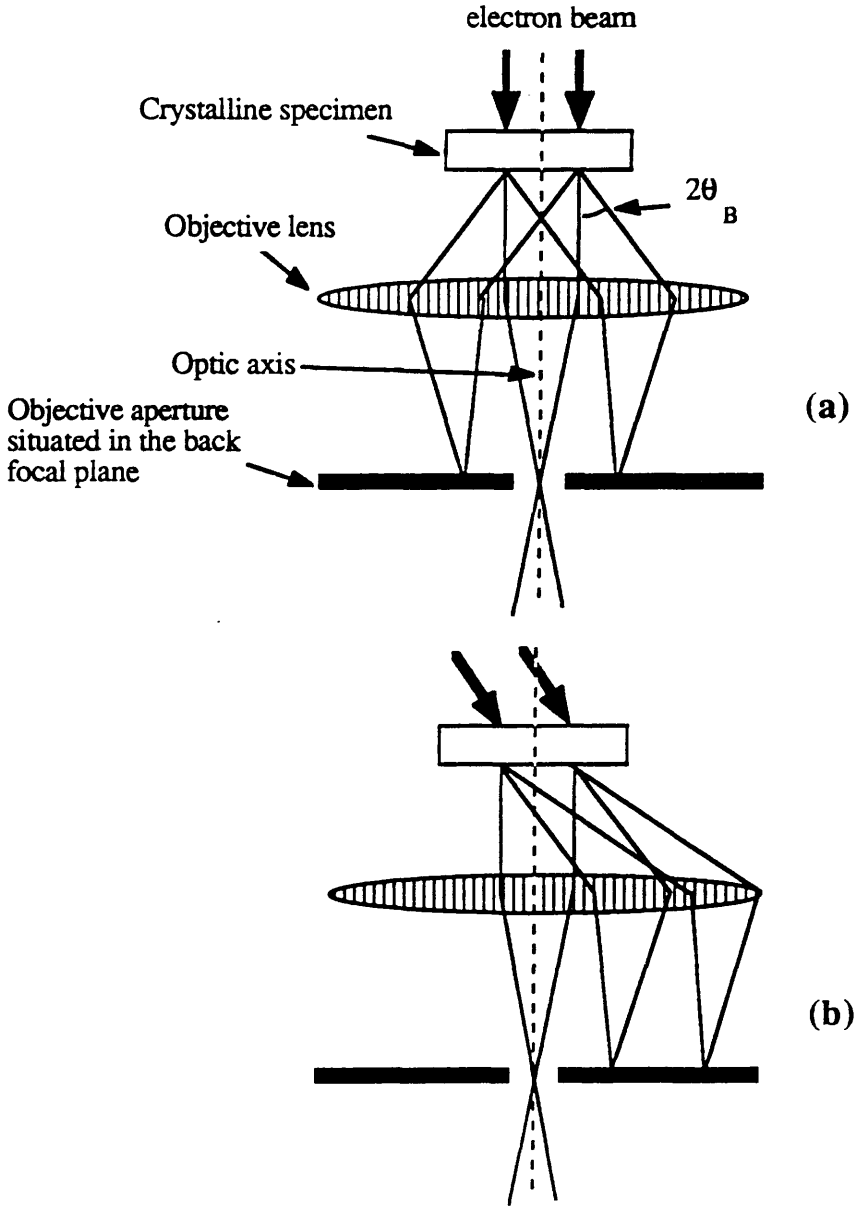

Figure 4.1: Schematic diagram showing the effect of the objective lens and the stop in bringing the diffracted beam to the focus, (a) off-axis and (b) on the optic axis. In both cases the beam is brought to a focus in the diffraction plane.

In Fig. 4.1(a) parallel incident illumination ensures that the transmitted beam is brought to a focus in the diffraction, or back focal, plane of the objective lens. Those parts of the incident beam which pass undeviated through the specimen are brought to a focus on the optic axis of the microscope and those which are diffracted through some angle θ_B, are brought to a focus at some position off the optic axis. In order to calculate the intensity contained in each of the diffraction spots it is necessary to perform a much more detailed

examination of the diffraction process. The scattering process itself arises due to the orbiting electrons of the atom. It can be shown[11] that the scattered wave is in the form of a spherical wave whose amplitude is proportional to the Fourier transform of the electrostatic lattice potential. The amplitude of the scattered wave is given by a "structure factor", $f(\theta)$, given by;

$$f(\theta) = (2\pi me)/h^2 \quad V(\underline{r}_i) \exp(-i\,\underline{K}_i \,.\, \underline{r}_i)\, d\tau_i \qquad (4.2)$$

where $\underline{r}_i$ are the positions of the atoms in the unit cell; $V(\underline{r}_i)$ is the electrostatic potential at a point $\underline{r}_i$; ; $d\tau_i$ is an element of volume in the unit cell and $\underline{K}$ is the difference in wavevector between the incident and scattered waves. The fact that the value of $f(\theta)$ relies on $V(\underline{r}_i)$ means that atoms with similar distributions of potential will have similar values of $f(\theta)$ and this may occur if for example, the atomic numbers of two species are similar. Values of $f(\theta)$ for elements (Ga and As) used in this study are given in table 4.1. It can be shown that $f(\theta)$ is a maximum when $\underline{K}_i$ coincides with a reciprocal lattice vector.
Hence for strong scattering conditions;

$$\underline{K} = A_1 \,.\, \underline{b}_1 + A_2 \,.\, \underline{b}_2 + A_3 \,.\, \underline{b}_3$$

where $\underline{b}_i$ are the reciprocal lattice vectors, and also

$$\underline{r} = B_1 \,.\, \underline{a}_1 + C_1 \,.\, \underline{a}_2 + D_1 \,.\, \underline{a}_3$$

where $\underline{a}_i$ are the lattice vectors in real space. It should be noted that by definition;

$\underline{a}_i \,.\, \underline{b}_i = \delta_{ij}$

It can be shown that the scattering from an assembly of unit cells is given by the sum of each of the structure factors of each unit cell multiplied by the appropriate phase factor. For strong diffraction from an array of unit cells, the structure factor is given by $F(\theta)$, where

$$F(\theta) = \Sigma_i f_i(\theta) \exp(-2\pi i (A_1 B_i + A_2 C_i + A_3 D_i)) \qquad (4.3)$$

It is assumed throughout that each electron only suffers one, if any, scattering event, and also that the energy transferred to the beam during a scattering event is negligible. This is

known as the Kinematic approximation, and is reasonably valid for the imaging mode used to examine the thin (≈70nm) wire specimens.

Element	$f(2\theta)_a$ (Å)
Ga	5.365
As	5.970

Table 4.1: The relativistically corrected atomic scattering factors f_a for Ga and As for 100keV electrons scattered through an angle 2θ of approximately 12mrad[12].

From Fig. 4.1(a), it can be seen that by carefully positioning an aperture, situated in the diffraction plane, only certain diffracted beams are allowed to be transmitted through the aperture in order to form the final image. Placing the aperture around e.g. the (002) spot would allow only those electrons which had been diffracted from (002) planes to form the final image. This type of image is called an (002) dark field image. In normal practice, rather than placing the aperture off-axis, as would be the case for Fig. 4.1(a), the incident beam is tilted prior to the specimen in such a way that the (002) diffracted beam travels down the optic axis, as shown in Fig. 4.1(b). Dark field images formed in this way tend to be significantly less astigmatic than those formed by shifting the aperture off-axis. Dark field TEM images reveal contrast which is related to the structure factor F_{hkl} of the material through which the beam has passed.

GaAs has a face centred cubic structure with a basis of 2 atoms (one Ga and one As) at each lattice point. The fractional co-ordinates of the atoms within a unit cell of GaAs are (0,0,0), (0,1/2,1/2), (1/2,0,1/2) and (1/2,1/2,0) for Ga and (1/4,1/4,1/4), (3/4,3/4,1/4), (1/4,3/4,3/4) and (3/4,1/4,3/4) for As. From equation 4.3, the structure factor F_{002} (GaAs) from a unit cell of GaAs is given by;

$$F_{002}\,(\mathrm{GaAs}) = 4\,(\,f_{002/\mathrm{Ga}} - f_{002/\mathrm{As}}\,) \qquad (4.4)$$

where $f_{002/\mathrm{Ga}}$ and $f_{002/\mathrm{As}}$ are the scattering factors of Ga and As at the Bragg angle appropriate to (002) planes. As the atomic numbers of Ga and As are similar, $f_{002/\mathrm{Ga}}$ and $f_{002/\mathrm{As}}$ are similar, (see table 4.1[12]) and hence F_{002} (GaAs) is very small. The intensity in an (002) dark field image from GaAs is given by;

$$I_{002}\,(\mathrm{GaAs}) \propto F_{002}\,F^{*}_{002} \qquad (4.5)$$

where F_{002} and F^*_{002} denote the (002) structure factor and complex conjugate of the (002) structure factor of GaAs respectively.
From equation 4.4, an (002) dark field image from a perfect GaAs crystal should be very low in intensity. The situation does change, if for example there is a deviation away from stoichiometry which changes the structure factor, F_{002} (GaAs), of the crystal leading to an increase in the intensity.
In general terms, equation 4.4 can be expressed as

$$F_{002} = 4 (p_2 S_{III} - p_1 S_V) \qquad (4.6)$$

where p_1 and p_2 are the probabilities that the group five and group three sites within the unit cell of GaAs are occupied. In pure GaAs with no defects, $p_1 = p_2 = 1$, S_V and S_{III} are the (002) structure factors of the atoms occupying the group five and group three sites in GaAs unit cell i.e. $f_{002/Ga}$ and $f_{002/As}$ respectively.

4.3. Specimen preparation and improvements

In this work, the TEM specimens were prepared as follows, Fig. 4.2:
Samples of GaAs (2μm thick epilayer, Si doped to $1x10^{17}cm^{-3}$ grown by MBE on a semi-insulating substrate) were cleaved to an area of $3x4mm^2$ and cleaned using ultrasonic agitation in trichloroethane, Acetone and methanol respectively, rinsed in IPA and blown dry. It should be mentioned that the procedure of preparing the wires have been modified considerably from the initial experiments by R. Cheung[5].
A double layer of PMMA resist was used; first 4% (BDH) was spun, coated and baked for an hour, then the second coat 4% Elvacite was spun and baked for 24 hours. The solvent was o-xylene, spin speed 7Krpm for 60 seconds and the bake temperature 180°C in both cases. The sample was exposed in a converted Philips SEM 500 at 50kV for the wire pattern at 5000X magnification (the frame size is $25x19\mu m^2$ and the pixel size is $6.1x4.64nm^2$) and a beam size of 8nm. This magnification was used to improve the wire definition (the minimum wire width corresponds to about 8 pixels). The wire pattern was 12μm long with widths between 40nm and 100nm with two square patterns to act as supporters when the wire is etched. The wire pattern was exposed repeatedly (using step

and repeat command) for 40 times in a row with separation distances of 12μm to increase the probability of finding "good" wires during TEM examination.

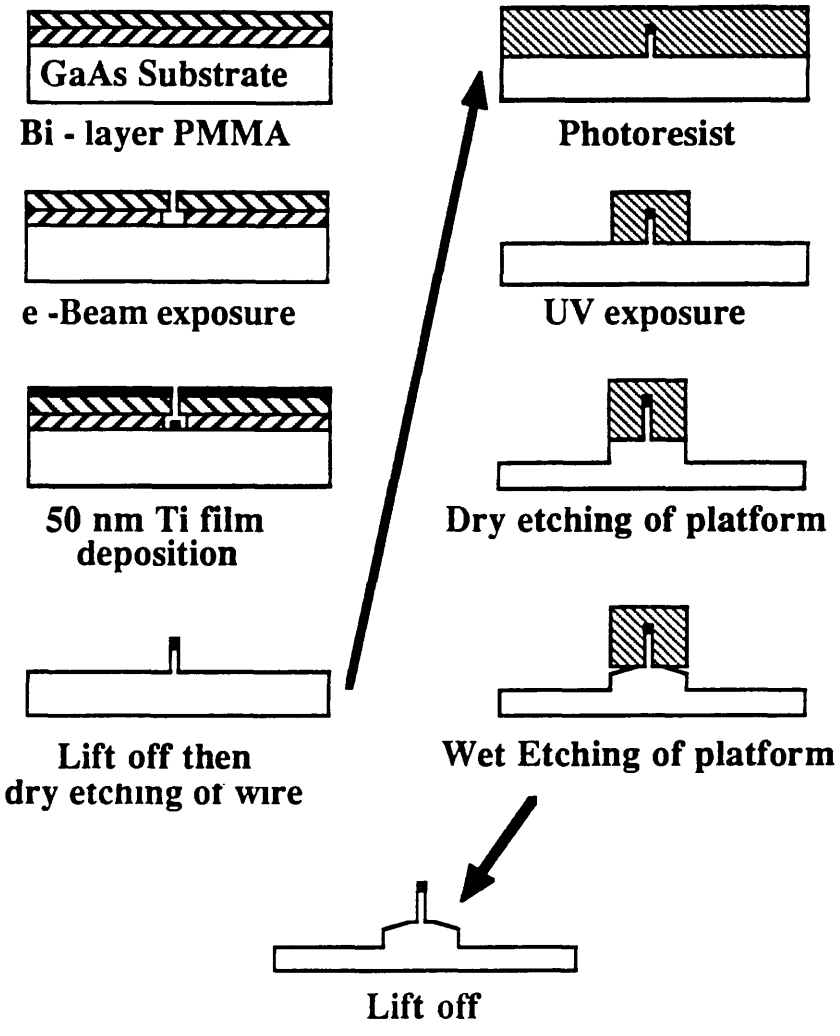

Figure 4.2: Stages for preparing TEM wire specimens.

The sample was developed in 1:3 solution of MIBK:IPA for 80-120sec at 23°C then rinsed in IPA. The surface oxide was removed by dipping the sample in a 1:1 solution of H_2O:HCl for 30sec.A 50nm thick film of Titanium was evaporated, (The ratio of the etch rate of GaAs and Ti in CH_4/H_2 is ~1:10). Liftoff of the metal film was done in warm acetone (50°C). The metal mask was used to form wires 50-80nm wide, 400-500nm high by RIE in CH_4/H_2 and $SiCl_4$. For CH_4/H_2, the etching was performed at a pressure of 17mtorr with a gas ratio of 1:5 CH_4/H_2 and flow rates of 6:30sccm respectively for 14 minutes, rf power of 150W and a corresponding dc bias of 940V. In the case of $SiCl_4$, the

etching was performed at a pressure 12mtorr for 2 minutes, rf power of 100W and a corresponding dc bias of 260V.

If the wires were to be used for transport measurements the fabrication of the wires would be complete. However, in this form they are not particularly suitable for examination in a TEM.

As discussed in section 4.2, the damaged regions in the wires are revealed by forming dark field images. In order to have the wires in the correct orientation with respect to the incident beam, the wires should be able to be tilted about the [110] axis. Hence the wires were fabricated in such a way that the long axis of the wires lay parallel to a [110] axis of the substrate on a (001) plane. Suitable mounting of the wires thus ensured that electrons, incident on the wire as shown in Fig. 4.3, were close to being perpendicular to the (110) plane. A sample holder was specially constructed which would enable the incident electrons to be directed approximately along the [110] direction and this is shown in Fig. 4.4. As the wires are in general only 500nm high, tilting about the [110] axis would be made considerably easier if the wires were on a high, yet narrow platform. This type of platform would mean that as the wires are tilted, neither the incident nor diffracted beams would collide with either the platform or the GaAs substrate.

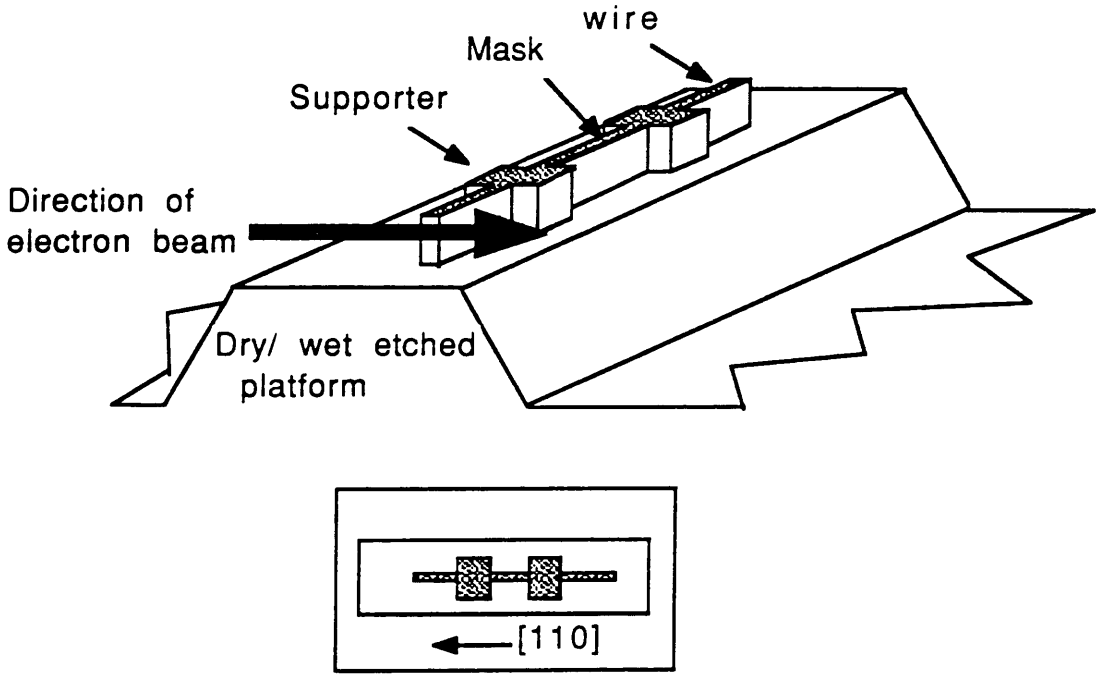

Figure 4.3: Schematic diagram showing the configuration of a wire ready for TEM examination. The diagram is not to scale.

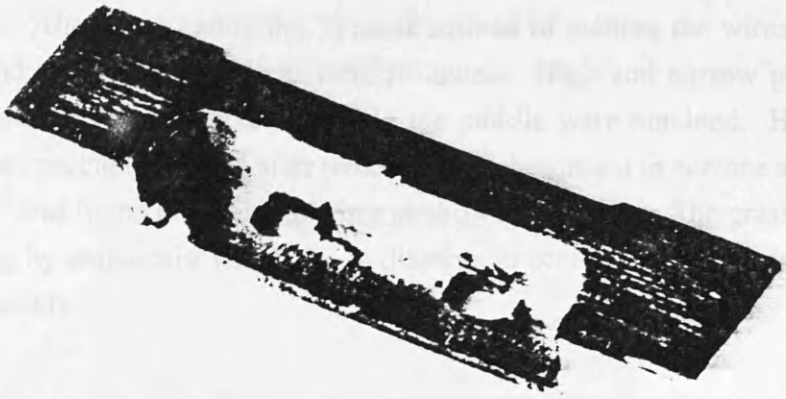

Figure 4.4: Photograph of the specimen holder constructed in order that the wires are near the correct orientation for analysis.Samples are mounted on the flat wall above the two holes through which the electron beam passes in the direction perpendicular to the plane of the hole.

To make a suitable platform, the entire specimen was spin-coated with S1400-31E photoresist (~2μm thick). The photoresist was then exposed accept for a stripe 10μm wide centred to the middle of the row of wires. The entire sample was dry etched in a $SiCl_4$ RIE for 30min. This results in a platform which has straight walls. The platform width was narrowed down to ~6μm by wet etching in a 1:8:1 solution of H_2O:H_2O_2:H_2SO_4. This step was introduced, as an improvement on Cheung's procedure, to increase the height of the platform above the substrate level to 8-10μm, narrow the width of the platform, remove any "grass" formed during etching the platform by micromasking and to introduce an inclination to the walls of the platform which allow the specimen to be tilted through relatively large angles, thus enabling the sample to be oriented correctly. The analysis of the wires is also made considerably easier. The photoresist was then removed in acetone. SEM micrographs of dry etched wires mounted on a dry-then-wet etched platform is shown in Fig. 4.5.

Finally the sample was mounted on a double-sided sticky tape and cleaved under the microscope to typical dimensions of 1mm x 70μm using a surgical blade. The specimen was then mounted on the special holder using silver dag. Extreme care should be exercised during the mounting stage.

In an attempt to increase the height of the platform, the sequence of preparing the sample was changed. After evaporating the Ti mask instead of etching the wires, the steps for patterning and etching the platform were followed. High and narrow platforms were produced, with the Ti wire mask centred in the middle were obtained. However, upon examining the specimen by SEM after removing the photoresist in acetone and etching the wires, "grass" was found to ingulf the wires as shown in Fig. 4.6. The grass is formed via micromasking by photoresist which fail to dissolve in acetone, probably due to crosslink during RIE etching.

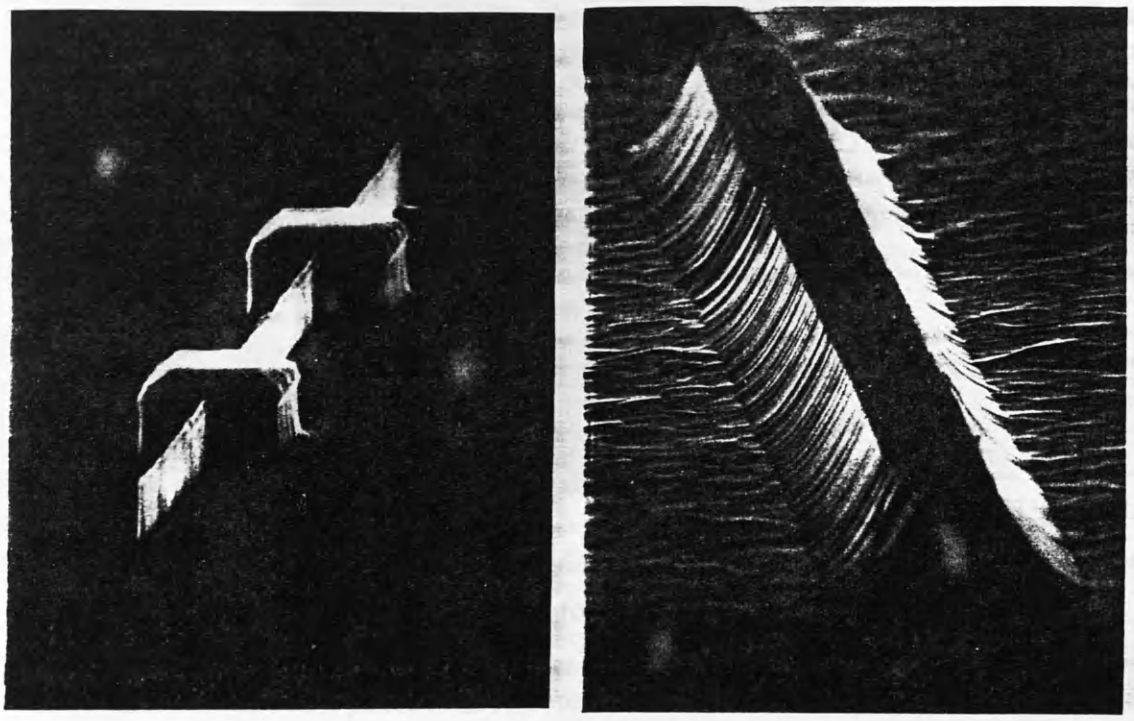

(a) (b)

Figure 4.5: Micrographs of (a) a wire 50nm wide etched using CH_4/H_2 RIE, and (b) a specimen ready for TEM examination showing wires (as in (a)) mounted on a platform.

4.3.1. Specimen alignment procedure

The etched samples were examined using a JEOL 1200EX microscope operating at voltage 120kV. This enabled the bright field (000) and dark fields formed by the (002) and (004) diffracted beams to be imaged.

The experimental arrangement for the study of the wires is outlined below. Diffraction patterns formed from suitably oriented wires allowed identification of the (002) diffraction spot. A diffraction pattern obtained from one of the wires is shown in Fig. 4.7(a), and each of the spots is indexed in Fig. 4.7(b).

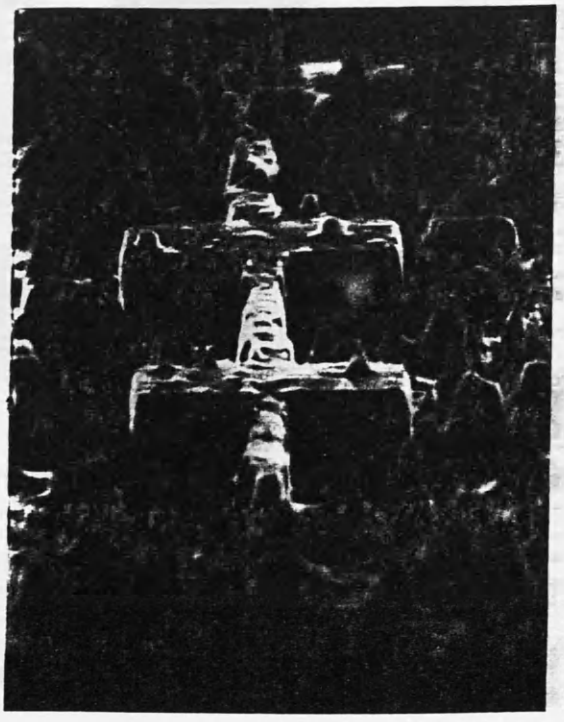

Figure 4.6: A micrograph of a wire etched using $SiCl_4$ RIE surrounded by 'grass' formed by micromasking. The wire is not suitable for TEM examination.

Only just over half of the pattern can be observed as the other half collides with the platform or the substrate, and hence is obscured. Further, using the Kikuchi[11] pattern, formed with convergent incident illumination, the intensity in the (002) spot could be maximised by placing the appropriate Kikuchi band on top of the relevant spot, i.e. the intensity in an (002) spot is maximised by having the (002) Kikuchi band on top of that spot. In practice the (002) Kikuchi band is so weak that it cannot be observed and so the intensity in the (002) is maximised by placing the (004) Kikuchi band (which is visible) approximately midway between the (002) and (004) diffraction spots. The specimen is then tilted slightly, while observing the (002) diffraction spot, in order to determine the orientation which maximises the intensity in the (002) spot. This ensures that the incident beam is at the Bragg angle appropriate to the (002) plane.

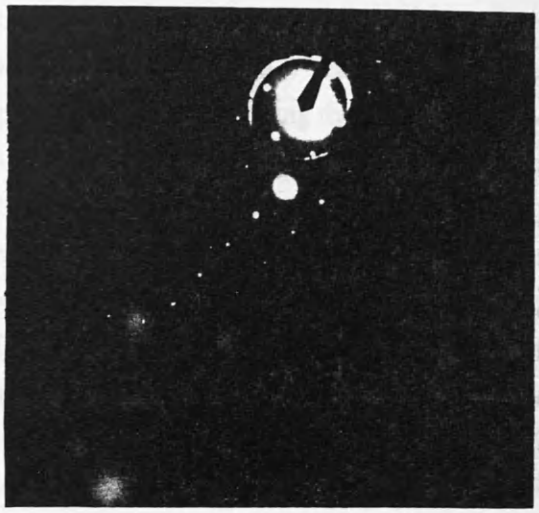

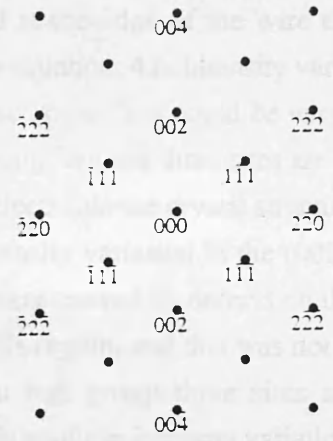

(a) (b)

Figure 4.7: (a) Diffraction pattern obtained from a wire etched using $SiCl_4$ RIE, with the spots indexed (b).

4.4. Results of $SiCl_4$ etched wires

The crystallinity of the wires was first examined in order to study if there was any loss of the crystal structure along the length of the wire. To enable this type of study to be undertaken, the smallest "spot" size was selected on the microscope, and then focused on the wire. Diffraction patterns from chosen areas of the specimen were then formed with a convergent incident beam. Under these circumstances a diffraction pattern is obtained from a region which is approximately 50nm in diameter. As the specimen is moved relative to the spot, any loss of crystallinity in the wire would be accompanied by a change in the form of the diffraction pattern. As the focused spot was moved over the wire, and in particular over the region near the end of the wire, (which had been exposed to $SiCl_4$ from the sides as well as the edge) no significant changes could be detected in the form of the diffraction pattern. It is therefore assumed that there is no apparent loss of the crystal structure at any point along the length of the wire.

A series of images were obtained in the TEM for various $SiCl_4$ etched wires. In each case an (000) or bright field and (002) dark field images were recorded. An image formed by electrons which had been inelastically scattered was also obtained as any intensity variations

in this type of image would be indicative of thickness variations along the length of the wire itself. An (000) image of the end of a wire etched in $SiCl_4$ is shown in Fig. 4.8a, with the corresponding (002) and inelastic images in Figs. 4.8b and 4.8c respectively. It can clearly be seen that in the (002) image there is a bright band at the edge of the wire extending approximately 50nm along the length of the wire. From equation. 4.6, intensity variations in the (002) image would indicate that any or all of p_1, S_v , p_2 or S_{III} could be varying. By definition p_1 and p_2 represent the probability that the group five and three sites are occupied respectively. If the etching process were to introduce defects into the crystal structure, either or both of p_1 and p_2 would vary, so resulting in an intensity variation in the (002) image. However, if the 50nm broad bright band in the image were caused by defects on this scale, the form of the diffraction pattern would vary around this region, and this was not found to be the case. Alternatively, if vacancies did exist at e.g. group three sites and were subsequently filled by group five atoms, this would again result in intensity variations in the final (002) image as S_V would vary. Intensity variations in the (002) image only serve to indicate that there is some deviation away from stoichiometry in those regions which appear darker or brighter than the apparently undamaged crystal.

It should also be noted that thickness variations must also be accounted for, because were the wire to become thinner towards the end of the wire, this would result in a similar change in intensity. By examining of the inelastic dark field image shown in Fig. 4. 8c, and from SEM inspection, it can be seen that the thickness variation along the length of the wire is within the resolution of electron beam lithography ($\pm$10nm) and therefore the changes in intensity in the (002) image are not attributable to thickness variations. The intensity variations in the (002) images can therefore be attributed to changes in the value of the structure factor, caused by compositional changes in the material.

Such features have very recently been reported by Cheung[9], during an investigation of thicker $SiCl_4$ etched wires ($\geq$150nm wide). It appears from the (002) image, Fig. 4.8b, that the extent of the damage is quite significant over a distance of < 20nm. From the intensity variations, the scale of the damage appears to decrease monotonically with increasing distance away from the edge of the wire.

From equation. 4.6, it can be seen that using the relatively simple (002) dark field imaging technique it is impossible to suggest whether the intensity variations arise from changes in S_v or S_{III}. This is due to the fact that the intensity in an (002) dark field image is proportional to the *SQUARE* of the difference in structure factors. However that such intensity variations do exist would indicate that there are deviations away from stoichiometry in the GaAs crystal.

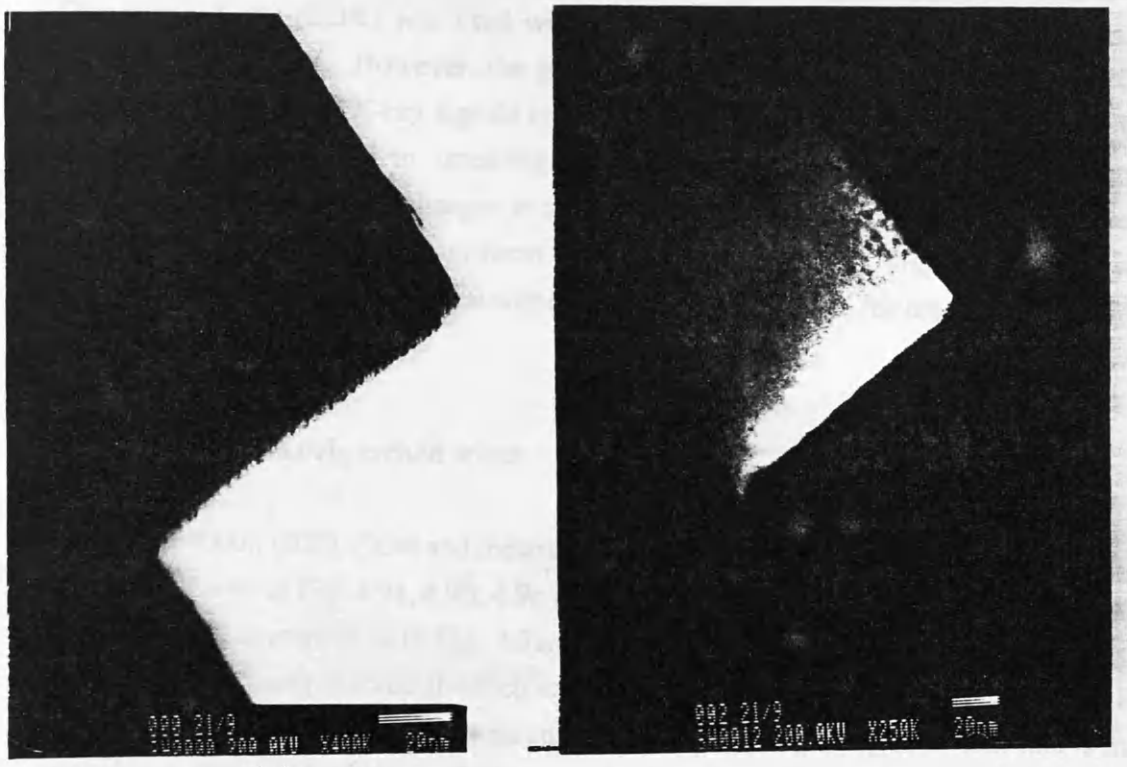

(a) (b)

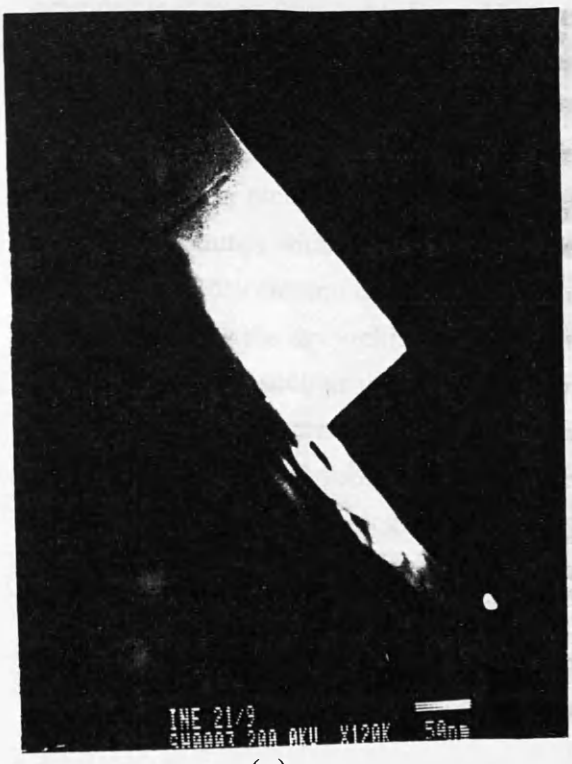

(c)

Figure 4.8: (a): (000) bright field image of a wire which had been etched using $SiCl_4$ RIE, (b) (002) dark field image of a wire which had been etched using $SiCl_4$ RIE, and (c) dark field image formed using electron which has been inelastically scattered (inelastic image).

In an attempt to analyse the change in composition in wires etched in $SiCl_4$, Energy Dispersive X-ray (EDX) was used with a spot size of ~5nm using HB-5 microscope operating at 120keV. However, the geometrical arrangement of the sample and X-ray detector was such that X-ray signals emitted from the platform as well as the wire were detected which resulted in smearing out any effects related to genuine change in composition. Fundamental changes in the detector geometry would have been required to isolate the signal from the platform from the wanted X-ray signal from the wire. Unfortunately that was not practical within the time span allocated for the experiment.

4.5. Results of CH_4/H_2 etched wires

A series of (000), (002), (004) and inelastic images were obtained for CH_4/H_2 etched wires which are shown in Fig. 4.9a, 4.9b, 4.9c and 4.9d respectively. It should be noted that the Ti metal mask is marked A in Fig 4.9a. From the same micrograph, it can be seen that there is a thin coating marked B which extend over the entire specimen. Analysis of Fig. 4.9a and Fig. 4.10 which is a high magnification SEM image, indicates that this is most probably a thin residual layer of photoresist which has not been removed fully in the development stage (this is confirmed later is § 4.8.2. for $SiCl_4$ etched wires). It should be mentioned that this coating was also observed on $SiCl_4$ etched wires observed by high magnification SEM. From the series of TEM images, Figs. 4.9a to 4.9d, it is immediately apparent that the nature of the damage in the CH_4/H_2 etched wires is very different from that of the $SiCl_4$ etched wires. From the (002) dark field image the wires appear to be "spotty". Features which resemble those observed in the wires have been reported by Freiser[13] after dry etching of Si. These features were attributed to dislocation loops in the crystal caused by the dry etching process particularly the presence of hydrogen in the etch gas. From images such as those of fig. 4.9b, it was estimated that these dislocation loops had an average diameter of approximately 7nm. Defects of this kind have also been reported by Sandana[14] following proton implantation of GaAs. From (002) dark field images recorded along the length of the wires no compositional changes could be detected. Convergent beam diffraction patterns were also recorded from various points along the wire, and no observable changes in the form of the pattern could be detected. It should be noted that the spot size used to form the diffraction patterns had a diameter of approximately 50nm, and that the average dislocation loop is only 7nm in diameter.

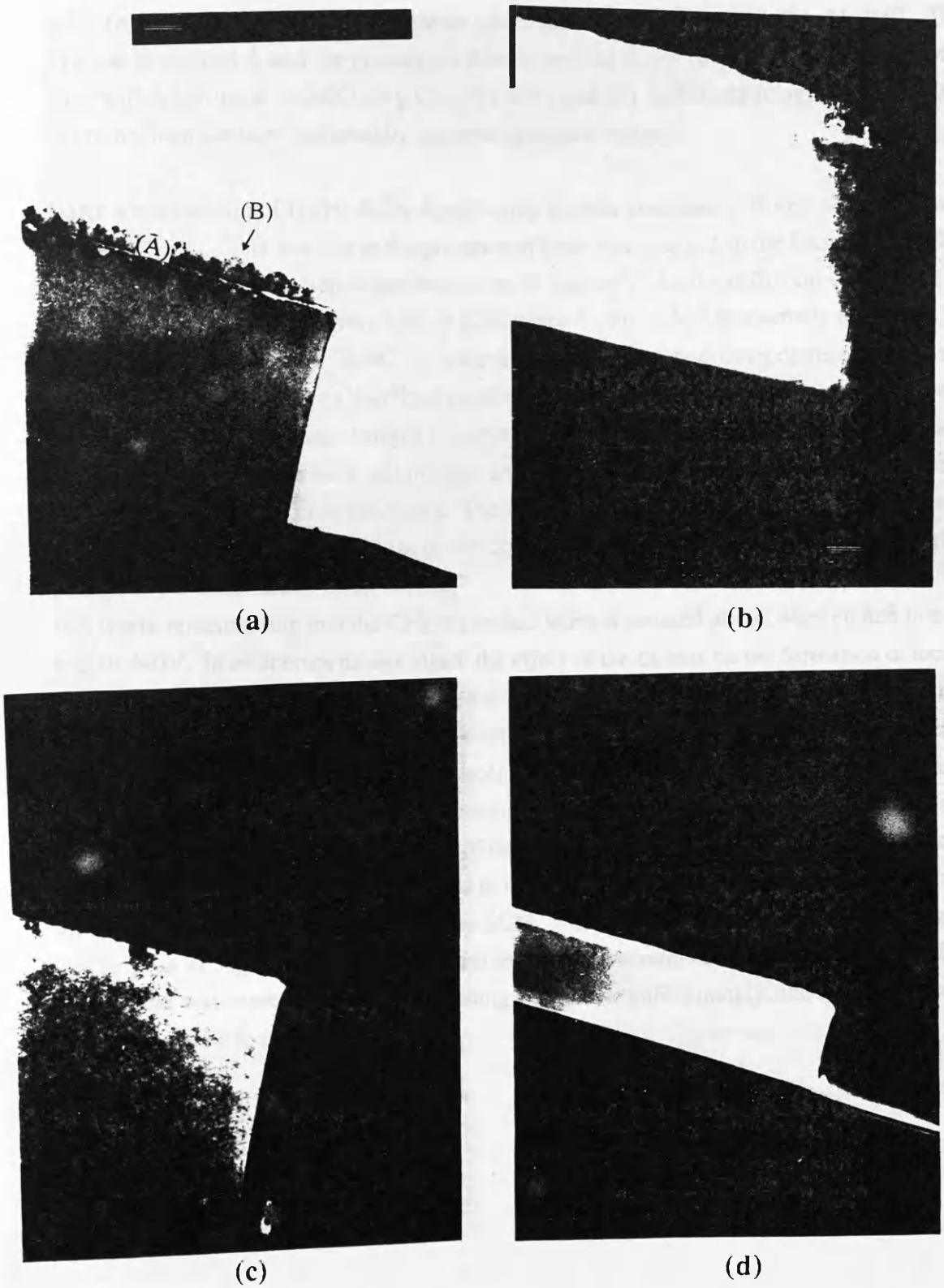

Figure 4.9: (a) (000) bright field image of a wire which had been etched using CH_4/H_2

RIE, (b) (002) dark field image of a wire which had been etched using CH_4/H_2 RIE. The Ti mask is marked A and the photoresist film is marked B, (c) (004) dark field image of a wire which had been etched using CH_4/H_2 RIE, and (d) dark field image formed using electron which has been inelastically scattered (inelastic image).

GaAs wires etched in CH_4/H_2 differ significantly in their electrical performance from those etched in $SiCl_4$. This was due to the presence of hydrogen trapped in the GaAs lattice after the etching process and which passivates the Si dopant[4]. As the diffusion coefficient of hydrogen and GaAs is relatively high ($\approx 0.4\mu m^2 sec^{-1}$), this effect is normally overcome by annealing the specimen at 380°C for 1sec in order that the hydrogen diffuses out of the lattice. The images of the CH_4/H_2 etched wires shown in figs. 4.9a through 4.9d were obtained prior to annealing. Images recorded from the same wire after annealing showed that the dislocation loops were still present, and in fact there were no observable differences in the form of the wires after annealing. The features attributed to dislocation loops are still present, there was no apparent loss of the crystal structure, nor was there any observable change in the composition of the crystal.

It is worth remembering that the CH_4/H_2 etched wires discussed above were etched in a dc bias of 940V. In an attempt to investigate the effect of the dc bias on the formation of loops, it was decided to prepare sets of wires at a dc bias of 70V-80V using an RIE80 etcher. The etch rate was very low, $1nm.min^{-1}$, which resulted in unpractically long etching time (500min) to obtain a wire height comparable to the wires used earlier. However, for wires etched for 30min, SEM examination has revealed the presence of deposition on the surface of the specimen as well as the sidewalls of the wires. To test whether the deposition is of a polymeric form, the specimen was ashed in Oxygen plasma for 30min, a standard method for removing polymers, then examined by SEM. The deposition has survived the ashing as can be seen in Fig. 4.11, indicating that it may be some non-volatile etch products. The experiment was repeated for shorter etching times but, unfortunately, the deposition was present on all the specimens.

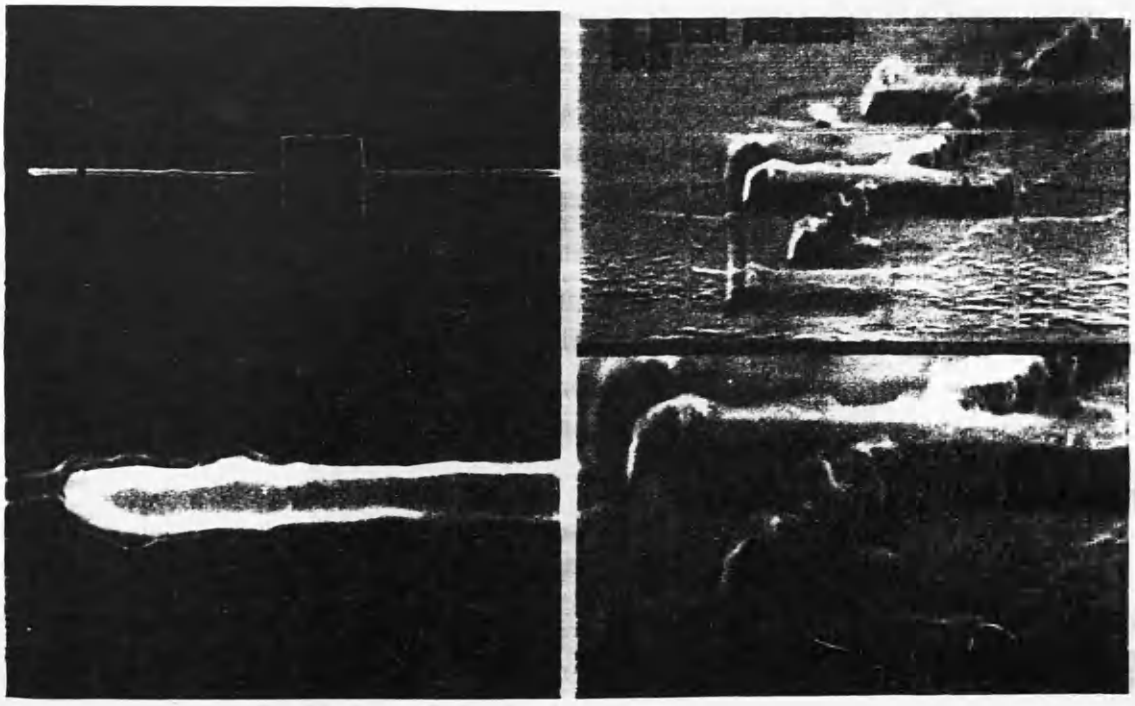

Figure 4.10 (left): High magnification SEM micrograph of a wire etched using CH_4/H_2 RIE showing the residual coating of photoresist

Figure 4.11 (right): Micrograph showing a wire etched using CH_4/H_2 RIE at a dc bias of 80V. Deposition can be seen on the sidewall of the wire.

4.6. HRTEM of $SiCl_4$ and CH_4/H_2 etched wires

For the high resolution TEM investigation, the wires were etched for a longer time so that for $SiCl_4$ etched wires, the Ti mask is just etched away and very thin regions of GaAs are formed. In the case of CH_4/H_2, lower pressure (~14mtorr) was used to enhance the "overcutting" effect[3] and to obtain perforation. A bright field TEM image of a wire etched in CH_4/H_2 for HRTEM examination is shown in Fig. 4.12.

The high resolution examination were carried out using an Akashi ABT 002B microscope operating at 200kV. The imaging conditions were such that all reflections corresponding to lattice spacings larger than 0.18nm were allowed to pass by the objective aperture, and that Scherzer defocus of 36.5nm a structure image down to 0.18nm should be obtained.

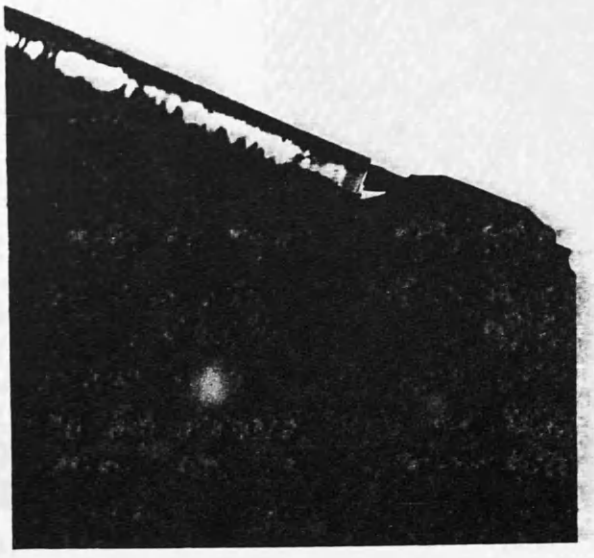

Figure 4.12: Bright field image showing a wire etched using CH_4/H_2 RIE modified specifically for high resolution TEM (HRTEM) examination.

The specimen was aligned for viewing on the (111) zone axis by small adjustments of tilt in both directions. The extinction distance in this projection was approximately 15nm. No radiation damage effect were observed.

The wires etched specifically for the high resolution examination were sufficiently thin and had a wedge shaped profile.

At the edges of the $SiCl_4$ RIE etched wire, there was an amorphous region approximately 2.5nm wide, tentatively corresponds to the native oxide, region A in Fig. 4.13a, however compositional analysis was not possible, at the time of examination, to prove it. This 'oxide' layer also existed on the upper and lower surfaces of the specimen, i.e. sidewalls of the wire, so that regions where lattice structure was absent i.e. all GaAs had been removed, there remained the oxide layer only, region B in Fig. 4.13a.

Three features of interest were observed in the micrograph:

1. Areas, possibly Voids, where lattice structure was absent leaving only the mottled effect. This could correspond to a vacancy loop or the result of uneven etching resulting in complete GaAs removal at this point. These areas ranged from 1-5nm in diameter, Fig. 4.13a.

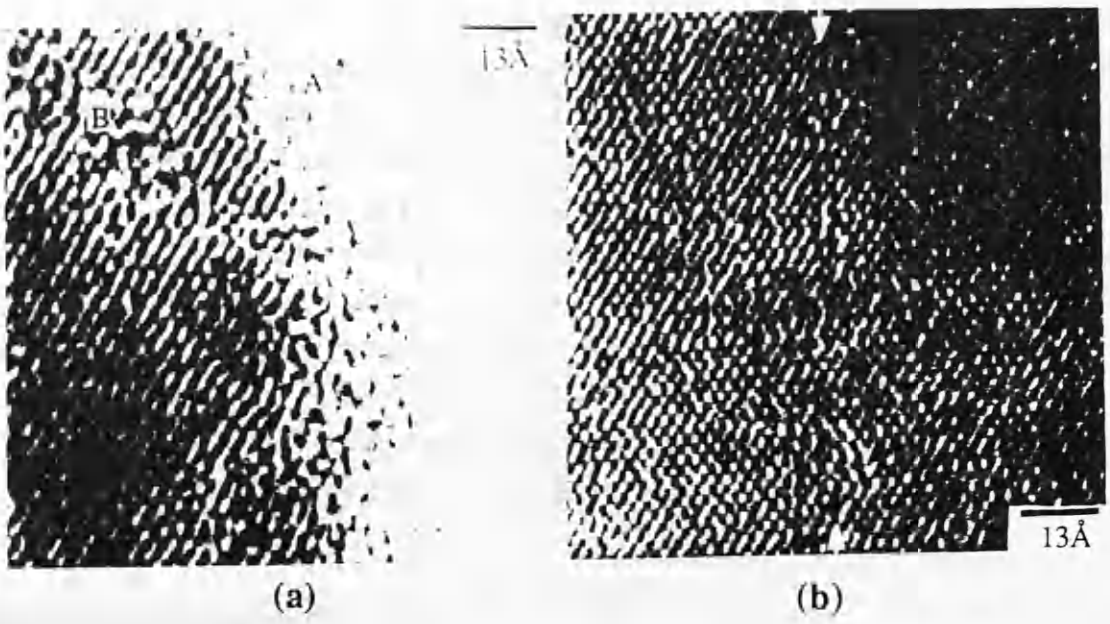

Figure 4.13: HRTEM images of a wire etched using $SiCl_4$ RIE (a) showing the oxide layer on the edge of the wire (marked A) and voids were the lattice structure is absent, marked B, (b).Void areas and disorder in the lattice in the form of a row approximately 1nm wide and 5nm long (arrowed) lying along the direction of bombarding ions, (c) lattice disorder in the form of extended dislocation having the appearance of a classic dislocation (arrowed).

2. Disorder in the lattice. This did not have an appearance of a line dislocation but the disorder was in a row approximately 1nm wide and up to 5nm long running along the direction of bombarding ions, Fig. 4 13b. Such an appearance may be presented by a vacancy loop with its plane parallel to the incident electron beam. This would support the vacancy loop interpretation of the voids, described in 1.

3. Extended dislocations which had the appearance of classical line dislocation- although in projection their Burger's vector could not be ascertained, region C in Fig. 4.13c. They appear less frequently than the features in 1 and 2.

High resolution examination of CH_4/H_2 RIE etched wires showed small features, possibly voids, but less frequently than in the $SiCl_4$ etched specimen, Fig. 4.14a. There were many regions of variable contrast which were attributed to strain within the wire, Fig. 4.14b

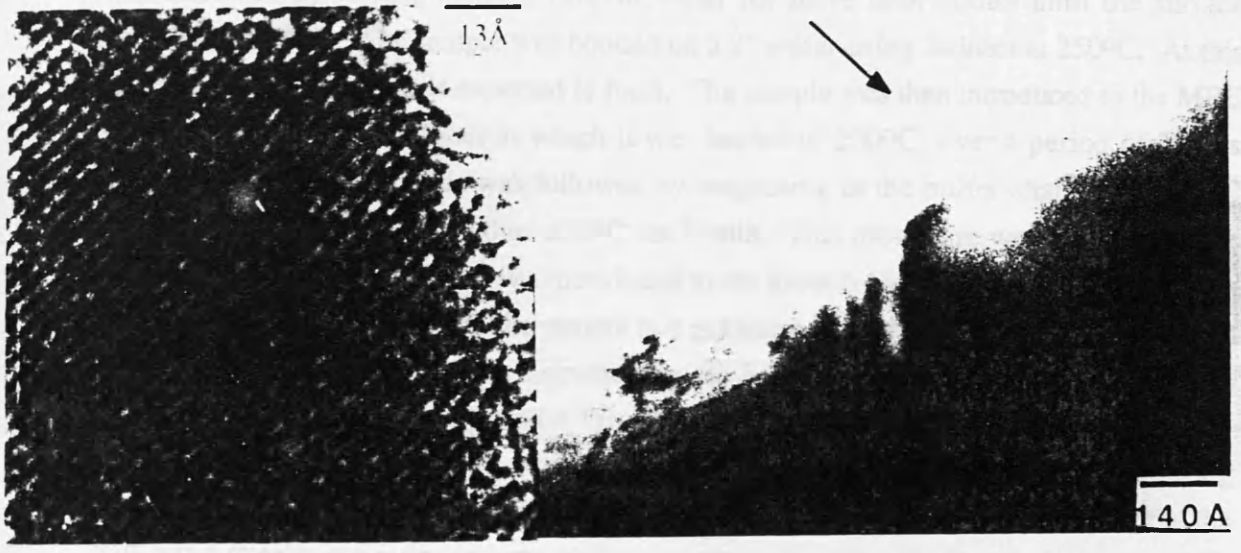

(a) (b)

Figure 4.14: HRTEM images of a wire etched using CH_4/H_2 RIE (a) showing small voids b) showing many regions of contrast which may be attributed to strain in the wire (the arrow points at the residual coating).

4.8. Dark field imaging of wires prepared by etching and regrowth of GaAs

As will be described in chapter 5 it was found that etching in $SiCl_4$ RIE causes As deficiency on the surface. The aim of this experiment was to investigate, using dark field imaging of TEM wires, the possibility of curing the As deficient etched surface by exposing

it to an As flux during regrowth of a GaAs epilayer by molecular beam epitaxy. The regrowth process, performed by Dr. C. Stanley of the MBE group in Glasgow University, was monitored by Reflection High Electron Energy Diffraction (RHEED)[15,16].

4.8.1. Etching and regrowth

One quarter of the wafer used in the experiments above was cleaned ultrasonically using trichloroethane, acetone and methanol then rinsed in IPA. The sample was then etched in $SiCl_4$ for 2min using the conditions described in section 4.3. The sample was then prepared for regrowth. The preparation procedure started by emersing the sample in concentrated H_2SO_4 for 5min using ultrasonic agitation to clean the surface of any organic contamination. The acid was changed and the process was repeated for another 5min. This was followed by rinsing under a flow of water for more than 30min until the surface become hydrofilic. The sample was bonded on a 2" wafer using Indium at 250°C. At this stage, some surface oxide is expected to form. The sample was then introduced to the MBE substrate entry / exit chamber at which it was heated to 200°C over a period of 3hours (pressure ~$1x10^{-8}$torr). This was followed by outgassing in the buffer chamber at 400°C for 60min, 500°C for 180min then 620°C for 20min. This procedure was used to remove the surface oxide. The sample was introduced to the growth chamber at which an electron beam (1.5keV) was incident on the sample at a grazing angle of 1 degree and the diffracted RHEED pattern was projected on a screen. The RHEED pattern was "spotty", an indication of surface roughness, Fig. 4.15a and 4.15b, but no evidence of surface oxide was found.
A flux of As_2 was introduced as the sample was maintained at 580°C for 25min during which the RHEED pattern along either the [110] or [$1\bar{1}0$] directions showed evidence of the half order streaks indicating that the surface was reconstructing and becoming flatter, Fig. 4.15c and 4.15d. The RHEED pattern then showed an As stable surface with a 2x4 construction. By changing the azimuthal angle by 90°, 4x2 pattern was obtained which indicated that the surface is As stable, Fig. 4.15e and 4.15f. Within 60sec of commencing GaAs growth at a rate of $1\mu m.hr^{-1}$, reasonable 2x4 construction was observed indicating that the surface was essentially atomically flat, Fig. 4.15g and 4.15h. An epilayer 150nm thick of GaAs was grown.
After regrowth, TEM specimens were prepared as described in section 3.4. such that the wires were etched through the growth interface.

4.8.2. Dark field imaging of regrown wires

The specimen was aligned as described in section 4.3.1. and the images recorded are shown in Fig. 4.16 a, 4.16b, 4.16c, 4.16d, 4.16e and 4.16f. The diffraction pattern, Fig 4. 16a, is similar to that in Fig 4.7a. The rings are due to the Ti mask since the electron beam was broad enough to pass through the wire as well as the Ti mask. The (000) images (bright field), Fig 4.16b and 4.16c at different magnifications, Show few features:

The regrowth interface can be seen half way through the height of the wire and it show roughness of about 7.3nm (distance from peak to valley measured from the micrographs) which is due to the $SiCl_4$ RIE etching process. In the original and the regrown material, there exist some circular (or semicircular) areas of variable contrast up to ~30nm in diameter in the regrown region, and smaller regions ~10nm in diameter and less frequently in the original material i.e. the bottom half of the wire. The Ti mask is still on top of the wire, better observed in the Inelastic image shown in Fig 4.16f, and the entire wire in enclosed in a film approximately 25nm thick of photoresist which has not been removed totally during the last stage of wire fabrication as seen in Fig 4.16c. The (002) images, Fig 4.16d and 4.16e, show a large contrast changes in the circular regions described above. It can also be seen that the edge of the wire is brighter than the bulk.

The inelastic image, Fig 4.16f shows a brighter wire edge indicating that less electrons are scattered inelastically at the edge i.e. it is thinner than the rest of the wire. Therefore the change in contrast observed in the (002) images at the edge of the wire may be attributed to the change in the thickness of the wire rather than to stoichiometric changes only.

It also shows some changes in the contrast in the interface region and in the circular areas described above.

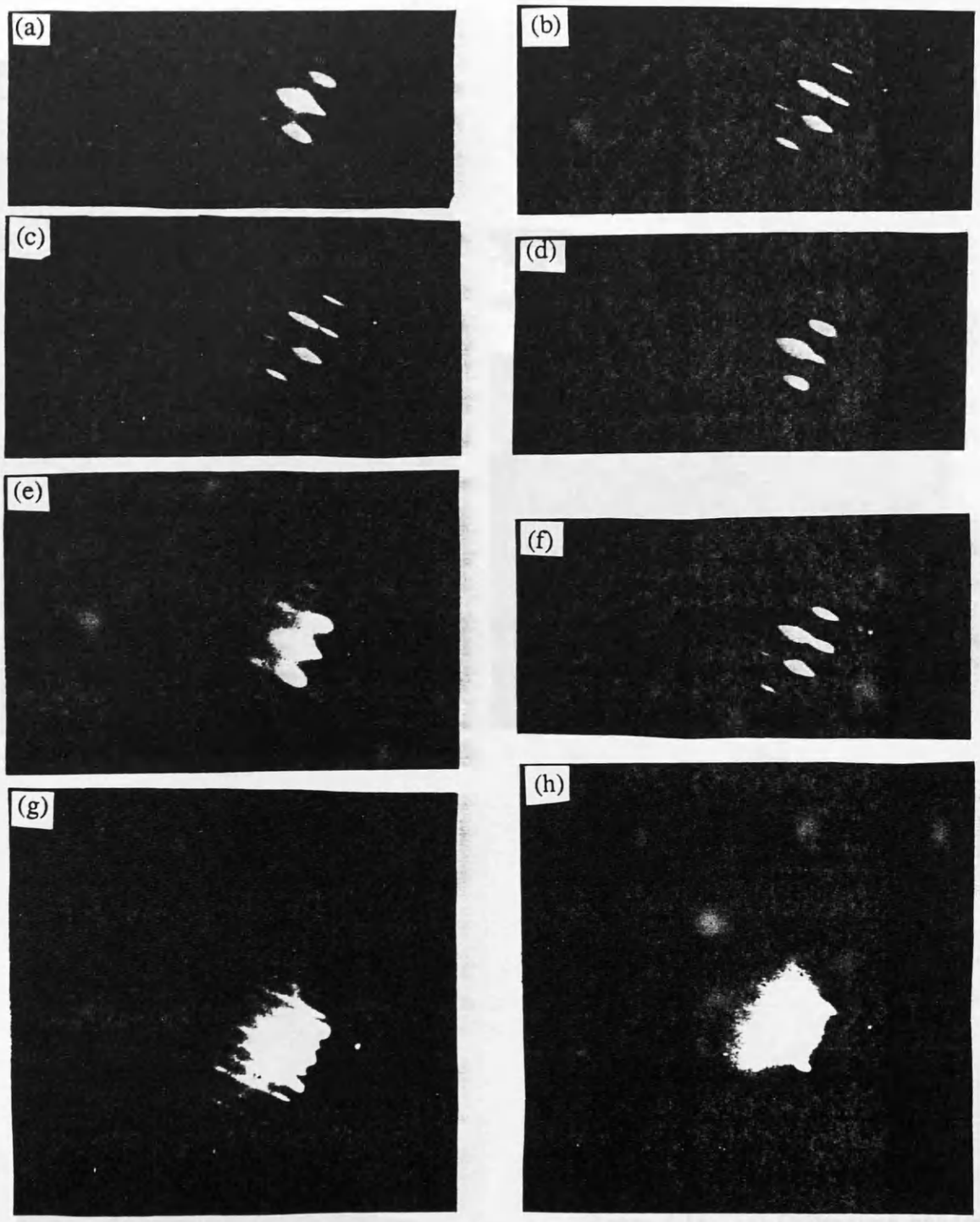

Figure 4.15: Reflection high electron energy diffraction (RHEED) patterns (a) and (b) along the [110] and [1$\bar{1}$0] directions respectively before exposing the etched surface to As_2 flux, (c) and (d) along the [110] and [1$\bar{1}$0] directions respectively showing elongation of the spots and the formation of 'arrow head', (e) and (f) along the [110] and [1$\bar{1}$0] directions respectively at the beginning of GaAs growth and (g) and (h) along the [110] and [1$\bar{1}$0] directions respectively after 1min of commencing GaAs growth.

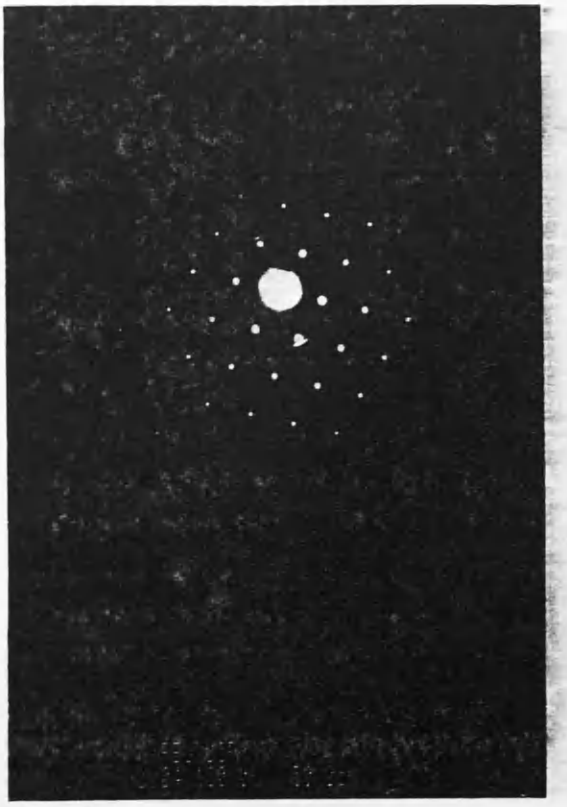

(a)

(b)

(c)

Figure 4.16: (a) Diffraction pattern obtained from a 'regrown' wire etched using $SiCl_4$ RIE, (b) and (c) (000) bright field images at high magnifications of a 'regrown' wire which had been etched using $SiCl_4$

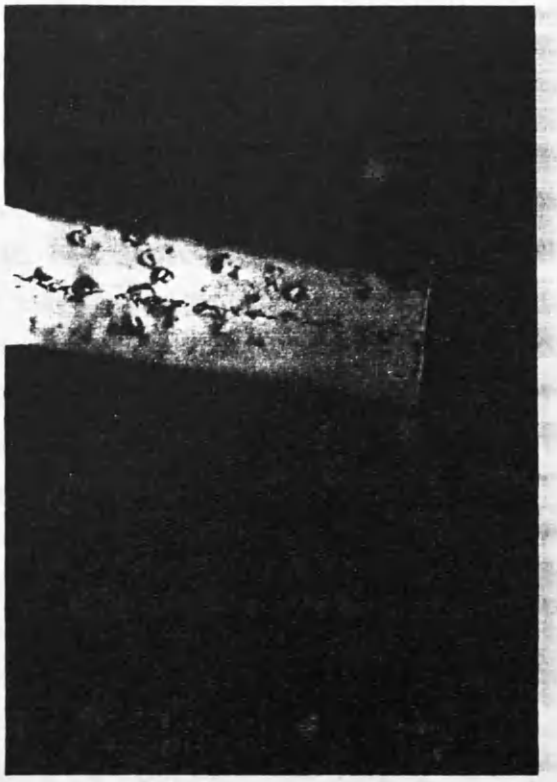

(d)

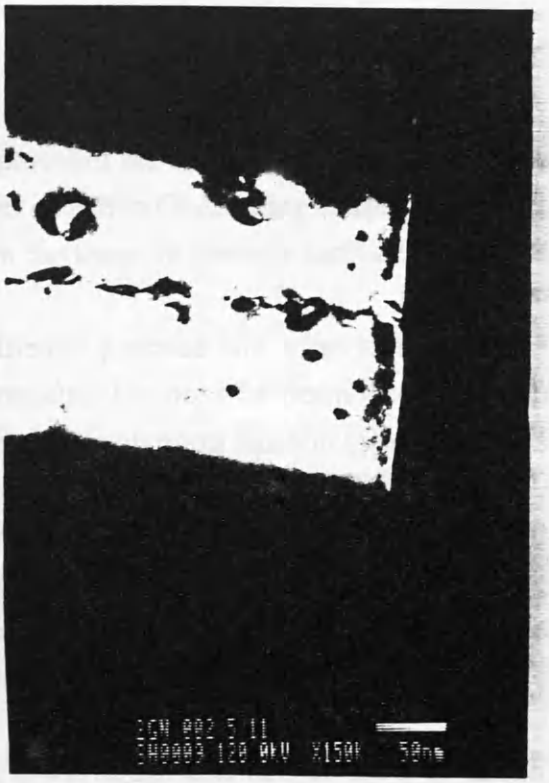

(e)

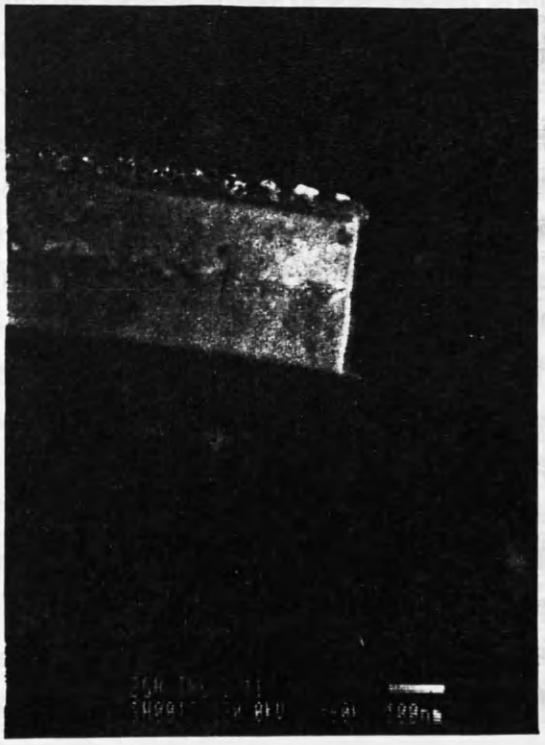

(f)

Figure 4.16: (d) and (e) (002) dark field images at different magnifications of a 'regrown' wire which had been etched using $SiCl_4$ RIE, and (f) dark field image formed using electron which has been inelastically scattered (inelastic image).

4.9. Discussion and conclusions

The TEM techniques used in this study have provided the first direct comparison of the sidewall damage in quantum wire-like structures etched in GaAs using CH_4/H_2 and $SiCl_4$ RIE. In contrast, other techniques were used in the thesis to observe and/or estimate the etching damage but in indirect way.

The procedure of making the wires was modified to produce thin wires so that the kinematic theory can be used to interpret the results. The use of e-beam lithography, to define the wires, and optical lithography to pattern the platform has eliminated problems encountered when positive and negative e-beam resists were used for both stages[5]. Improvements such as thinner wires, longer platform, to accommodate many wires and increase the probability of finding wires suitable for examination, narrower and higher platform, to simplify finding the wires and alignment of the TEM, have helped is finding the wires, alignment of the wires in the right orientation for examination and in interpreting the results of the TEM examination.

Using the TEM dark field imaging technique, it was found that RIE of GaAs in silicon tetrachloride and methane-hydrogen plasmas does not cause amorphisation of the sidewalls. From the inelastic image of wires etched in silicon tetrachloride, Fig 4.8c, it can be seen that the contrast along the wire is uniform indicating that the width of the wire examined is uniform (the fact that the wire looks brighter near the edge is due to using a small electron beam for detailed examination of sections of the wire). So the change to brighter contrast in the (002) image, Fig 4.8b, observed at the edge indicates compositional changes off-stoichiometric GaAs rather than an effect related to thickness variation. There is a region < 20nm wide starting from the edge of the wire with bright contrast after which the contrast reduces gradually to that of the bulk of the wire. Similar observation has been made by Cheung[5] with region width of ~25nm. It is evident that the $SiCl_4$ etching process does cause some damage in the form of change in composition in the following way:

(a) In the bulk of the wire, i.e. a way from the edge, the contrast observed is due to the sum of undamaged GaAs sandwiched between two damaged layers at the sidewall of the wire since both sides were exposed to ion bombardment during etching.

(b) At the edge of the wire, the brighter contrast observed may indicate severe damage due to the fact the edge of the wire is exposed to the ion bombardment from three sides resulting in damage of the entire GaAs matrix across the thickness of the wire.

It is difficult to quantify the damage depth from measuring the width of bright contrast region at the edge of the wire since as mentioned in (b), this change in contrast is due to an additional damage component from the edge of the wire. The film's exposure dose versus film contrast curve should be linear over the range of contrast used, for the quantitative results to be acceptable.

High resolution TEM examination of $SiCl_4$ RIE etched wires has revealed the presence of void areas were lattice structure was absent, Fig. 4.13a. The areas are 1-5nm in diameter which may be infered as vacancy loops. Disorder in the lattice was also observed in rows approximately 1nm wide and up to 5nm long mainly along the [100] direction i.e. the direction of ion bombardment, Fig. 4.13b. These features may be attributed to the vacancy loops suggested above with its plane parallel to the incident electron beam. Finally extended dislocations which had the appearance of a classical dislocation, Fig. 4.13c, although in projection their Burger vector could not be ascertained

For wires etched in CH_4/H_2 RIE, the nature of the contrast variation is different from what is observed in $SiCl_4$ etched wires, indicating a different type of damage, Fig. 4.9b and 4.9c. Regions of contrast variation up to 7nm in diameter which may be infered as dislocation loop-like defects. It is known that hydrogen can diffuse easily in GaAs during CH_4/H_2 RIE and passivates the dopants. It is also known that annealing at 380°C for 1sec is sufficient to re-active the dopants. (002) images of wires prepared by CH_4/H_2 RIE before and after annealing were very similar indicating that annealing at this temperature may be sufficient in removing hydrogen and activating GaAs electrically, however, the physical disorder hydrogen creates is not removed.

Features similar to what is observed in wires etched in CH_4/H_2 RIE have been shown by Frieser[13] upon etching Si using hydrogen and Sandana[14] near the projected range after proton implantation of GaAs at 300keV and annealing at 500°C for 20min.

It should be mentioned that in one (and only one) of the CH_4/H_2 RIE etched wires, plate-like features were observed after annealing, Fig. 4.17, defined along the {111} planes. Similar plate-like defects have been observed by Sandana who suggested that these defects are hydrogen precipitates which were formed from accumulation of high concentration of vacancies. However, the plate-like defects were not observed in any other wires and can not therefore be thought of as a common etching-related defect.

Figure 4.17: (000) bright field image of a wire which had been etched using CH_4/H_2 showing plate-like defects (a magnifying lens is needed to observe the defects in the form of bright/dark fringes).

High resolution TEM examination of wires etched in CH_4/H_2 RIE showed small features, possibly voids, similar to, but less frequently than in the $SiCl_4$ etched specimen, Fig. 4.14a. It also showed many regions of different contrast levels which may be attributed to strain within the wires, Fig. 4.14b. It should be noticed that the HRTEM examination and analysis of etched GaAs wires performed in this study is neither extensive nor exhaustive and more work is needed to analyse the origin and evolution of the defects observed in this study.

The etching-regrowth experiment was interesting from the MBE growth point of view since it provides a novel way of imaging interfaces directly enabling information about the interface roughness to be correlated with the RHEED patterns recorded during the regrowth process. The interface roughness, which is due to the $SiCl_4$ etching process, was estimated to be up to ~7.3nm. It is worth mentioning that Cheung[5] has estimated the root mean square roughness of GaAs surface etched in $SiCl_4$ RIE at rf power of 100W to be ~1.7nm using specular X-ray reflectivity[5].

The presence of the large circular defects in the regrown wires can not be attributed the etching process only since etched wires previously examined did not show any similar features. Nor can these defects be related to the annealing procedure/temperature

accompanied the growth process since 580°C is not considered as very high growth temperature in MBE[17] and high quality GaAs have been grown in the temperature range of 520°C to 610°C[18]. At present, one can only speculate that the defects generated during the etching process might have agglomerated during annealing the sample to form larger defects. However that does not explain how larger defects were formed in the regrown region. On the other hand, the possibility of formation of As precipitated should not be ruled out since the etched surface has been exposed to an As_2 flux for 25min before commencing growth as described in section 4.8.1.

By comparing the inelastic image, Fig. 4.16d, and the (002) image at the same magnification, Fig. 4.16f, it can be seen that these circular defects are accompanied by thickness variation. That is, regions inside the defects with bright contrast in the (002) image, i.e. non-stoichiometric, show dark contrast in the inelastic image i.e. they are thicker. This observation supports the idea that these features are related to As precipitates, in addition, it indicates that the local etch rate of these regions may be lower resulting in less material being etched. This indication also implies that there is a local change in composition in the circular defects.

The question 'whether the exposure of the etched surface to As_2 flux at the beginning of the regrowth process has cured the As deficiency?' can not be answered straight forwardly due to the large contrast variation in the (002) image on the whole wire and some thickness variations at the interface region.

To conclude the results presented in this chapter:

1. The method for preparing TEM specimens for examining the sidewall damage directly has been refined to enable wires 50-80nm thick to be prepared and examined reproducibly using dark field imaging technique .

2. Wires etched using $SiCl_4$ and CH_4/H_2 RIE were compared and it was found that wires etched using the former process show some change in composition near the edge of the wire. While wires etched using the later process display a 'spotty' texture on the entire wire which is attributed to dislocation loops up to 7nm in diameter and is likely to be related to hydrogen bombardment of the sidewalls. Annealing the wires at 380°C for 1 second reactivates the dopants, however it does not recover the lattice disorder caused by the bombardment.

3. HRTEM examination of $SiCl_4$ etched GaAs wires revealed the presence of lattice disorder in the form of dislocation loops 1nm wide and up to 7nm long, areas (possibly voids) where the lattice structure is absent and extended dislocations having the appearance

of classic dislocation. Wires etched in CH_4/H_2 RIE showed small void-like features occuring less frequently than the case of $SiCl_4$ and regions with strain.

4. Wires etched through etch/regrowth interface have enabled direct measurement and correlation of growth interface roughness (up to 7.3nm) with RHEED patterns recorded during the regrowth process. Circular and semicircular defects, up to 30nm in diameter in the regrown region and up to 10nm in diameter in the original epilayer, were observed the origin of which is not clear. It would be interesting if more wires are made using unetched regrown material to determine the origin of the defects observed and to examine the quality of GaAs regrown under various conditions.

4.10. References

1. J. A. Adams, I. G. Thayne, N. I. Cameron, M. R. S. Taylor, S. P. Beaumont, C. D. W. Wilkinson, N. P. Johnson, A. H. Kean, and C. R. Stanley, Microcircuit Engineering 89 ed. Ahmed et al, pp65 Elsevier (1990) Amsterdam.
2. M. Kelly, and C. Weisbuch, ed. "Physics and Fabrication of Microstructures and Microdevices", springer, pp36 (1986) Berlin.
3. R. Cheung, S. Thoms, S. P. Beaumont, G. Doughty, V. Law, and C. D. W. Wilkinson, Electronic Lett., **23**, 857 (1987).
4. R. Cheung, S. Thoms, I. McIntyre, C. D. W. Wilkinson and S. P. Beaumont, J. Vac. Sci. Technol., **6**, 1911 (1988).
5. R. Cheung PhD thesis, University of Glasgow (1990).
6. M. Watt, C. M. Sottomayor-Torres, R. Cheung, C. D .W. Wilkinson, H. E. G. Arnot, and S. P. Beaumont , J. Modern Optics, **35**, 365 (1988).
7. S. J. Pearton, M. J. Vasile, K. S. Jones, K. T. Short, E. Lane, T. R. Fullowan, A. E. Von Neida, and N. M. Haegel, J. Appl. Phys., **65**, 1281 (1989).
8. S. Thoms, S. P. Beaumont, C. D. W. Wilkinson, J. Frost, and C. R. Stanley, Microelectronic Engineering, **5**, 249 (1986).
9. R. Cheung, A. Birnie, N. J. Chapman, and C. D. W. Wilkinson, Microcircuit Engineering 89 ed. Ahmed et al, pp591, Elsevier, (1990) Amsterdam.
10. C. Kittel, "Introduction to Solid State Physics", Wiley (1986).
11. J. M. Cowley,"Diffraction Physics", North-Holland (1975).
12. P. A. Doyle, and P. S. Turner. Acta Crys., **A24**, 390 (1967).

13. R. G. Frieser, F. J. Montillo, N. B. Zingerman, W. K. Chu, and S. R. Mader, J. Electrochem. Soc., **130**, 2237 (1983).
14. Figures 1a and 5 in D. K. Sadana, J. M. Zavada, H. A. Jenkinson, and T. Sands, Appl. Phys. Lett., **47**, 691 (1985).
15. A. Y. Cho, and I. Hayashi, J. Appl. Phys, **41**, 2780 (1971).
16. E. A. Woods, J. Appl. Phys., **35**, 1306 (1964).
17. Private communication with Dr A. Kean, MBE grower, Glasgow University (1991).
18. C. R. Stanley, M. C. Holland, R. H. Hutchins, A. H. Kean, and N. P. Johnson, Int. Symp. GaAs and related compounds, Inst. Phys. Conf. Ser. No.112, Chapter 3, pp67, Jersey (1990).

Chapter 5: Characterisation of reactive ion etching-induced modifications of GaAs surfaces by X-ray Photoelectron Spectroscopy (XPS)

5.1. Introduction

The importance of using the core level X-ray photoelectron spectroscopy (XPS) lies in its high surface sensitivity and the ability to elementarily analyse the surface region qualitatively as the core binding energies are characteristic of an element. In addition, characterisation of the bonding state and chemical environment of the atom concerned can be achieved through the interpretation of the measured binding energy shift. The set of experiments described below have been undertaken to investigate the modifications in the chemistry of (100) GaAs surfaces following reactive ion etching using CH_4/H_2 and $SiCl_4$. The samples have been etched at Glasgow University then transfered to the department of Physics, University of Wales Cardiff for the XPS analysis, consequently they have been exposed to air for a minimum of 20 hours before being analyzed. The technical assistance of C. Dunscomb in XPS analysis is acknowledged.

5.2. Theory of XPS

Surface analysis by XPS is accomplished by irradiating a sample with monoenergetic soft X-rays and analysing the photoelectrons emitted, Fig. 1. Al K_α X-ray (1486.6eV) or Mg K_α X-ray (1253.6eV) are normally used. These X-ray photons have a limited penetrating power in a solid, of the order of 1-10 μm. They interact with atoms in the surface region by the photoelectric effect, causing electrons to be emitted. The electrons leaving the sample are detected by an electron spectrometer according to their kinetic energy. The analyzer is operated normally as an energy window, accepting only those electrons having an energy within the range of this fixed window, refered to as the 'pass energy'.

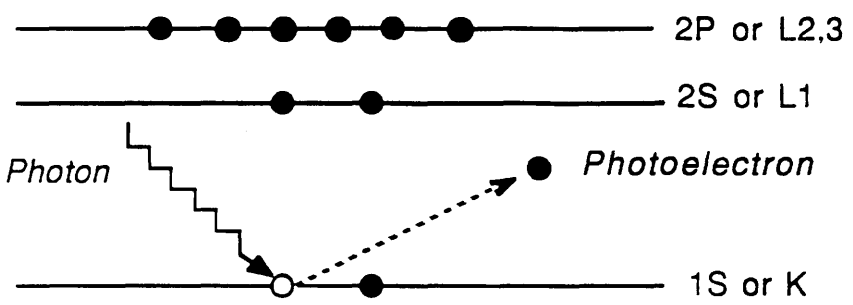

Figure 5.1: Schematic diagram showing the photoelectron emission process.

When an X-ray photon is incident on a substance, it will give rise to a photoelectron emission according to the equation:

$$E_K = h\upsilon - E_B - \Phi \qquad (5.1)$$

here, E_K is the measured electron kinetic energy, $h\upsilon$ the energy of the exciting X-ray radiation, E_B the binding energy of the electron in the solid and Φ the 'work function' (a catch all term whose precise value depends on both the sample and the spectrometer). Since an electron is a charged particle, its orbit around a nucleus induces a magnetic field whose intensity and direction depend upon the velocity and radius of the orbit. These latter quantities are characterised by the orbital angular momentum l (l = 0, 1, 2, 3,...etc). The electron spin, positive or negative, induces an inherent magnetic field. The later, in-turn has an associated spin momentum, characterised by the spin quantum number s (s =+1/2,-1/2). In order to understand the XPS spectrum, the binding energy E_B of the electrons must be known. An electron in a solid can occupy one of great many energy levels. Strongly bound electrons occupy the core levels. These levels are characteristic of the element involved. Weakly bound electrons which have trajectories on the outer most layers of the electron cloud occupy energy levels whose position is affected by the presence of other atoms, and so whose precise binding energy depends on the chemical binding of the surface of the material. Hence, by comparing the binding energy of the electrons detected with E_B values reported in the literature, information about the elements of the surface can be obtained.
The energy levels of the core electrons are described using two models for the interaction between the angular momentum (l) and the spin (s) of the electrons, *j-j Coupling or L-S coupling*.
The total angular momentum is simply the vector sum of the two momenta which can be carried out in two ways:
a) *j-j Coupling* : In this method the total angular momentum (J) of an isolated electron is obtained by using the equation :

$$j = l + s \quad (j = 1/2, 3/2, 5/2, 7/2...\text{etc}) \qquad (5.2)$$

A summation is performed on all electrons resulting in the total atomic angular momentum J, where

$$J = \Sigma j \qquad (5.3)$$

j-j coupling is the best description for elements with $Z > 75$, but the nomenculture based on it has been used for all parts of the periodic table. However, j-j coupling is inadequate for doubly ionised interactions between two holes (Auger process).

b) *L-S Coupling* : The other way of obtaining the total angular momentum of an atom is by summing all the orbital angular momenta of the electrons of the atom by letting,

$$L = \Sigma l \qquad (5.4)$$

and the same for the spin numbers

$$S = \Sigma s \qquad (5.5)$$

Coupling of the two momenta to give the total angular momentum J:

$$J = / L \pm S / \qquad (5.6)$$

L-S coupling is applied for elements with $Z < 20$, it has been mostly used for recording high energy resolution Auger spectra for comparison with theoretical calculations, so as the intermediate coupling which is used for part of the periodic table in which neither the L-S nor the j-j coupling is adequate. In this study, the j-j coupling model was used.

Every wide scan XPS spectrum shows many features of which are[1,2]:

a. Peak due to core levels: These are sharp peaks, which have variable intensities and widths and they are doublets except for S levels . Doublets arise through the spin - orbit j-j coupling $j = l + s$ in which two possible states arise when $l > 0$. The difference in energy of the two states, ΔE_j, reflects the 'parallel' and 'anti-parallel' nature of the spin and orbital angular momentum vectors of the remaining electrons. ΔE_j increases as Z increases for a given subshell (n, l constant), or as l decreases for constant n (i.e. splitting energy of $3p$ > $3d$). For every sharp peak there is a background upward-step to the high binding energy side. This is because the photoemission is an inelastic process and the photoelectrons suffer energy loss between photoemission from an atom in the solid and detection in the spectrometer.

The broad background (which is superimposed on the peaks) is due to Bremsstrahlung

Sample	Etch gas (sccm)	Pressure (mtorr)	rf power (W)	dc bias (V)	Etch time (min)
1	CH_4/ H_2	15	150	1000	5
	5/25				
2	CH_4/ H_2	15	150	1000	5 *
	5/25				
3	CH_4/ H_2	15	2	70	10
	5/25				
4	$SiCl_4$	11.9	150	380	0.5
	9				
5	$SiCl_4$	11.9	100	290	0.5
	9				
6	$SiCl_4$	11.7	80	240	0.5
	9				
7	$SiCl_4$	11.9	2	0	1
	9				

* This sample has been annealed after etching at 380°C for 1sec.

Table I: Conditions for RIE of GaAs samples for the purpose of XPS analysis .

The choice of conditions reflects:

1. It has been reported[3] that RIE in CH_4/H_2 passivates the donors in GaAs. To investigate the effect that annealing has on the surface, Sample 2 was etched, for 1sec at 380°C in a mixture of 95% Ar : 5% H_2 and then annealed.
2. The etching times for these samples were chosen (except for samples 3 and 7) so that a layer, 100nm thick is etched away from the surface.
3. In the case of samples etched in 2W rf power, the plasma was initiated at 90W for CH_4/H_2 and 20W for $SiCl_4$, then reduced to 2W within 2sec.
4. A control sample (unetched) was also examined for comparison.

5.3.2. XPS spectra acquisition

The XPS spectrometer was a V.G. ESCALAB MKII, equipped with a dual anode (Mg/Al) non-monochromated X-ray sources. It consists of a loadlock chamber, a preparation and analysis chambers. The sample was introduced to the loadlock chamber and evacuated to a pressure < $5x10^{-2}$ Torr, where it was then introduced to the preparation chamber at a

pressure of 1-4x10^{-10} Torr). The sample was then transfered into the analysis chamber. After aligning the sample and optimising the signal-to-noise ratio, data was collected using Al K_α X-ray line and a concentric hemispherical analyser. This particular analyser is preferred for XPS because it can maintain adequate luminosity at high-energy resolution, in addition the narrow acceptance angle is particularly suitable for angular dependence measurements. Scans for selected energy ranges of interest were accumulated.
Energy range of the peaks of interest are listed in Table II.

Peak	Energy range (eV)	Pass energy (eV)
full scan	0-1400	50
Ga 3d	16-24	20
Ga 2p	1113-1122	20
As 3d	38-47	20
As 2p	1317-1334	20
Cl 2p +As 3s	190-210	20
C 1s	260-290	20
O 1s	528-538	20

Table II: Energy range of the peaks investigated and the pass energy used in the XPS analysis.

It should be mentioned that a pass energy of 20eV yields an overall spectral resolution of approximately 1eV (FWHM).
It is known that the escape depth of the electrons emerging from the d subshell is larger than that for electrons emerging from the p subshell, approximately 30Å and 10Å respectively. Using this phenomenon, for both Ga and As, it is possible to gain information about the depth distribution of the oxide within the top 30Å. Table III lists the electron escape depths of the d and p subshells for both Ga and As as reproduced from reference 4.

Peak	Escape depth (Å)
Ga 3d	30
Ga 2p	11
As 3d	25
As 2p	8

Table III: Escape depth of the electrons detected in this study.

5.3.3. Fitting of the selected peaks

The Ga 3d and As 3d peaks were fitted to two elemental peaks, taking the spin-orbit energy splitting into account, with a peak area ratio of 2:3 for j values of 3/2 and 5/2 for the d subshell[1]. Values of the splitting energy for Ga and As 3d peaks were $\Delta E_j = 0.45$ and 0.68eV respectively. The same fitting procedure was applied for the accompanied peak (s) of gallium oxide (Ga_2O_3) and assuming only arsenic trioxide (As_2O_3) is present on the surface. However, other arsenic oxides have also been reported, for example, AsO[5] in addition to As_2O_5 and AsO_2[6] during exposure to excited oxygen (Ozone), but they were not included in these fitting calculations since excited oxygen was not present at any stage of sample processing.

The fitting method synthesizes a spectrum by least square fitting based on the experimental spectrum, by summing a number of peaks of arbitrary position and peak width. Each peak is a mixed Gaussian/ Lorentzian function represented by[1]:

$$f(x) = \text{peak height} / [1 + M\ (x-x_0)^2 / \beta^2\ ] \exp\ \{(1 - M)\ .\ [\ln 2\ (x-x_0)^2] / \beta^2\} \qquad (5.7)$$

where x_0 is the peak centre; β =0.5 FWHM; M: Gaussian / Lorentzian mixing ratio (M=1 for pure Lorentzian; M= 0 for pure Gaussian). These functions represent the intrinsic peak shape, expected to be asymmetrical for conductors with the extent of the asymmetry depending on the density of states at the Fermi level, as broadened by the instrument (represented by a Gaussian function)[7]. The quality of the fit is defined by evaluating the weighted chi-squared (χ^2), the smaller the value of χ^2, the better the fit. The background was defined by Shirley's method which assumes the background intensity at a point determined, by iterative analysis, to be proportional to the intensity of the total peak area above the background[(1)] . This method is superior to the straight line background method especially when considering a mixture of two states e.g. an element and its oxide[1]. An example of fitted peaks is presented in Fig.5 3.

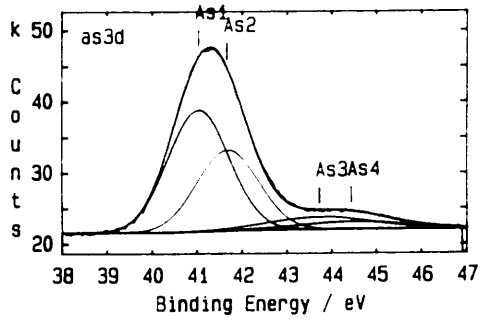

Peak	Centre (eV)	FWHM (eV)	Hght %	G/L %	Area %
As11	41.0	1.59	67	0	51
As22	41.7	1.59	44	0	34
As23	43.7	2.73	7	0	9
As24	44.4	2.73	4	0	5

100% Height (Counts) : 25674
100% Area (kceV/sec) : 14.16
Reduced Chi Squared : 1.70

Figure 5.3: An example of a fitted As 3*d* XPS spectrum.

5.4. Results of CH_4/H_2 etched GaAs surfaces

The spectra of the selected energy ranges of electrons emitted from the As 3*d*, As 2*p*, Ga 3*d* and Ga 2*p* subshells are shown in Fig.5.4. a, b, c, d. The values of peak area of the Ga 3*d*, As 3*d*, C 1*s* and O 1*s* peaks and the binding energies of the control sample and samples etched in CH_4/H_2 are listed in Table IV:

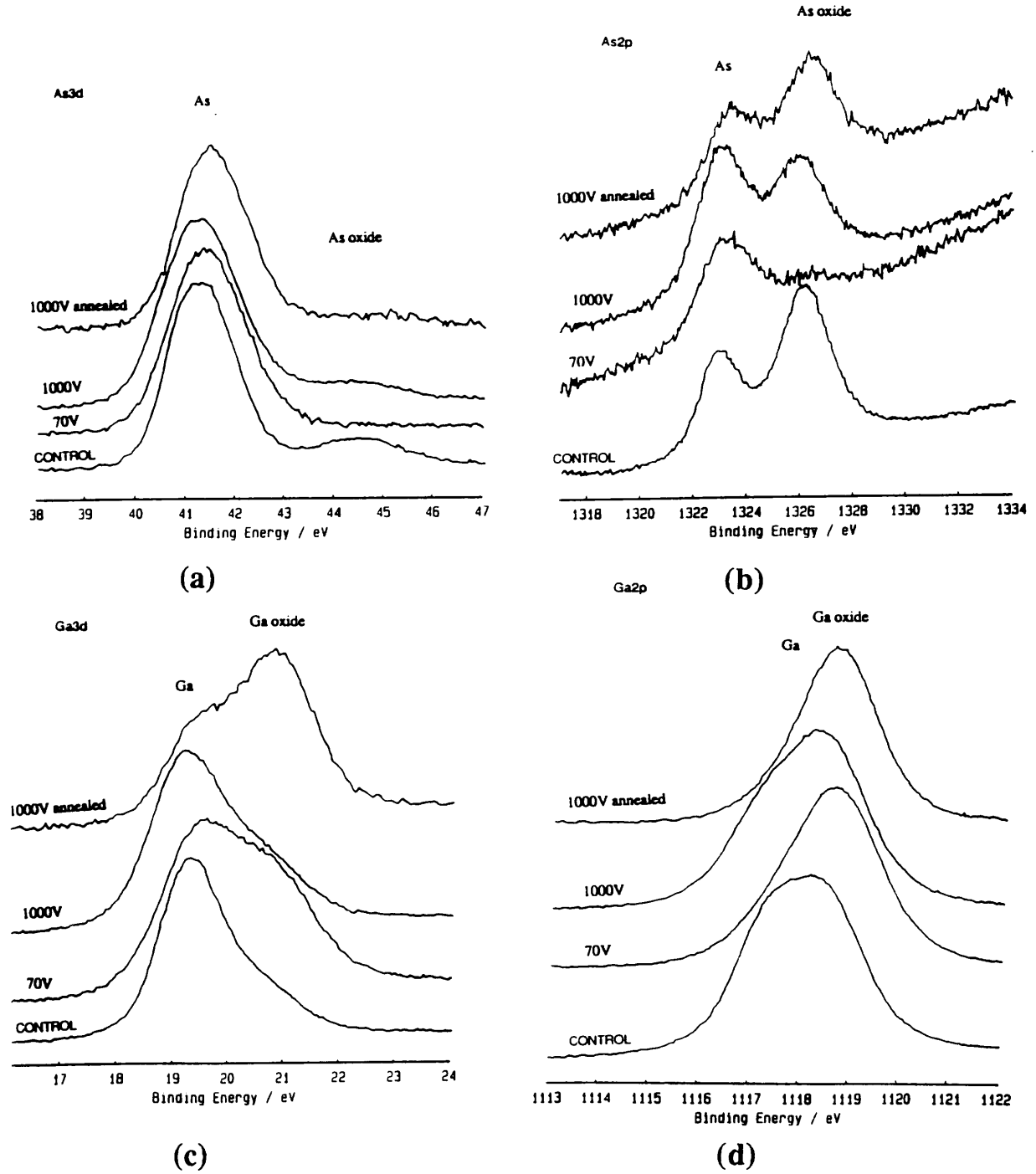

Figure 5.4: XPS spectra of GaAs control sample and samples 3, 1 and 2, reactive ion etched

in CH_4/H_2. The spectra are for: a) As 3*d* , b) As 2*p* , Ga 3*d* and Ga 2*p*. The dc bias developed during the etching is quoted in the figure.

Sample	Control	Sample 1	Sample 2	Sample 3
Peak area of Ga	78	74	39	62
Binding energy (eV)	19.09	19.05	19.26	19.28
χ^2	2.96	1.44	1.14	0.84
Peak area of Ga_2O_3	22	25	62	38
Binding energy (eV)	20.52	20.50	20.70	20.71
Peak area of As	81	85	91	96
Binding energy (eV)	41.30	41.30	41.50	41.35
χ^2	3.15	1.70	2.08	1.54
Peak area of As_2O_3	18	14	9	5
Area of C peak	12.01	15.76	2.33	20.05
Area of O peak	37.5	19.4	12.81	46.59

Table IV: Peak areas (Arbitrary units), binding energies (eV) and χ^2 values of the control sample and samples 1-3, etched in CH_4/H_2.

For semiquantitative XPS measurements, the values of the peak areas should be normalized for the photoionisation cross section and the electron escape depth. The number of atoms of the element per cm^3 of the sample n is given by[2]:

$$n = I / f\sigma\theta y\lambda AT \qquad (5.8)$$

where I is the number of photoelectrons per second in a specific spectral peak, f is the X-ray flux in photons/cm^2.sec, σ is the photoelectric cross section for the atomic orbital of interest in cm^2, θ is an angular efficiency factor for the instrument arrangement based on the angle between the photon path and the detected electron, y is the efficiency in the photoelectic process for formation of photoelectrons of the normal photoelectron energy, λ is the mean free path of the photoelectron in the sample, A is the area of the sample from which photoelectrons are detected and T is the detection efficiency for electrons emitted from the sample. The denomiator in equation 5.8 can be assigned the symbol S, defined as the atomic sensitivity factor. A set of relative values of S have been developed in the literature for all the elements[1,2]. However, it should be stressed that the values of S quoted in the literature can be applied to semiquantitative analysis only if the transmission characteristics of the electron energy analyzer are similar. The transmission function for the ESCA LAB II spectrometer used in this study varies with the inverse of the electron kinetic energy which is similar to that of Briggs and Seah[1], therefore the S values quoted in that reference were

used.

The atomic fraction percentages in the matrix C_x% is calculated for the detected elements (Ga, As, O, and C) using the equation:

$$C_x\ \% = N_x / \Sigma_i N_i = \{(I_x / S_x) / \Sigma_i F_{i,x} (I_i / S_i)\}\% \qquad (5.9)$$

where $\Sigma_i N_i$ is the summation of all atomic fractions of the elements detected i.e. Ga, As, O and C. The values of the sensitivity factors used in the calculations are listed below[1]:

Element	S
Ga 3*d*	0.31
As 3*d*	0.53
O 1*s*	0.66
C 1*s*	0.25

The ratios of the atomic fraction of the oxide to that of the element, NGa_2O_3/ NGa and NAs_2O_3/ NAs and the ratio NAs/ NGa are also calculated, where

$$N_1 / N_2 = F_{1,2} (I_1 / S_1) / (I_2 / S_2) \qquad (5.10)$$

here, N_x is the atomic fraction of the element x, $F_{1,2}$ is the matrix factor with value put equal to unity[7], I_x is the area of the peak of the element x as obtained using the fitting process in section 5.3.3, and S_x is the atomic sensitivity factor for the element x.

The atomic fraction percentage in the matrix C_x% and the ratios of the atomic fraction of the oxide to element, NGa_2O_3/ NGa, NAs_2O_3/ NAs, and NAs/ NGa for the control sample and samples etched in CH_4/H_2, are presented in Table V:

Sample	%Ga	%As	%O	%C	NGa_2O_3 /NGa	NAs_2O_3 /NAs	NAs /NGa
Control	49.46	30.05	11.16	9.44	0.282	0.222	0.607
Sample 1	48.57	32.62	5.98	12.82	0.337	0.164	0.670
Sample 2	38.56	52.63	5.95	2.85	1.58	0.098	1.365
Sample 3	37.60	34.03	13.27	15.08	0.62	0.052	0.905

5.5. Results of $SiCl_4$ etched GaAs surfaces

For the samples 4-7, etched in $SiCl_4$, the spectra of the Ga 3*d* , Ga 2*p* , As 3*d* and As 2*p* have been recorded as in section 5.4 and are shown in Figure 5.5. a, b, c, and d.

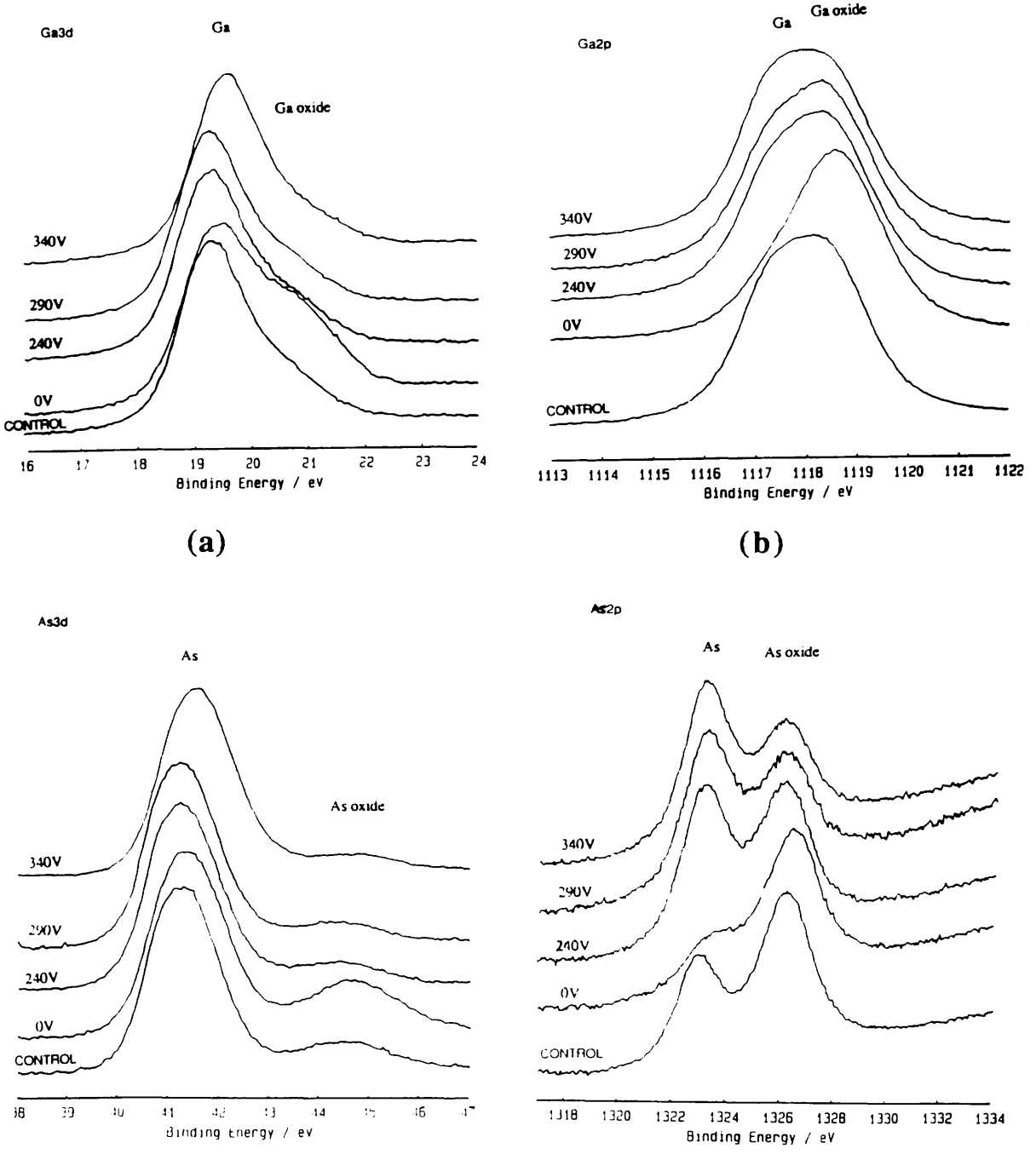

Figure 5.5: XPS spectra of GaAs samples etched in $SiCl_4$, a) Ga 3*d*, b) Ga 2*p*, c) As 3*d* and d) As 2*p*. The dc bias developed during etching is quoted in the figure.

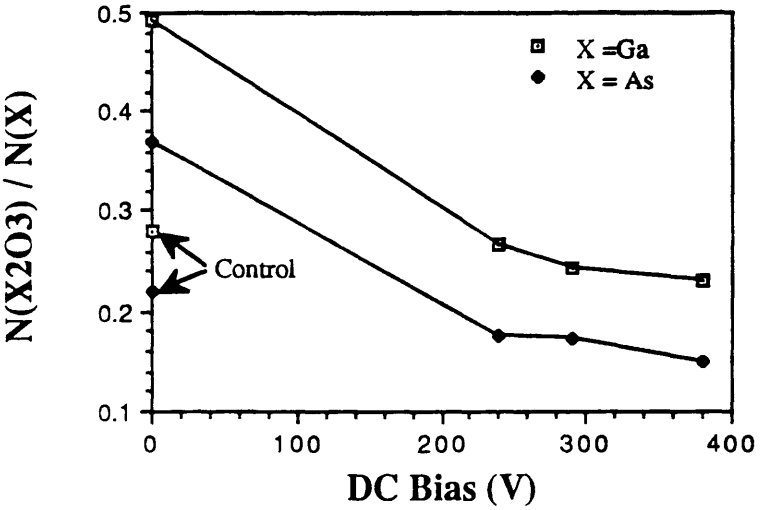

Figure 5.6. a: The ratios NGa_2O_3/ NGa, NAs_2O_3/ NAs as a function of the dc bias for GaAs samples etched in $SiCl_4$.

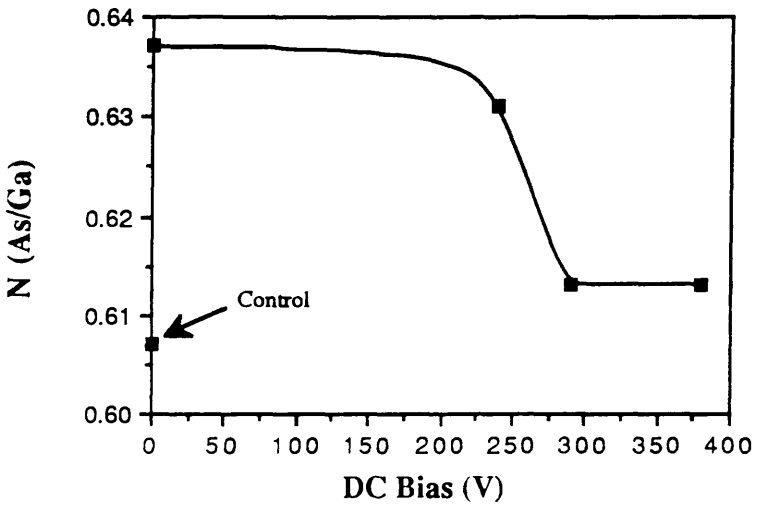

Figure 5.6. b: The ratio of NAs/ NGa as a function of the dc bias for samples etched in $SiCl_4$.

In an attempt to estimate the thickness of the oxide layer, sample 5 was chosen to perform angle resolved XPS analysis. This technique is known to be even more surface-sensitive than conventional XPS. The major requirement for surface sensitivity enhancement is that the surface should be flat. Surface roughness leads to an averaging of electron exit angles and also to shadowing effects (both of the incident X-ray and the emerging electrons). Unfortunately, this was the case with sample 5. The spectra recorded were noisy despite the fact that longer scanning times were used. R. Cheung reported that surface roughness of

$SiCl_4$ etched samples has been estimated from X-ray reflectively experiments in which the roughness was estimated to be approximately 30Å[8].

5.6. Discussion and conclusions

5.6.1. The origin of the chemical shift

A core electron is subjected to a combination of forces, the resultant is known as its binding energy. From the nucleus, it experiences a strong attractive force proportional to the magnitude of the nuclear charge or atomic number. The outer or valance shell electrons exert a repulsive force which in effect screens the core electrons from the nuclear charge, diminishing the nuclear attractive force. The resulting force by which the electron is bound to the atom is the binding energy. If an electron is removed from the outer shell, the screening of the inner electrons is reduced by one electron charge and the core electrons therefore feel an increased force of attraction from the nucleus.
A negative charge in an oxidation state, i.e. the gain of an outer electron has the opposite effect by effectively increasing the shielding and decreasing the binding energy[9].

5.6.2. Arsenic oxides

It has been shown[6] that when cleaved GaAs (110) is exposed to O_2 in a controlled manner, an Arsenic oxide peak with an offset of 2.9eV appears. However, when excited oxygen species (Ozone) have been introduced onto cleaved GaAs (110), up to three different As oxides have been observed. In the experiments described above, only one type of As oxide (As_2O_3) is assumed to present on the surface and therefore fitted to the spectra.
It should be noted that the value of the peak areas quoted in table IV for Ga, As and their oxides cannot be compared directly, since during data acquisition, the strength of the signal may vary from sample to sample depending on the many parameters, for example, sample alignment , smoothness of the surface, surface contamination, the aperture of the detector. However, the value of the atomic fraction ratios calculated in table V is likely to result in a better picture of the actual effect occuring on the surface, since for an individual sample, the above mentioned parameters should remain the same and so effectively cancel out. It is worth mentioning that some workers normalize their results for photoionisation cross sections and electron escape depths using values and equations given by Scofield, and Seah and Dench respectively[10,11].
The values of the ratios $N_{Ga_2O_3}/N_{Ga}$, $N_{As_2O_3}/N_{As}$, and N_{As}/N_{Ga} were checked using the latter method and were found to agree within 3% with the values obtained using the sensitivity factor.

5.6.3. Spectra of CH_4/H_2 etched GaAs samples

The quality of the spectra recorded by automatic repetitive scanning is determined by the vacuum conditions which govern the maximum scanning time. If a coverage change of at most 1% is permissible during measurement even under the worst conditions (sticking coefficient =1), then for an undisturbed measuring time of one hour , ideally, a residual pressure of $1\text{-}2x10^{-11}$ Torr is necessary. If the background pressure is too high for long scanning times, carbon may build-up from weakly absorbed CO in the residual gas[12]. Carbon may also be deposited during the etching process since some of the etch gases contain carbon, CH_4/H_2.

It can be seen in Fig. 5.4.a that the As 3*d* peak for the control and sample 1 (dc bias = 1000V) appears at 41.30eV. However, the peak for sample 1 is broader and the oxide peak less intense. The As 2*p* spectrum of sample 1 Fig.5.4.b shows an increase in the As signal and a decrease in the oxide signal. For sample 2 (dc bias = 1000V, annealed) the As 3*d* peak is shifted to 41.50eV and the oxide peak is reduced. The As 2*p* spectrum for this sample shows a decrease in the As peak. Sample 3 (dc bias = 70V) represents an interesting situation in which the etching was dominantly chemical i.e. by chemisorption of excited species (very low energy ion bombardment is involved). The As 3*d* peak present at 41.40eV and there was no detectable oxide. The As 2*p* spectrum also shows a large reduction in the oxide peak.

The Ga 3*d* peak of the control sample, Fig.5.4.c occurs at 19.31eV and it is asymmetric from the high energy side (Ga_2O_3 is present). The Ga 3*d* spectrum of sample 2 (dc bias = 1000V) exhibited a chemical shift to 19.27eV and broader peak. The Ga 2*p* spectrum when compared with the control sample, shows a reduction in the Ga signal, Fig. 5.4.d. when annealed (sample 3) remarkable changes occur. The Ga 3*d* peak is decreased in intensity, shifted to 19.50eV and accompanied by a large oxide peak at 20.93eV. The Ga 2*p* signal on the other hand, is greatly reduced.

For sample 3 (dc bias = 70V) the Ga 3*d* peak is reduced and a large oxide peak is present at 19.50eV. A large oxide peak is also present in the Ga 2*p* spectrum of this sample.

From the observation made above and using the ratios in table V and Fig. 5.4. a, b, c, d, one can deduce the following:

When GaAs is etched using CH_4/H_2 plasma at dc bias=1000V, the As increases within the top 10Å of the surface and the As_2O_3 reduces throughout the top 30Å. On the other hand, the Ga detected within the top 10Å of the surface decreases while the Ga_2O_3 increases within the top 30Å of the surface. Spicer et al[6] have studied the kinetic of oxygen sorption on GaAs surface and proposed the following mechanism: "When GaAs surface is exposed to oxygen, Ga_2O_3 and As_2O_3 may form and since As_2O_3 is volatile, it probably evaporates

from the surface leaving a deficit of As. Since the heat of formation of Ga_2O_3 is higher than that for As_2O_3, the Ga_2O_3 probably "steals" oxygen from the As oxides, leaving metallic As". It is suspected that this reaction takes place immediately following the etch process and during handling when the sample is exposed to air. As the Ga 'takes-up' oxygen from the arsenic oxide to form gallium oxide, it meanwhile reduces the arsenic oxide to 'metallic arsenic'. The changes in the intensity of the As 3*d* peak was accompanied by a blue shift of 0.2eV. Interestingly, these phenomena have been related to the presence of metallic As on the surface[1] and have been observed in native oxide growth for practical devices[6]. This mechanism may also explain the behaviour the oxide and metallic arsenic formation in the present work. Anodic oxidation experiments of GaAs[12] have also shown that arsenic oxides are unstable in the presence of GaAs. In particular, arsenic oxide decomposes and metallic 'solid' arsenic forms at the oxide-GaAs interface from the reaction

$$2GaAs + As_2O_3 \Longleftrightarrow Ga_2O_3 + 4As \qquad (5.11)$$

Wang and Holloway[13] have shown that upon sputtering of GaAs using Ar in the energy range between 1 to 5keV, As depletion occurs but not in a uniform manner. At low energy (~1keV) As is depleted all the way to the outer layer, while at higher energies (3 and 5keV), As appears to be stoichiometric or in excess at the outer layer but depleted deeper in the substrate. The depth of depletion appers to correlate with the range of ions (5 to >30Å), therefore, it become larger at larger ion energies. Over this depth, the GaAs is expected to be amorphous and the XPS data show that excess concentration of Ga or As appears to be accommodated by elemental bonding states. This implies that when As is depleted, As vacancies will exist in the damaged layer. Chiang and Pearson[14] have reported that As vacancies have a donor character. Therefore, the observation of As depletion by preferential sputtering is consistent with Wang and Holloway's earlier postulate based on electrical properties of sputter creation of donor-like damage layer at the metal/ semiconductor interface. Obviously, defects other than As vacancies will be created, however most of these other defects are deep in the forbidden band and may be acceptors in n-GaAs.

More recently, Valeri and Lolli[15] have reported on Ar sputtering of GaAs at ion energies ranging from 0.5 to 5KeV. They concluded that upon sputtering, the surface layer of GaAs become As depleted. The depletion becomes more severe and extends to a larger depth at increasing the ion energy. They also reported that the outer atomic layer is richer in As than the subsurface region over the whole range of the ion energy used.

They attributed their results to As radiation-enhanced Gibbsian segregation i.e. concentration changes in the surface with respect to the bulk to minimize surface free energy. This is usually a thermally activated process. However, in the presence of large density of ion-induced point defects, the diffusion coefficients are modified and

desegregation often occurs at room temperature[16]. It should be mentioned that other mechanisms, for example, defect-related As segregation from the bulk of GaAs towards the surface has been reported in the literature for low energy Ar sputtered GaAs at temperature range of 294-600 K[17].

The red chemical shift of the Ga 3*d* peak of sample 1 may be due to the ion bombardment effect occuring during etching and has been observed in Ar sputtered GaAs[1]. The observed broadening of the Ga peak only (not the As peak) may be an indicative of a second order effects taking place on the Ga site due to chemisorption at the As site, as suggested by Chye et al[18]. It has been later confirmed, theoretically, that the oxygen will chemisorb on an As site and not Ga site[19].

Annealing the sample after etching has resulted in a remarkable increase in the Ga_2O_3 /Ga fraction ratio in comparison with the unannealed sample, due to the formation of excess Ga_2O_3 within the top 30Å. The As_2O_3 /As ratio, on the other hand, has decreased due to the reduction in As_2O_3. It can be observed also that the As/Ga fraction ratio and the As atomic fraction percentage have both increased. Spicer's mechanism mentioned previously, may be applied to these observations.

For sample 3 (dc bias=70V) i.e. very low energy ion bombardment is involved, the amount of As_2O_3 formed is the lowest among the samples etched in CH_4/H_2 and examined in this work. The As_2O_3 /As ratio is also reduced to less than half the value for sample 1. On the other hand, the Ga_2O_3 /Ga ratio is increased to more than double the value for the control sample, mainly due to an increase in the Ga_2O_3. It is noteworthy that the As/Ga ratio is the closest to unity among the etched samples. This may imply that ion bombardment during RIE could enhance preferential etching, presumably of As.

5.6.4. Spectra of $SiCl_4$ etched GaAs samples

The As 3*d* peak for the control sample, sample 4, 5 and 6 (dc bias=380, 290 and 240V respectively), Fig.5.5a were very similar to that of the control sample, all appearing at 41.30eV. However, the spectrum of the control sample shows slightly more As_2O_3. The As 2*p* spectrum for sample 4, 5 and 6 show an As peak similar to that for the control sample, but, the As_2O_3 peak decreases progressively as the dc bias increases. Sample 7 (dc bias=0V) displayed different behaviour. The As 3*d* peak has decreased markedly and shifted to 41.35eV, and a large As_2O_3 peak appeared in both the 3*d* and 2*p* spectra.

The Ga 3*d* peak of the control sample and sample 6 (dc bias=240V), Fig.5.5.a both occur at 19.35eV however, for sample 5 (dc bias=290V) the Ga peak is shifted to 19.25eV. Red chemical shifts in the Ga 3*d* peak have been reported for sputtered GaAs[1]. All the samples mentioned above have similar Ga_2O_3 peak (a shoulder on the high energy side of the Ga peak). However, for the Ga 3*d* peak of sample 4 (dc bias=240V), the Ga peak is shifted to 19.45eV. Sample 7 (dc bias=0V) showed a Ga_2O_3 shoulder larger than that for the above

samples.

It can be seen that the Ga 2*p* spectrum, Fig.5.5.b for the control sample shows more Ga than the spectra of samples 5 and 6. For sample 7, however the Ga peak is dramatically reduced and relatively large Ga_2O_3 peak is observed in both the 3*d* and 2*p* spectra.

An interesting observation should be made concerning the detection of chlorine on surfaces etched in $SiCl_4$. Among the samples etched in $SiCl_4$, Cl 2*p* signal has been detected at ~199eV in the spectrum of sample 7 only (dc bias=0V) as can be seen clearly in Fig. 5.8. The figure also show that there is a trace of a peak at ~208eV but can not be identified at present.

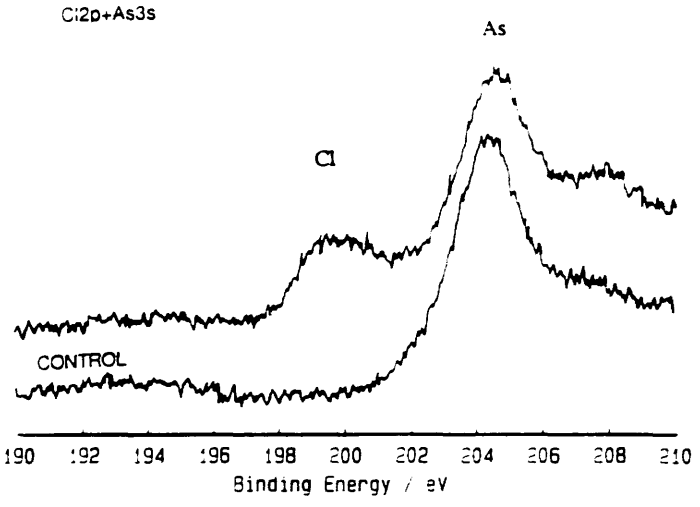

Figure 5.8: XPS spectra showing the presence of chlorine on GaAs surface etched in $SiCl_4$ at 0V dc bias.

From the observations made above one can conclude the following:

When a GaAs sample is etched in $SiCl_4$ at dc bias=240V, 'metallic' As is detected within the top 10Å of the surface, and less As_2O_3 is formed than for the control sample at 10Å and at deeper layers, 30Å. when the dc bias (energy of bombarding ions) is increased to for example, 290 or 340V, less As_2O_3 is formed in the top 10Å of the surface. however, more Ga_2O_3 is formed within the top 30Å of the surface. This may be explained using the same mechanism suggested earlier in section 5.6.3.

Sample7, etched at dc bias=0V, represents an interesting case in which the etching was dominantly chemical. Both the Ga_2O_3 and As_2O_3 are formed and extend to a depth greater than 30Å from the surface with distinctive reduction in the 'metallic' Ga and As. The fact that Cl is detected on the surface of this sample may indicate the presence of chlorinated compounds adsorbed 'deposited' on the surface. It also suggests that the ion bombardment enhances the desorption rate of these compounds.

The above analysis sheds light on the importance of the ion bombardment that accompanies the reactive ion etching process. It clearly shows that not only the physical structure of the semiconductor crystal will be affected, but also the surface stoichiometry and dynamical processes such as segregation and diffusion.

Both the mechanism suggested by Spicer et al on the kinetics of oxide formation and the observations by Valeri et al on As segregation upon sputtering may be applicable in the case of reactive ion etching of GaAs in CH_4/H_2 and $SiCl_4$.

5.7. References

1. 'Practical Surface Analysis By Auger and X-Ray Photoelectron Spectroscopy'. ed. D. Briggs, and M. P. Seah, J. Wiley & sons (1983).
2. 'Handbook of X-Ray Photoelectron spectroscopy', ed. C. D. Wagner, W. M. Riggs, L. E. Davis, J. F. Moulder, and G. E. Muilenberg , Perkin-Elmar Corporation (1978).
3. R. Cheung, S. Thoms, I. McIntyre, C. D. W. Wilkinson, and S. P. Beaumont, J. Vac. Sci. Technol., **B6**, (6), 1911 (1988).
4. H. Gant, and W. Monch, Surface Science, **105**, 217 (1981).
5. B. J. Flinn, and N. S. McIntyre, Surf. interface anal., **15**, 19 (1990).
6. W. E. Spicer, P. W. Chye, C. M. Garner, I. Lindau, and P. Pianetta, Surface Science, **86**, 763 (1979).
7. C. J. Powell, and M. P. Seah, J. Vac. Sci. Technol., **A8**, 735 (1990).
8. Private communication with Dr.R Cheung.
9. 'Characterisation of Solid Surfaces', ed. P. F. Kane, and G. B. Larrabee, Plenum Press, pp313 (1974)
10. J. H. Scofield, J. Electron Spectroscopy and Related phenomena, **8**, 129 (1976).
11. M. P. Seah, and W. A. Dench, Surface and Interface Analysis, **1**, 2 (1979).; 'Photoemission and the electronic properties of surfacs', ed. B. Feuerbacher, B. Fitton, and R. F. Willis, J. Wiley & sons, pp385 (1978).
12. G. P. Schwartz, B. Schwartz, D. DiStefano, G. J. Gualtieri, and J. E. Griffiths, Appl. Phys. Lett., **34**, 205 (1979).
13. Y.-X. Wang, and P. H. Holloway, J. Vac. Sci. Technol., **B2**, 613 (1984).
14. S. Y. Chiang, and G. L. Pearson, J. Appl. Phys, **46**, 1786 (1975).
15. S. Valeri, and M. Lolli, Surf. Interface Anal., **16**, 59 (1990).
16. R. Kelly, Surf. Interface Anal, **7**, 1 (1985).
17. K. G. Orrman-Rossiter, A. H. Al-Bayati, and D. G. Armour, Surface Science, **225**, 341 (1990).

18. P. W. Chye, P. Pianetta, I. Lindau, and W. E. Spicer, J. Vac. Sci. Technol., 1- (1977).
19. E. J. Mele, and J. D. Joannopoulos, Phys. Rev. Letters, **40**, 361 (1978)

Chapter 6: Characterisation of GaAs surfaces and sidewalls etched using Electron Cyclotron Resonance (ECR) etcher

6.1. Introduction

The interest in Reactive Ion Etching using Electron Cyclotron Resonance (ECR-RIE) has surged over the last few years due to its advantage over the conventional RIE etching systems[1-3]. The system offers two main benefits : 1. Higher ionization efficiency due to the nature of electron acceleration and motion, as described in chapter 2. 2. The ability to control the bombarding ion energy by the rf power to the electrode, independently from ionization efficiency of the gas which is controlled by the applied microwave signal and the magnetic field. Thus in principle it is possible to use low ion energies thereby minimizing the damage in the etched material, while maintaining an anisotropic profile using very low etch pressures (P< 1mtorr) to reduce collisions in the space above the sample. To examine the ECR etching induced effect, a process has been optimised using CCl_2F_2/He on an ECR etcher. This process was chosen to extend the investigations of etching induced effects initiated by R. Cheung in IBM, Yorktown. The strategy adopted was to optimise an etch process, to produce high aspect ratio structures while maintaining very low dc bias in the range 60-70V. The induced damage created by this process was assessed electrically using the TLM method for surfaces and narrow conducting wires for sidewalls and optically using plasmon - LO phonon coupled Raman scattering and by comparing the FWHM of the LO Phonon for bulk GaAs with other RIE processes.

6.2. Optimisation of CCl_2F_2/He etching process

The flow rates, etch pressure, dc bias (rf power) and the microwave power were verified against the etch rate and etch profile, whilst the CCl_2F_2/He ratio was kept at 1:1. Samples of GaAs were patterned using either photolithography or e-beam lithography. In the former, photoresist AZ1400-31 was used as a mask. In the later a metal mask, (50nm thick layer of both Al and NiCr) were examined as masks, but the NiCr was found to have better selectivity for etching at high microwave powers and therefore was used for this study.
The criteria for "good plasma" is taken to be bright, stable and uniform light, not filckering (i.e. variation in light intensity with time), a violet in colour and showing a conical shape.

On the other hand, "a poor plasma" has non uniform regions, flickers and has a columnar shape at the centre of the table producing hot spots resulting in Carbon deposition.
At high microwave powers (400-600W) and flow rates of 10/10 sccm of CCl_2F_2/He the etched surface was very rough and deposition was found on the surface and sidewalls of the etched structure. At a power of 200W however, no deposit was found, therefore the microwave power was fixed at 200W for the rest of the study. Since the low pressure Baratron is a sensitive device, it was necessary to set the Baratron to zero every working day, otherwise an error of ~0.08mtorr may result in the pressure reading. The flow rates of CCl_2F_2/He were varied between 3.1/3.1 sccm (the minimum flow rates possible on the mass flow controllers) and 20/20sccm to examine the relationship with the etch pressure, Fig 6.1. This relationship was used to insure that the Baratron and the pumps are in good working order. For various pressures, Fig. 6.2, the dc bias was plotted as a function of the applied rf power. It was found that the dc bias varied by a maximum of 100V when the pressure changed from 0.18 to 1.27mtorr.

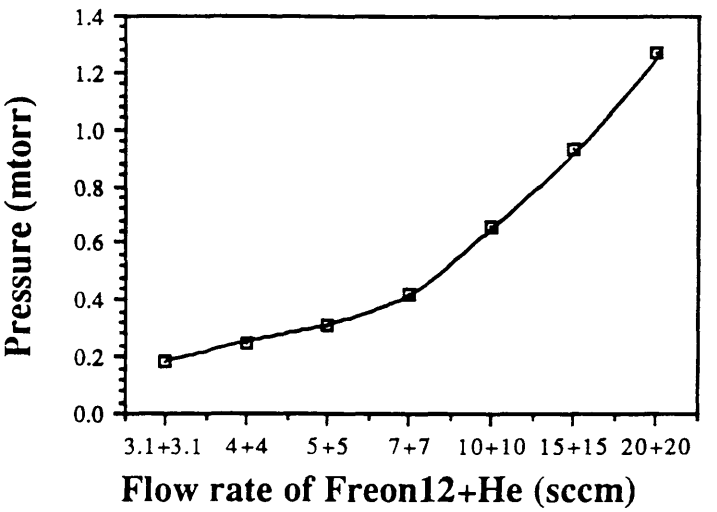

Figure 6.1: The gas pressure as a function of the flow rates of CCl_2F_2/He in an ECR etcher.

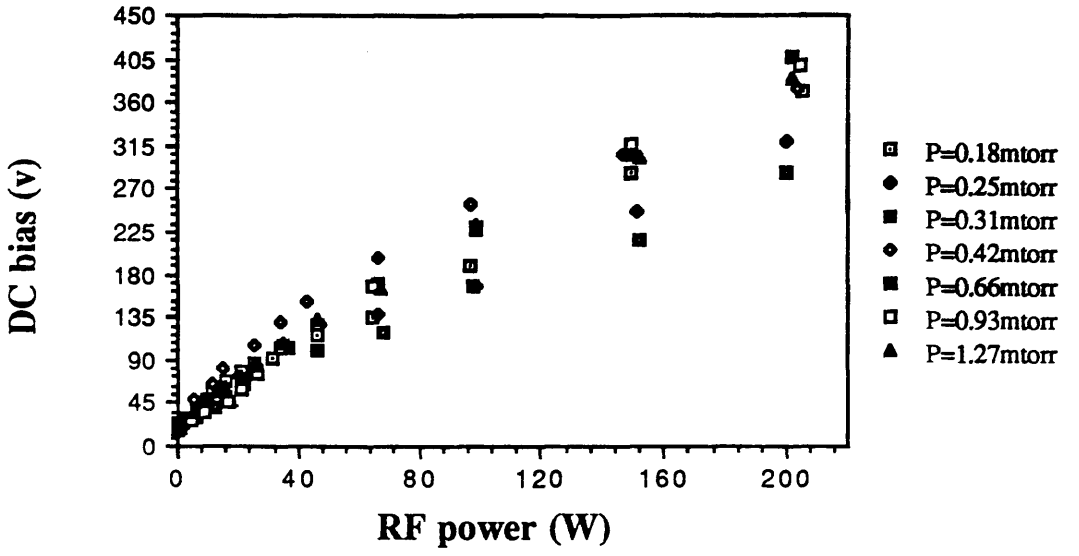

Figure 6.2: The dc bias voltage as a function of the rf power applied in CCl_2F_2/He ECR etching at various etch pressures.

However unlike the case of RIE, there was not a clear relationship between the dc bias voltage and the etch pressure. To investigate the etch rate and the verticality of etched profiles a set of GaAs samples were etched at various etch pressures from 0.18 to 0.7mtorr. The etch rate was found to peak at around 47nm min^{-1} for a pressure of ~0.5mtorr, Fig 6.3.

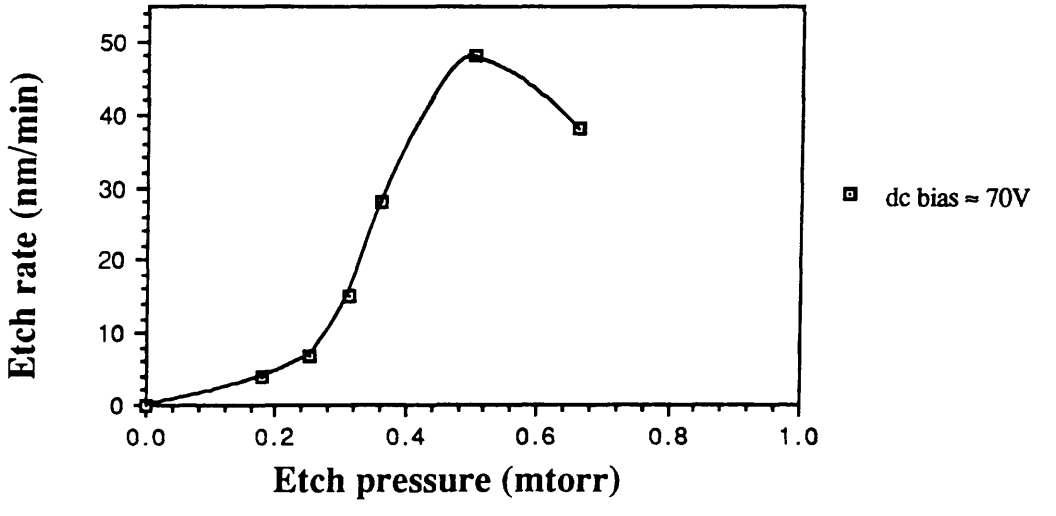

Figure 6.3: The etch rate of GaAs as a function of the etch pressure for CCl_2F_2/He ECR etching. The applied microwave power was 200W and the dc bias voltage was fixed to 70V.

From SEM micrographs,the sidewall angle off the normal was estimated, for samples etched at various pressures with a dc bias ranging between 63-83V, Fig.6.4.
The most vertical profile was found to be 6° off the normal corresponding to a flow ratio of 4/4 sccm of CCl_2F_2/He a pressure of 0.3 mtorr and a dc bias of 70V. The etch rate under these conditions was ~ 8nm min^{-1} and these conditions were considered the most suitable for etching nanostructures and were used throughout the rest of this study. At a constant etch pressure of ~0.3mtorr, the etch rate increases with the dc bias as shown in Fig.6.5.

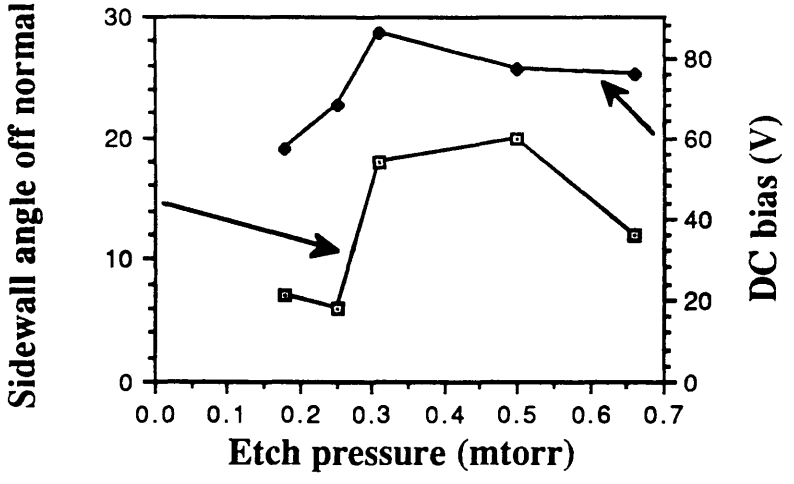

Figure 6.4: Sidewall angle off the normal as a function of the etch pressure for GaAs etched in CCl_2F_2/He ECR. the pressure was varied by varying the flow rate of Freon 12 and He keeping the ratio at 1:1.

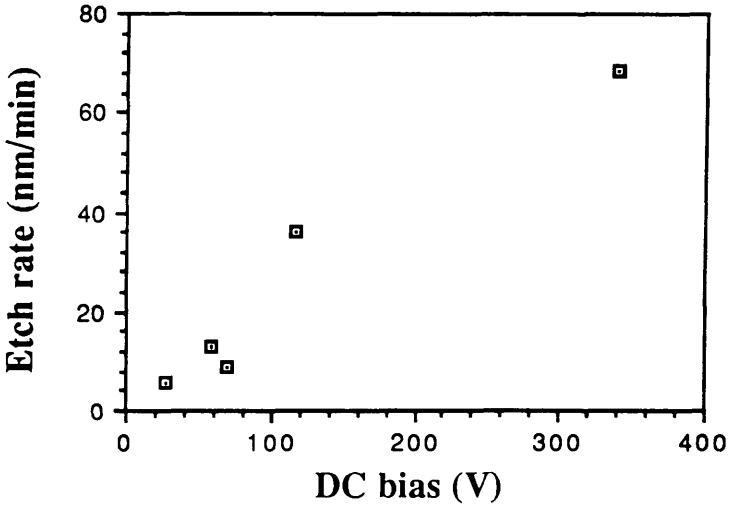

Figure 6.5: The etch rate of GaAs in CCl_2F_2/He ECR-RIE as a function of the dc bias voltage at an etch pressure of 0.3mtorr.

6.3. Characterisation of ECR-RIE surface damage using the TLM method

TLM samples were prepared as described in chapter 3 using an epitaxial layer 140nm thick Si doped to ~ $2.5x10^{18}$ cm^{-3}. A set of wet etched samples were prepared and used as a control. Samples were etched for various times (depths) using CCl_2F_2/He at flow rates of 4/4sccm, pressure in the range 0.30 - 0.32mtorr and dc bias of 70V. The etch depth was measured using a Tallystep and the percentage remaining mobility measured at room temperature and percentage remaining conductivity were calculated. It was found that the mobility remained constant with the etch depth within 10% (10% is the uncertainty in measuring the mobility across the untreated wafer), Fig 6.6. On the other hand, the percentage remaining conductivity curve, Fig 6.7, showed the saturation kink at ~ 12nm and it cutsoff at a depth of ~ 12nm shorter that the wet etched samples, i.e. a surface damage depth of ~ 12nm.

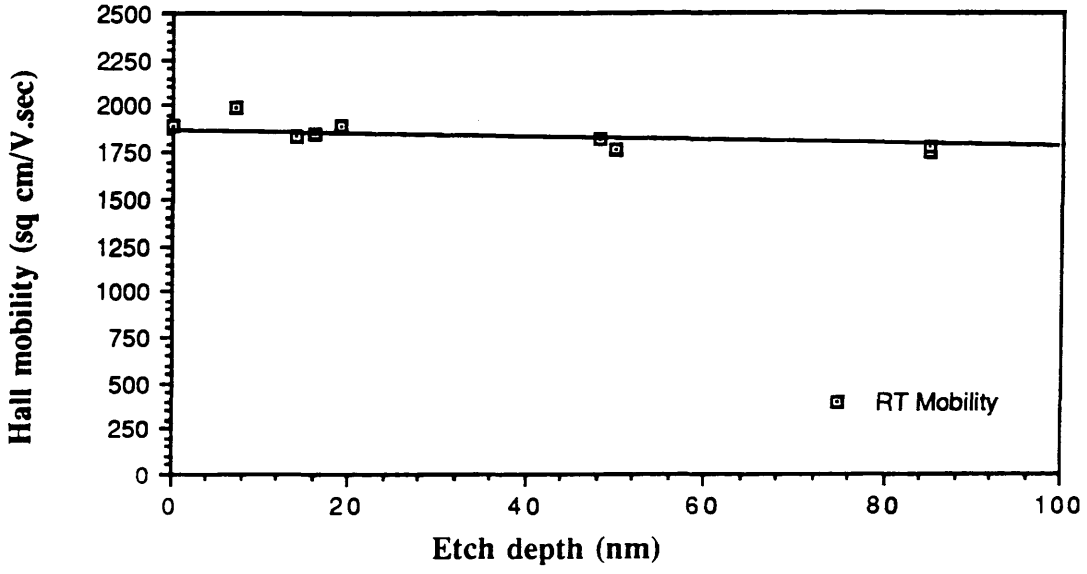

Figure 6.6: % Remaining Hall mobility as a function of the etch depths of GaAs measured at room temperature. The etch gas was 1:1 parts of CCl_2F_2/He at a pressure of 0.32mtorr and with a dc bias 70V. The applied microwave power was 200W.

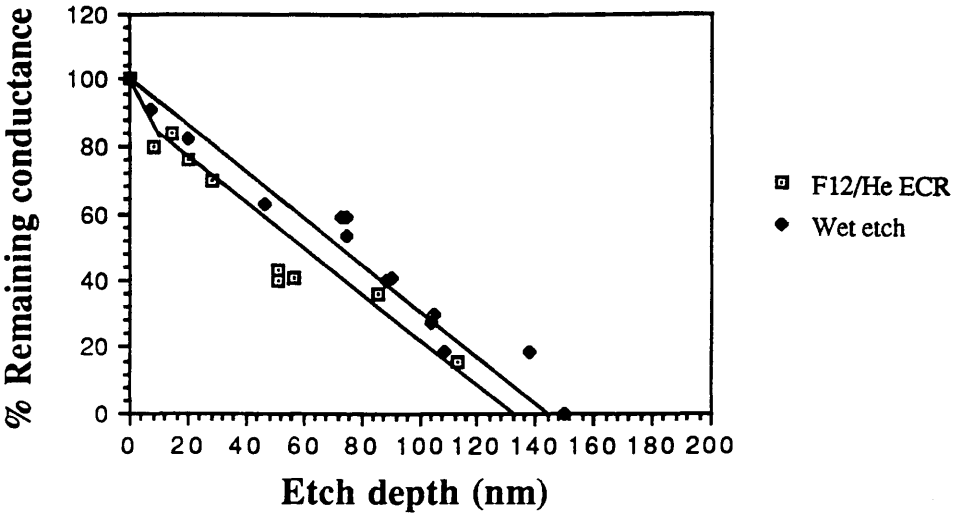

Figure 6.7: % Remaining conductance as a function of the etch depth of GaAs. The etch gas was 1:1 parts of CCl_2F_2/He, the pressure was 0.32mtorr, the dc bias was 70V and the applied microwave power was 200W.

6.4. Characterisation of ECR-RIE Sidewall damage using n^+ GaAs wires

To examine the effects of ECR etching using CCl_2F_2/He on the sidewalls of various nanostructures, thin n^+ GaAs wires were etched in a joint experiment with M. Rahman, at Glasgow University. The principle of this technique[4] relies on measuring the depletion depth of the sidewall. The damage depth is defined here as the extra depletion depth introduced as a result of the etching process. The conductance measurements (G) of wires of different widths should satisfy the relation[5]

$$G = 1 / R_S L (W - 2X_d)$$

where L and W are the wire length and width, R_S is the sheet resistance of the epitaxial layer and X_d is the sidewall depletion depth. When the measured wire conductance is plotted as a function of the wire width, a straight line relationship is obtained. If this line is extrapolated to zero conductance, the cut off width can be obtained which is equal to twice the depletion layer depth, (one from each side of the wire).

For an undamaged wire, the cut off width X_d should be equal to twice the depletion layer depth of the virgin material as calculated using 1 - dimensional Poisson equation[6]. If the

sidewalls of the wire are damaged, the cut off width will increase to X_1 and hence the difference between the cut off width of the etched wire and the cut off width of the undamaged wire, will equal twice the damage depth, i.e $X_1 - X_d = 2d_d$,where d_d is the sidewall damage depth.

An epitaxial layer 50nm thick; Si doped to $7x10^{18}$ cm^{-3} was grown by MBE on a semi-insulating substrate. The depletion depth of this epilayer is 12nm. The wires, schematically shown in Fig 6.8, were prepared as follows : -

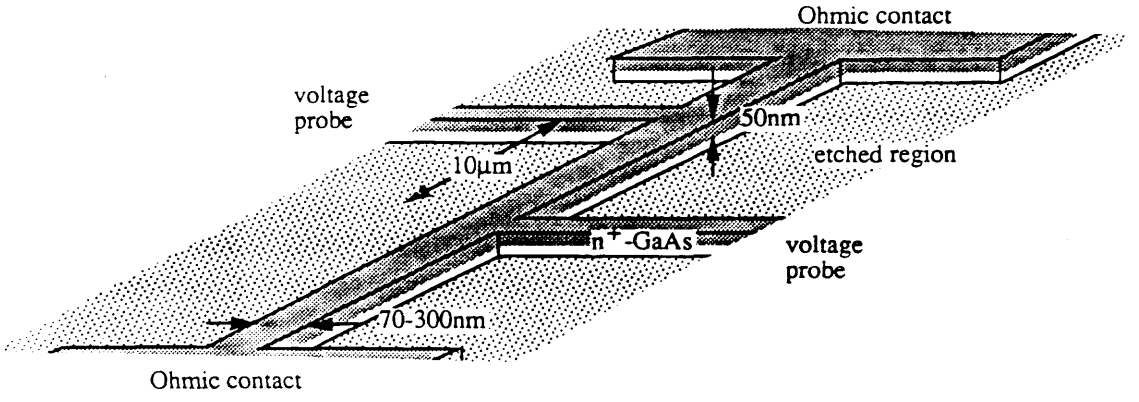

Figure 6.8: Schematic diagram showing the wire configuration used in this study.

1. The GaAs chip ($5x5mm^2$) was cleaned using Trichloroethane, Acetone and Methanol for 5 minutes each using ultrasonic agitation. The sample was then rinsed using Isopropyl alcohol (IPA) then blown dry.
2. E-beam resist (15% PMMA (BDH) in chlorobenzene) was spun at 5Krpm for 60 sec, the sample was then baked at 180°C overnight.
3. 6 sets of alignment marks were exposed on the chip, patterning at magnification of 320 and spot size of 0.125μm using Philips PEM500 converted microscope. The sample was developed in 1:1 solution of IPA:MIBK for about 50sec at 23°C.
4. After development, low resistivity Ohmic contacts (An/Ni/Ge/Au) were evaporated as described in section 3.3.
5. The e-beam resist was then removed by lift-off in Acetone.
6. E-beam resist (15% PMMA (BDH) in chlorobenzene) was spun at 5Krpm for 60sec, the sample was then baked at 180°C overnight.
7. Bonding pads pattern were aligned and exposed at magnification of 160x. This was followed by development in 1:1 solution of IPA:MIBK for 50sec at 23°C.

8. Ohmic contacts were evaporated as in step 4 and the remaining e-beam resist was removed by lift off as described in step 5 and the contacts were alloyed at 350°C for 1 minute.
9. A bi-layer e-beam resist (4% PMMA (BDH) in o-xylene / 4% PMMA (Elvacite) in o-xylene) was spun next at 5Krpm and baked for 1 hour and overnight respectively.
10. Wires pattern was aligned and exposed at a magnification of 1250x and spot size of 16nm. The sample was developed in 1:2.5 solution of IPA:MIBK for 50sec at 23°C.
11. Ni (~50nm thick) was evaporated to act as a mask for the patterned wires. The e-beam resist was removed by lift off in Acetone.
12. The patterns were inspected by SEM a final check, Fig. 6.9, each of the 6 wire sets consisted of 4 wires 10μm long with widths between 120-250nm.

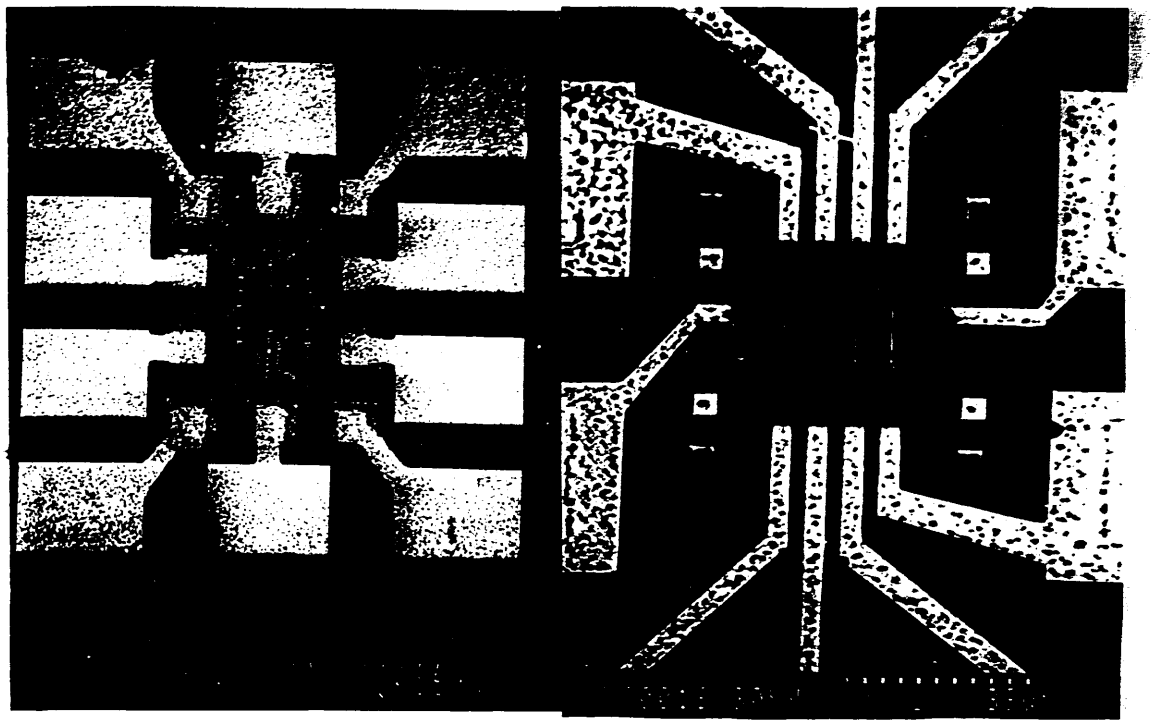

Figure 6.9: Micrographs showing an etched set of wires at different magnifications.

The chip was etched at a pressure of 0.35mtorr and a dc bias of 70V for 10min, resulting in a final etch depth of 80nm.
The conductance of the 10μm long wires were measured by a 4-terminal measurement system using a semiconductor parameter analyser model HP4145B. The width of the wires

were measured, using a Hitachi S900 SEM, at a direction normal to the sample. It should be mentioned that each value of the wire width is an average of 11 individual width measurements down the length of the wire. This procedure was followed to minimize the error in measuring the wire width due to the sloping sidewalls of the wires and the lithography resolution (± 10nm). The conductance of the wires was plotted as a function of the wire width and presented in Fig. 6.10. Conductance data produced for wires etched using $SiCl_4$ at dc bias of ~240V (prepared by M. Rahman at Glasgow University) are also plotted for comparison.

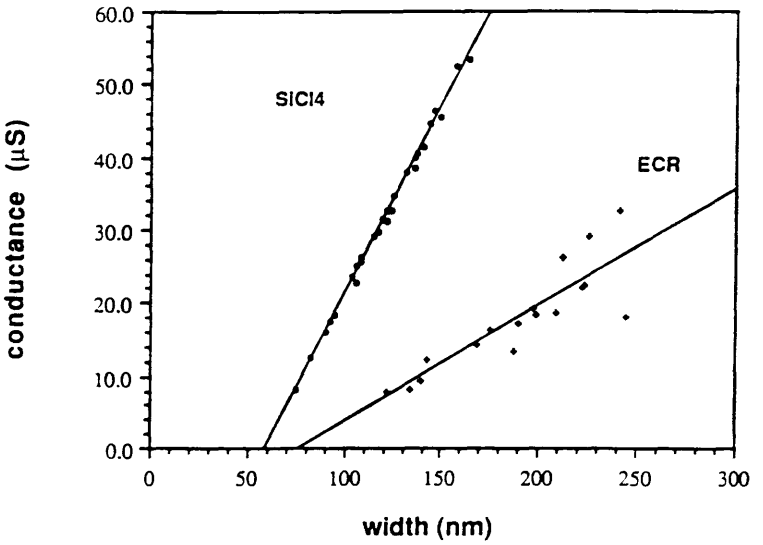

Figure 6.10: The conductance as a function of the wire width for wires etched in CCl_2F_2/He ECR-RIE and $SiCl_4$ RIE. the cut off widths are 75nm and 58nm respectively.

The conductance data were fitted to a straight line which was extrapolated to the zero conductance to obtain the cut off width X_1 which was ~75nm. Knowing that the depletion depth for the starting material was ~12nm, i.e. X_d = 24nm, this gives a ' $2d_d$' value of ~51nm and a sidewall damage depth of ~25nm. Compared to a sidewall damage depth of ~17nm for samples etched using $SiCl_4$.

6.5. Characterisation of surface damage using plasman- LO phonon coupled Raman scattering.

The n^+ GaAs samples prepared and used for the TLM measurements, described in § 6.3., were examined using the technique and procedure described in § 3.8. The calculated depletion depth were plotted as a function of the measured etch depth. The data was compared with depletion depths of wet etched and RIE samples using CH_4/H_2 as shown in Fig. 6.11. An initial increase in the width of the depletion layer can be seen in the figure as the etch depth increases. This was followed by a saturation effect at which the depletion depth remains almost constant at ~30nm. The saturation occurs at an etch depth of ~25nm. Knowing that the depletion layer width of the starting material was ~18nm (see the wet etching curve), surface damage depth is estimated to be ~12nm, in a good agreement with the depth estimated from the TLM method, section 6.3. In comparison, the damage depth estimated for samples etched in CH_4/H_2 is ~50nm at dc bias of 930±30V.

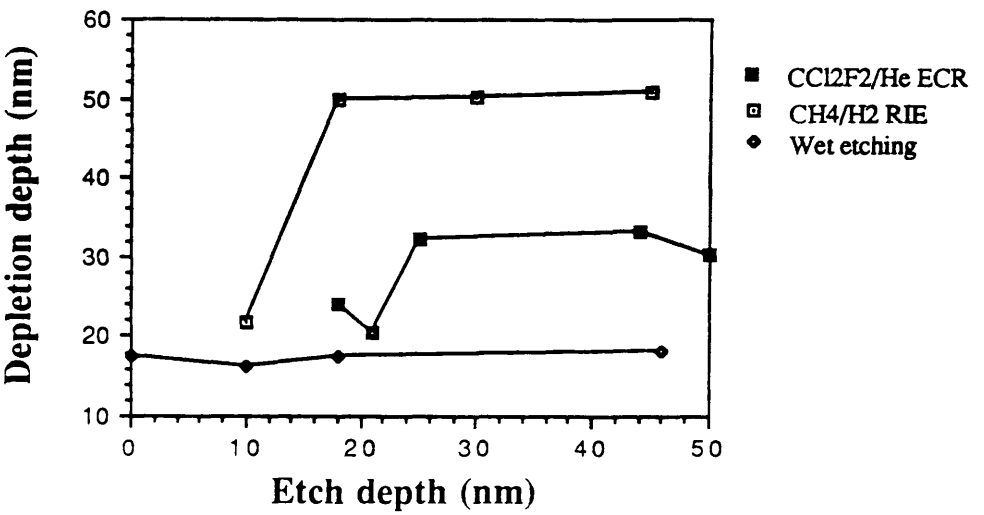

Figure 6.11: The depletion depth as a function of the etch depth for GaAs samples etched using CCl_2F_2/He ECR-RIE and wet etching, CH_4/H_2 RIE curve is plotted for comparison.

6.6. The effect of various etching processes (including ECR-RIE) on bulk GaAs as examined using the FWHM of the Raman scattered LO phonon

In this preliminary study, substrate quality samples of bulk GaAs silicon doped to 0.7-1.5x$10^{18}cm^{-3}$, was variously etched as listed in table I and were examined using Raman

scattering. The Raman measurements were performed by Dr. M. Watt.

Sample	etch	etch depth/ comments
1	Control	not etched
2	wet etch in 1000:20:8 solution of H_2O:NH_3:H_2O_2	>200nm
3	CCl_2F_2/He; ECR	200W microwave power
4	CCl_2F_2/He; ECR	400W microwave power
5	$SiCl_4$ RIE	200nm
6	CH_4/H_2 RIE	200nm
7	CH_4/H_2 RIE	annealed at 380°C for 1sec

Table I: Etching conditions for samples examined in this study.

In the Raman spectrum of the control (unetched) sample, Fig. 6.12. It can be seen that instead of a single sharp peak of the LO phonon at 292cm^{-1}, which is expected for (100) GaAs in the back scattering geometry, there is an additional shoulder extending to the TO phonon energy at 269cm^{-1}, but which is not sufficiently well defined to be regarded as the TO phonon. This shoulder was investigated and found to be stronger when longer wavelength light was used i.e. as the penetration depth increased. Clearly, this is not an effect due to surface phenomenon. More probably, it relates to the crystalline imperfections within the bulk material. When the experimental geometry was changed from near-back scattering to near-right angle scattering, a move designed to enhance any TO phonon contribution, a well defined TO phonon could be observed superimposed on the shoulder. Manipulation of the spectra to deconvolute the LO and the shoulder contributions yielded a maximum at 280cm^{-1} for the peak producing the shoulder.

The spectra were deconvoluted into an LO phonon and a shoulder peak in order to study the differences in the LO linewidth produced by the etching processes. This introduced an error into the values obtained, in addition to this, the spectra was recorded using a CCD multichannel acquisition detector and therefore has a laser scattering background which had to be subtracted from the spectra thereby introducing even more uncertainty. The values of the FWHM recorded for various etching processes are presented in table II.

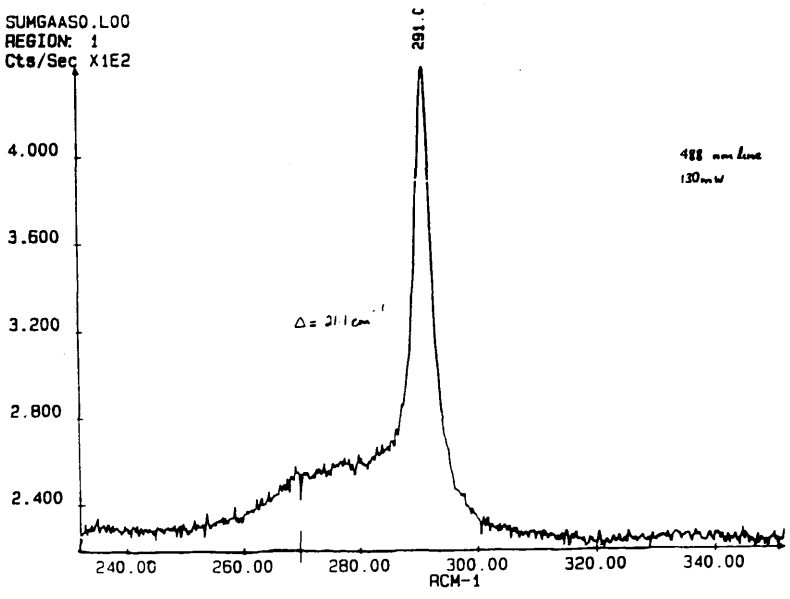

Figure 6.12: Raman spectrum, recorded in near backscattering geometry, of unetched bulk (100) GaAs showing the LO phonon at 291cm^{-1} and a shoulder at 269.9cm^{-1} coincideswith the TO phonon.

Sample	dc bias (V)	FWHM (cm^{-1})
1	--	3.17
2	--	3.17
2*	--	3.12
3	55	3.3
4	30	3.3
5 (CCD)	240	3.24
5 (PMT)	240	3.4
6	900	4.18
7	900	3.71

Table II: The FWHM of the LO phonon for bulk GaAs samples etched as in table I. The wet etching was repeated for sample 2*. CCD and PMT refer to the multichannel and single channel detectors respectively.

It can be seen that the FWHM for samples etched in CCl_2F_2/He using the ECR etcher at microwave powers of 200 and 400W is identical for dc bias in the range of 30 to 55V.

Table II also show that the FWHM for samples etched in CCl_2F_2/He using the ECR-RIE and $SiCl_4$ RIE are comparable.

It was found that the left half width was consistently bigger than the right half width by about $0.2cm^{-1}$, however in the case of CH_4/H_2 etched sample, the LHHW = $2.3cm^{-1}$ and the RHHW = $1.9cm^{-1}$. It is expected that peak broadening due to any crystalline disorder would be asymmetric with the increase on the low energy side of the peak. This appears to be the case for the unannealed CH_4/H_2 etched sample. As the experimental resolution was $1cm^{-1}$, the values above can only be taken as an indication of a trend.

6.7. Discussion and conclusions

The main advantages that ECR etchers have over the conventional RIE etchers are the high ionisation efficiency (1-10% of the etching gas is ionised) and a larger degree of freedom in controlling etching parameters such as etch rate.

Chang et al[7] have measured the electron density and temperature for Ar ECR plasma using Langmuir probe. He measured a density of $\sim 3.5 \times 10^{10} cm^{-3}$ and a temperature of ~7eV for etch pressures of 0.3mtorr. He also calculated an electron-neutral collision frequency of 17MHz for a pressure of 0.1mtorr and an ECR layer thickness of 2-3mm. Tobinaga[8] suggested that if the pressure was $\leq$ 0.2mtorr in an ECR etcher, the ions generated in the plasma chamber will be able to pass through the space of the chamber and reach the sample surface without any collisions. In this case, the ion trajectory is ballastic becoming ion beam-like and therefore will fall on the sample surface at a near-right angle even at ion energies around 20-40eV, but the etch rate decreases significantly under these conditions. He showed that an aspect ratio of 10 was possible for etching polysilicon using Cl_2. Noh et al[9] have reported an increase in the ideality factor and a reduction in the barrier height, of Schottky barriers fabricated on ECR etched GaAs using Ar, as the microwave power increases. Pearton et al[10] have characterised surfaces of In-based III-V alloys etched in $CH_4/H_2/Ar$ using ECR etcher, as well as showing that the etch rate increases with increasing the microwave or the rf powers.

Hara et al[11] have correlated the displaced atom density in GaAs, measured using Rutherford BackScattering (RBS), during etching with SF_6. He concluded that the displaced atom density increases as the applied microwave power increases, for example, for an ion current density of $2mA.cm^{-2}$, the displaced atom density increased from 2.9 to $4.4 \times 10^{15} atom.cm^{-3}$ as the microwave power increased from 500 to 800W. Moreover Hara showed that the

displaced atom density was $3.2x10^{15}$atom.cm^{-3} for ECR etching, lower than the RIE case ($6.9x10^{15}$atom.cm^{-3}) for a constant ion current density.
The CCl_2F_2/He gas mixture was adopted as a trial etch gas for the ECR etcher after one of the earliest reports on using the ECR-RIE for semiconductor device fabrication by Cheung et al[12,13]. She found that the ideality factor of Schottky diodes fabricated on etched surfaces increases to 1.06 from 1.04 for the untreated surface However, the reverse leakage current, measured at -2V, has been found to increase from -48pA for an untreated surface to -850pA for surfaces etched using CCl_2F_2/He at a dc bias of 80V.

From the results presented in this chapter, it can be concluded that :
1. The surface and sidewall damage depths for samples etched using ECR etching in CCl_2F_2/He are comparable to corresponding depths for samples etched using RIE in $SiCl_4$ although the dc biases are 70V and 240V respectively. The relatively high damage depth produced by the ECR etching process is attributed to the presence of He in the etching gas mixture which would confirm the suggestion that light ions produces more damage, presented in chapter 3.

2. The sidewall damage depth is greater than the surface damage depth for both RIE in $SiCl_4$ and ECR-RIE in CCl_2F_2/He. This may be due to a higher defect creation rate at the sidewall. This would happen if, for example, in addition to the primary incident ion flux there was an even larger secondary flux due to ions ricocheting from the surface being etched.
Another interesting possibility is that the image potential between an ion and an etched sidewall is found to be an important effect in submicron etching at low ion energies[14]. Image potentials attract ions towards etched sidewalls resulting in ion-wall collision rates which increase with decreasing the ion energy. The fact that the gradient of the CCl_2F_2/He (ECR-RIE) conductance line in Fig. 6.10 is lower than the $SiCl_4$ line also indicates that for a fixed wire width, the $SiCl_4$ wires conduct better than the CCl_2F_2/He etched wires. This implies that the CCl_2F_2/He wires are more damaged.

3. There is a good agreement between the surface damage depths estimated by the TLM method and the plasmon-LO phonon Raman scattering.
In fabricating nanostructures, vertical sidewalls and very small damage depths are crucial requirements. From the results obtained in this study however, there appears to be a compromise between the two factors since extremely vertical sidewalls can not be obtained at low dc biases even at very low etch pressures (~0.3mtorr). Also "damage free" etching

was not obtained even at very low dc biases (70V) using CCl_2F_2/He. It is predicted that the elimination of the use of He or any light ions from the etching gas mixture should reduce the etch damage significantly to the extent that it may be regarded as insignificant.

As a result of the study presented in this chapter, some suggestions for future experiments are made.

It is important to investigate other etching chemistries such as $SiCl_4$ and CH_4/H_2 both of which have been used extensively in RIE etchers at Glasgow University. A fast etch or a selective etching process for GaAs/AlGaAs can perhaps be developed if Freon 12 is used only.

Etch rate and anisotropy should be investigated as a function of the position of the table i.e. the distance between the ECR layer and the sample. Of particular interest is the case at which the sample is immersed in the ECR layer since a high density of ionised species are generated and will impinge on the sample at normal incidence, due to the converging magnetic field. The effect of high intensity UV radiation on the crystal can also be addressed. In general, more work is needed to understand the effects and optimise the parameters of the ECR etcher.

6.8. References

1. J. Asmussen, J. Vac. Sci. Technol., **A 7**, 883 (1989).
2. K. Asakawa, and S. Sugata, J. Vac. Sci. Technol., **A 4**, 677 (1986).
3. R. Cheung, Y. H. Lee, K. Y. Lee, T. P. Smith III, D. P. Kern, S. P. Beaumont, and C. D. W. Wilkinson, J. Vac. Sci. Technol., J. Vac. Sci. Technol., **B 7**, 1462 (1989).
4. S. Thoms, I. McIntyer, S. P. Beaumont, M. Al-Mudares, R. Cheung, and C. D. W. Wilkinson, J. Vac. Sci. Technol., **B6**, 127 (1988).
5. M. Rahman, Ph.D. Thesis, University of Glasgow (1992).
6. A. Chandra, C. E. Wood, D. A. Woodard, and L. F. Eastman, Solid State Electronics, **22**, 986 (1986).
7. H. Y. Chang, S. K. Song, and Y. J. Kim, Physics Letters A, **149**, 159 (1990).
8. Y. Tobinaga, N. Hayashi, H. Araki, and S. Nakayama, J. Vac. Sci. Technol., **B6**, 272 (1988).
9. S. K. Noh, K. Ishibashi, Y. Aoyagi, and S. namba, J. Appl. Phys., **67**,. 2591 (1990).
10. S. J. Pearton, U. K. Chakrabarti, A. Katz, A. P. Perley, and W. S. Hobson, J. Vac. Sci. Technol., **B9**, 1421 (1991).

11. T. Hara, J. Hiyoshi, and H. Hamanaka, J. Appl. Phys., **67**, 2836 (1990).
12. R. Cheung, Y. H. Lee, C. M. Knoedler, Y. K. Lee, T. P. Smith III, and D. P. Kern, Appl. Phys. Lett., **54**, 2130 (1989).
13. R. Cheung, Y. H. Lee, K. Y. Lee, T. P. Smith, III, D. P. Kern, S. P. Beaumont, and C. D. W. Wilkinson, J. Vac. Sci. Technol., **B7**, 1462 (1989).
14. R. J. Davis, and S. Tiwari, Proceedings of LEOS 1991 Summer Topical Meeting on Microfabrication for Photonics and Optoelectronics, pp30, California USA August (1991).

Chapter 7: Development of reactive ion etching process for II-VI semiconductors (ZnTe, ZnSe, ZnSeS, CdTe, CdMnTe, ZnS and CdS)

7.1. Introduction

The recent advances in growing high purity II-VI semiconductors by MBE and MOCVD[1-4] have renewed interest in these technologically important compounds. Not only is there interest in growing homo-epitaxial layers with improved electrical performance, but also the potential of quantum well layers in these materials are being exploited. Devices such as blue and green semiconductor lasers, efficient solar cells, IR detectors and medical thermographs can be made using II-VI semiconductors.

The fabrication of optical and electronic devices, particularly those containing structures with low-dimensionality (quantum well lasers and quantum dot arrays) requires the use of high resolution pattern definition and transfer techniques. While electron beam lithography is capable of 10-20nm resolution[5], the transfer of this pattern into the underlying material requires a high resolution etching technique. Dry etching of II-VI compounds is a relatively unexplored area, and only the etching of ZnSe and ZnS using chlorine-based plasmas[6-8] has been reported extensively.

In this chapter, the development of a universal high resolution reactive ion etching process employing a methane/hydrogen mixture is described. This process has proved capable of producing nanostructures less than 50nm wide in a variety of II-VI semiconductors, e.g. ZnTe, ZnSe, CdTe, ZnS, CdS and the ternary compounds, e.g. CdMnTe and ZnSeS.

In order to assess the quality of the etching process, nanostructures were fabricated by electron beam lithography and the pattern transferred to the substrate using high resolution dry etching process.

A figure of merit "*the anisotropy factor (A)* "[9] was adopted to assess the quality of the etched structure. The anisotropy factor is expressed as

$$A = 1 - V_h / V_v$$

where V_h and V_v are the horizontal etch rate and the vertical etch rate respectively. Isotropic etching is presented by A = 0 and anisotropic etching by A = 1. The

anisotropy factor can be determined by estimating the vertical and horizontal etch depths, Fig. 7.1.

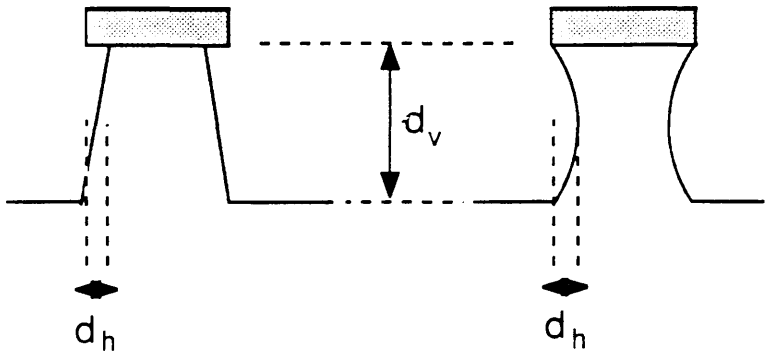

Figure 7.1: Schematic diagrams showing the vertical and horizontal etch depth d_v and d_h, respectively from which the anisotropy factor can be estimated.

7.2. Growth of ZnTe and ZnSe and sample preparation

The ZnTe layers used in this work were grown in Regensburg university by MOCVD under atmospheric pressure on (001) GaAs substrates. An Aixtron system equipped with a horizontal quartz reactor cell was used. The polished substrates were first cleaned in propanol, then etched in a solution of H_2SO_4: H_2O_2: H_2O in a ratio of 4: 1: 1. The substrates were then rinsed in deionised water, blow dried in N_2 and immediately introduced to the reactor cell where they were mounted on the graphite susceptor which is heated by IR radiation to the growth temperature of 350°C.
The precursors, diethylzinc (DEZn) and diiospropyltelluride (DiPTe), were kept at 17°C and transported through the reactor using hydrogen as a carrier gas with a flow rate of about 7l/min. The optimal partial pressure ratio of the reactants is two, and the flow rates under these conditions were 17mmol/min and 34mmol/min for DEZn and DiPTe respectively. The thickness of the layers ranging from 1 to 2 μm was determined by examining the interference pattern as described in reference 14.
The ZnSe layer, on the other hand was grown by low pressure metalorganic chemical vapour deposition at Thomson CSF[15]. The substrate, (100) GaAs, was misorientated by 2° off towards the (01$\bar{1}$). Diethylzinc (DEZn) and diethyselenium (DESe) were used as precursors to grow ZnSe at a rate of 100Å/min at growth temperature of 400°C

and pressure of 100mbar. Table I presents the thicknesses of the epitaxial.layers used and the source of the semiconductor.

For preliminary etching experiments, samples of the semiconductor were patterned using S1400-31 (Shipley) photoresist. The patterns were four series of curved ridges, covering 360°, designed especially to reveal any differential crystallographic etching effects.

Material	Thickness (μm)	Comments
(100) ZnTe	1-2	MOCVD on GaAs / Regensburg University
(100) ZnSe	0.53	MOCVD on GaAs / Thomson CSF
(100) ZnSSe	> 3	8-11% S, MOCVD on GaAs / UMIST
(111) CdTe	Bulk	Purchased from Eagle Picher
CdMnTe	1.98	12% Mn, MOCVD on CdTe / Hull University
ZnS	Bulk	Polycrystaline
CdS	Bulk	---

Table I: The thickness of the II-VI semiconductor epitaxial layers used in this study.

For optimisation of the etching process, patterns for nanostructures were used. The samples were coated with a bi-layer of PMMA and exposed using high-resolution electron beam lithography, as described in chapter 2. The mask for dry etching was a 50nm thick film of Titanium, deposited then patterned using lift-off. Alternatively, high resolution negative electron beam resist (HRN) was used as a mask. The etch conditions were optimised to achieve a smooth surface and vertical sidewall with no redeposition on the etched surfaces.

After etching, the samples were examined using a scanning electron microscope (SEM) and the etch depth was measured using a tally step.

7.3. Reactive ion etching of ZnTe in $SiCl_4$ and CHF_3

Samples of ZnTe were scribed and cleaned, using ultrasonic agitation, in trichloroethane, methanol, and acetone each for 5 minutes. The samples were then, patterned using S1400-31 photoresist. Two preliminary etchant gases, CHF_3 and $SiCl_4$.were tried. The etching conditions are presented in table II.

Gas	$SiCl_4$	CHF_3
Flow rate (sccm)	9	7.5
Pressure (mtorr)	11.3	8.9
RF Power (W)	100	100
dc bias voltage (V)	250	420
Etching time (min)	10	10

Table II: Conditions for etching ZnTe using CHF_3 and $SiCl_4$ RIE.

SEM micrographs taken after etching in CHF_3 and removal of the photoresist, showed some evidence of redeposition, on the etched surface possibly a polymer. The deposition was ashed in O_2 plasma for 30min but did not remove all the deposition. The etch rate on the other hand was very small. From the literature[16], it is speculated that Tellurium flourides (volatile compounds) and zinc flourides (nonvolatile compounds) might have been formed.

A ZnTe sample was etched in $SiCl_4$ at the conditions given above. Although the etch rate was found to be about 20nm/min, deposition was observed on the etched surface.

A second sample was etched in $SiCl_4$ using double the flow rate (18sccm) and double the pressure (22mtorr). The etch rate was increased to about 30nm/min, however deposition on the etched surface can still be seen, Figure 7.1.

The conclusion reached from the results of the experiments above indicated the need to explore other plasma chemistries to produce better etching characteristics i.e. vertical profiles, smooth, uniform, and clean surfaces. The problem with etching Zn-containing II-VI semiconductors is that there are very few volatile Zn compounds that can be produced in a successfully designed plasma etching chemistry and almost all of them are organometallics[16]. So a reasonable choice for etch gas, at this point, was CH_4/H_2.

Figure 7.2: Micrograph showing the surface of ZnTe etched using $SiCl_4$. Deposition on the surface and the sidewall roughness can be seen in the bottom half of the micrograph.

7.4. Reactive ion etching (RIE) of II-VI semiconductors in CH_4/H_2

7.4.1. RIE of ZnTe

Dry etching using CH_4/H_2 can, presumably, be thought of as an inverse of metal organic chemical vapour deposition with the formation of organo-metallic compounds and hydrides as etch products[11]. The samples consisted of a 1μm thick epitaxial layer of ZnTe which were coated with a bi-layer of PMMA and exposed using high-resolution electron beam lithography. The mask for dry etching was a 50nm thick film of vaccum deposited Titanium, then patterned using lift-off.

The hydrogen flow rate was varied with a constant methane flow rate of 5sccm, and a rf power of 150W, with a corresponding bias voltage of 870±30V. Fig. 7.3 shows the etch rate of ZnTe as a function of the $\%CH_4$ in the CH_4/H_2 gas mixture at a constant etch pressure of 23 mtorr.

It was found that in pure hydrogen, ZnTe etches at a rate of 20nm/min but the surface looked rough. At a high methane concentration (1/2 CH_4/H_2), the profile was overcut, and a deposit, presumably polymeric[17], was formed which was easily removed in an oxygen plasma.

At lower methane concentrations, the etched profile improved, becoming key-hole shaped at a flow rate of 30sccm i.e. CH_4/H_2 ratio of 1/6, Fig. 7.4a. However at the optimum conditions of 40 sccm of hydrogen (CH_4/H_2 ratio of 1/8), and a total pressure between 23 and 25mtorr, the sidewalls were almost vertical after etching and the surface was smoother than the as-grown surface and no deposition was observed. Figure 4b, 4c,and 4d show a selection of nanostructures etched under the optimum conditions with the Titanium mask still in place, comprising a rib 65nm wide and dots 55nm and 70nm in diameter, respectively.

The anisotropy factor was ~ 0.91. The etch rate was ~ 72nm/min.

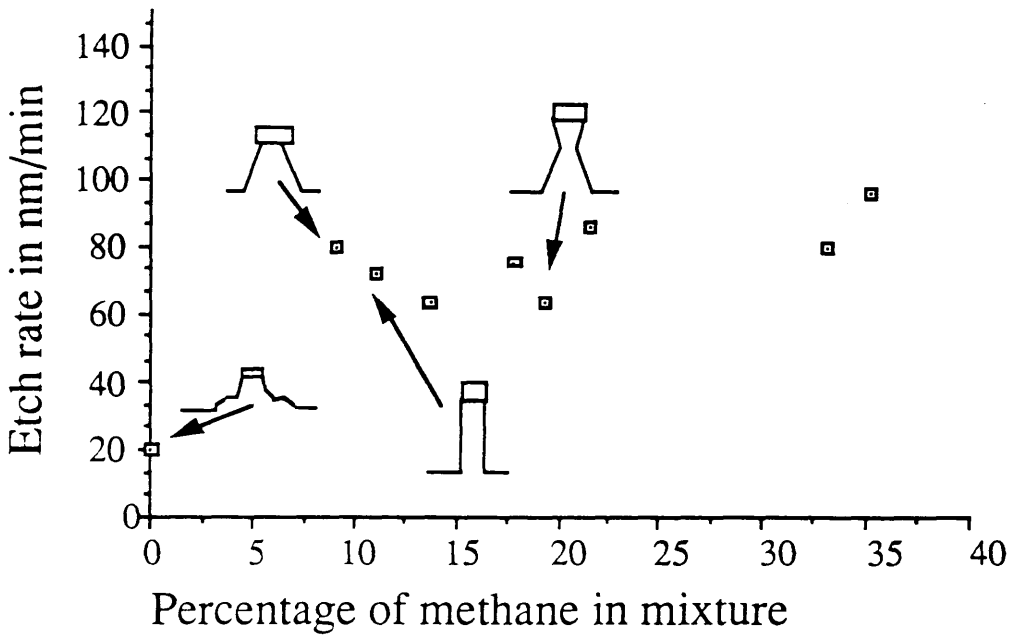

Figure 7.3: The etch rate of ZnTe as a function of the $\%CH_4$ in the CH_4/H_2 gas mixture at a constant etch pressure of 23 mtorr.

7.4.2. RIE of ZnSe and ZnSeS

ZnSe was etched in various CH_4/H_2 ratios in order to find the optimum one. In pure hydrogen, ZnSe etches slowly yielding a rough surface.

At high CH_4 percentage i.e. a CH_4/H_2 ratio of 1/2 - 1/3, deposition was found on the surface. The optimum conditions for etching ZnSe was found to be similar to that of ZnTe, that is a CH_4/H_2 ratio of 1/8. At an etch pressure of 23mtorr, the etch rate was 34nm.min^{-1}, the sidewalls were vertical, the surface was smoother than the as-grown material and no deposition was found.

To test the resolution of the etch process, ZnSe samples were coated with HRN negative electron beam resist and were exposed for an array of dots. Fig. 7.5a, 5b, 5c and 5d show high magnification micrographs of dots 26nm in diameter, 200nm high (Fig. 7.5a and 5b) and rows of dots at lower magnifications (Fig. 7.5c and 5d). It can be seen that this etch process produces structures with high aspect ratio and extremely vertical sidewalls (anisotropy factor close to 1). Two observations can be made on Fig. 7.5. Firstly, in Fig. 7.5a, and 5b, the dots are shrouded with a thin layer. This layer is a contaminent from the electron microscope deposited during exposing the micrograph. Secondly, the profile of some of the structures is not uniform, for example Fig. 7.5c. This may be due to the inhomogeneity of the epitaxial layer, i.e. local variations in stoichiometry, which in turn changes the etch rate locally producing non-uniform profiles.

Epitaxial layers of $ZnSe_{1-x}S_x$ with (alloy composition in the range $0.08 \leq x \leq 0.11$) were etched using the same conditions as for ZnSe, i.e. at CH_4/H_2 ratio of 1/8. The etched structures exhibited near vertical sidewalls and no deposition was found on the surface. However, the etching process has revealed white regions (appearing as white spots, probably Se-rich, in Fig. 7.6a and as cones in Fig. 7.6b) which were covered by the etched epitaxial layer (compare the etched and masked areas in Fig. 7.6a). The etch rate of $ZnSe_{1-x}S_x$ was ~ 25nm.min^{-1}, smaller than that for ZnSe, and the anisotropy factor was ~ 0.89.

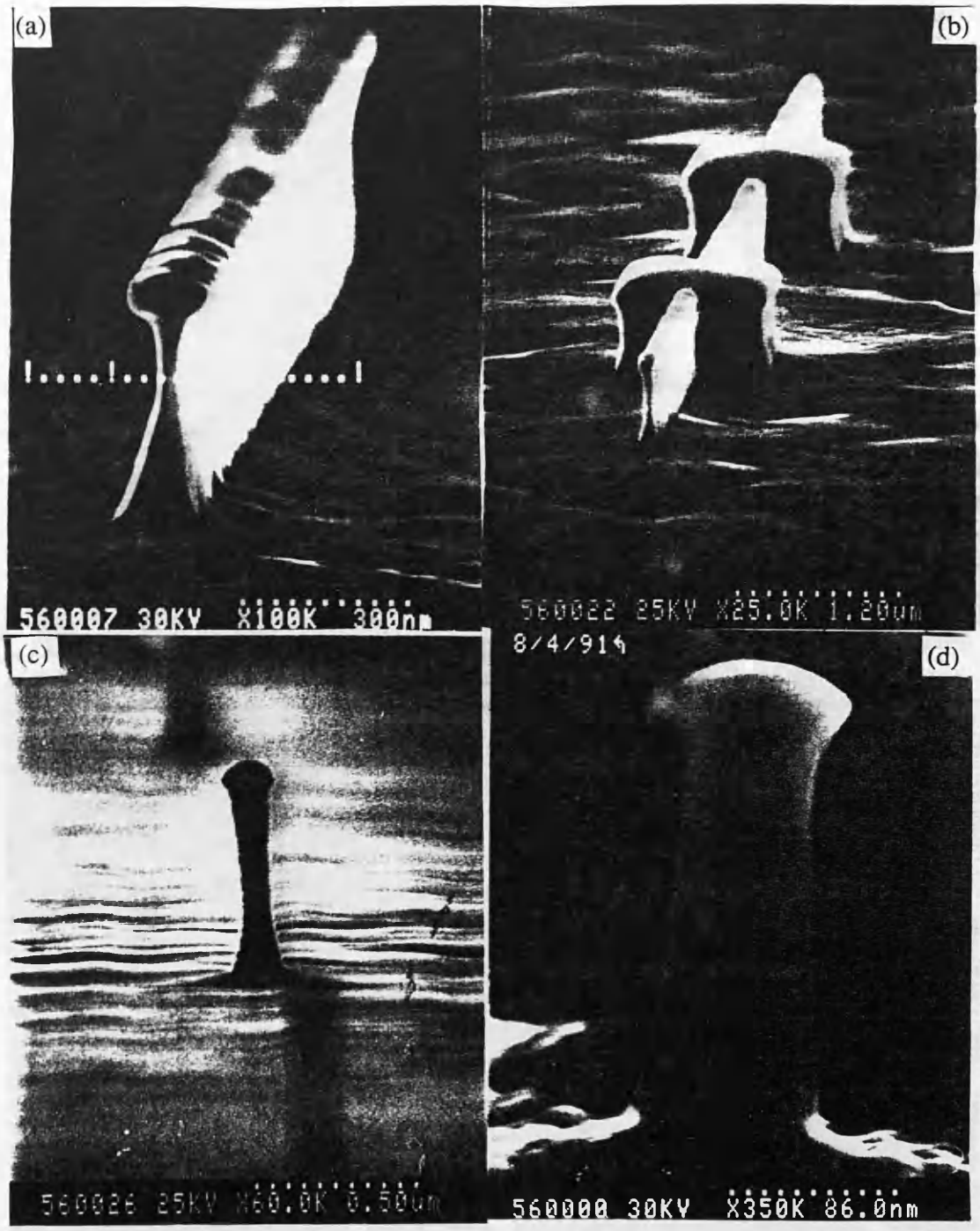

Figure 7.4: Micrographs of nanostructures etched in ZnTe using CH_4/H_2 at a pressure of 23mtorr. a) a rib etched at a CH_4/H_2 ratio of 1/6 displaying the 'key hole' profile, the narrowest region is approximately 35nm wide. b) a rib 65nm wide etched at a CH_4/H_2 ratio of 1/8. c) a dot 55nm in diameter etched at a CH_4/H_2 ratio of 1/8. d) a dot 70nm in diameter etched at a CH_4/H_2 ratio of 1/8.

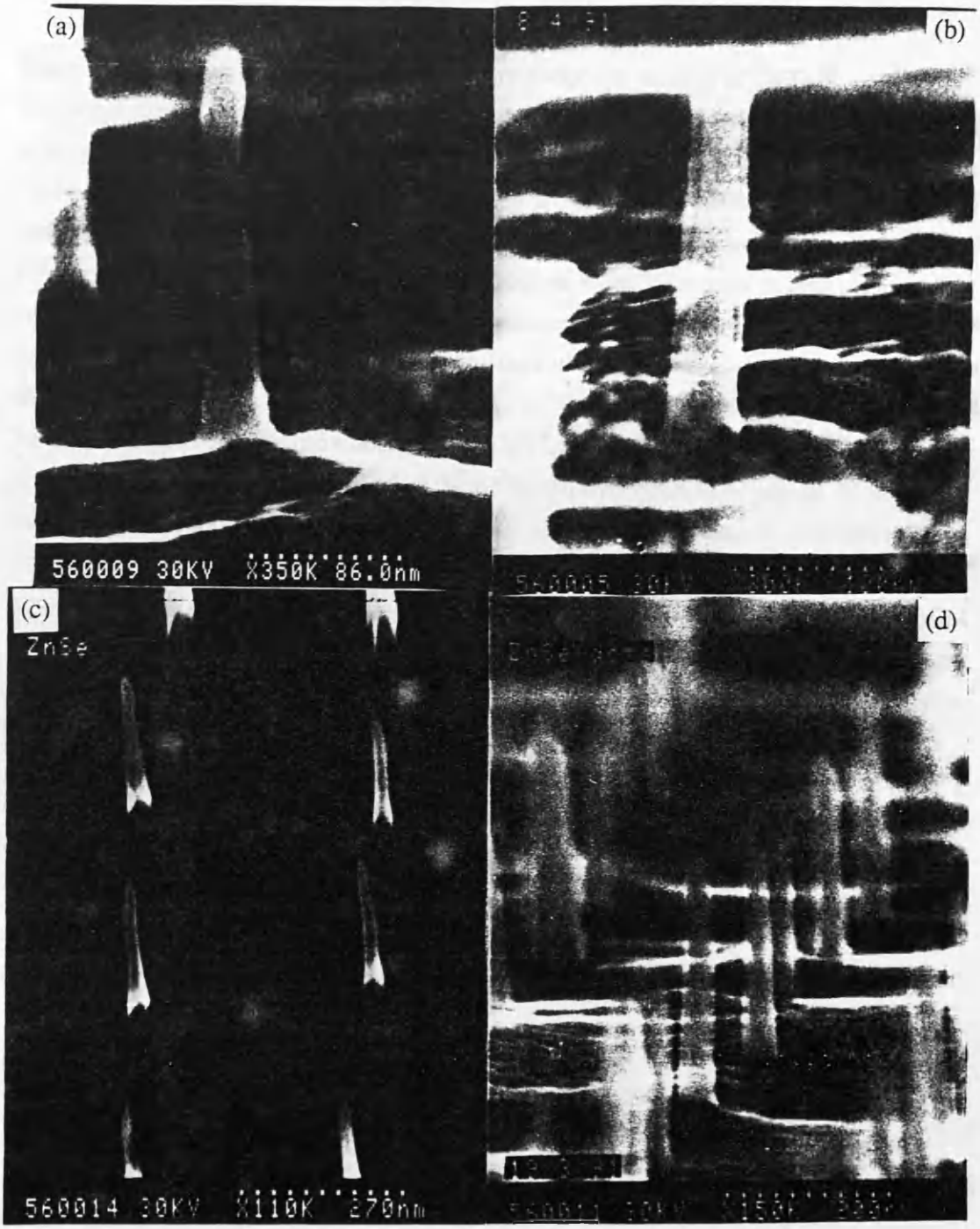

Figure 7.5: Micrographs of nanostructures etched in ZnSe using CH_4/H_2 ratio of 1/8 at a pressure of 23mtorr. a) a dot 26nm in diameter and 200nm high. b) a dot 35nm in diameter and 240nm high. c) and d) dot arrays showing the inhomogeneity of starting material.

7.4.3. RIE of CdTe and CdMnTe

There has been limited reports in the literature about dry etching of CdTe[18].
The properties of etched CdTe structures and surfaces were investigated by varying the hydrogen flow rate with a constant methane flow rate of 5sccm. With pure hydrogen, CdTe etches at a rate of 165nm/min leaving a very rough surface and sidewalls, in addition droplets, presumably of Cd, up to 150nm in diameter were also present, Fig. 7.7a. (It is worth mentioning that indium droplets have been seen during unoptimised etching of InP using CH_4/H_2[19]). At high methane concentration (CH_4/H_2 ratio of 1/2), the sidewall profile was overcut but the surface was smoother than the pure hydrogen etch.
As the methane concentration decreases, i.e. CH_4/H_2 ratios of 1/4, 1/6 ..etc, the etched profile improves becoming vertical at the optimum hydrogen flow rate of 40 sccm. At this optimised conditions, CH_4/H_2 ratio of 1/8, and a total pressure of 22mtorr, the etch rate was ~ 72nm/min and the surface after etching was smooth and clean. The anisotropy factor for CdTe was ~ 0.92. Fig. 7.7b shows a high magnification SEM micrograph of a 100nm wide ridge etched under these conditions with the Ti mask still in place. A graph of the CH_4/H_2 ratio as a function of CdTe etch rate is presented in Fig. 7.7c.
It was found that $Cd_{1-x}Mn_xTe$ (with the alloy composition in the range $0.127 \leq x \leq 0.14$), can also be etched using the same optimised conditions as for CdTe producing similar vertical sidewalls. The anisotropy factor was ~ 0.91. However, the etch rate for $Cd_{1-x}Mn_xTe$ at the optimum conditions was found to be ~41nm.min^{-1}. Fig. 7.7d shows structures etched in
$Cd_{1-x}Mn_xTe$ using CH_4/H_2 ratio of 1/8 and a pressure of 22mtorr.

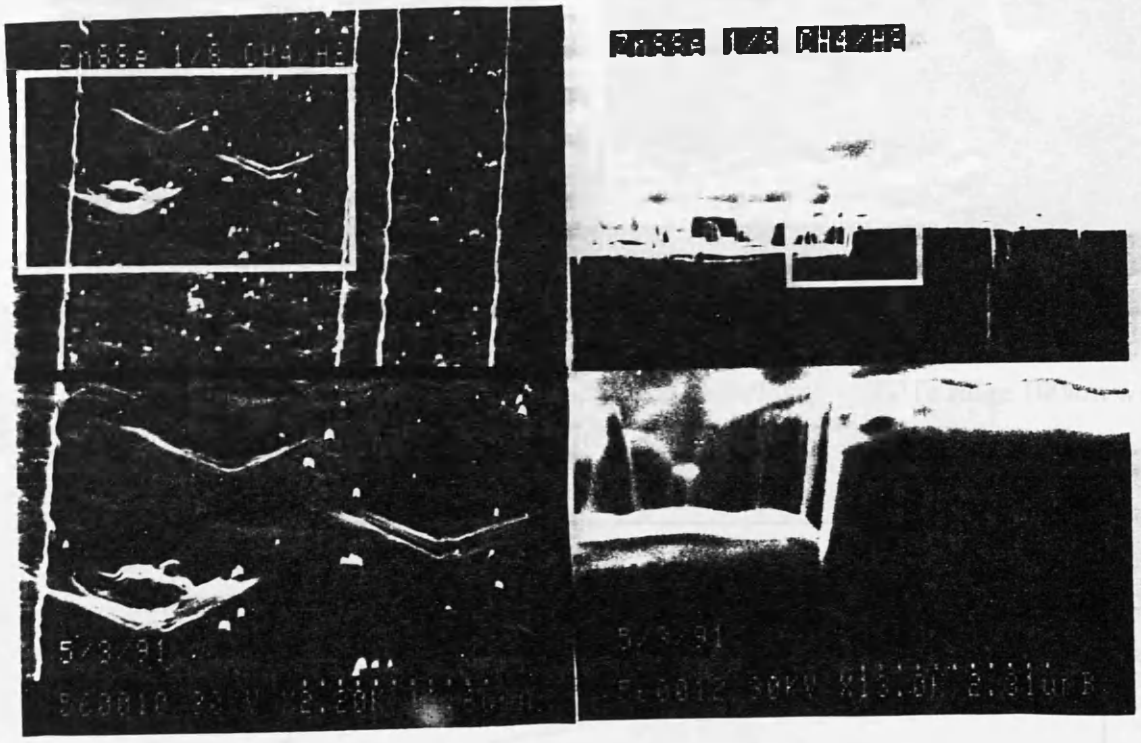

(a) (b)

Figure 7.6: Micrographs showing ZnSeS surface etched in CH_4/H_2 ratio of 1/8 and a pressure of 22mtorr. a) a top view showing native defects (diamond shaped) and also small white regions uncovered by the etching process. b) a side view of the surface at micrograph (a) showing the etch profile. The white regions in micrograph (a) appear as cones.

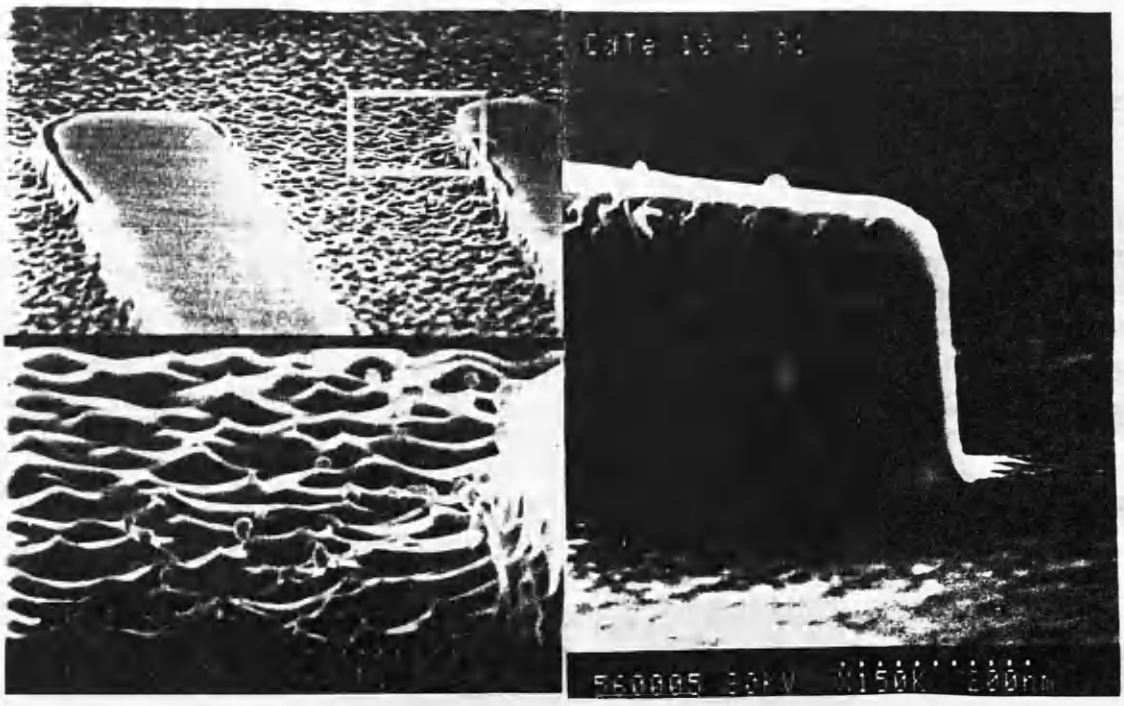

(a) (b)

Figure 7.7: Micrographs showing a) CdTe etched in pure hydrogen. Droplets up to 150nm in diameter, presumably of Cd, appear after etching. b) CdTe ridge 100nm wide etched in CH_4/H_2 ratio of 1/8 with the Titanium mask still in place.

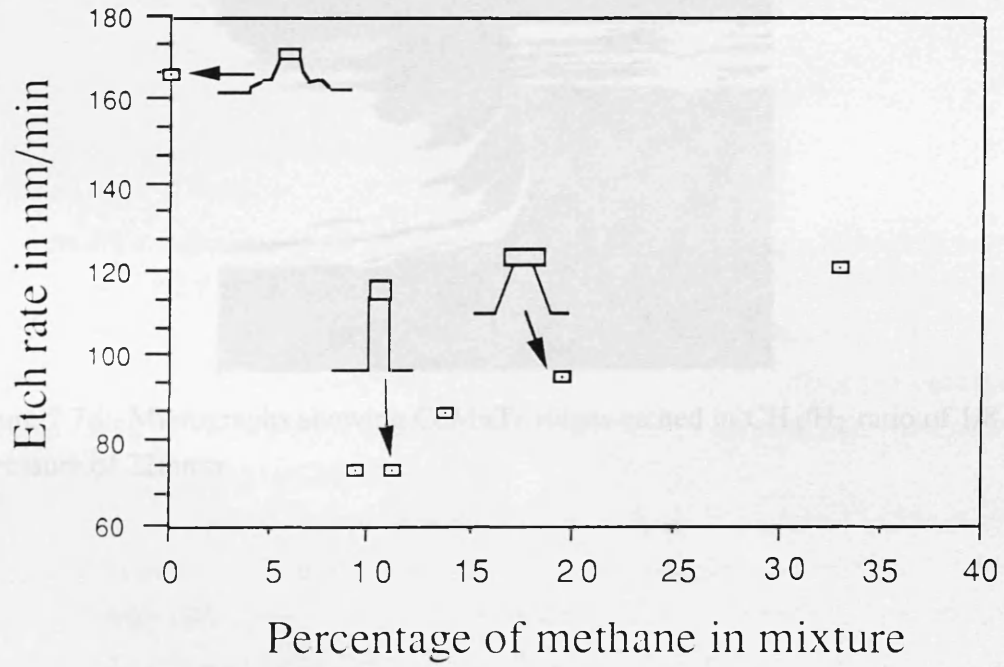

Figure 7.7c: The etch rate of CdTe as a function of the $\%CH_4$ in the CH_4/H_2 gas mixture at a constant etch pressure of 22 mtorr.

7.4.4. RIE of ZnS and CdS

Polycrystalline ZnS was patterned using S1400-31E photoresist and etched in CH_4/H_2 at ratios of 1/6, 1/8 and 1/10. After etching, it was noticed that, for CH_4/H_2 ratio of 1/10, a film of deposition, presumably polymeric, was covering the photoresist mask in areas where it was difficult to remove. It was also observed that the grain boundaries were clearly defined in the etched area, Fig. 7.8a. The etch rate at 1/8 is ~ 160nm.min^{-1}. The anisotropy factor was ~ 0.85.

CdS etched at CH_4/H_2 ratio of 1/8 showed no trace of deposition on the etched surface, Fig. 7.8b, and the etch rate was ~ 115nm.min^{-1}. The anisotropy factor was ~ 0.88.

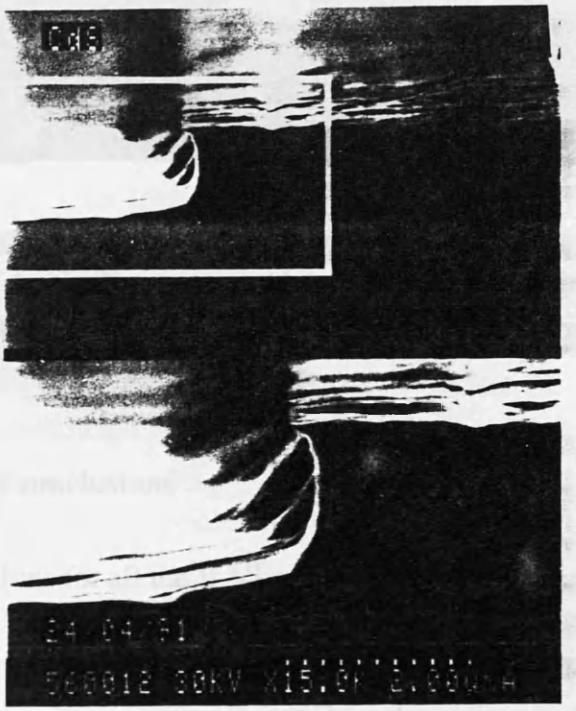

Figure 7.7d: Micrographs showing CdMnTe ridges etched in CH_4/H_2 ratio of 1/8 and a pressure of 22mtorr.

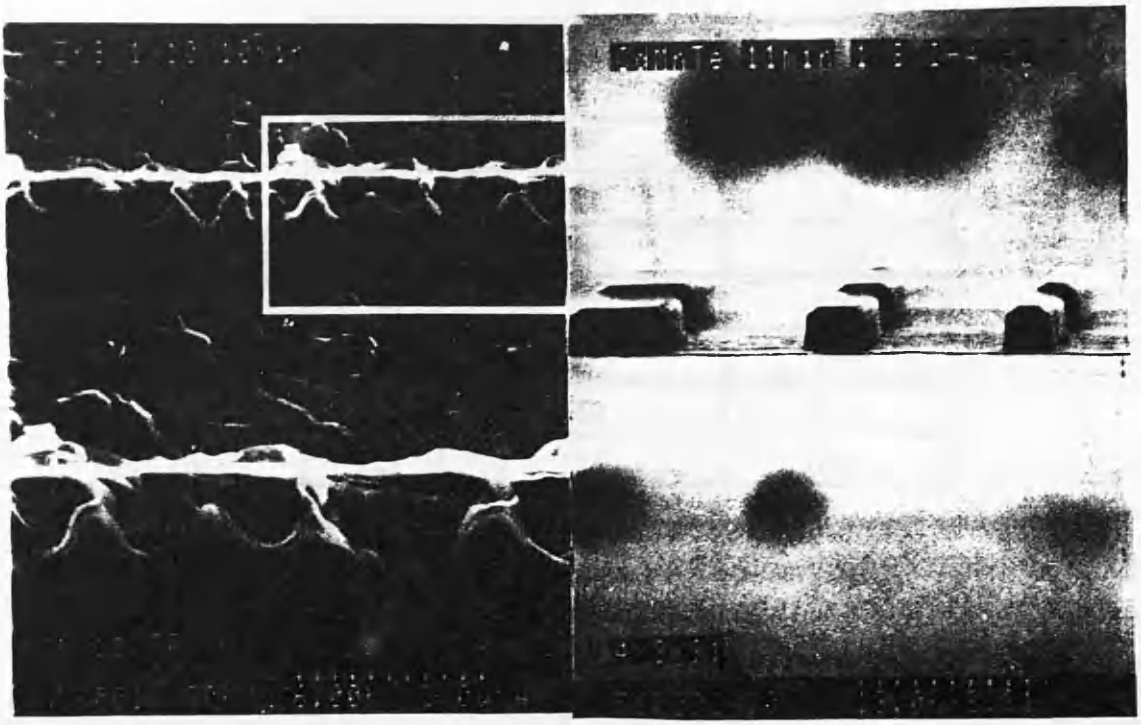

(a) (b)

Figure 7.8: Micrographs showing a) ZnS etched in CH_4/H_2 ratio of 1/10 and a pressure of 23mtorr. A thin film, presumably polymeric, is deposited on the photoresist mask. b) CdS etched in CH_4/H_2 ratio of 1/8 and a pressure of 23mtorr.

7.5. Discussion and conclusions

The optimum conditions for all the II-VI semiconductors etched in this study were at CH_4/H_2 ratio of 1/8 and a pressure ranging between 23 to 25mtorr. The RF power used was 150W and the dc bias voltage was 870±30V. The surface after etching was generally smoother than the as-grown material (or the polished surfaces in the case of ZnS and CdS). The etch rates and the anisotropy factors estimated at the optimum conditions are presented in table III.

It can be seen that the etch rate of ZnSe has decreased from 34nm.min^{-1} to 25nm.min^{-1} after the addition of Sulfer to the compound. The reduction of etch rate upon forming an alloy (ternary compound) was also observed for CdTe and CdMnTe indicating that the presence of Mn also slows down the etch rate. The fact that the optimum conditions are constant for all the II-VI compounds studied implies that almost any quantum well structure or heterojunctions can be etched using this process.

Material	Etch rate ($nm.min^{-1}$)	anisotropy factor
ZnTe	72	0.91
ZnSe	34	~1
ZnSSe	25	0.89
CdTe	72	0.92
CdMnTe	41	0.91
ZnS	160	0.85
CdS	115	0.88

It is believed that the key to the success of CH_4/H_2 as a universal high resolution reactive ion etching process can be understood if this process is thought of as an inverse of metal organic chemical vapour deposition process. As a result, one would expect the etch product to be in the form of organo-metallic compounds and hydrides, depending on which compound has the highest partial vapour pressure. However it should be pointed out that there is no experimental evidence in the literature , as yet, to prove the validity of this claim for etching II-VI semiconductors. However, a recent unpublished work by Murad et al[20] using optical emission spectroscopy has shown that phosphorus and arsenic hydrides are formed during etching of InP and GaAs.

The ability to etch a wide range of II-VI as well as III-V semiconductors, e.g. GaAs[10,11], InP[12], InAs and GaSb[13], puts the CH_4/H_2 etch in a unique position to process II-VI and III-V, and probably hybrid semiconductor structures, commercially.

7.6. References

1. J. O. Willams, Chemtronics, **2**, 43 (1987).
2. N. Samarth, H. Luo, J. K. Furdyna, R. G. Alonso, Y. R. Lee, A. K. Ramadas, S. B. Qadri, and N. Otsuka, Appl. Phys. Lett., **56**, 1163 (1990).
3. R. N. Bickell-Tassius, A. Waag, Y. S. Wu, T. a. Kuhn, and W. Ossau, J. Crysral Growth, **101**, 33 (1990).
4. H. P. Wagner, W. Kuhn, and W. Gebhardt, J. Crysral Growth, **101**, 199 (1990).
5. C. D. W. Wilkinson, and S. P. Beaumont in 'The physics and fabrication of microstructures and microdevices', ed. C. Weisbuch and M. J. Kelly, Springer, (1986).

6. E. M. Clausen, Jr. H. G. Craighead, M. C. Tamargo, J. L. deMiguel, and L. M. Schiavone, Appl. Phys. Lett., **53**, 690 (1988).
7. K. Ohkawa, T. Karasawa, A. Yoshida, T. Hirao, and T. Mitsuyu, Appl. Phys. Lett., **54**, 2553 (1989).
8. T. Saitoh, T. Yokogawa, and T. Narusawa, Appl. Phys. Lett., **56**, 839 (1990).
9. S. M. Sze,' VLSI Technology', second ed., 198 (1988).
10. U. Niggebrugge, M. Klug, and G. Garus, Ins. Phys. conf. ser. no. 79, pp367 (1985).
11. R. Cheung, S. Thoms, S. P. Beaumont, G. Doughty, V. Law, and C. D. W. Wilkinson, Electronics Lett., **23**, 857 (1987)
12. T. R. Hayes, M. A. Dreisbach, P. M. Thomas, W. C. Daurtemont-Smith, and L. A. Heimbrook, J. Vac. Sci. Technol., **B7**, 1130 (1989).
13. J. Werking, J. Schramm, C. Nguyen, E. L. Hu, and H. Kroemer, Appl. Phys. Lett., **58**, 2003 (1991).
14. H. Leiderer, E. Jahn, M. Silberbauer, W. Kuhn, H. P. Wagner, W. Limmer, and W. Gebhardt, J. Appl. Phys., **70**, 398 (1991).
15. M Razeghi, 'The MOCVD Challenge', Adam Hilger, (1989)
16. 'Handbook of Chemistry and Physics', ed. R. C. Weast, 70th ed, CRC press Ohio (1990).
17. D. L. Flamm, and V. M. Donnelly, Plasma Cham. & Plasma Process., **1**, 317 (1981).
18. S. S. Choi, and G. Lucovsky, J. Vac. Sci. Technol., **B6**, 1198 (1988)
19. R. Mcloed, University of Glasgow, unpublished work.
20. S. Murad et al, University of Glasgow, unpublished work.

Chapter 8: Assessment of reactive ion etched II-VI semiconductors

Acknowledgments

I would like to thank Mr A. Smart and Dr M. Watt for performing the photoluminescence spectroscopy and Raman scattering experiments on my etched II-VI samples, and Dr S. Walters, Department of Physics, University of Wales Cardiff for Examining my CdTe samples using X-ray photoelectron spectroscopy.

8.1. Introduction

In the previous chapter, a reactive ion etching process has been described for etching a variety of II-VI semiconductors. However, it is known, from the work on III-V semiconductors, that dry etching introduces damage to the surface of the semiconductors. In this chapter, the question of the etching induced modification by the etching process, described in chapter 8, is addressed.
Since electrical characterisation of ZnTe and ZnSe, using, for example, the TLM method or Schottky diode evaluation was not possible, non- destructive and contactless optical assessment techniques such as photoluminescence spectroscopy and Raman scattering were employed. In addition, the surface chemistry was investigated using X-ray photoelecton spectroscopy.
For CdTe, n-doped bulk material has been available commercially and electrical characterisation by evaluating the performance of Schottky diodes was possible. Etched surfaces were characterised chemically in detail using X-ray photoelectron spectroscopy and X-ray excited Auger electron spectroscopy.

8.2 Techniques used in this study

8.2.1. Photoluminescence spectroscopy

The theory of photoluminescence will be presented briefly in this section. Photoluminescence can be defined as the optical radiation emitted by a physical system resulting from the excitation to a non-equilibrium state by irradiation with light. Band gap photoluminescence (PL) occurs when a photon creates an electron-hole pair. Both of these quasi particles relax down to the bottom of their respective energy bands and recombine emitting a photon with energy equivalent to the transition energy. The

emitted photon can therefore have energy different to that of the band-gap energy if there are other energy levels present, such a case occurs when impurities are present in the crystal. Luminescence processes are distinct in that light is generated without the generation of heat. PL experiments are usually undertaken at low temperatures (<77K) as this effectively decreases the phonon population and the probability of non-radiative recombination processes, thus increasing the emission intensity and narrowing the linewidth.

The basic transitions in semiconductors are shown schematically in Fig. 8.1. These transitions may be classified as follow[1] :

Interband transition: (a) intrinsic transition corresponding very closely in energy to the band-gap, where phonons or excitons(1) may be involved and (b) high energy emission involving energetic or hot carriers, sometimes related to avalanche emission. The group (2) involving chemical impurities or physical defects; (a) conduction band to acceptor (b) donor to valance band, (c) donor to acceptor pair emission and (d) deep levels. The group (3) is intraband transition involving hot carriers. Not all transitions are radiative or can occur in the same material.

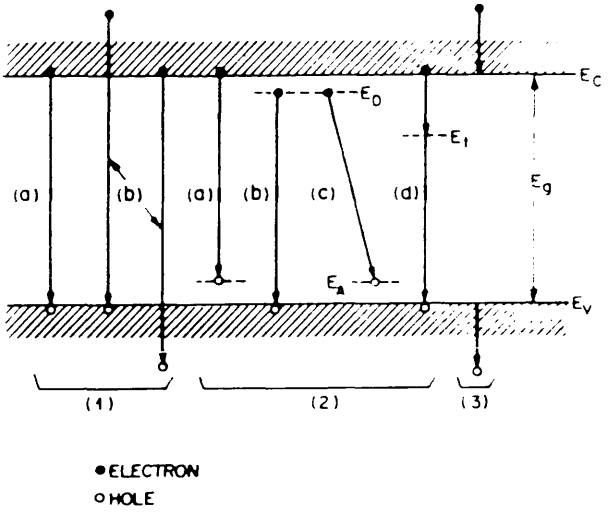

Figure 8.1: Basic transitions in semiconductors (after Ivey, reference 1).

(1) An exciton consists of an electron and a hole that orbit around each other. It has lower energy than the band-gap because some energy goes towards binding the exciton together. It is free to wander through the crystal hence the restriction is imposed that the translational velocities of the hole and the electron must be identical. The hole and electron can recombine radiatively. A free hole can combine with a nutral donor to form a positively charged excitonic ion, the hole moving in the electrostatic field of a 'fixed' dipole, determined by the instantaneous position of the electron, hence this complex is somtimes called bound exciton[5].

8.2.2. Raman scattering

The presentation of Raman scattering theory in this section will be a simple and brief one. Raman scattering relies on examining the light scattered of a material. The scattering could be off a quantized lattice vibration within the crystal. Such lattice vibrations are called phonons. If a light of energy hν is incident on a crystal, the scattered light will have different energies; $h(\nu - \Delta\nu)$ and $h(\nu + \Delta\nu)$. These are the *Stokes* and *anti-Stokes* lines and are due to the annihilation or creation of phonons respectively. The former process is usually more dominant (brighter line) since the incident photon is more likely to lose energy via creating a phonon rather than absorbing it. Phonons can be classified as Acoustic or Optical groups and each group is further divided into Longitudinal and Transverse, for example, Longitudinal Optic phonons (LO) and Transverse Optic phonons (TO), depending on their polarisations.
There are certain selection rules that have to be obeyed in Raman scattering[2]. One of these rules states that when the (100) plane of the crystal is illuminated, then only the longitudinal optic LO phonon can be excited. If however, the (100) plane of the crystal is disordered (damaged) in some way, the otherwise forbidden transverse optical TO phonon can be excited[3], therefore the appearance of a TO phonon when illuminating the (100) plane is a sign of disorder (damage). The Raman spectra of an ordered crystal shows sharp narrow peaks at the frequency of the phonons, typically of width 1-2cm^{-1} for elemental semiconductors and 2-4cm^{-1} for compound semiconductors. This is very different however from the Raman spectrum shown for amorphous material which exhibit very broad peaks existing over many tens of wavenumbers and reflecting the phonon density of many states[4]. In between these extremes, the phonon peaks show asymmetric broadening to lower energies, getting broader as the degree of crystal disorder is increased.

8.2.3. Schottky diode evaluation

There are four basic mechanisms which determine the properties of Schottky barriers under forward bias for an n-type semiconductor.
a) emission of electrons from a semiconductor over the top of the barrier into the metal,
b) quantum mechanical tunneling though the barrier,
c) recombination in the space charge (depletion) region,
d) recombination in the neutral region.
The inverse processes occur at reverse bias. A schematic diagram of the transport mechanisms is presented Fig. 8.2, where θ_b is the height of the barrier measured from

the metal energy Fermi level, V_d is the band bending, ξ is the energy difference between the conduction band and the semiconductor Fermi level.

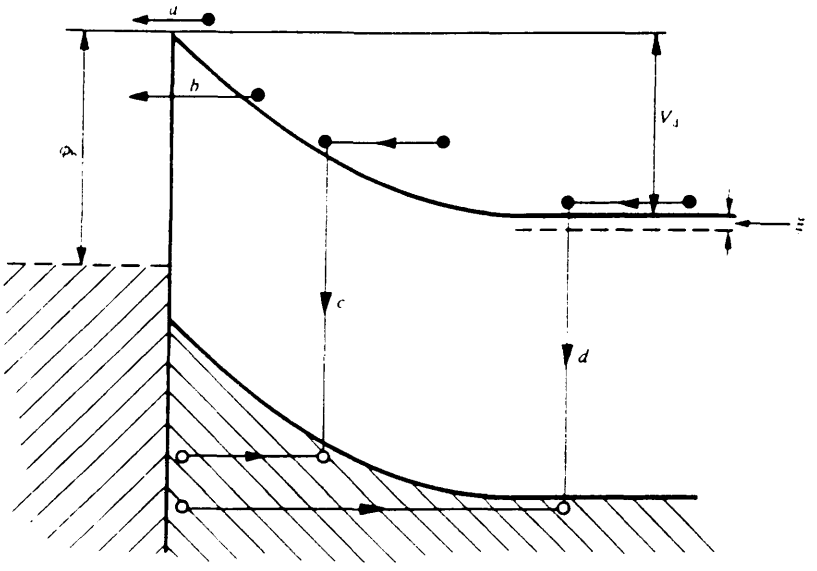

Figure 8.2: Transport processes in a forward biased Schottky barrier (after Rhodrick and Williams, reference 5).

When process (a) described above is the dominant transport mechanism in a Schottky diode, the diode can be considered as nearly ideal, $n \approx 1$; while processes b, c and d cause departure from the ideal behaviour i.e. $n >> 1$, where n is the ideality factor. Furthermore, there are two ways in which the electrons emit over the Schottky barrier in mechanism (a). Before the electrons emitted over the barrier into the metal, they must first be transported from the interior of the semiconductor to the interface. In transversing the depletion region of the semiconductor, their motion is governed by the diffusion and drift mechanisms in the electric field of the barrier. When they arrive into the interface, their emission into the metal is controlled by the number of Bloch states in the metal which can influence the states in the semiconductor. These two processes are effectively in series, and the current is determined predominantly by whichever causes the larger impediment to the flow of electrons. According to the diffusion theory of Wagner[6] and Schottky et al[7], the first of these processes is the limiting factor, whereas in the thermoionic- emission theory of Bethe[8], the second is more important. However, in Roderick's analysis[9] of Smith's experimental data[10] on GaAs diodes, it was shown that the forward current in these diodes at room temperature is almost certainly limited to the thermionic emission provided the forward bias is not too large. In addition, contributions to the electron transport across the GaAs Schottky junction through recombination in the depletion region (process c) due to the short lifetime of the electrons. Tunneling through the barrier (process b) however occurs because the small

electron effective mass makes it difficult to fabricate an ideal diode. Furthermore, the quantum mechanical tunneling appear to be very sensitive in the reverse bias when measuring the reverse leakage current.
By assuming that the electron transport is governed almost entirely by thermionic emission, the current voltage characteristic of a practical diode is given by[5]:

$$I = I_o \exp \{eV/nkT\} \{1-\exp [-eV/kT]\} \quad (8.1)$$

where

$$I_o = A^* T^2 \exp \{-\theta_b/kT\} \text{ x area} \quad (8.2)$$

where A^* is Richardson constant ($4.4x10^4 Am^{-2}K^{-2}$), T is the absolute temperature and n is the ideality factor; $n \geq 1$.
when $V > 3kT/e$, equation 8.1 approximated to

$$I = I_o \exp \{eV/nkT\} \quad (8.3)$$

A straight line results when ln I is plotted as a function of V for small forward bias ($\approx$ 0.5V), and the ideality factor n can be calculated from the slope of the graph. If large values of n are calculated or ln I versus V plots are non linear, the diode is far from ideal probably due to the presence of a thick interfacial layer or to recombination in the depletion region via localised traps.
The measurements of the ideality factor and the reverse leakage current for Schottky diodes as a quantitative indication of the degree of damage induced at the semiconductor surface after dry etching has been used by a number of workers[11-16].

8.3. Characterisation of CH_4/H_2 etched ZnTe

8.3.1. Reflectivity measurements, Photoluminescence spectroscopy and TEM examination

ZnTe epitaxial layers were grown by MOCVD as described in chapter 8. Measurements of reflectivity were performed at Regensburg University at 1.7K on as grown 1.97μm thick layer under normal incidence. The spectrum shown in Fig. 8.3 revealed the splitting of the excitonic structure (ET) into heavy and light hole transitions. It was noted that from this splitting and using the known deformation potential[17], it can be deduced that there is a small biaxial strain in the surface layer.

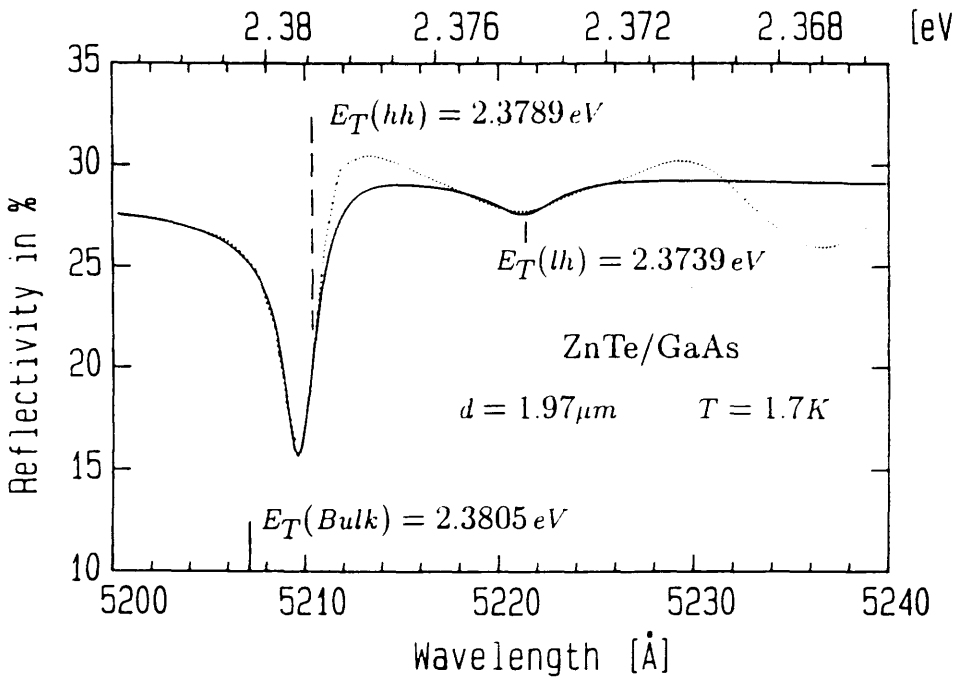

Figure 8.3: Experimental (....) and theoretical (——) low temperature reflectivity spectrum of unetched ZnTe surface grown by MOCVD at 350°C. Heavy and light hole transitions appear at 2.3789 and 2.3739eV, respectively.

If the large lattice mismatch-induced strain of 7.48% had completely relaxed at the surface of a 1μm thick sample, then it would be expected that only the thermal strain of +0.15% would remain. This is caused by the difference in the thermal expansion coefficients between the ZnTe layer and the GaAs substrate, after cooling the sample from the growth temperature of 623K to the measurement temperature of about 2K. It is noteworthy that the measured strain is always found to be slightly below this value[18]. It has been noticed that by increasing the surface roughness for example by examining a poorer quality sample the splitting of the excitonic structure (ET) into heavy and light hole transitions broadens and becomes less prominent.

The photoluminescence measurements of ZnTe epitaxial layers were carried out at 2K using a 1m Jarrel Ash double monochrometer and detected by a GaAs photomultiplier. The 457.9nm line of an argon ion laser was used as an excitation source. A typical PL spectrum in the range of 2.2 to 2.4eV,Fig. 8.4. The peaks denoted by 1 and 2 are luminescence from free excitons split by biaxial strain. Peaks 3 and 4 are due to an exciton bound to an Arsenic-acceptor and to another presently unidentified acceptor, respectively. The luminescence of a donor-acceptor pair appears as a band denoted by 6. Very little deep trap luminescence was found which indicates the high purity of the

grown layer. Increasing the surface roughness for example by examining a poorer quality sample broadens this structure and makes it less prominent.

ZnTe specimens were prepared for [110] cross-sectional TEM by mechanical thinning followed by argon ion milling to perforate the specimen. A Philips CM300 transmission electron microscope operating at 300kV was used at the physics department in Regensburg University. A bright-field image of a 750nm thick ZnTe layer on GaAs is shown in Fig. 8.5. The micrograph clearly displays the defect structures near the ZnTe/GaAs interface. In a region, approximately 200nm wide extending from the interface, a large density of misfit dislocations can be seen. When the ZnTe layer thickness is increased, the density of dislocations decreases and defect-free areas can be seen further from the interface.

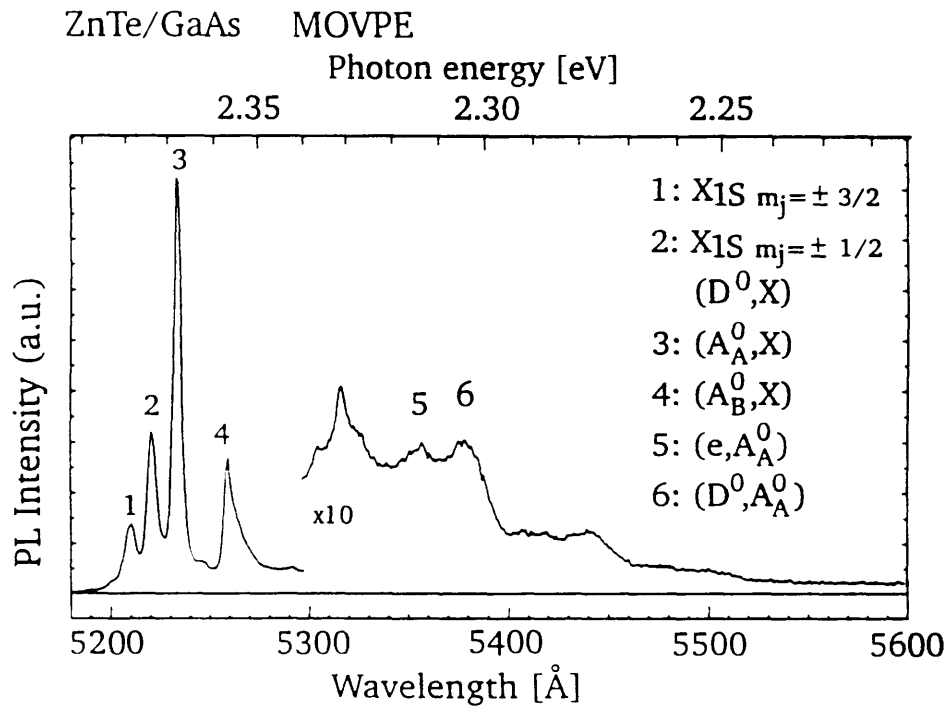

Figure 8.4: Low temperature photoluminescence spectrum of ZnTe/GaAs layer grown by MOCVD excited with the 457.9nm Argon laser line.

The spectra of ZnTe and ZnSe samples were collected using the 488nm and 364nm lines, respectively of a Spectra-Physics argon ion laser as the excitation source and for the low temperature measurements the samples were held in a helium flow cryostat. A 90° scattering geometry were used for the luminescence experiment of ZnTe and ZnSe. The emitted light was dispersed in either a Jobin-Yvon single or double pass 1m spectrometer and detected by a GaAs photomultiplier tube operating in current or photon counting mode, respectively.

Figure 8.5: Bright field image of cross sectional TEM showing ZnTe/GaAs interface of ZnTe layer grown by MOCVD.

Figure 8.6 shows the 5K photoluminescence (PL) spectrum from as-grown ZnTe. Well-defined excitonic structure in the near-band-edge region of the spectrum are observed. The dominant peak at 2.368eV, (4), is identified as an exciton bound to an Arsenic acceptor[19]. The shoulder to the low energy side (5) is a second acceptor bound exciton presently unidentified. Peaks (2) and (3), at 2.380 and 2.373eV, respectively, can be identified as the strain-split free exciton emission corresponding to a strain of 0.09% resulting from an incomplete strain relaxation. The 6LO and 7LO Raman scattering lines also appear in this spectral region, peaks (1) and (6) respectively, and provide a good wavelength calibration and order of magnitude intensity marker. Peak (7) is unidentified at the present time. The sample was then cleaved into four pieces and three pieces were reactive ion etched in CH_4/H_2, using the conditions described in chapter 8, while the fourth was retained as a control. The three etch gas ratios studied were 1/10, 1/8 and 1/6 ratios of CH_4/H_2.

The spectra obtained after etching are compared with the spectrum of as-grown (control) sample, Figure 8.7. The overall intensity of the near band edge luminescence has decreased in all cases by two orders of magnitude with respect to the intensity of the unetched sample. The strongest reduction in intensity occurs for the dominant (4) peak and correlates with the proportion of Hydrogen in the etch gas: the largest decrease occurs in the sample etched with the largest proportion of hydrogen i.e. CH_4/H_2 ratio of 1/10. This suggests that hydrogen incorporation may be the cause of the intensity decrease. Reduction in the luminescence intensity of p-type semiconductors after hydrogen exposure has been observed in ZnTe and CdTe[20,21] and in silicon[22].

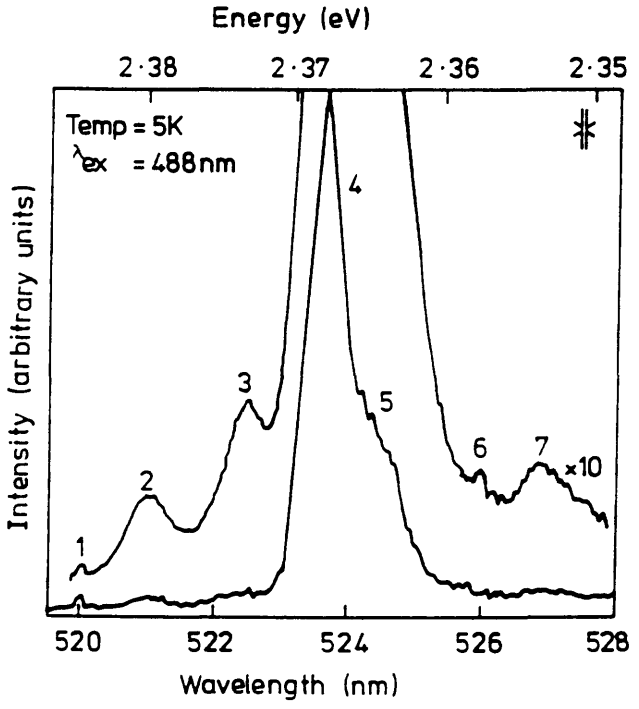

Figure 8.6: 5K photoluminescence spectrum of as-grown ZnTe/GaAs.

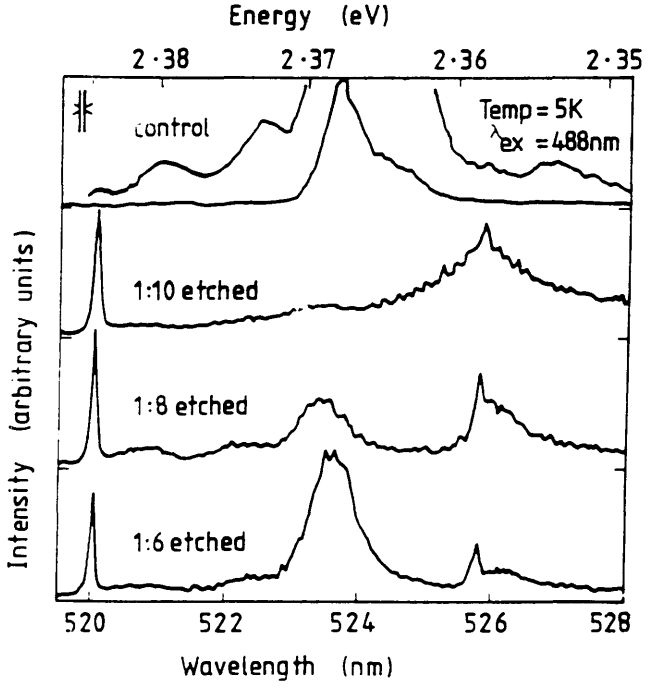

Figure 8.7: 5K photoluminescence spectra of four samples of ZnTe/GaAs, three of which have been reactive ion etched in CH_4/H_2 at ratio 1:6, 1:8 and 1:10.

Changes in the deep level emission from the samples after etching are shown in Fig. 8.8. The spectrum from the control sample shows donor acceptor pair (DAP) emission at 2.305eV with FWHM of 12meV and its two LO phonon replicas lying at longer wavelengths. After etching, the DAP emission decreases in intensity with peak (4). It is believed that the DAP emission is related to an arsenic acceptor recombining with an unknown donor. This assignment is consistent with the arsenic ionization energy of 78.3meV[19] assuming a donor ionization energy of 18meV[23]. The deep level spectra of the etched samples show two new broad features at lower energy than the DAP: at 2.23eV (FWHM = 61meV) and at 2.15eV (FWHM = 13meV). Neither the control nor the etched samples exhibited emission related to oxygen impurities which is expected at about 1.9eV[24]. The 2.15eV feature observed in the etched samples coincides in energy with an unidentified peak observed by Wilson[25] in both MBE and MOVPE grown ZnTe/GaAs and its origin remains unknown.

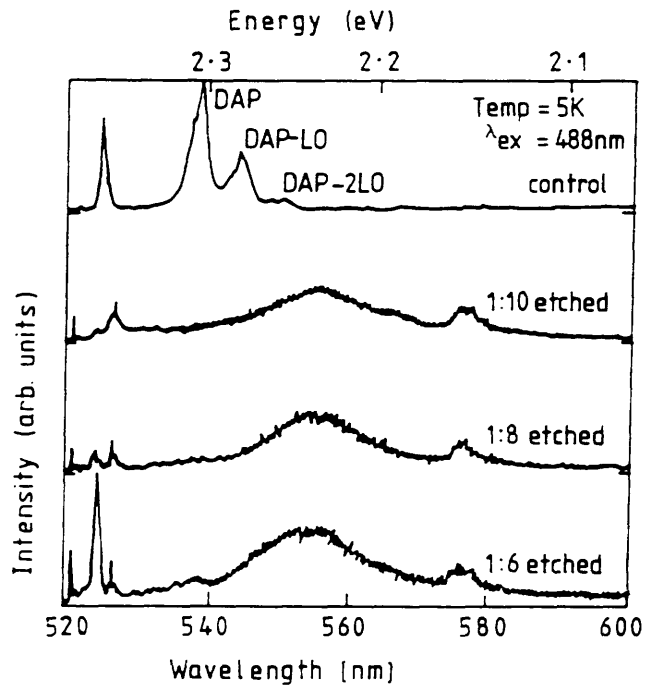

Figure 8.8: 5K deep level emission of the same four samples of ZnTe/GaAs shown in Fig. 8.7. The spectrum of the control sample is an order of magnitude weaker in intensity in this region than those of the etched samples. The peak at 2.23eV is probably related to a Zn-vacancy impurity complex. The spectral resolution is 0.1nm.

In order to remove the hydrogen incorporated into the samples during etching, they were annealed at 250°C for 15 minutes in flowing pure N_2 together with the control sample. The near band edge and deep level spectra obtained from the samples after annealing are shown in Figures 8.9 and 8.10 respectively. The excitonic spectrum of the control

sample remains largely unchanged with no significant broadening of the dominant bound exciton emission. Qualitatively, the spectra now resemble that of the control sample with the dominant excitonic emission, the arsenic bound acceptor (peak (4)), displaced by 2meV to higher energies in all three etched samples.

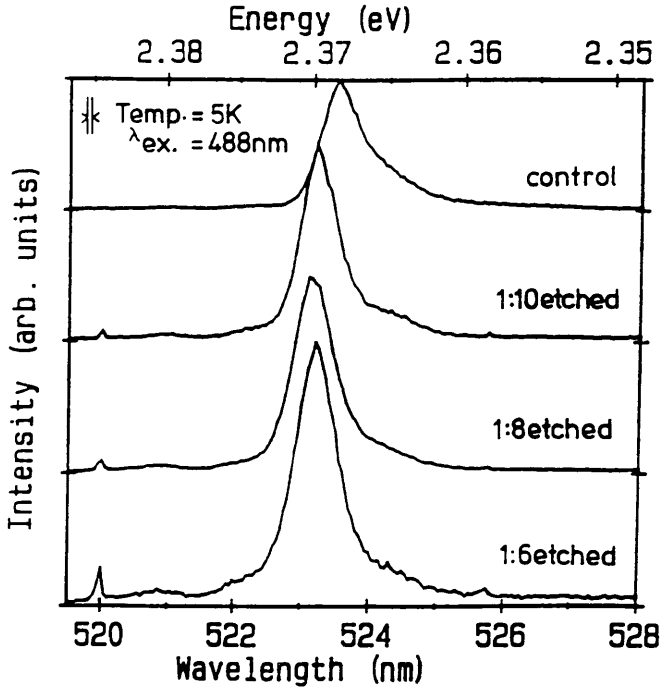

Figure 8.9: Near band edge photoluminescence spectra of the same four samples of ZnTe/GaAs shown in Figure 8.7, after annealing. The intensity of the etched samples has increased by an order of magnitude but is still an order of magnitude weaker than the control sample. All the etched samples show a blue shift of their dominant emission peak of 2meV with respect to the control sample.

This shift may be related to some form of strain being relaxed in the etched surfaces. Complementary work on annealing etched and unetched samples in flowing Argon shows similar energy shifts of this peak after etching. The FWHM of peak (4) in the etched samples has broadened by 0.5meV at most, suggesting minimal degradation of the optical quality of the material but the overall intensity of the near band edge emission has recovered by an order of magnitude after annealing.

After annealing, the deep level emission of the etched samples shows some recovery of the DAP emission intensity together with the associated phonon replica with respect to the spectrum of the annealed control sample. The peak at 2.15eV remains, although reduced in intensity. The broad feature at 2.23eV now shows more structure, revealing a well-defined peak at 2.23eV with evidence of two phonon replicas. It now closely

resembles the spectra reported by Wilson et al[25] and Meese and Park[26] with a FWHM of some 20meV which compares well with the values they measured. This suggests that after annealing, a much narrower range of energies is involved in the Zn-vacancy-impurity complex and that the annealing process has gone some way to removing any possible etch-induced damage.

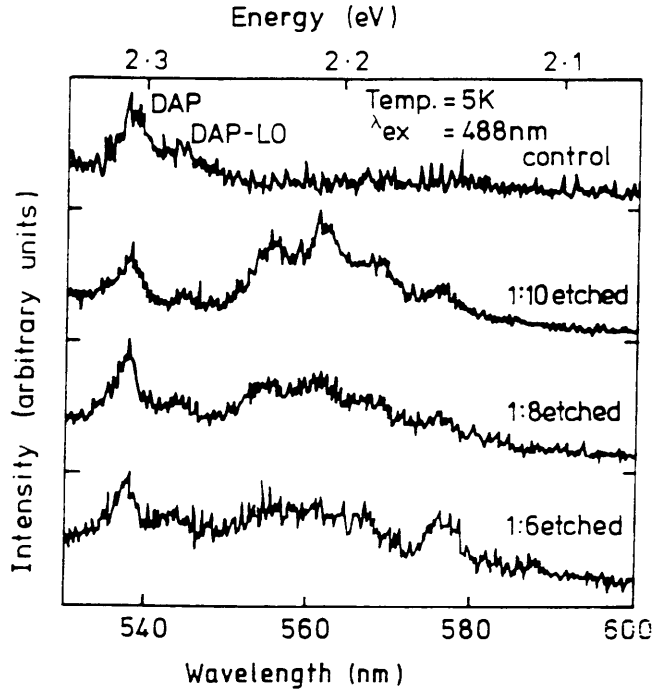

Figure 8.10: Deep level emission region of the same four samples of ZnTe/GaAs shown in Figure 8.7, after annealing. The intensity of the DAP emission from the control sample has decreased while that of the etched samples has partially recovered. The peak at 2.150eV remains in the emission of the etched samples, while the broad band at 2.23eV shows some structure, particularly in the emission of the sample etched at 1:10 CH_4/H_2. The spectral resolution is 0.1nm.

8.3.2. Raman scattering

Samples of ZnTe were cleaned in acetone and IPA and blow dryed in Nitrogen prior to the experiment. The near back-scattering geometry configuration was used for the Raman scattering spectroscopy. The samples were cooled to 5K so that a near resonance condition was obtained between the 514.5nm line of the Argon ion laser and the energy gap of ZnTe. The laser produced 1.6mW (CW) and the beam was focused to a spot on the (100) plane giving an estimated laser penetration depth of 300nm. A Jobin-Yvon 1m double spectrometer and CCD were used for the experiment with a resolution of 1.4 cm^{-1}.

The Raman spectrum recorded before etching shows the 1LO phonon at 209cm^{-1} with FWHM of 2.3cm^{-1}, as predicted by the selection rules, Fig. 11a. Three smaller peaks at 207cm^{-1}, 215cm^{-1} and 219cm^{-1} were also visible. These peaks were attributed to combinations of the LO-TA, LO+TA and LO+LA phonons respectively[27].

By analogy with what had been observed in III-V semiconductors, namely undoped GaAs[28], the damage due to the reactive ion etching process would be expected to manifest itself as an asymmetric broadening of the 1LO phonon peak to lower energies due to a reduction in the long-range crystallinity of the material thus relaxing the q=0 selection rule[29]. This effect is accompanied by the appearance of phonon modes normally forbidden, e.g. the TO phonon in this geometry at 180cm^{-1}. The appearance of an emission representing the phonon density of states of the material might occur if the damage is sufficiently high to produce an amorphous structure[4]

After etching approximately 0.2μm of the epitaxial layer however, none of the previously mentioned possibilities, previously observed in III-V semiconductors, revealed themselves, as seen Fig. 11c for the ZnTe sample etched at the optimum conditions of 1:8 CH_4/H_2. This indicates that the etching process did not cause any detectable crystalline damage. The phonon combination peaks at the base of the 1LO phonon decreased in intensities probably due to variation of material quality as the etched surface gets closer to the ZnTe/GaAs interface. TEM examination of ZnTe/GaAs epitaxial layer approximately 0.8μm thick, has shown that the ZnTe layer contains a high density of misfit dislocations nearer to the interface, Fig. 8.5. After etching therefore, the layer sampled by the laser light may be of poorer quality thus yielding a different spectrum independently of the effect of the reactive ion etching. This hypothesis was tested by examining the spectra of a 2μm thick ZnTe epitaxial layer of which 40nm was etched away. The spectrum of the etched sample was very similar to that of the control sample.

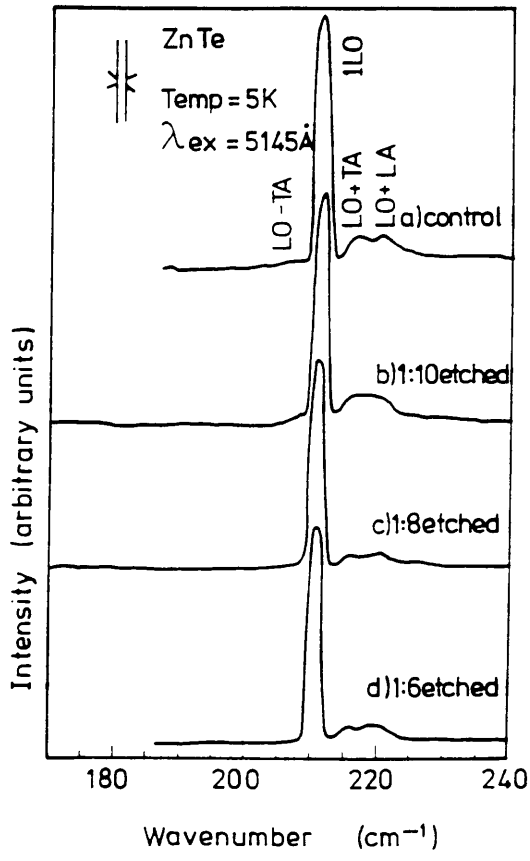

Figure 8.11: Raman spectra of a control ZnTe sample and samples etched as in Figure 8.7. The LO phonon is seen at 209cm^{-1} and the peaks at 207, 215 and 219cm^{-1} are assigned to combinations modes of LO-TA, LO+TA and LO+LA, the intensity of which has decreased due to the poorer crystalline quality of the epitaxial layer near the ZnTe/GaAs interface.

8.3.3. X-ray photoelectron spectroscopy

The etched surfaces were examined by XPS, as described in chapter 5, employing an ESCALAB MK II machine, with an electron analyser of concentric hemispherical design and using the Al K_α X-ray line at near normal acceptance angle. During scans, the base pressure of the analysis chamber was ~ 5x10^{-10}mbar. The core level signals emitted from Te (3*d*, 4*d*) and Zn (2*p*, 3*d*) electrons for ZnTe were observed.
The use of electrons with two different kinetic energies enables one to monitor any modification within two spatially resolved depths, approximately 1 and 3nm of the uppermost layer of the surface[30]. Three samples were examined by XPS, two of which were etched at CH_4/H_2 ratios of 1/6 and 1/8. The third sample was unetched and used for comparison. Fig. 8.12a, b, c and d show regions associated with emission from the Te 3*d*, Te 4*d*, Zn 2*p* and Zn 3*d* core levels respectively for an as-grown ZnTe sample and samples etched at CH_4/H_2 ratios of 1/6 and1/8·

The binding energy shifts seen between the same core level emission peaks or the different surface treatments are associated with charging effects on the surface, resulting in a displacement of all the peaks by the same amount to higher binding energies. The effect is corrected by an amount sufficient to result in the alignment of all the C *1s* peak binding energies.

All the Te *3d* spectra show two Te peaks, the Te $3d_{5/2}$ and Te $3d_{3/2}$, at energies of 573.5 and 584 eV, respectively. These peaks are accompanied by two extra peaks at 577 and 587.5eV which are known to be due to emission from the *3d* core levels of Te in an oxide environment[31]. It can be seen that the intensity of the Tellurium oxide peak, presumably a combination of TeO_2 and TeO_3[32], has decreased after etching as the CH_4/H_2 ratio changes from 1/8 to 1/6, i.e. as the hydrogen content decreases in the etch gas, within the sampling depth of the XPS measurements. The Te *4d* spectrum of the control sample shows an unresolved spin-orbit doublet around 41-42eV, accompanied by an oxide doublet at higher binding energies. The oxide doublet intensity decreases markedly after etching as the CH_4/H_2 ratio changes from 1/8 to 1/6. This implies that the amount of tellurium oxide formed after etching has decreased within a layer approximately 3nm beneath the surface.

The Zn *2p* spectra recorded before and after etching were very similar and show two peaks at 1022 and 1045eV, the Zn $2p_{3/2}$ and Zn $2p_{1/2}$, respectively. The Zn *3d* spectra recorded before and after etching were also very similar, indicating that there is little or no change in the binding energy of the zinc within approximately the top 3nm of the surface.

The areas of the Te *4d* and Zn *3d* peaks, determined by curve fitting the emission spectra, were integrated and the ratios of NTe oxide/ NTe, NZn oxide/ NZn and NTe/ NZn were calculated. These ratios were corrected for the photoionisation cross section and the escape depths of the emitted electrons[33] as described in chapter 5. The peak areas and the ratios are presented in table I

Sample	Te	Te oxide	Zn	Zn oxide	NTe oxide /NTe	NZn oxide /NZn	NTe /NZn
Control	61	38	100	0	0.623	0	0.137
1/6	100	0	100	0	0	0	0.226
1/8	77	22	89	11	0.286	0.123	0.195

Table I: The peak areas of the Te *4d* and Zn *3d* core levels and the ratios of NTe oxide/ NTe, NZn oxide/ NZn and NTe/ NZn for ZnTe control sample(unetched) and samples etched in 1/6 and 1/8 (optimum) ratios of CH_4/H_2. χ^2 values were between 1.28 and 6.13.

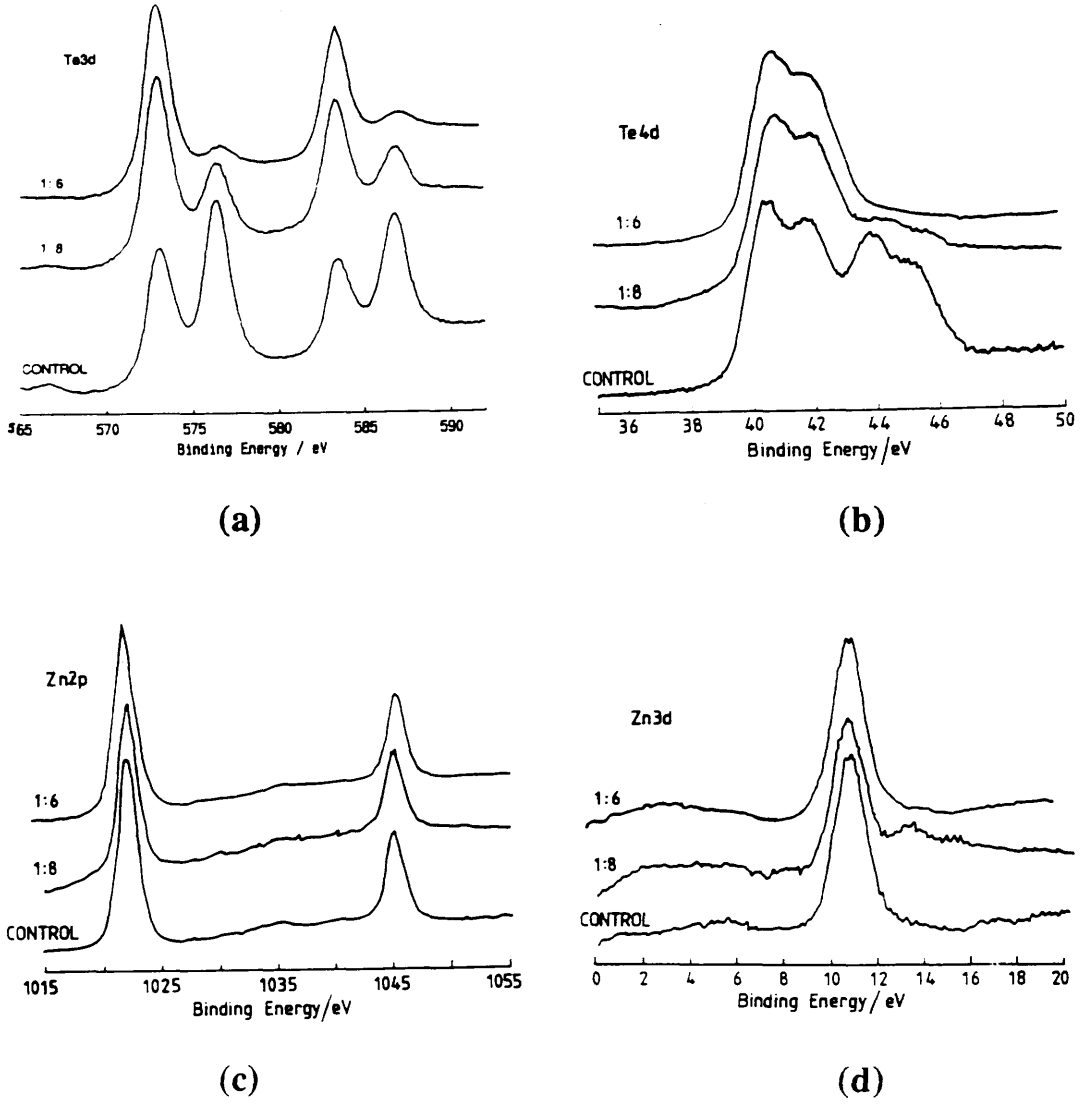

Figure 8.12: XPS spectra of: (a) Te 3*d*, (b) Te 4*d*, (c) Zn 2*p*, and (d) Zn 3*d* for unetched ZnTe (bottom), etched ZnTe in 1:8 (middle) and 1:6 (top) mixture of CH_4/H_2.

8.4. Characterisation of CH_4/H_2 etched ZnSe

8.4.1. Photoluminescence spectroscopy

The spectra of ZnSe samples were collected using the 488nm and 364nm lines, respectively of a Spectra-Physics argon ion laser as the excitation source. Photoluminescence spectra of ZnSe was collected using near back scattering geometry. Three pieces of a ZnSe sample were etched in a methane to hydrogen gas ratio of 1/2, 1/3 and 1/4, while a fourth piece was retained as a control sample. The low temperature photoluminescence (5K) spectra of the four samples with a spectral resolution of

0.1nm. Fig. 8.13. All the samples showed deep level emission at 530nm. The intensity of this emission has decreased monotonically, with respect to the near band edge emission, as the hydrogen content in the etching gas is increased from 1/2 through 1/4 indicating an effect related to hydrogen. A more detailed near band edge emission spectra is shown in Fig. 8.14 in which peaks 1 to 6 were assigned as follows:
Peak (1), appears at 443.4nm, is credited to the light and heavy hole free exciton[34].

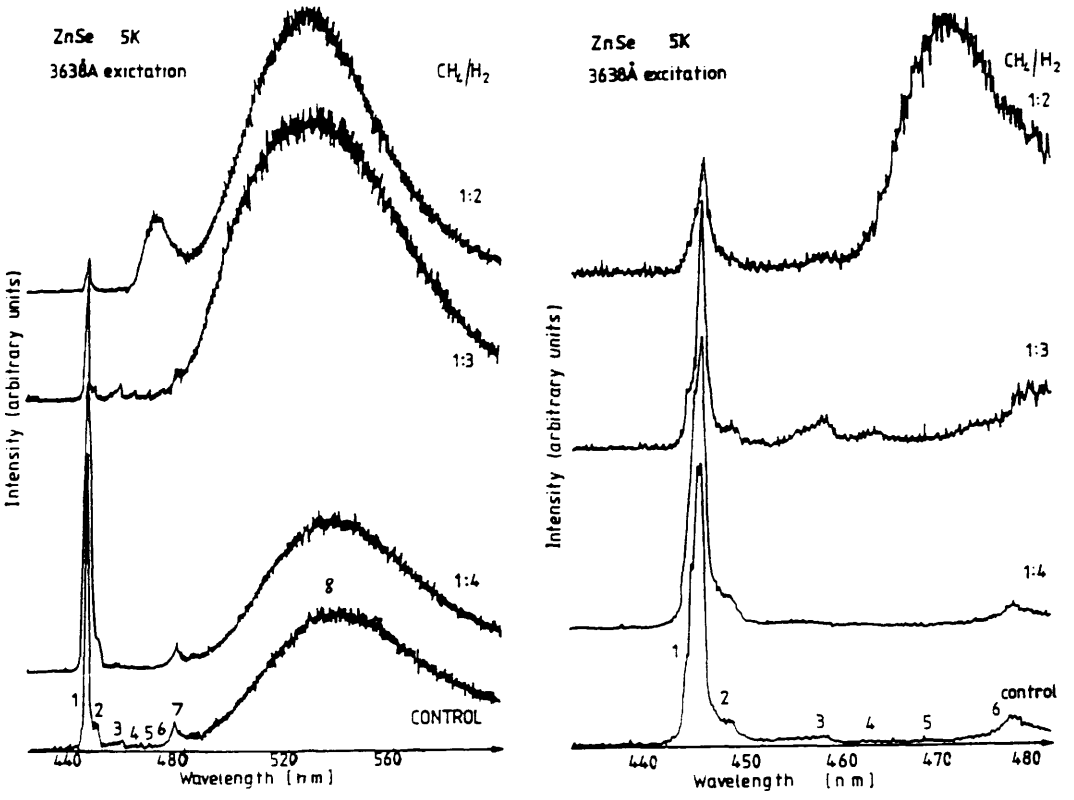

Figure 8.13 *(left)*: 5K photoluminescence of ZnSe/GaAs etched in CH_4/H_2 at various ratio. The spectrum is from the control sample. Peaks 1 is the light and heavy hole exciton, peak 2 the bound exciton to a Zinc vacancy acceptor, peaks 3, 4 and 5 are phonon replicas, peak 6 is unidentified, peak 7 is the so-called "Y-line" associated with dislocations and peak 8 is related to deep levels.
Figure 8.14 *(right)*: Expanded near band gap 5K photoluminescence of control and etched ZnSe/GaAs samples. The assignment is given in Fig. 8.13 as well as the text.

Using a higher resolution (0.01nm), peak 1 can be resolved into three separate peaks, Fig. 8.15. The peaks are identified, according to the literature, as (1a) the light and heavy hole free exciton (FE), (1c) a neutral donor bound exciton $(D^\circ, X)_{n=0}$ and (1b) its excited state $(D^\circ, X)_{n=1}$.

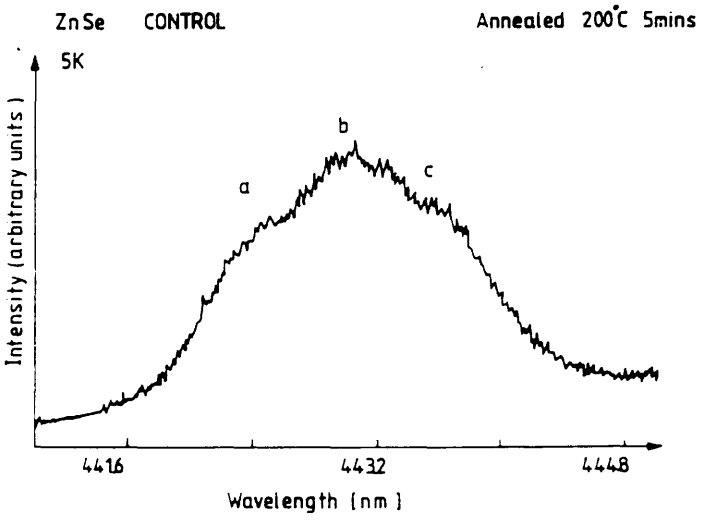

Figure 8.15: Expanded peak 1 in the 5K emission of ZnSe/GaAs control sample. After annealing the three peaks 1a, 1b and 1c are clearly resolved and assigned to the light and heavy hole exciton, to an excited state of the neutral donor bound exciton and to the ground state of the neutral donor bound exciton, respectively.

Since the strain in these epitaxial layers is unknown, the information is very limited. Peak (2) is assigned to Zinc vacancies (A°, X) while peaks (3), (4) and (5) are its phonon replicas since they occur at intervals equal to the 1LO phonon energy of 31meV. Peak (6) matches a phonon replica in the control and in the etched samples (see, for example, spectra for 1/2 ratio of CH_4/H_2 in Figs. 8.13 and 8.14). However, it appears to change its intensity in the etched samples (Fig. 8.14) but not significantly in the etched and annealed samples (Fig. 8.16) as discussed below. Peak (7), occurs at 4763Å and it is labelled the 'Y line' in the literature being assigned to extended dislocations[34]. The broad peak denoted (8) is unidentified, probably related to deep levels.

In order to remove the hydrogen incorporated into the samples during etching, were all annealed at temperatures of 100, 150 and 200°C for a period of 5 minutes in pure N_2 atmosphere. After annealing at (Fig. 16) the intensity of peak (7) , related to extended dislocation[34], has decreased while the intensity of peak (2), due to Zinc vacancies, and its associated phonon replicas have increased dramatically in intensity.

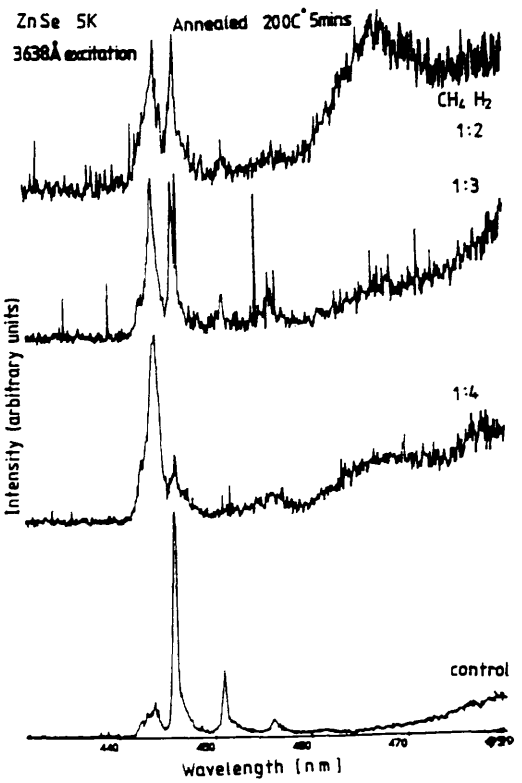

Figure 8.16: 5K photoluminescence of etched and annealed ZnSe/GaAs.

The improved ratio of intensities of the bound exciton over the deep level emission is a clear indication of the decreasing presence of activity, defect, and/or compensating centres. Peak (6) has also decreased monotonically in intensity as the amount of hydrogen increases in the etching gas indicating that the hydrogen is passivating this as a yet undefined impurity level.

8.4.2. Raman scattering

The Raman spectrum of ZnSe was recorded at 457.9nm the control sample, Fig. 8.17, and it shows the 1LO phonon at 250cm^{-1} and the 2LO phonon at 500cm^{-1}. There is also a broad peak centred at 461.0nm and this wavelength did not vary by changing the excitation line from 457.9nm to 454.5nm which therefore implies a photoluminescence background, Fig. 8.18.

The Raman spectra of the etched samples are also shown in Fig.8.17. After etching, the relative intensities of the 1LO and 2LO phonons remained unchanged. There was neither evidence of asymmetric broadening of the 1LO phonon nor evidence of the symmetry forbidden TO phonon indicating no detectable etching-induced damage.

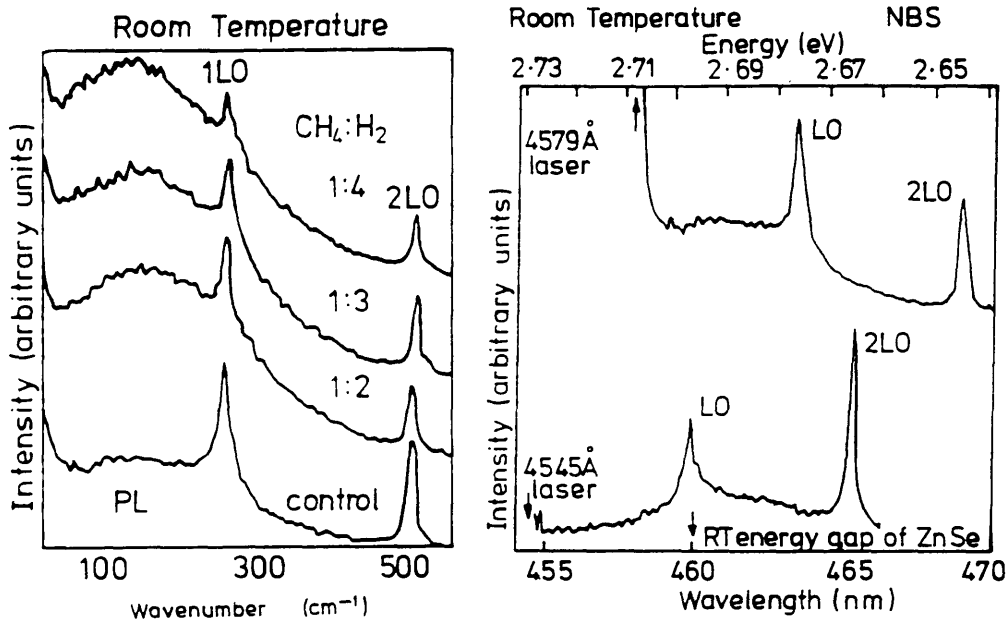

Figure 8.17 *(left)*: Room temperature Raman spectra of the control and etched samples of ZnSe/GaAs

Figure 8.18 *(right)*: Room temperature Raman spectrum of ZnSe/GaAs control sample probed using the 4579Å and 4545Å laser lines.

The intensity of the luminescence background has increased after etching which is probably a reflection of the enhanced near-gap luminescence after exposure to hydrogen.

8.4.3. X-ray photoelectron spectroscopy

The core level signals emitted from electrons of Se $3d$ and Zn ($2p$, $3d$) for ZnSe, were observed. Figure 8.19a, b and c shows the Se $3d$, Zn $2p$ and Zn $3d$ spectra of ZnSe samples etched in CH_4/H_2 ratios of 1/8 and 1/10, and a control (unetched) sample. All the Se $3d$ spectra show a peak at approximately 57eV, in addition, the spectrum of the control sample shows a peak at 61.5eV which may be an emission from a $3d$ core level of Se in an oxide environment. The fact that the peak at 57eV has decreased implies that the selenium oxide layer thickness has decreased remarkably as a result of the etching process.

The Zn $2p$ spectra recorded before and after etching were very similar to those of ZnTe and show two peaks at 1022 and 1045eV, the Zn $2p_{3/2}$ and Zn $2p_{1/2}$, respectively. The Zn $3d$ spectra recorded before and after etching were also similar to their ZnTe counterpart showing a peak at 11eV, implying that the zinc binding energy did not change after etching.

The areas of the Se 3*d* and Zn 3*d* peaks, determined by curve fitting the emission spectra, were integrated and the ratios of NSe oxide/ NSe, NZn oxide/ NZn and NSe/ NZn were calculated. These ratios were corrected for the photoionisation cross section and the escape depths of the emitted electrons. The peak areas and the ratios are presented in table II

Sample	Se	Se oxide	Zn	Zn oxide	NSe oxide /NSe	NZn oxide /NZn	NSe /NZn
Control	72	28	100	0	0.388	0	0.257
1/8	92	8	96	4	0.086	0.041	0.343
1/10	100	0	100	0	0	0	0.358

Table II: The peak areas of the Se 3*d* and Zn 3*d* core levels and the ratios of NSe oxide/ NSe, NZn oxide/ NZn and NSe/ NZn for ZnSe control sample and samples etched in 1/8 and 1/10 ratios of CH_4/H_2. χ^2 values were between 1 and 5.27.

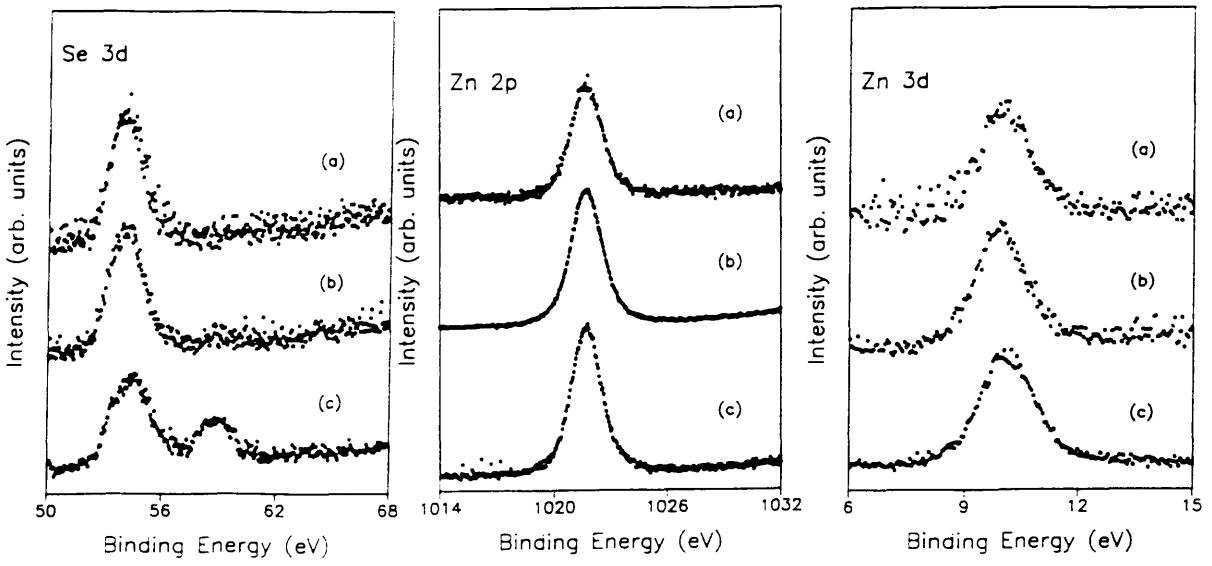

Figure 8.19: XPS spectra of: (A) Se 3*d*, (B) Zn 2*p*, and (C) Zn 3*d* for ZnSe RIE in (a)1:8, (b)1:10 mixture of CH_4/H_2 and (c) netched ZnSe.

8.5. Characterisation of CH_4/H_2 etched CdTe

8.5.1. Evaluation of Schottky diode parameters

To examine the effect of the etching process on n-type (111)-CdTe (resistivity =0.209Ω-cm) Schottky diodes have been made on RIE surfaces, with surfaces wet

etched in Br/MeOH for comparison. Ohmic contacts were made by alloying in In/Ga at 150°C for 1min. The samples were patterned for Schottky contacts using photoresist as a mask and they were then etched with CH_4/H_2 using the conditions given in chapter 8 and at ratios of 1/6, 1/8 and 1/10. After etching approximately 100nm, the samples were exposed to air for less than 5min before loading in the evaporator. Four Schottky contacts, 70nm thick gold layer and 200μm in diameter were deposited on each sample at a base pressure of $1\text{-}2x10^{-6}$mbar. A HP4145B Semiconductor Parameter Analyser was used to probe the contacts and the forward and reverse bias characteristics examined. The barrier height Φ_B, the ideality factor n and the reverse leakage current I_r were calculated/measured for each of the four contacts and the values were averaged for each sample.

Results

The forward bias characteristics of the RIE samples are shown in Fig. 8.20.
The Barrier hight Φ_B was calculated using the equation 8.2, the ideality factor n and the reverse leakage current I_r measured at 0.6V, were evaluated and the results are listed in table I. Wet etched CdTe is used for comparison. However, CdTe samples etched in 1% Br/MeOH had resistivities of 6.94Ω-cm and 1.52Ω-cm and the contacts were made on the (111)A face. The value of m* was taken as $0.11m_e$[35] and the effective Richardson constant A*[(1)] as $12A.cm^{-2}K^{-2}$.

sample	Barrier height Φ_B (V)	Ideality factor (n)	Reverse leakage current I_r (nA)
1/6: CH_4/H_2	0.69±0.03	1.73±0.16	1.67±0.33
1/8:CH_4/H_2	0.73±0.01	1.830±0.005	2.76±0.32
1/10:CH_4/H_2	0.71±0.03	1.75±0.03	40.99±6.1
1% Br/MeOH	0.85±0.01	1.33±0.19	--

Table I: The barrier height, Ideality factor and reverse leakage current of CdTe samples RIE etched using CH_4/H_2 at various ratios.

It can be seen that at the optimum etching conditions, i.e. 1/8 ratio of CH_4/H_2, the barrier height is 0.73V lower than the height of the wet etched sample but in agreement with values in the literature[36,37]. However, the ideality factor for the 1/8 ratio appears to be slightly higher than the rest of the samples.

(1) The effective Richardson constant used here was calculated using the formula $A^* = (4\pi qm^*k^2)/h^3$ from the thermionic emission theory. It neglects the optical phonon scattering and quantum mechanical reflection.

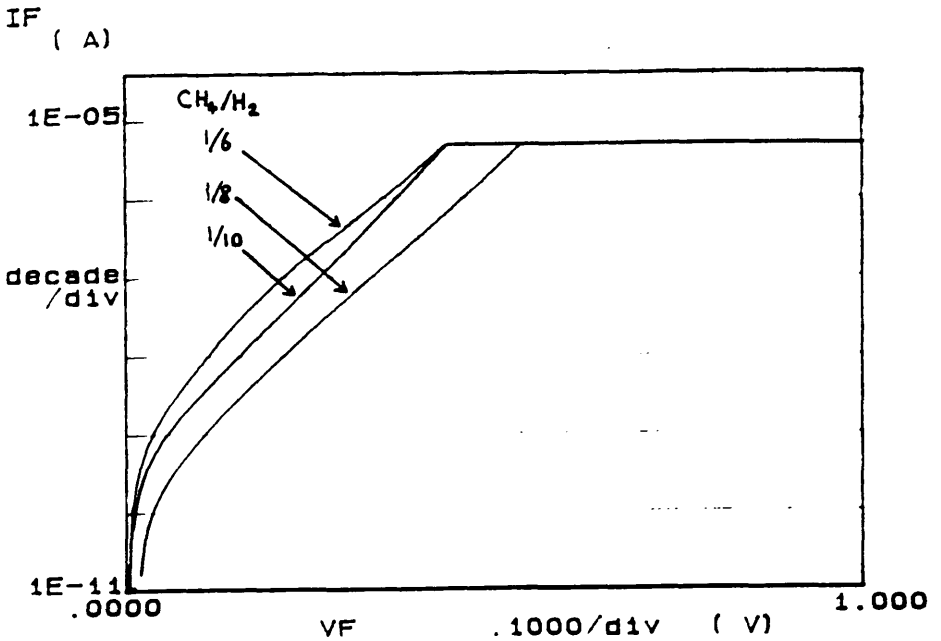

Figure 8.20: An example of the I-V characteristics of forward biased CdTe Schottky diodes made on samples etched in CH_4/H_2 ratios of 1/6, 1/8 and 1/10.

8.5.2. X-ray photoelectron spectroscopy.

The X-ray photoelectron spectroscopy (XPS) and X-ray excited Auger electron spectroscopy (XAES) experiments were performed using Al K_α radiation and a concentric hemispherical analyzer in the analysis chamber of ESCALAB MK II. Broad scans over the whole accessible energy range were taken with an analyzer pass energy of 50eV (overall resolution ~1.5eV), whereas detailed core level emission spectra were recorded with a pass energy of 20eV (overall resolution ~1.2eV).

All samples, with the exception of the one undergoing the Bromine- methanol (Br/MeOH) wet etch treatment, were stored and transported under methanol until about 10min before insertion in the loadlock chamber of the ESCALAB MK II, at which point they were exposed to air. The 1% Br/MeOH wet etch treatment was performed on the as-grown sample surface after which the surface was exposed to air for less than 10min. The samples were degreased by ultrasonic agitation for 5min in each of trichloroethylene, acetone and methanol respectively.

The sample was emersed in the etchant and swiveled gently for 2min. This was followed by etch quenching with methanol until the distinctive orange colour of 1% Br/MeOH is no longer present. The sample was then rinsed in fresh methanol for 10min using ultrasonic agitation, repeating the procedure to remove any trace of Bromine from the surface.

By inspecting the XPS broad scans (-2 to 1400eV binding energy) shown in Fig. 8.21, differences in the amount of oxygen and carbon contamination are evident between the as-grown, RIE and Br/MeOH wet etched (111) surfaces of the n-CdTe. The as-grown surface, which had been exposed to air for undeterminable period of time, is the most heavily contaminated, exhibiting the strongest oxygen and carbon emission intensities. These emissions, by comparison, are less intense for all the etched surfaces, being noticeably more reduced for the Br/MeOH etched surface than for the RIE surfaces, but there is no evidence of Br contamination on the Br/MeOH etched surface. However, any variation in contamination levels i.e. amount of oxygen and carbon among the three RIE surfaces is clearly not detectable by visual inspection alone. Although detailed emission spectra have been recorded for the oxygen 1*s* and carbon 1*s* core levels, interpretation of their line shape in difficult.

The emission spectra of the Cd 4*d* and Te 4*d* core levels for the different surface treatments can be used as a visual illustration of the changes in the stoichiometry of the surface layers (figure 8.22). These core levels have been selected because the difference between their kinetic energy is ~30eV, very small compared to their average kinetic energy ~1460eV therefore they have approximately the same photoelectron escape depth. Therefore they should be affected to the same degree by the surface containments, although their photoionisation cross-sections are different. For the stoichiometric surface (i.e. equal quantities of Cd and Te) the Cd emission will be less intense than that for Te (Cd emission area ~ 0.6 x Te emission area).

From Fig. 8.22, it can be seen that the Cd 4*d* emission with respect to the Te 4*d* substrate emission is greatest for the as-grown surface and least for the Br-MeOH wet etched surface. The more subtle differences in stoichiometry are readily demonstrated from the ratio of the areas under the emission peaks, determined by curve fitting the emission spectra. Cd 3*d* and Te 3*d* core level emissions have been used for ratio determination as presented in table III.

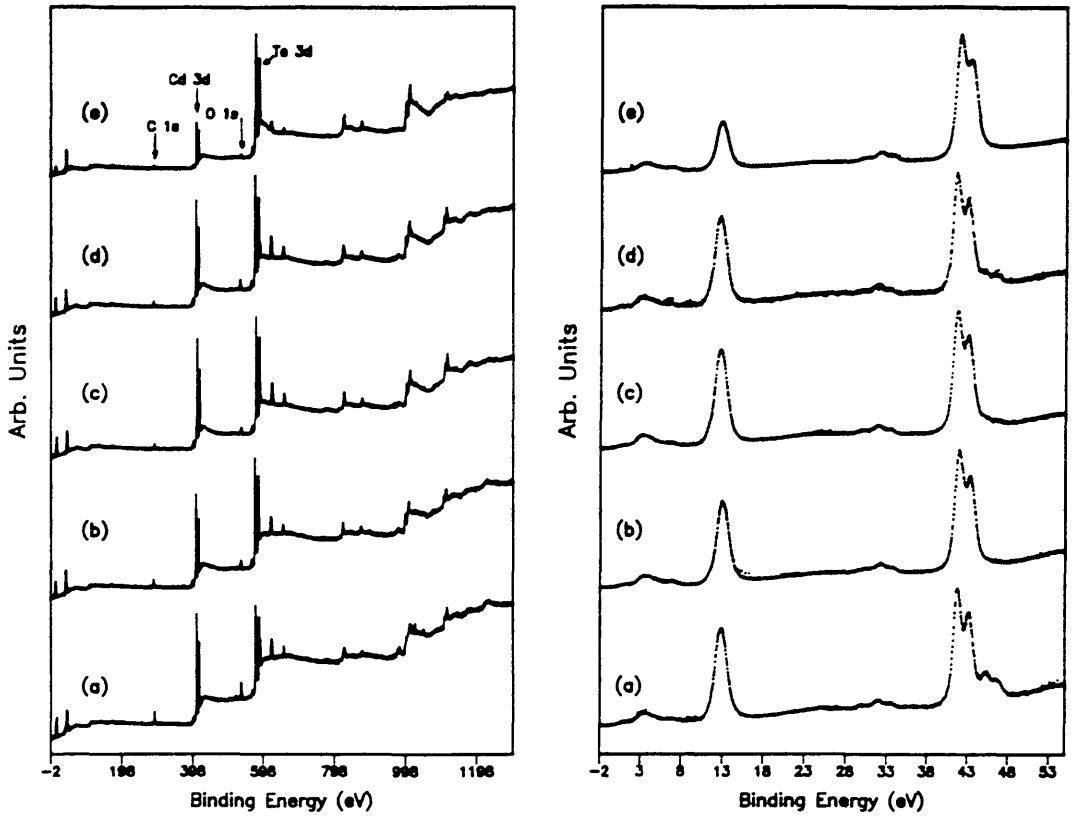

Figure 8.21 *(left)*: Broad scan XPS spectra of (111) n-CdTe surfaces after different treatments: (a) as grown, (b) CH_4/H_2 ; 1/6, (c) CH_4/H_2 ; 1/8, (d) CH_4/H_2 ; 1/10 and (e) Br/MeOH etched.

Figure 8.22 *(right)*: XPS spectra of the Cd 4*d* and Te 4*d* core levels from the (111) surface of n-CdTe after different treatments: (a) as grown, (b) CH_4/H_2 ; 1/6, (c) CH_4/H_2 ; 1/8, (d) CH_4/H_2 ; 1/10 and (e) Br/MeOH etched.

Sample	Te/Cd	(Te+Te oxide)/Cd	Te/Te oxide
as-grown	0.97	1.42	2.13
	(0.59)	(0.86)	(1.28)
S1 (1/6 : CH_4/H_2)	1.28	1.36	15.67
	(0.77)	(0.82)	(9.46)
S2 (1/8 CH_4/H_2)	1.22	1.34	10.11
	(0.74)	(0.81)	(6.11)
S3 (1/10 CH_4/H_2)	1.19	1.43	4.88
	(0.72)	(0.86)	(2.95)
S3*	1.35	1.45	13.29
	(0.82)	(0.88)	(8.03)
Br/MeOH	2.85	2.86	---
	(1.72)	(1.78)	---

Table III: Ratio of peak intensities of Te to Cd and Te to Te oxide of the 3*d* core levels for various surface treatments of the n-CdTe (111) established from curve fitting the photoelectron spectra. The values in parentheses have been corrected for differences in photoelecton escape depths and photoionisation cross section. S3* is a second scan of sample S3 after 3 days storage in UHV with constant illumination from the X-ray source. For comparison, the vacuum cleaved stoichiometric surface Te/Cd = 1.43 before correction and (0.86) after. The error in the above values is ±0.06.

The RIE surfaces appear to be slightly rich in Cd for the 1/6 and 1/8 ratios irrespective of whether the total Te emission, i.e. Te plus Te oxide, or just the Te emission alone is considered. Although, taking the error limits into account, these surfaces could be considered stoichiometric. However, the 1/10 ratio suggests a stoichiometric surface for the total Te emission (i.e. Te plus Te oxide) for the 'initially' scanned surface, S3. Both the Te/Cd peak intensity ratio and Te/Te oxide ratio were observed to increase as the storage time in vacuum increased during which the sample surface was under illumination from an x-ray source for a period of ~3 days. For the as-grown surface if the total Te emission is considered, the (Te + Te oxide) /Cd ratio is comparable with that from a cleaved surface (i.e. stoichiometric surface), whereas, consideration of the Te emission signal alone would suggest this surface to be Cd rich. In contrast to the other surface, the Br-MeOH wet etched surface is Te rich i.e. Cd deficient.

8.5.3. Changes in the chemical environment of the surface atoms

Changes in the chemical environment of the Cd and Te atoms in the etched layers can be illustrated by a comparison of line shapes of Cd 4*d* and Te 4*d* emission spectra, Fig. 8.22. A greater amount of Te oxide is observed for the as-grown surface, by comparing the intensity of the Te emission and Te oxide emission peaks i.e. the latter appearing on the high binding energy side of the Te emission. For the RIE surfaces, the Te oxide is less than on the as-grown surface and the intensity decreased as the ratio of CH_4/H_2 was varied from 1/10 to 1/6. For the Br/MeOH etched surface, only minimal Te oxide emission is observed, being only just detectable on the slightly more surface sensitive Te 3*d* emission spectra, Fig. 8.23. It is worth mentioning that the photoelectron escape depth for the Te 3*d* core level is ~20Å as compared with ~30Å for the Te 4*d* core level. The changes in the amount of the Te oxide are reflected in the (Te)/(Te oxide) ratio presented in table III.

It should be remembered that whereas the Br/MeOH etched surface was exposed to air for less than 5min before insertion in the ESCALAB loadlock, the other surfaces were stored under methanol for several weeks, during transport and storage, then exposed to air for < 5min before entering the vacuum chamber. Whether methanol reduces the surface oxide, has not been determined but it is worth noting that a reduction in the surface oxide upon RIE of other II-VI semiconductors surfaces was observed earlier in this chapter. It was also noticed for sample S3, the intensity of the Te oxide signal decreased with storage under constant X-ray illumination in the vacuum chamber, see (Te)/(Te oxide) ratio in table III. This effect was not observed for the wet etched surface which, by comparison, had not been stored under methanol. The effect of storage of these surfaces under vacuum were not studied for the other RIE etched samples.

8.5.4. X-ray excited Auger emission spectroscopy

Inspection of the bulk Te emission lines suggests Te to be present in more than one chemical environment, i.e. possibly Te in CdTe and elemental Te environment. Since the binding energy separation between Te in CdTe and Te in the elemental state is reported to be only 0.15-0.4eV[38] with the experimental resolution of the XPS, these two peaks cannot be resolved. However, the effect is clearly seen by comparison of how well the two spin-orbit components (j=5/2 and 3/2) in the Te 4*d* emission spectra are resolved.

The spin-orbit split components are better resolved for the as-grown surface, the resolution diminishing for the RIE surfaces (the spectral line being comparable for these

three samples), and finally, being least well resolved for the Br/MeOH etched surface. This suggests the chemical environment of the Te atom in the etched layers to vary with the surface treatment. For Br/MeOH etched surface, the above observations suggest Te to be present in both its elemental and CdTe environments. In comparison, surfaces etched in Be/MeOH :ethylene glycol solution[39] have been reported to show mostly Te in the elemental rather than CdTe state.

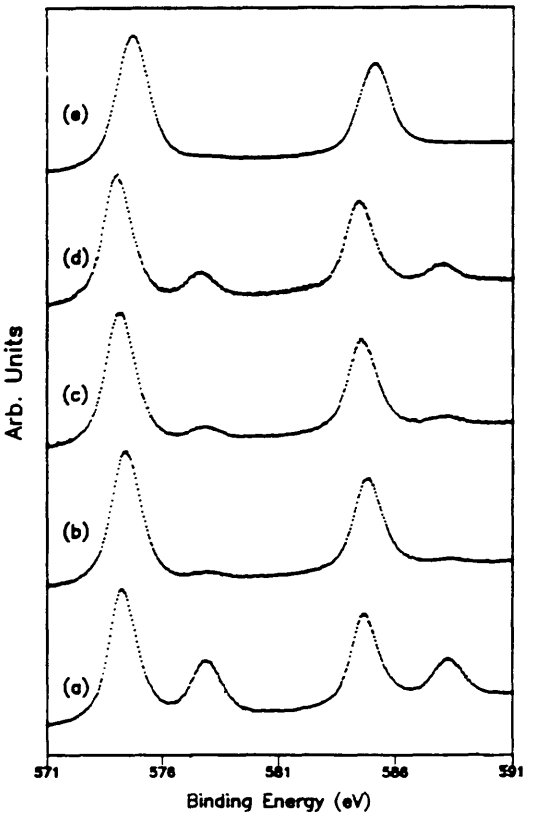

Figure 8.23: XPS spectra of the Te 3*d* core level from differently treated (111) surface of n-CdTe: (a) as grown, (b) CH_4/H_2 ; 1/6, (c) CH_4/H_2 ; 1/8, (d) CH_4/H_2 ; 1/10 and (e) Br/MeOH etched.

It is possible that for all the RIE surfaces Te in these two chemical forms is present but in different amounts to these observed for Br/MeOH etched surface i.e. this would account for the difference in resolution of the Te 4*d* core level emission spectra. The changes in the chemical environment of the Te is also evident by changes in the FWHM of the Te emission. The FWHM of the Te 3*d* core level is 1.4± 0.05eV for the as-grown, 1.5±0.05eV for all the RIE surfaces and 1.6±0.05eV for the Br/MeOH etched surface.

In contrast, no significant changes Cd 4*d* or 3*d* core level emissions were observed, table IV. However, changes in the chemical environment of Cd are less easy to detect from the XPS peaks, since the binding energy for Cd in CdTe and $CdTeO_3$ is identical. Such effect, however, can be detected in the changes in position and line shape of the Cd Auger peaks (X-ray excited Auger Emission Spectroscopy (XAES)).

	FWHM					
Sample	Te 3d		Cd 3d		Te 4d	Cd 4d
	$J_{5/2}$	$J_{3/2}$	$J_{5/2}$	$J_{3/2}$	$J_{5/2}$ + $J_{3/2}$	$J_{5/2}$ + $J_{3/2}$
as-grown	1.40	1.35	1.20	1.20		
S1 (1/6 CH_4/H_2)	1.50	1.50	1.25	1.25	2.65	1.65
S2 (1/8 CH_4/H_2)	1.50	1.45	1.15	1.25	2.60	1.75
S3 (1/10 CH_4/H_2)	1.50	1.45	1.20	1.20	2.55	1.70
Br/MeOH	1.65	1.60	1.15	1.10	2.65	1.70

Table IV: Variation of full width half maximum (FWHM) of Cd and Te photoelectron emission peaks. The error in FWHM is ±0.05eV.

To identify differences in the XAES spectra, a combination of line shape analysis and comparison of the modified Auger parameter (α')[39] has been adopted. The α' is given by:-

$$\alpha' = h\nu - \{ E_{B.E.}(M_4N_{4,5}N_{4,5}) - E_{B.E.}(3d_{5/2}) \} \qquad (8.4)$$

where hν is the photon energy of the excitation source (hν =1486.6eV).

$E_{B.E.}$ ($M_4N_{4,5}N_{4,5}$) is the binding energy of the Auger ($M_4N_{4,5}N_{4,5}$) line.

For the three RIE surfaces, the line shape of the Auger emissions were virtually identical, Fig. 8.24, exhibiting only very small changes in intensity of some features, acceptable within experimental error. The line shape is comparable with that associated with Cd-Te bonding. For the Br-MeOH etched surface, the line shape was not significantly different from the RIE surfaces, suggesting the Cd environment to be that of CdTe. It is unlikely on this surface that Cd-O bonds will form in view of the minimal amount of oxide present. Within the error limits, values of (α') for all surfaces treated in this study suggest the Cd bonding to be that of CdTe, table V. The (α') value of the as-grown surface again suggests the environment of Cd to be that of CdTe. However, a closer inspection of the line shape revealed it to be distinctively different from the treated surfaces, tending towards that of Cd-O bonding[40]. It would appear that for this surface, the Cd is in more than one environment, namely a combination of Cd in CdTe and some

form of Cd oxide, with the CdTe component dominating sufficiently for the (α') to suggest CdTe.

As a natural extension, the X-ray excited Auger spectra of Te ($M_4N_{4,5}N_{4,5}$) were used to investigate the etched surface. These signals are complicated by the presence of the Te 3*s* XPS signal and O (KL_1L_1) Auger lines at the same energies. Even for the Te ($M_4N_{4,5}N_{4,5}$), which has been used in the modified Auger parameter, the Auger line overlaps a satellite emission from the Te 3*s*. This is however of low intensity and should not affect the value obtained. For all the RIE surfaces, the Te Auger signal looked identical to Te in CdTe[40]. However, the value of (α') for CdTe (1063.5eV) and TeO_2 (1063.2eV) are indistinguishable with the experimental resolution used, and the value obtained for these surfaces fall within this range, table V.

Sample	$(\alpha')_{Cd}$ (eV)	$(\alpha')_{Te}$ (eV)
as-grown	787.1	1063.4
S1 (1/6 CH_4/H_2)	787.4	1063.4
S2 (1/8 CH_4/H_2)	787.4	1063.2
S3 (1/10 CH_4/H_2)	787.1	1063.2
Br/MeOH	787.1	1064.7
Elemental Te	--	1064.9

Table V: Modified Auger parameter (α') calculated using the $3d_{5/2}$ core level emission and $M_4N_{4,5}N_{4,5}$ Auger peaks for both Cd and Te. The error in (α') is ±0.15eV.

For the Br/MeOH wet etched surface, the Te Auger line shape is different as compared with the RIE etched surfaces or elemental Te, possibly suggesting Te in more than one environment. The value of (α') is closer, but not that of elemental Te or Te in CdTe. [N.B. line shape similar to Br/MeOH: ethylene glycol etched surfaces][41]. For the as-grown surface, a different line shape is observed. There is evidence of Te in CdTe environment but mixed with Te oxide features which are stronger than for the treated surfaces. The (α') is closer to the value of CdTe but the line shape clearly shows the presence of Te oxide (oxygen Auger signal also present).

Characterisation of the surface oxides can be made by comparison of binding energy shifts between the respective constituent atoms of the semiconductor and their corresponding oxides. This shift has been measured for the Te 3*d* core level emissions for different surfaces and it is 3.5±0.05eV for all the different surface treatments. [N.B. measurements made between the centres of the bulk and the oxide peaks which can be confused by the presence of elemental Te in CdTe peak]. This separation may correspond to either $CdTeO_3$ or TeO_2 as quoted in the literature[40]. Hence caution must

be exercised in allocation of the specific oxide composition. For the RIE and Br/MeOH wet etched surfaces, it is suggested that the oxide is TeO_2 since no evidence was found to support the presence of Cd oxide in the Auger line spectra, Fig. 8.24.
For the as-grown surface, the oxide is suspected to be that of $CdTeO_3$, since Cd Auger spectra suggests the presence of Cd-O bonding, and FWHM in XPS of Cd emissions show no broadening as would be seen with CdO formation.
The binding energy shifts seen between the same core level emission peaks or the different surface treatments are associated with charging effects on the surface, resulting in a displacement of all peaks by the same amount to higher binding energies. The effect is commonly seen with CdTe and is associated with the low electrical conductivity of CdTe caused by low free carrier concentration and low carrier mobilities[40]. For the spectra shown in section 8.5.2. onward, the binding energy shifts have been corrected by an amount sufficient to result in the alignment of all the
C *1s* peak binding energies.

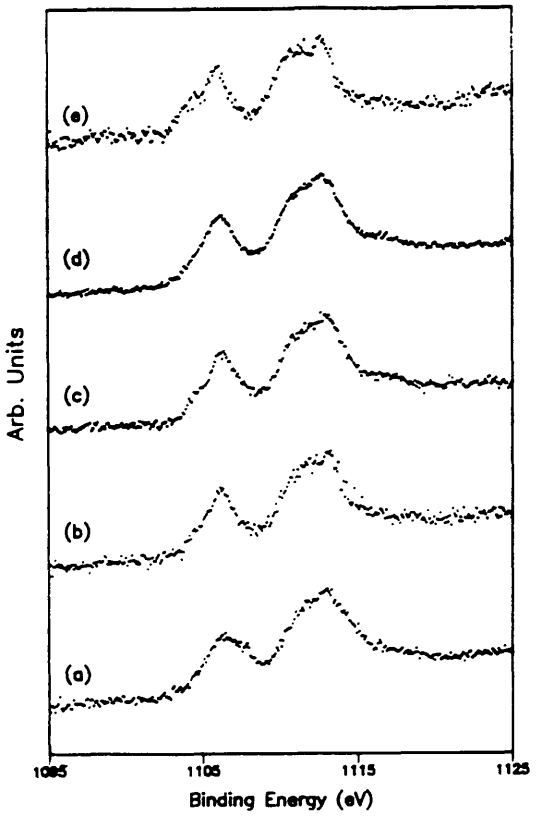

Figure 8.24: X-ray excited Cd(MNN) Auger lines from the differently treated (111) surface of n-CdTe: a) as grown, b) CH_4/H_2 ; 1/6, c) CH_4/H_2 ; 1/8, d) CH_4/H_2 ; 1/10 and e) Br/MeOH etched.

8.6. Discussion and conclusions

In the previous chapter, an etch process was described for etching ZnTe ZnSe and CdTe. In this section, the optical properties of CH_4/H_2 etched ZnTe and ZnSe will be discussed first. The XPS analysis of ZnTe and ZnSe etched surfaces will then be discussed. Since electrical measurements were possible on etched CdTe surfaces using Schottky diodes, these will be discussed jointly with the detailed XPS and XEAS analyses.

Photoluminescence (PL) examination of RIE etched ZnTe in CH_4/H_2, Fig. 8.7 and 8.8, suggested that there is a link between the decrease in intensity of the near band edge luminescence (the dominant excitonic peak at 2.368eV was decreased by two orders of magnitude with respect to the intensity of the unetched sample) and the hydrogen content in the etch gas. The DAP emission, which is probably related to Zn-vacancy impurity complex, has also showed a similar behaviour.

To remove the hydrogen diffused into the etched samples during the etching process, the samples were annealed at 250°C for 15min. The near band edge PL spectra after annealing have shown, on one hand, an increase in the intensity of the dominant excitonic peak by an order on magnitude i.e. still an order on magnitude weaker than the control sample before annealing. In addition, this peak showed a blue shift of 2meV, probably an indication of strain relaxation, and broadening ($\leq$ 5meV) which may be an indication of a minimal optical degradation of the optical quality of the material. However, it should be born in mind that the thickness of the epilayer was 1μm, and was etched for a depth of ~200nm i.e. the examined epilayer is 0.8μm thick. So after etching the laser light might have been sampling poorer quality material with high density of dislocations (penetration depth of the 488nm laser line used is ~ 79nm) as can be seen in the TEM micrograph shown in Fig. 8.5.

On the other hand, the DAP emission of the etched and control samples showed marked reduction in intensity after annealing. For the etched samples, this broad peak showed a well defined peak at 2.23 which may suggest that after annealing, a narrower range of energies is involved in the Zn-vacancy impurity complex.

Raman spectra of etched ZnTe samples showed no change in the 1LO phonon FWHM not the forbidden TO phonon appeared, indicating no etching-induced damage to the crystal. However, the intensity of the combination phonons, shown in Fig. 8.11, has decreased slightly. This can be explained in the way as above since the epilayer thickness after etching was 0.8μm and the penetration depth of the 514.5nm laser line is ~ 105nm.

For ZnSe, PL spectra of the samples etched at CH_4/H_2 ratios of 1/2, 1/3 and 1/4 were examined by PL and Raman spectriscopies. The PL spectra of the etched samples show

a monotonic decrease in the intensity of the deep level emission at 530nm (peak 8), with respect to the near band edge emission, as the hydrogen content in the etching gas increases from 1/2 to 1/4. The etched and control samples were annealed in order to remove the incorporated hydrogen at 100°C, 150°C and 200°C for 5min. Annealing at 200°C was the most effective in influencing the PL spectra and the spectrum of the control sample showed a decrease in the intensity of peak (1) and peak (7), related to extended dislocations. Meanwhile, the intensity of peak (2), related zinc vacancies, has increased upon annealing. In the etched samples, the relative change in intensity of peaks (1) and (2) is not monotonic, Fig. 8.16. However the intensity of peak (6) has decreased monotonically as the amount of hydrogen content in the etch gas increased indicating that the hydrogen is affecting this unidentified impurity level.
The relative intensity of the 1LO and 2LO phonons of Raman spectra did not show any change upon etching in CH4/H2 RIE neither did the symptoms of crystal damage, outlined in section 8.4.2., appear. This is a clear indication that in ZnSe, as for ZnTe, no etching-induced damage can be detected in Raman scattering

XPS analysis of the ZnTe etched surfaces showed no change in the binding energies of the zinc and tellurium, however tellurium oxides was observed to be less than that of the control sample with the minimum amount of oxide on the surface etched at CH_4/H_2 ratio of 1/6. In other word, the ZnTe surface etched at the optimum ratio of 1/8 exhibited some tellurium oxide over the probing depth of the photoelectrons , approximately 3nm. Generally, the Te/Zn ratio, table I, has increased upon etching, relative to the control surface, indicating that the surface has become slightly tellurium rich (Te/Zn ratios of 0.137, 0.226 and 0.195 for the control sample, etched at ratio 1/6 and 1/8 of CH_4/H_2 respectively).
By comparing the Te/Zn ratios for surfaces etched at 1/6 and 1/8 parts of CH_4/H_2, it can be seen that the addition of extra hydrogen in the etching gas may result in the formation of extra tellurium hydride, as an etch product, and therefore less tellurium will be left of the surface and detected by XPS.
If tellurium rich surfaces can be thought of as zinc deficient i.e. there are zinc vacancies on the surface, then the appearance of the broad peak at 2.23eV in Fig. 8.8 in the spectra of etched ZnTe can be explained (this peak is related to a Zn-vacancy impurity complex). As the hydrogen content in the etch gas increases, additional tellurium hydride will form leaving surfaces less rich in tellurium (smaller Te/Zn ratio in table I) i.e. less Zn- vacancies will form giving rise to a peak with weaker intensity at 2.23eV (Fig. 8.8).
It is worth noting that the broad peak at 2.23eV was assigned to a Zn-vacancy impurity complex. Since less tellurium oxide was formed on the etched surfaces shown by the

XPS measurements, oxygen can therefore be ruled out as the impurity that give rise to the peak at 2.23eV

The XPS analysis of ZnSe showed that the Se/Zn ratio increases upon etching i.e. the surfaces become Se rich (or Zn deficient) after etching, in agreement with the case of etched ZnTe discussed above. This may be due to the fact that the Zn etch products are most likely to be organometallics such as di-methylzinc (DMZn) and di-ethylznic (DEZn), both of which have higher partial pressures than the analogous Te and Se organometallic compounds e.g. DMTe, DETe, DMSe and DESe[44]. Therefore more Zn organometallic compounds are likely to form as etch products leaving Te/Se-rich etched surfaces.

It is also possible for Te and Se to form hydrides as etch products in the presence of hydrogen as in the case of CH_4/H_2 RIE. These compounds, H_2Te and H_2Se would have higher partial pressures than the Te/Se organometallic compounds mentioned above.

Unlike the case of etched ZnTe surfaces however, the ratio of Se/Zn has increased with increasing the hydrogen content in the etching gas (CH_4/H_2), the reason for which is not clear from this experiment.

In the next part of the discussion, the results of the XPS and Schottky diode evaluation will be considered. From table III it can be seen that all the etched CdTe surfaces have less tellurium oxide than the as-grown surface (the Te/Te oxide ratio). In particular, more tellurium oxide is detected on the CH_4/H_2 RIE etched CdTe as the hydrogen content increases in the etching gas, in agreement with what was observed for ZnTe.

The corrected Te/Cd ratios table III (values in brackets) show that the as-grown CdTe surface is Cd-rich relative to the vacuum cleaved stoichiometric surface. After CH_4/H_2 RIE, the ratio approaches that stoichiometric CdTe but still on the Cd-rich side being richest for the highest hydrogen content in the etching gas i.e. CH_4/H_2 ratio of 1/10. This may be so because the Cd organometallic compounds have a smaller partial pressure than Te organometallic compounds or hydrides[44] leading to the formation of relatively more Te volatile etching compounds. It is worth remembering that CdTe etches at a relatively high etch rate in pure hydrogen, chapter 8, leaving Cd droplets on the etched surface, as evidence of the formation of tellurium hydride as an etch product. On the other hand, CdTe surfaces etched in Br/MeOH are Te-rich which is in agreement with the literature[37,44,45].

It should be mentioned that the XPS ratios have been corrected for the electron escape depths and the ionisation cross sections. Lu et al[39] have obtained the relative composition of CdTe using several different approaches including calculated Scofield cross sections[42], atomic sensitivity factors (ASF) from the Perkin-Elmar XPS

handbook[38], ASF values from the work of Briggs and Seah[43] and the ASF values derived specifically for their ESCALAB MK II spectrometer. The relative compositions are remarkablly similar within ± 2%. This demonstrates that using the values for sensitivity factors available in the literature for quantitative XPS analysis can produce reasonable results.

For the Schottky diodes prepared on CH_4/H_2 RIE CdTe, table I, The barrier heights were in the range 0.7±0.01eV - 0.69±0.03eV comparable to that of Schottky diodes prepared on air-cleaved CdTe[47]. However, these barrier heights are lower than those of diodes prepared on Br/MeOH etched CdTe, namely 0.85±0.01eV (see table I and reference 46) . It can also be seen that the ideality factor of the CH_4/H_2 RIE CdTe are higher than that of Br/MeOH etched surfaces. This may be due to the fact that the CdTe crystal used for the CH_4/H_2 RIE is n-doped to ~$2.99 \times 10^{16} cm^{-3}$ compared to doping in the range of ~$10^{15} cm^{-3}$ for the crystal used for Br/MeOH etching. Higher doping concentration leads to a decrease in the barrier height and an increase in the probability of tunneling through the top of the barrier thus a departure for the ideal thermionic behaviour.

Recently, Van Meirhaeghe et al[45] have correlated the surface composition of annealed (111) n-CdTe with the barrier height of gold Schottky diodes made on these surfaces. They found that upon annealing, CdTe surface changes from Te-rich (For $T_{annealing}<200^oC$) to stoichiometric ($200^oC<T_{annealing}<240^oC$) to Cd-rich for $T_{annealing}>240^oC$. Meanwhile, the barrier height increases from ~0.85eV for Te-rich surface to 0.92eV for stoichiometric CdTe then decreases for Cd-rich surface. Van Meirhaeghe et al have suggested that the decrease in the barrier height is due to the presence of defects in the interface or to an increase interfacial interdiffusion or a combination of both.

For stoichiometric surfaces (low defect density) the interfacial reactivity is low and the barrier height is determined by the work function of gold (Φ_B =0.92eV). For the non-stoichiometric surface containing many defects, interaction between gold and CdTe occurs, and Φ_B is determined either by the interaction products or by defects, pinning the Fermi level.

For the CH_4/H_2 RIE CdTe, The drop in Φ_B could be attributed to defect related to Cd excess which can behave as shallow donors[48] (Cd_i^{2+}) and provoke substantial tunneling through the barrier top.

To conclude this chapter:

1. low temperature photoluminescence spectroscopy (PL) has shown that CH_4/H_2 RIE of ZnTe results in a two orders of magnitude reduction in intensity of the near band edge emission and the DAP. The reduction is proportional to the hydrogen content in the etching gas. Annealing at 250°C for 15min restores an order of magnitude of the intensity of the near band edge emission and the DAP and more defined features are present in the broad peak at 2.23eV.
2. low temperature PL of etched ZnSe using CH_4/H_2 RIE showed a reduction in the deep level emission which is proportional to the hydrogen content of the etch gas. Annealing at 200°C for 5min reduces the intensity of the peak related to extended dislocations and increases the intensity of the peak related to Zn vacancies.
3. Raman scattering of etched ZnTe and ZnSe did not show any evidence of damage in the form of asymmetric broadening of the LO phonon or the appearance of the symmetry forbidden TO phonon.
4. X-ray photoelectron spectroscopy (XPS) of etched ZnTe and ZnSe surfaces showed a reduction in the oxide of group II (Te and Se). This was accompanied by an increase in the group II / Zn ratio indicating that the etched surfaces are rich in group II element i.e. Te and Se.
5. XPS of CH_4/H_2 etched CdTe showed that the surfaces become Cd rich in contrast to Br/MeOH wet etched surfaces which become Te rich. The barrier height of Schottky junctions made on dry etched CdTe surfaces were in the range of 0.69-0.71eV lower than those for wet etched surfaces, namely 0.85eV. The XPS and the Schottky barrier results inter-correlate and are in agreement with the literature.

8.7. References

1. S. M. Sze in 'Physics of Semiconductor devices' 2nd ed. J. Wiley & sons (1981), pp684; also H. F. Ivey, IEEE Quantum Electron., **QE2**, 713 (1966).
2. A. Pinczuk, and E. Burstein in ' Light Scattering in Solids I', Springer (1983).
3. M. Watt, C. M. Sotomayor Torres, H. G. Arnot, and S. P. Beaumont, Semicond. Sci. Technol., **5**, 285 (1990).
4. M. Holtz, R. Zallen, O. Brafman, and S. Matteson, Phys.Rev., **B37**, 4609 (1988).
5. E. H. Roderick, and R. H. Williams in ' Metal-Semiconductor Contacts', 2nd ed. , Oxford Science Publications (1988).
6. C. Wagner, Phys. Z., **32**, 641 (1931).
7. W. Schottky, and E. Spenke, Phys. Z., **113**, 367 (1939).

8. H. A. Bethe, MIT Radiation Lab. Report (1942).
9. E. H. Roderick, J. Phys. D, **5**, 1920 (1972).
10. B. L. Smith, Ph.D. Thesis, Manchester University (1969).
11. S. W. Pang, M. W. Geis, N. N. Efremow, and G. A. Lincoln, J. Vac. Sci. Technol., **B3**, 399 (1985).
12. S. W. Pang, G. A. Lincoln, R. W. McClelland, P. D. DeGraff, M. W. Gies, and W. J. Piacentini, J. Vac. Sci. Technol., **B1**, 1334 (1983).
13. S. W. Pang, J. Electrochem. Soc., **133**, 784 (1986).
14. D. E. Aspnes, and A. Heller, J. Vac. Sci. Technol., **B1**, 602 (1983).
15. R. Cheung, S. Thoms, S. P. Beaumont, G. Doughty, V. Law, and C. D. W. Wilkinson, Electron. Lett., **23**, 857 (1987).
16. K. Yamasaki, K. Asai, K. Shimada, and T. Makimura, J. Electrochem. Soc., **129**, 2760 (1982).
17. F. H. Pollak, and M. Cardona, Phys. Rev., **172**, 816 (1968).
18. H. Leiderer, E. Jahn, M. Silberbauer, W. Kuhn, H. P. Wagner, W. Limmer, and W. Gebhardt, J. Appl. Phys., **70**, 398 (1991).
19. H. P. Wagner, W. Kuhn, and W. Gebhardt, J. Cryst. Growth., **101**, 199 (1990).
20. L. Svob, and Y. Marfaing, Solid State Comm., **58**, 343 (1986).
21. L. Svob, and Y. Marfaing, in 'Defects in Semiconductors', ed. H. J. von Bardeleben, Materials Science Forum Vol 10-12, Trans Tech Publications Ltd, Switzerland, (1986).
22. M. Singh, J. Weber, and M. Konuma, Proc 6th Trieste ICTP-IUPAP Semiconductor Symposium "Hydrogen in semiconductors: Bulk and surface properties" Eds, M. Stutzmann and J Chevallier, North Holland, The Netherlands, pp218 (1991).
23. 'Landolt-Börnstein Numerical Data and Functional Relationships in Science and Technology' , Vol 17(b), ed. O. Madelung, Springer-Verlag, Berlin (1982).
24. M. Ekawa, Y. Kawakami, T. Taguchi, and A. Hiraki, J. Cryst. Growth, **93**, 667 (1988).
25. B. A. Wilson, C. E. Bonner, R. D. Feldman, R.F. Austin, D.W. Kisker, J. J. Krajewski, and P. M. Bridenbaugh, J. Appl. Phys., **64**, 3210 (1988).
26. J. M. Meese, and Y. S. Park, in 'Radiation Damage and Defects in Semiconductors', Inst. Phys. Conf. Ser. No. 16, ed P. Baruch, IOP, London, pp51 (1973).
27. Y. Oka, and M. Cardona, Sol. St. Commun., **30**, 447 (1979).
28. M. Watt, C. M. Sotomayor Torres, R. Cheung, C. D. W. Wilkinson, H. E. G. Arnot, and S. P. Beaumont, J. Mod. Phys., **35**, 365 (1988).
29. K. K. Tiong, P. M. Amirtharaj, F. D. Pollack, and D. E. Aspnes, Appl. Phys. Lett, **44**, 122 (1984).

30. H. Gant, and W. Mönch, Surf. Sci., **105**, 217 (1981).
31. M. H. Patterson, and R. H. Williams, J. Phys. D, **11**, L83 (1978).
32. C. D. Wagner, W. M. Riggs, L. E. Davis, J. F. Moulder, and G. E. Muilenberg, 'Handbook of X-Ray Photoelectron Spectroscopy', Perkin-Elmer Corporation (1978).
33. A. Jablonski, Surface and interface Analysis, **14**, 659 (1989).
34. J. Gutowski, N Presser, and G. Kudlek, Phy. Stat. Sol. (a), **120**, 11 (1990).
35. K. Zanio in 'Semiconductors and Semimetals', Academic press volume 13, pp107 (1979).
36. I. M. Dharmadasa, W. G. Herrenden-Harker, and R. H. Williams, Appl. Phys. Lett., **48**, 1802 (1986).
37. I. M. Dharmadasa, J. M. Thornton, and R. H. Williams, Appl. Phys. Lett., **54**, 137 (1989).
38. C. D. Wagner, W. M. Riggs, L. E. Davis, and J. F. Moulder in ' Handbook of X-ray Photoelectron Spectroscopy', Perkin-Elmer, Physical Electronics Division, Eden Prairie, MI (1979).
39. Y. C. Lu, and R. S. Feigelson, J. Appl. Phys., **67**, 2583 (1990).
40. S. S. Choi, and G. Lucovsky, J. Vac. Sci. Technol., **B6**, 1198 (1988).
41. Privete communication with Dr S. Walters, Department of Physics and Astronomy, University of Wales college of Cardiff (1991).
42. J. H. Scofield, J. Electron Spectrosc. Relat. Phenom., **8**, 129 (1976).
43. D. Briggs, and M. P. Seah, Eds in ' Practical Surface Analysis by Auger and X-ray Photoelectron Spectroscopy', Wily, New York, Appendix 4 (1983).
44. G. B. Stringfellow in 'Organometallic Vapor-Phase Epitaxy: Theory and Practice, Academic Press.
45. M. Ekawa, K. Yasuda, S. Sone, Y. Sugiura, M. Saji, and A. Tanaka, J. Appl. Phys., **67**, 6865 (1990).
46. R. L. Van Mierhaeghe, R. Van de Walle, W. H. Laflere, and F. Cardon, J. Appl. Phys., **70**, 2200 (1991).
47. T. F. Kuech, J. Appl. Phys., **52**, 4874 (1981).
48. F. A. Kroger in 'The Chemistry of Imperfect Crystal', North-Holland, Amsterdam (1984).

Chapter 9: Conclusions and future work

In the work presented in this thesis, an understanding of the origin, nature and effect of damage inflicted on surfaces and sidewalls during dry etching of GaAs has been pursued. Dry etching of semiconductors can take many forms such as purely physical interaction, as in ion beam etching, or as a mixture of both physical and chemical interactions, as in reactive ion etching. Plasma discharges used for reactive ion etching are partially ionised gases composed of ions, electrons, and a host of neutral species in both ground and excited states. Many mechanisms have been postulated for the plasma-surface interaction (the etching). Neutral species interact with the semiconductor surface to produce volatile products. Positive ions bombard the surface during etching (e.g. in RIE), thereby sputtering the adsorbed reaction products. Bombarding ions also produce lattice disorder, creating active sites which extend for several monolayers below the surface, where reactions proceed at an accelerated rate.

As a result of the ion bombardment, some of the bombarding energy is passed to the crystal by a momentum transfer mechanism during the collision of the bombarding ion with the surface atoms. This energy transfer produces disordering in the crystal structure of the subsurface of the semiconductor and a change in its stoichiometry. The crystal disorder takes the form of point defects (vacancies and interstitials) and extended defects (line dislocations and dislocation loops). This disorder results in the degradation of the optical and electrical properties of the semiconductor.
In this thesis, a variety of techniques has been used to characterise the dry etching damage in GaAs and II-VI semiconductors.

The structural disorder and defects were investigated using Transmission Electron Microscopy (darkfield imaging and High Resolution) and the quality of the crystal structure was assessed using Raman scattering. The defects act as electron traps, thus reducing the conductivity of surfaces and wires(as in the surface conductivity measurements using the Transmission Line Model and cutoff width measurements of wires). The defects also introduce shallow and deep energy levels in the semiconductor band gap (Photoluminescence examination).

On the other hand, small changes in stoichiometry were observed very close to the surface (as in the X- ray Photoelectron and X-ray Excited Auger Electron Spectroscopies) which

affected the barrier height and the ideality factor of Schottky junctions. Stoichiometry changes deep into the bulk of the semiconductor were also observed using Transmission Electron Microscopy (darkfield imaging of wire sidewalls).

It was found that the factors which result in high dry etching damage are ions that bombard the surface with high energy (high dc bias in RIE), low ion mass and slow etching rates. The nature and extent of the surface damage were found to differ from the sidewall damage. The thickness of the damaged layer of reactive ion etched surfaces was found to increase initially then saturate as the etching proceeds. This is due to the fact that an equilibrium state was reached at which the rate of introduction of damage to the material is equal to the rate of removal of damaged material. On the other hand, the damage at the sidewalls appeared to be more severe than the surface damage and increased as the etching proceeded. This is due to the fact that the sidewalls are exposed to a flux of ions incident at a grazing angle and very little, if any, material is being etched from the sidewalls during etching. Moreover, the sidewalls are subjected to an additional flux of atoms that are sputtered of the surface and redeposited on the walls.

The problem of the surface and sidewall damage induced by dry etching becomes more serious if the etching of nanostructures is considered. Consequently, dry etching processes have to be devised very carefully. It is suggested that an etching process which uses relatively large mass ions with very low bombarding energy ($50eV < E_{ion} < 100eV$) and has a high etch rate would be suitable for etching nanostructures with negligible damage. However sufficiently low etch pressures have to be used to maintain the integrity of the etching process (i.e. the morphology and etch profile). It is planned that such a process is to be developed in Glasgow University using a mixture of $SiCl_4$/Xe and the ECR etcher.

In this thesis, the dry etching induced surface damage has been characterised in a novel way, for thin n^+ GaAs epitaxial layers, by measuring the surface conductance using the Transmission Line Model (TLM) technique and Hall measurements. Various dry etching processes have been investigated: for example, rf Reactive Ion Etching (rf-RIE) using CH_4/H_2 and $SiCl_4$, Electron Cyclotron Resonance (ECR-RIE) using CCl_2F_2/He and Ion Beam etching using Ar and Ne. The results of which have been compared with wet etching and damage depths have been obtained. The damage saturation effect, predicted by the theory, has been observed for the RIE GaAs. The modification in the depletion layer thickness induced by dry etching has been determined using Raman scattering of LO coupled phonon- plasmon modes for the TLM samples.

Modifications in the chemistry induced by the dry etching in the top 3nm of GaAs surfaces has been investigated using X-ray Photoelectron Spectroscopy (XPS). GaAs etched using CH_4/H_2 shows an increase in Ga oxide and As, with a decrease in arsenic oxide, while, after $SiCl_4$ etching, the same behaviour was observed, but to a different extent, within the top 3nm.

Damage to the sidewalls of nanostructures was examined using Transmission Electron Microscopy by the dark field imaging technique and High Resolution TEM. Quantum wire-like structures with widths down to 50nm etched using CH_4/H_2 showed circa similar to dislocation loops up to 7nm in diameter, as well as small voids and general disorder in the wire. Wires etched using $SiCl_4$ showed changes in stoichiometry at the edge of the wires, presumably As deficiency, however this is not in contrast with the XPS results since As segregation may occur on a larger scale deep into the wire, leading to As enrichment of the top surface but As deficiency in the bulk of the wire.
Wires made of etched-regrown material showed that the roughness of the etched surface was about 17nm and large circa were observed in both the original and the regrown material.

A high resolution etch process for GaAs has been developed using ECR-RIE in CCl_2F_2/He. The process is capable of producing nanostructures with low damage. The damage has been characterised using TLM, n^+ GaAs quantum wires, Raman scattering using LO coupled Phonon-Plasmon modes and LO phonon Raman scattering using undoped GaAs. It is, however, suggested that the damage can be reduced even further if He is eliminated from the etching gas.

A novel high resolution reactive ion etching process has been developed for a variety of binary and ternary II-VI semiconductor compounds using CH_4/H_2. This process is optimised to produce nanostructures in ZnTe, ZnSe, ZnSSe, ZnS, CdTe, CdMnTe and CdS. Dots 200nm high and 26nm in diameter have been demonstrated in ZnSe. The advantage of the process lies in the fact that exactly the same etching conditions are suitable for all II-VI Semiconductors, so that quantum wells of any variety can be easily etched.

Finally, the modifications induced by the RIE in II-VI semiconductors are investigated by XPS, Photoluminescence and Raman scattering in ZnTe and ZnSe and by XPS and Schottky diode parameter evaluation in CdTe.

The work presented in this thesis can be extended further to improve the understanding of the nature of the damage and to develop low damage processes:
A process for etching GaAs using CCl_2F_2, which can be either highly selective (etch stops at AlGaAs layer) or has high etch rate (depending on the etch parameters such as residence time) can be developed for the ECR etcher, making use of the very low dc bias (~70V).

More work is needed to investigate the properties of the regrown layer on etched surfaces using TEM wires. One particular set of experiments would be to correlate results of electrical (low temperature electronic transport measurements) and structural (TEM examination) of quantum wires fabricated in 2DEG structures. The effect of etching and regrowth on the electrical and structural properties of the 2DEG structure could also be investigated.

The preliminary results obtained from the DLTS measurements (not reported in this thesis) suggested that the etching process induces point defects into the semiconductor. However, the nature of these defects is still largely unknown. If Electron Paramagnetic Resonance is used in conjunction with DLTS, more information may be gained about the nature of these point defects. Ultimately, high resolution Scanning Tunneling Microscopy (HRSTM) in UHV could be used to image these defects by scanning a vacuum cleaved edge that is at a right angles to an etched surface. In this way, small areas could be scanned starting from the top subsurface region (under the level of the etched surface) and a quantitative profile of the defects (e.g. observation of single vacancies and point defects) could possibly be obtained.

Using the TLM method, the effect of the etching process can be characterised electrically in doped II-VI semiconductors such as ZnTe, ZnSe, and CdTe which have recently become available.
To reduce the dry etching damage, it is proposed that very low ion energies ($50eV < E_{ion} < 100eV$), such as those obtained in an ECR etcher, may produce negligible damage, whilst preserving the integrity of the etching process (i.e. the morphology and etch profile). The use of relatively large mass ions is also thought to reduce the damage, as the sputtering yield increases with ion mass.